

STUDY OF MAGNETOELECTRIC RESPONSE IN FERROELECTRIC AND FERRITE BASED COMPOSITES

Ph.D. THESIS

by

YOGESH KUMAR



**DEPARTMENT OF PHYSICS
INDIAN INSTITUTE OF TECHNOLOGY ROORKEE
ROORKEE - 247 667 (INDIA)
FEBRUARY, 2019**

STUDY OF MAGNETOELECTRIC RESPONSE IN FERROELECTRIC AND FERRITE BASED COMPOSITES

A THESIS

*Submitted in partial fulfilment of the
requirements for the award of the degree*

of

DOCTOR OF PHILOSOPHY

in

PHYSICS

by

YOGESH KUMAR



**DEPARTMENT OF PHYSICS
INDIAN INSTITUTE OF TECHNOLOGY ROORKEE
ROORKEE - 247 667 (INDIA)
FEBRUARY, 2019**

**©INDIAN INSTITUTE OF TECHNOLOGY ROORKEE, ROORKEE- 2019
ALL RIGHTS RESERVED**



INDIAN INSTITUTE OF TECHNOLOGY ROORKEE ROORKEE

CANDIDATE'S DECLARATION

I hereby certify that the work which is being presented in this thesis entitled, **“STUDY OF MAGNETOELECTRIC RESPONSE IN FERROELECTRIC AND FERRITE BASED COMPOSITES”** in partial fulfilment of the requirements for the award of the Degree of Doctor of Philosophy and submitted in the Department of Physics of the Indian Institute of Technology Roorkee, Roorkee is an authentic record of my own work carried out during a period from July, 2013 to February, 2019 under the supervision of Dr. K. L. Yadav, Professor, Department of Physics, Indian Institute of Technology Roorkee, Roorkee.

The matter presented in this thesis has not been submitted by me for the award of any other degree of this or any other Institute.

(**YOGESH KUMAR**)

This is to certify that the above statement made by the candidate is correct to the best of my knowledge.

(K. L. Yadav)
Supervisor

The Ph.D. Viva-Voce Examination of **Mr. Yogesh Kumar**, Research Scholar, has been held on August 29, 2019.

Chairman, SRC

Signature of External Examiner

This is to certify that the student has made all the corrections in the thesis.

Signature of Supervisor

Head of the Department

Date:

ABSTRACT

Multiferroics represents a class of multifunctional materials which exhibits several ferroic orders like ferroelectricity/antiferroelectricity, ferromagnetism/antiferromagnetism and ferroelasticity simultaneously. The prospect of the existence of cross coupling, generally known as magnetoelectric (ME) coupling amongst the two order parameters, specifically ferroelectricity and magnetism is the most exciting attribute of the multiferroics. The presence of ME coupling in the multiferroics permits us to control induced polarization and magnetization, with the help of magnetic and electric field respectively. ME coupling in the multiferroics allows us to exploit their uses in various potential applications including spintronics, magnetic field sensors, data storage etc. Multiferroics are divided into two categories viz. single phase and composite multiferroics. Several issues have to be addressed before using the single phase multiferroics in device applications. One is tuning of their operational temperatures because most single phase multiferroics exhibit ME coupling below room temperature and other is very low value of ME coupling associated with them.

In order to overcome the problems posed by single phase multiferroics, nowadays focus is shifted on synthesis and study of magnetoelectric composites comprising of a ferroelectric and ferrite phase simultaneously. The formidable progress in device miniaturization and their multi-functionality in late years have shifted the interest of science fraternity towards proliferation and development of magnetoelectric composites, owing to their large magnetoelectric coupling which can be exploited for use in diverse potential applications including data storage, high sensitivity magnetic field sensors, transducers etc.

Given the importance of magnetoelectric composite systems from specific application point of view and to obtain higher magnetoelectric coupling, magnetoelectric composites comprising of piezoelectric (ferroelectric) and magnetostrictive (ferrite) phase have been studied. Various phenomena associated with structural, dielectric, magnetic, ferroelectric and magnetoelectric properties of the magnetoelectric composites has to be understood for exploiting their use in novel multifunctional devices. In order to achieve this, it requires many experimental data and characterizations acquired through various possible techniques. Outlining the progress made so far on the study of magnetoelectric composites, we present in this thesis the structural, microstructural, dielectric, magnetic, ferroelectric

and magnetoelectric properties of lead-free magnetoelectric composites including $(\text{K}_{0.5}\text{Na}_{0.5})\text{NbO}_3\text{-Ni}_{0.2}\text{Co}_{0.8}\text{Fe}_2\text{O}_4$, $(\text{K}_{0.5}\text{Na}_{0.5})\text{NbO}_3\text{-CoMn}_{0.2}\text{Fe}_{1.8}\text{O}_4$, $(\text{Bi}_{0.5}\text{Na}_{0.5})\text{TiO}_3\text{-Co}_{0.8}\text{Zn}_{0.2}\text{Fe}_2\text{O}_4$, $(\text{Bi}_{0.5}\text{Na}_{0.5})\text{TiO}_3\text{-CoMn}_{0.2}\text{Fe}_{1.8}\text{O}_4$, $(\text{Bi}_{0.5}\text{Na}_{0.5})\text{TiO}_3\text{-Ni}_{0.2}\text{Co}_{0.8}\text{Fe}_2\text{O}_4$ and $(\text{K}_{0.5}\text{Na}_{0.5})\text{NbO}_3\text{-BaFe}_{12}\text{O}_{19}$.

The present thesis is divided into six chapters followed by a bibliography. A brief summary of the work presented in each of the chapter is as under:

Chapter 1 contains the literature survey of the relevant work and brief introduction for magnetoelectric effect and its origin. It also includes brief discussion about ferroelectricity, magnetism, perovskite structure, spinel ferrites, classification of multiferroics, magnetoelectric composite systems and their applications.

Chapter 2 contains a brief summary of experimental techniques and tools to be utilized in characterization of synthesized composites.

Chapter 3 deals with the study of two magnetoelectric composites namely $(x)\text{Ni}_{0.2}\text{Co}_{0.8}\text{Fe}_2\text{O}_4\text{-(1-x)}(\text{K}_{0.5}\text{Na}_{0.5})\text{NbO}_3$ and $(x)\text{CoMn}_{0.2}\text{Fe}_{1.8}\text{O}_4\text{-(1-x)}\text{K}_{0.5}\text{Na}_{0.5}\text{NbO}_3$. In the first section of this chapter we have discussed about $(x)\text{Ni}_{0.2}\text{Co}_{0.8}\text{Fe}_2\text{O}_4\text{-(1-x)}(\text{K}_{0.5}\text{Na}_{0.5})\text{NbO}_3$ (for $x = 0.0, 0.10, 0.20, 0.30, 0.40, 0.50$ and 1.0) composites synthesized using solid state reaction method. Structural analysis has been carried out by using X-ray diffraction (XRD) which confirms the existence of both the constituent phases in the composites without any intermediate phase. Dielectric properties are studied as a function of temperature at three distinct frequencies (1, 5 and 10 kHz). P-E and M-H hysteresis loops are measured which confirms the presence of ferroelectric and magnetic ordering at room temperature. Magnetization vs. temperature studies provide a better insight of magnetic ordering in the composites. Zero field cooled curves for pure ferrite and composites indicate that they undergo charge ordering, metal insulator transition commonly known as Verwey transition around 140-145 K. Magnetoelectric coupling is observed in the composites and is confirmed by measuring ME voltage coefficient (α_{ME}) corresponding to different compositions. The highest α_{ME} is found to be 5.389 mV/cm-Oe for $x = 0.20$ composition. **In the second section** of this chapter, we have discussed the structural, dielectric, ferroelectric, magnetic and magnetoelectric properties of $(x)\text{CoMn}_{0.2}\text{Fe}_{1.8}\text{O}_4\text{-(1-x)}\text{K}_{0.5}\text{Na}_{0.5}\text{NbO}_3$ (for $x = 0.0, 0.10, 0.20, 0.30, 0.40, 0.50$ and 1.0) composites synthesized using solid state reaction method. Structural and microstructural analysis of the composites has been carried out using XRD and field emission scanning

electron microscopy (FE-SEM). Dielectric properties including dielectric constant (ϵ') and dielectric loss ($\tan \delta$) are studied as a function of temperature and found to enhance with addition of ferrite. M-H hysteresis loops are obtained at 300 K and 5 K and indicate the presence of ferromagnetic ordering in the composites. Ferroelectric properties are found to decrease with addition of ferrite, unlike magnetic properties which improve with ferrite addition. ME voltage coefficient (α_{ME}) is measured which indicates the presence of ME coupling in the composites. We obtained maximum $\alpha_{ME} = 5.941$ mV/cm-Oe for $x = 0.10$ composition.

Chapter 4 deals with the study of ME composites based on $\text{Bi}_{0.5}\text{Na}_{0.5}\text{TiO}_3$ namely (x) $\text{Co}_{0.8}\text{Zn}_{0.2}\text{Fe}_2\text{O}_4-(1-x)$ $\text{Bi}_{0.5}\text{Na}_{0.5}\text{TiO}_3$, $(1-x)$ $\text{Bi}_{0.5}\text{Na}_{0.5}\text{TiO}_3-(x)$ $\text{CoMn}_{0.2}\text{Fe}_{1.8}\text{O}_4$ and (x) $\text{Bi}_{0.5}\text{Na}_{0.5}\text{TiO}_3-(1-x)$ $\text{Ni}_{0.2}\text{Co}_{0.8}\text{Fe}_2\text{O}_4$. **In the first section** of this chapter we have discussed the (x) $\text{Co}_{0.8}\text{Zn}_{0.2}\text{Fe}_2\text{O}_4-(1-x)$ $\text{Bi}_{0.5}\text{Na}_{0.5}\text{TiO}_3$ (for $x = 0.0, 0.10, 0.20, 0.30, 0.40, 0.50$ and 1.0) composites synthesized using solid state reaction method. XRD analysis confirms the presence of both the constituent phases in the composites. Average grain size of the composites is determined from FESEM micrographs and found to decrease with addition of ferrite. Dielectric response of the composites is measured as a function of temperature and frequency and found to decrease with addition of ferrite. Ferroelectric properties are diluted with addition of ferrite unlike magnetic properties. Impedance analysis suggests the negative temperature coefficient of resistance (NTCR) behaviour of the composites and indicates bulk and grain boundary contribution to the overall electric properties. Maximum α_{ME} of 7.11 mV/cm-Oe is obtained for $x = 0.10$ composition. **In the second section** of this chapter we have discussed about the $(1-x)$ $\text{Bi}_{0.5}\text{Na}_{0.5}\text{TiO}_3-(x)$ $\text{CoMn}_{0.2}\text{Fe}_{1.8}\text{O}_4$ ($x = 0.0, 0.10, 0.20, 0.30, 0.40$ and 0.50) ME composites. Dielectric response of the composites is measured as a function of temperature and frequency and is found to decrease with addition of ferrite. Addition of ferrite significantly improves the magnetization but lowers the polarization and coercive field (E_C). Impedance analysis suggests the NTCR behaviour of the composites. The composites exhibit room temperature ME coupling which shows a decreasing trend with addition of ferrite. **The third section** of this chapter discusses the structural, dielectric, magnetic and magnetoelectric properties of (x) $\text{Bi}_{0.5}\text{Na}_{0.5}\text{TiO}_3-(1-x)$ $\text{Ni}_{0.2}\text{Co}_{0.8}\text{Fe}_2\text{O}_4$ ($x = 0.30 - 0.80$) composites. XRD analysis confirms the mixed spinel-perovskite phase of the composites. Dielectric response of the composites is measured as a function of temperature and frequency which is found to enhance with addition of $\text{Bi}_{0.5}\text{Na}_{0.5}\text{TiO}_3$ (BNT). The magnetic characteristics of the composites are diluted with

addition of BNT as expected. ME coupling in the composites was found to enhance with BNT concentration up to $x = 0.60$ which exhibits highest α_{ME} of 7.538 mV/cm-Oe.

Chapter 5 deals with the study of novel lead-free ME composite viz. $(1-x)$ $(K_{0.5}Na_{0.5})NbO_3$ - (x) $BaFe_{12}O_{19}$ ($x = 0, 0.30, 0.40, 0.50$ and 1.0) synthesized using hybrid processing route in which $BaFe_{12}O_{19}$ is synthesized using sol-gel method and $(K_{0.5}Na_{0.5})NbO_3$ is synthesized using solid state reaction method. FE-SEM micrograph asserts the existence of both the individual phases and the average grain size varies between 232 – 540 nm. Dielectric properties of the composites are studied as a function of temperature and the dielectric constant of the composites was found to decrease with addition of $BaFe_{12}O_{19}$. Magnetization of the composites is found to enhance with addition of $BaFe_{12}O_{19}$ unlike coercivity and anisotropy field which show a decreasing trend. Variation of magnetization with temperature is studied and gives a hint of spin glass behaviour in the lower temperature regime. Impedance and modulus studies of the composite signify the non-Debye type of relaxation in the composites and NTCR behaviour of the composites. ME coupling of the composites is determined by measuring α_{ME} and we obtained highest value of 4.08 mV/cm-Oe for composite with $x = 0.30$.

Finally, **Chapter 6** presents a detailed and overall summary of the thesis work, which is mainly concerned with the synthesis and studies of structural, dielectric, magnetic, ferroelectric and magnetoelectric properties of lead-free ME composites under consideration. Systematic and exhaustive studies of electrical (dielectric constant and dielectric loss tangent), ferroelectric, magnetic and magnetoelectric properties of the synthesized ME composites have provided important information about the magnetoelectric coupling which makes the studied composites quite promising from application point of view.

Acknowledgements

I bow to Almighty GOD for giving me an opportunity to submit Ph. D. thesis and holding my hand through this journey. In this beautiful journey, I have been accompanied and continuously supported by many well wishers, and this is the time to express my heartfelt gratitude toward them all. I am deeply indebted to my supervisor *Prof. K. L. Yadav* for giving me the opportunity to work on this project. Without his guidance and support, I would not be able to take the necessary steps required for the completion of this phase of my thesis. His motivation and help during the period of work has been invaluable. There are not enough words to express my gratitude for his willingness to share his knowledge with me, numerous discussions and support that he give me. It would not have been possible to accomplish my scientific goals without his guidance. I consider myself fortunate to have worked under his supervision.

I would like to express my sincere thanks again to my supervisor *Prof. K.L. Yadav* as Head of Department of Physics and *Prof. Rajesh Shrivastava*, former Head of Department of Physics for making all the basic infrastructural facilities available during my research work. In addition I extend my sincerest thanks to all the members of my Student Research Committee (SRC); *Prof. B.D. Indu* (SRC chairman), *Prof. R.Nath* (Internal expert) and *Prof. A. Sil* (External expert) for their valuable remarks and suggestions throughout my research work. I also wish to convey my deep and sincere thanks to all the faculty members of Physics Department for their encouragements and support. During this course, I am also indebted to the official staff members of the Department of Physics and Institute Instrumentation Center (I. I. C.), CSIR-National Physical Laboratory, New Delhi for providing me necessary facilities to carry out my research work.

I would also like to thank all my past and present lab members; Dr. Hemant Singh, Dr. Piyush Kumar Patel, Dr. Nidhi Adhlakha, Dr. Jyoti Rani, Dr. Meera Rawat, Dr. Manjusha, Mr. Somesh, Mr. Sandeep Saini, Mr. Deepak, Ms. Smruti and Ms. Udeshwari for putting up with me and helping to make the lab a pleasant environment. The support which I have received from my friends is beyond the scope of any acknowledgement. Yet I would like to express my heartfelt thanks to my friends *Gaurav, Avijit, Dharmendra, Rohit, Sandeep, Sanjeev, Vikas, Narendra, Lalit, Pramod, Ravi, Anirudh, Sidharth, Dr. A. Raghav, Dr. A. Ray, Dr. K. Sil, Dr. Gagandeep, Dr. S. Kumar, Dr. H. Singh, Dr. T. Bag and Dr. S. Sharma* for their company and constant encouragement during this period. A

Acknowledgements

special thanks to *Gaurav, Avijit, Sandeep and Dharmendra* who were always there during my hard times.

A very special thank to *Dr. Hemant Singh, Dr. Manjusha, Dr. Piyush Patel, Dr. Nidhi* and *Dr. Meera* for enthusiastic discussions on my research work. I also express my thanks to all research scholars of the department for their support and encouragement.

I also wish to thank *Dr. R. K. Kotnala* and *Dr. Jyoti Shah* (National Physical Laboratory, New Delhi) for allowing me to use the magnetoelectric measurement facility.

I gratefully acknowledge the financial support provided by *Ministry of Human Resource and Development (MHRD)*, New Delhi, India in the form of junior and senior research fellowships during the period of research.

Vocabulary fails to put proper words expressing my sentiments and emotions towards my parents *Shri Nem Singh* and *Smt. Rajvala* and all my family members for their unconditional support, love and encouragement during the period of research.

Finally, I would like to convey the soul-felt feelings of gratitude to the almighty GOD for giving me the strength and such a nice environment that made my project possible.

(Yogesh Kumar)

Figure Captions

Figure No.	Title	Page No.
Figure 1.1	Schematic of different types of ceramics	2
Figure 1.2	Schematic of multiferroics	3
Figure 1.3	The schematic picture and phase control in ferroics and multiferroics	5
Figure 1.4	Illustration of strain mediated direct ME effect in a composite with an applied magnetic field H having magnetic layer (blue) and ferroelectric layer (pink)	8
Figure 1.5	Schematic of P-E hysteresis loop for a ferroelectric material	10
Figure 1.6	Schematic of M-H hysteresis loop for a ferromagnetic material	11
Figure 1.7	Arrangement of spins in ferro-, ferri- and antiferromagnetic material	12
Figure 1.8	Different types of antiferromagnetic ordering present in materials	13
Figure 1.9	Structure of general ABO_3 perovskite	14
Figure 1.10	Structure of typical AB_2O_4 spinel	16
Figure 2.1	General flowchart of ceramic processing	30
Figure 2.2	Schematic diagram of diffraction of X-rays from parallel planes in crystal	35
Figure 2.3	Bruker D8 Advance powder X-ray diffractometer	35
Figure 2.4	Schematic diagram of X-ray diffractometer	36
Figure 2.5	Schematic diagram showing various interaction of an electron beam with specimen	37
Figure 2.6	(a) Schematic diagram of scanning electron microscope and (b) Carl Zeiss Ultra Plus model of FE-SEM	38
Figure 2.7	Schematic diagram showing working principle of Vibrating sample magnetometer	40
Figure 2.8	(a) Block diagram of Vibrating sample magnetometer and (b) Setup of Vibrating sample magnetometer	41

Figure Captions

Figure 2.9	Schematic representation of a Josephson junction	43
Figure 2.10	(a) Schematic of DC SQUID and (b) Periodic relationship between voltage across the SQUID and the applied magnetic flux having a period of one flux quantum ϕ_0 , where $\phi_a = n\phi_0$	44
Figure 2.11	Quantum Design MPMS Evercool system with integrated Cryocooler Dewar system	44
Figure 2.12	Schematic representation of Schering bridge	46
Figure 2.13	Photograph of HIOKI 3532-50 LCR Hi Tester	46
Figure 2.14	Schematic of Sawyer-Tower circuit for P-E loop measurement	47
Figure 2.15	Schematic diagram of Magnetolectric measurement setup	48
Figure 3.1	XRD patterns of (x) $\text{Ni}_{0.2}\text{Co}_{0.8}\text{Fe}_2\text{O}_4-(1-x)$ ($\text{K}_{0.5}\text{Na}_{0.5}$) NbO_3 ($x = 0.10, 0.20, 0.30, 0.40$ and 0.50) composites along with individual KNN and NCFO phases where (asterisk, *) represents KNN and (plus, +) represents NCFO phase	55
Figure 3.2	FE-SEM micrographs of (x) $\text{Ni}_{0.2}\text{Co}_{0.8}\text{Fe}_2\text{O}_4-(1-x)$ ($\text{K}_{0.5}\text{Na}_{0.5}$) NbO_3 composites (a) $x = 0.0$, (b) $x = 0.10$, (c) $x = 0.20$, (d) $x = 0.30$, (e) $x = 0.40$, (f) $x = 0.50$ and (g) $x = 1.0$	56
Figure 3.3	EDAX images of (x) $\text{Ni}_{0.2}\text{Co}_{0.8}\text{Fe}_2\text{O}_4-(1-x)$ ($\text{K}_{0.5}\text{Na}_{0.5}$) NbO_3 (a) $x = 0.10$, (b) $x = 0.30$ and (c) $x = 0.50$ composites	57
Figure 3.4	Elemental mapping showing distribution of constituent elements in $0.30\text{Ni}_{0.2}\text{Co}_{0.8}\text{O}_4-0.70(\text{K}_{0.5}\text{Na}_{0.5})\text{NbO}_3$ composite	58
Figure 3.5	Temperature dependence of dielectric constant (ϵ') and dielectric loss ($\tan \delta$) at various frequencies for (x) $\text{Ni}_{0.2}\text{Co}_{0.8}\text{Fe}_2\text{O}_4-(1-x)$ ($\text{K}_{0.5}\text{Na}_{0.5}$) NbO_3 ($x = 0, 0.10, 0.20, 0.30, 0.40$ and 0.50) composites	60
Figure 3.6	P-E hysteresis loops of (x) $\text{Ni}_{0.2}\text{Co}_{0.8}\text{Fe}_2\text{O}_4-(1-x)$ ($\text{K}_{0.5}\text{Na}_{0.5}$) NbO_3 ($x = 0.0, 0.10, 0.20, 0.30, 0.40$ and 0.50) composites	61
Figure 3.7	Variation of remnant polarization ($2P_r$) and coercive field ($2E_c$) with NCFO content	62
Figure 3.8	(a) M-H loops of (x) $\text{Ni}_{0.2}\text{Co}_{0.8}\text{Fe}_2\text{O}_4-(1-x)$ ($\text{K}_{0.5}\text{Na}_{0.5}$) NbO_3 ($x = 0.10, 0.20, 0.30, 0.40, 0.50$ and 1.0) composites and (b) Variation of saturation magnetization (M_s) and remnant magnetization (M_r) with NCFO content	63

Figure Captions

Figure 3.9	FC and ZFC temperature dependent magnetization curves for (x) Ni _{0.2} Co _{0.8} Fe ₂ O ₄ -(1-x) (K _{0.5} Na _{0.5})NbO ₃ (x= 0.10, 0.20, 0.30, 0.40, 0.50 and 1.0) composites	64
Figure 3.10	Nyquist plots for (x) Ni _{0.2} Co _{0.8} Fe ₂ O ₄ -(1-x) (K _{0.5} Na _{0.5})NbO ₃ (x = 0.0, 0.10, 0.20, 0.30, 0.40 and 0.50) composites at 300, 350, 400, 450 and 500 °C	66
Figure 3.11	Variation of relaxation time (ln τ) with 10 ³ /T for (x) Ni _{0.2} Co _{0.8} Fe ₂ O ₄ -(1-x) (K _{0.5} Na _{0.5})NbO ₃ (x = 0.10, 0.20, 0.30, 0.40 and 0.50) composites	69
Figure 3.12	Variation of α _{ME} with DC magnetic field for (x) Ni _{0.2} Co _{0.8} Fe ₂ O ₄ -(1-x) (K _{0.5} Na _{0.5})NbO ₃ (a) x = 0.10, (b) x = 0.20, (c) x = 0.30, (d) x = 0.40, (e) x = 0.50 composites and (f) variation of α _{ME} with NCFO content, inset shows variation of resistivity with NCFO content	70
Figure 3.13	XRD patterns of (x) CoMn _{0.2} Fe _{1.8} O ₄ -(1-x) (K _{0.5} Na _{0.5})NbO ₃ (x= 0.10, 0.20, 0.30, 0.40 and 0.50) composites along with individual KNN and CMFO phases where (asterisk, *) represents KNN and (plus, +) represents the CMFO phase	72
Figure 3.14	FE-SEM micrographs of (x) CoMn _{0.2} Fe _{1.8} O ₄ -(1-x) (K _{0.5} Na _{0.5})NbO ₃ composites (a) x = 0.0, (b) x = 0.10, (c) x = 0.20, (d) x = 0.30, (e) x = 0.40, (f) x = 0.50 and (d) x = 1.0	73
Figure 3.15	EDAX images of (x) CoMn _{0.2} Fe _{1.8} O ₄ -(1-x) (K _{0.5} Na _{0.5})NbO ₃ (a) x = 0.10, (b) x = 0.30 and (c) x = 0.50 composites	74
Figure 3.16	Temperature dependence of dielectric constant (ε') and dielectric loss (tan δ) at 1, 5 and 10 kHz frequencies for (x) CoMn _{0.2} Fe _{1.8} O ₄ -(1-x) (K _{0.5} Na _{0.5})NbO ₃ (x = 0, 0.10, 0.20, 0.30, 0.40 and 0.50) composites	76
Figure 3.17	P-E hysteresis loops of (x) CoMn _{0.2} Fe _{1.8} O ₄ -(1-x) (K _{0.5} Na _{0.5})NbO ₃ (x = 0.0, 0.10, 0.20, 0.30, 0.40 and 0.50) composites	78
Figure 3.18	M-H hysteresis loops of (x) CoMn _{0.2} Fe _{1.8} O ₄ -(1-x) (K _{0.5} Na _{0.5})NbO ₃ (x = 0.10, 0.20, 0.30, 0.40, 0.50 and 1.0) composites at 300 and 5 K respectively with magnified images shown in the inset	80
Figure 3.19	Variation of magnetic parameters with CMFO content at (a) 5 and (b) 300 K	80
Figure 3.20	FC-ZFC temperature dependent magnetization curves of (x)	81

Figure Captions

	$\text{CoMn}_{0.2}\text{Fe}_{1.8}\text{O}_{4-(1-x)} (\text{K}_{0.5}\text{Na}_{0.5})\text{NbO}_3$ ($x = 0.10, 0.20, 0.30, 0.40, 0.50$ and 1.0) composites	
Figure 3.21	Variation of real part of impedance (Z') with frequency for (x) $\text{CoMn}_{0.2}\text{Fe}_{1.8}\text{O}_{4-(1-x)} (\text{K}_{0.5}\text{Na}_{0.5})\text{NbO}_3$ ($x = 0.10, 0.20, 0.30, 0.40$ and 0.50) composites at different temperatures	82
Figure 3.22	Variation of imaginary part of impedance (Z'') with frequency for (x) $\text{CoMn}_{0.2}\text{Fe}_{1.8}\text{O}_{4-(1-x)} (\text{K}_{0.5}\text{Na}_{0.5})\text{NbO}_3$ ($x = 0.10, 0.20, 0.30, 0.40$ and $x = 0.50$) composites at different temperatures	83
Figure 3.23	Nyquist plots for (x) $\text{CoMn}_{0.2}\text{Fe}_{1.8}\text{O}_{4-(1-x)} (\text{K}_{0.5}\text{Na}_{0.5})\text{NbO}_3$ ($x = 0.10, 0.20, 0.30, 0.40$ and 0.50) in the temperature range $300 - 500^\circ\text{C}$	84
Figure 3.24	Variation of α_{ME} with DC magnetic field for (x) $\text{CoMn}_{0.2}\text{Fe}_{1.8}\text{O}_{4-(1-x)} (\text{K}_{0.5}\text{Na}_{0.5})\text{NbO}_3$ (a) $x = 0.10$, (b) $x = 0.20$, (c) $x = 0.30$, (d) $x = 0.40$, (e) $x = 0.50$ composites and (f) variation of α_{ME} with CMFO content, inset shows variation of resistivity with CMFO content	87
Figure 3.25	Variation of relaxation time ($\ln \tau$) with $10^3/T$ for (x) $\text{CoMn}_{0.2}\text{Fe}_{1.8}\text{O}_{4-(1-x)} (\text{K}_{0.5}\text{Na}_{0.5})\text{NbO}_3$ ($x = 0.10, 0.20, 0.30, 0.40$ and 0.50) composites	88
Figure 4.1	XRD patterns of (x) $\text{Co}_{0.8}\text{Zn}_{0.2}\text{Fe}_2\text{O}_4-(1-x) \text{Bi}_{0.5}\text{Na}_{0.5}\text{TiO}_3$ (a) $x = 10, 20, 30, 40$ and 50 wt.% composites along with pure BNT and CZF phases and (b) XRD patterns of the composites in the angle range $31.4^\circ - 37^\circ$.	96
Figure 4.2	FE-SEM micrographs of (x) $\text{Co}_{0.8}\text{Zn}_{0.2}\text{Fe}_2\text{O}_4-(1-x) \text{Bi}_{0.5}\text{Na}_{0.5}\text{TiO}_3$ (a) BNT (b) $x = 10$, (c) $x = 20$, (d) $x = 30$, (e) $x = 40$, (f) $x = 50$ wt.% composites and (g) CZF respectively	96
Figure 4.3	Log normal distribution of grain size of (x) $\text{Co}_{0.8}\text{Zn}_{0.2}\text{Fe}_2\text{O}_4 - (1-x) \text{Bi}_{0.5}\text{Na}_{0.5}\text{TiO}_3$ (a) BNT, (b) $x=10$, (c) 20 , (d) 30 , (e) 40 , (f) 50 wt.% and (g) CZF respectively. Inset shows the average grain size	97
Figure 4.4	EDAX spectrum of (x) $\text{Co}_{0.8}\text{Zn}_{0.2}\text{Fe}_2\text{O}_4-(1-x) \text{Bi}_{0.5}\text{Na}_{0.5}\text{TiO}_3$ (a) $x = 30$ wt.% and (b) $x = 40$ wt.% composites	98
Figure 4.5	Frequency dependence of (a) dielectric constant (ϵ') and (b) dielectric loss ($\tan \delta$) for (x) $\text{Co}_{0.8}\text{Zn}_{0.2}\text{Fe}_2\text{O}_4-(1-x) \text{Bi}_{0.5}\text{Na}_{0.5}\text{TiO}_3$ ($x = 10, 20, 30, 40$ and 50 wt %) composites at room temperature	98

Figure Captions

Figure 4.6	Temperature dependence of (a) dielectric constant(ϵ') and (b) dielectric loss ($\tan \delta$) for (x) $\text{Co}_{0.8}\text{Zn}_{0.2}\text{Fe}_2\text{O}_4-(1-x)\text{Bi}_{0.5}\text{Na}_{0.5}\text{TiO}_3$ ($x = 10, 20, 30, 40,$ and 50 wt %) composites at a frequency of 1 kHz	99
Figure 4.7	Frequency dependence of AC conductivity for (x) $\text{Co}_{0.8}\text{Zn}_{0.2}\text{Fe}_2\text{O}_4 (1-x)\text{Bi}_{0.5}\text{Na}_{0.5}\text{TiO}_3$ ($x = 10, 20, 30, 40$ and 50 wt %) composites at room temperature	101
Figure 4.8	P-E hysteresis loops for (x) $\text{Co}_{0.8}\text{Zn}_{0.2}\text{Fe}_2\text{O}_4-(1-x)\text{Bi}_{0.5}\text{Na}_{0.5}\text{TiO}_3$ (a) BNT, (b) $x = 10$, (c) $x = 20$, (d) $x = 30$, (e) $x = 40$, (f) $x = 50$ wt.% composites measured at room temperature and (g) variation of remnant polarization ($2P_r$) and coercive field ($2E_C$) with CZF content	102
Figure 4.9	Complex impedance spectra of (x) $\text{Co}_{0.8}\text{Zn}_{0.2}\text{Fe}_2\text{O}_4-(1-x)\text{Bi}_{0.5}\text{Na}_{0.5}\text{TiO}_3$ ($x = 10, 20, 30, 40$ and 50 wt.%) composites measured at room temperature. Inset shows complex impedance spectra for $x = 40$ and 50 wt.% composites	104
Figure 4.10	(a) M-H hysteresis loops of (x) $\text{Co}_{0.8}\text{Zn}_{0.2}\text{Fe}_2\text{O}_4-(1-x)\text{Bi}_{0.5}\text{Na}_{0.5}\text{TiO}_3$ ($x = 10, 20, 30, 40$ and 50 wt.%) composites at room temperature and (b) variation of remnant magnetization (M_r) and coercivity (H_C) with CZF content	105
Figure 4.11	XPS Spectra of Co $2p_{3/2}$, Fe $2p_{3/2,1/2}$, Zn $2p_{3/2}$ and O $1s$ for $\text{Co}_{0.8}\text{Zn}_{0.2}\text{Fe}_2\text{O}_4$	106
Figure 4.12	Variation of α_{ME} with DC magnetic field for (x) $\text{Co}_{0.8}\text{Zn}_{0.2}\text{Fe}_2\text{O}_4-(1-x)\text{Bi}_{0.5}\text{Na}_{0.5}\text{TiO}_3$ ($x = 10, 20, 30, 40$ and 50 wt.%) composites	107
Figure 4.13	X-ray diffraction patterns of $(1-x)\text{Bi}_{0.5}\text{Na}_{0.5}\text{TiO}_3-(x)\text{CoMn}_{0.2}\text{Fe}_{1.8}\text{O}_4$ ($x = 0.10, 0.20, 0.30, 0.40$ and 0.50) composites along with BNT and CMFO phases, where (asterisk,*) represents BNT and (hash, #) represents CMFO phase	109
Figure 4.14	FE-SEM micrographs of $(1-x)\text{Bi}_{0.5}\text{Na}_{0.5}\text{TiO}_3-(x)\text{CoMn}_{0.2}\text{Fe}_{1.8}\text{O}_4$ (a) $x = 0.0$, (b) $x = 0.10$, (c) $x = 0.20$, (d) $x = 0.30$, (e) $x = 0.40$, (g) $x = 1.0$ composites and (h-i) secondary and backscattered mode for $x = 0.20$ composite	110
Figure 4.15	Frequency dependence of (a) Dielectric constant (ϵ') and (b) dielectric loss ($\tan \delta$) for $(1-x)\text{Bi}_{0.5}\text{Na}_{0.5}\text{TiO}_3-(x)\text{CoMn}_{0.2}\text{Fe}_{1.8}\text{O}_4$ ($x = 0, 0.10, 0.20, 0.30, 0.40$ and 0.50) composites	111

Figure Captions

Figure 4.16	Temperature dependence of dielectric constant for $(1-x)$ $\text{Bi}_{0.5}\text{Na}_{0.5}\text{TiO}_3$ - (x) $\text{CoMn}_{0.2}\text{Fe}_{1.8}\text{O}_4$ (a) $x = 0$, (b) $x = 0.10$, (c) $x = 0.20$, (d) $x = 0.30$, (e) $x = 0.40$, (f) $x = 0.50$ composites	112
Figure 4.17	Temperature dependence of dielectric loss for $(1-x)$ $\text{Bi}_{0.5}\text{Na}_{0.5}\text{TiO}_3$ - (x) $\text{CoMn}_{0.2}\text{Fe}_{1.8}\text{O}_4$ (a) $x = 0$, (b) $x = 0.10$, (c) $x = 0.20$, (d) $x = 0.30$, (e) $x = 0.40$, (f) $x = 0.50$ composites	114
Figure 4.18	(a) Plot of $\ln(1/\epsilon' - 1/\epsilon'_{\max})$ vs. $\ln(T - T_m)$ at a frequency of 1 kHz for $(1-x)$ $\text{Bi}_{0.5}\text{Na}_{0.5}\text{TiO}_3$ - (x) $\text{CoMn}_{0.2}\text{Fe}_{1.8}\text{O}_4$ ($x = 0, 0.10, 0.20, 0.30, 0.40$ and 0.50) composites and (b) Variation of diffusivity parameter (γ) with CMFO content	115
Figure 4.19	P-E hysteresis loops of $(1-x)$ $\text{Bi}_{0.5}\text{Na}_{0.5}\text{TiO}_3$ - (x) $\text{CoMn}_{0.2}\text{Fe}_{1.8}\text{O}_4$ (a) $x = 0.10$, (b) $x = 0.20$, (c) $x = 0.30$, (d) $x = 0.40$, (e) $x = 0.50$ composites at room temperature and (f) variation of remnant polarization ($2P_r$) and coercive field ($2E_C$) with CMFO content	116
Figure 4.20	(a) M-H hysteresis loops $(1-x)$ $\text{Bi}_{0.5}\text{Na}_{0.5}\text{TiO}_3$ - (x) $\text{CoMn}_{0.2}\text{Fe}_{1.8}\text{O}_4$ ($x = 0.10, 0.20, 0.30, 0.40, 0.50$ and 1.0) composites at room temperature and (b) variation of remnant magnetization (M_r) saturation magnetization (M_s) and magnetic moment with CMFO content	118
Figure 4.21	Variation of real part of impedance (Z') with frequency for $(1-x)$ $\text{Bi}_{0.5}\text{Na}_{0.5}\text{TiO}_3$ - (x) $\text{CoMn}_{0.2}\text{Fe}_{1.8}\text{O}_4$ (a) $x = 0$, (b) $x = 0.10$, (c) $x = 0.20$, (d) $x = 0.30$, (e) $x = 0.40$ and (f) $x = 0.50$ composites at different temperatures	119
Figure 4.22	Variation of imaginary part of impedance (Z'') with frequency for $(1-x)$ $\text{Bi}_{0.5}\text{Na}_{0.5}\text{TiO}_3$ - (x) $\text{CoMn}_{0.2}\text{Fe}_{1.8}\text{O}_4$ (a) $x = 0$, (b) $x = 0.10$, (c) $x = 0.20$, (d) $x = 0.30$, (e) $x = 0.40$ and (f) $x = 0.50$ composites at different temperatures	120
Figure 4.23	Nyquist plots for $(1-x)$ $\text{Bi}_{0.5}\text{Na}_{0.5}\text{TiO}_3$ - (x) $\text{CoMn}_{0.2}\text{Fe}_{1.8}\text{O}_4$ (a) $x = 0$, (b) $x = 0.10$, (c) $x = 0.20$, (d) $x = 0.30$, (e) $x = 0.40$ and (f) $x = 0.50$ composites	121
Figure 4.24	XPS Spectra of Co $2p_{3/2}$, Fe $2p_{3/2,1/2}$, Mn $2p_{3/2,1/2}$ and O $1s$ for $\text{CoMn}_{0.2}\text{Fe}_{1.8}\text{O}_4$	123
Figure 4.25	Variation of α_{ME} with DC magnetic field for $(1-x)$ $\text{Bi}_{0.5}\text{Na}_{0.5}\text{TiO}_3$ - (x) $\text{CoMn}_{0.2}\text{Fe}_{1.8}\text{O}_4$ (a) $x = 0.10$, (b) $x = 0.20$, (c) $x = 0.30$, (d) $x = 0.40$, (e) $x = 0.50$ and (f) variation of α_{ME} with CMFO content, inset shows the variation of resistivity with CMFO content	125

Figure 4.26	X-ray diffraction patterns of (x) $\text{Bi}_{0.5}\text{Na}_{0.5}\text{TiO}_3-(1-x)\text{Ni}_{0.2}\text{Co}_{0.8}\text{Fe}_2\text{O}_4$ ($x = 0.30-0.80$) composites along with pure BNT (*) and NCFO (+) phases	126
Figure 4.27	FE-SEM micrographs of (x) $\text{Bi}_{0.5}\text{Na}_{0.5}\text{TiO}_3-(1-x)\text{Ni}_{0.2}\text{Co}_{0.8}\text{Fe}_2\text{O}_4$ (a) $x = 0.30$, (b) $x = 0.40$, (c) $x = 0.50$, (d) $x = 0.60$, (e) $x = 0.70$, (f-g) secondary and backscattered mode for $x = 0.80$ composition	127
Figure 4.28	Frequency dependence of (a) Dielectric constant (ϵ') and (b) dielectric loss ($\tan \delta$) for (x) $\text{Bi}_{0.5}\text{Na}_{0.5}\text{TiO}_3-(1-x)\text{Ni}_{0.2}\text{Co}_{0.8}\text{Fe}_2\text{O}_4$ ($x = 0.30-0.80$) composites	128
Figure 4.29	Temperature dependence of dielectric constant for (x) $\text{Bi}_{0.5}\text{Na}_{0.5}\text{TiO}_3-(1-x)\text{Ni}_{0.2}\text{Co}_{0.8}\text{Fe}_2\text{O}_4$ (a) BNT, (b) $x = 0.30$, (c) $x = 0.40$, (d) $x = 0.50$, (e) $x = 0.60$ and (f) $x = 0.70$ composites	130
Figure 4.30	Temperature dependence of dielectric loss for (x) $\text{Bi}_{0.5}\text{Na}_{0.5}\text{TiO}_3-(1-x)\text{Ni}_{0.2}\text{Co}_{0.8}\text{Fe}_2\text{O}_4$ (a) BNT, (b) $x = 0.30$, (c) $x = 0.40$, (d) $x = 0.50$, (e) $x = 0.60$ and (f) $x = 0.70$ composites	131
Figure 4.31	(a) M-H hysteresis loops of (x) $\text{Bi}_{0.5}\text{Na}_{0.5}\text{TiO}_3-(1-x)\text{Ni}_{0.2}\text{Co}_{0.8}\text{Fe}_2\text{O}_4$ ($x = 0.30-0.80$) composites at room temperature. Inset shows magnified image of M-H loops around the origin, (b) variation of coercivity (H_C) and saturation magnetization (M_S) and (c) variation of squareness (M_r/M_S) of composites with BNT content	132
Figure 4.32	Variation of α_{ME} with DC magnetic field for (x) $\text{Bi}_{0.5}\text{Na}_{0.5}\text{TiO}_3-(1-x)\text{Ni}_{0.2}\text{Co}_{0.8}\text{Fe}_2\text{O}_4$ ($x = 0.30-0.80$) composites	134
Figure 4.33	(a) Combined plot of ME voltage coefficient, α_{ME} with DC magnetic field for (x) $\text{Bi}_{0.5}\text{Na}_{0.5}\text{TiO}_3-(1-x)\text{Ni}_{0.2}\text{Co}_{0.8}\text{Fe}_2\text{O}_4$ ($x = 0.30-0.80$) composites and (b) variation of α_{ME} with BNT content	135
Figure 4.34	XPS spectra of Ni 2p _{3/2} , Co 2p _{3/2} , Fe 2p _{3/2,1/2} and O 1s for $\text{Ni}_{0.2}\text{Co}_{0.8}\text{Fe}_2\text{O}_4$	136
Figure 5.1	XRD patterns of (1-x) $(\text{K}_{0.5}\text{Na}_{0.5})\text{NbO}_3-(x)\text{BaFe}_{12}\text{O}_{19}$ (a) pure $\text{BaFe}_{12}\text{O}_{19}$ and (b) ($x = 30, 40$ and 50 wt.%) composites along with individual KNN and BHF phases where (hash,#) represents KNN and (asterisk,*) represents the BHF phase	142
Figure 5.2	FE-SEM micrographs of (1-x) $(\text{K}_{0.5}\text{Na}_{0.5})\text{NbO}_3-(x)\text{BaFe}_{12}\text{O}_{19}$ (a) KNN (b) $x = 30$ wt.%, (c) $x = 40$ wt.%, (d) $x = 50$ wt.%	144

Figure Captions

	composites (e) BHF and (f) EDAX spectrum of composite with $x = 40$ wt.%	
Figure 5.3	Log normal distribution of grain sizes of $(1-x)$ $(\text{K}_{0.5}\text{Na}_{0.5})\text{NbO}_3$ $-(x)$ $\text{BaFe}_{12}\text{O}_{19}$ ($x = 30, 40$ and 50 wt.%) ME composite along with pure KNN and BHF phases	145
Figure 5.4	Elemental mapping showing distribution of different elements in $(1-x)$ $(\text{K}_{0.5}\text{Na}_{0.5})\text{NbO}_3$ $-(x)$ $\text{BaFe}_{12}\text{O}_{19}$ composite with $x = 40$ wt.%	146
Figure 5.5	Temperature dependence of dielectric constant (ϵ') at various frequencies for $(1-x)$ $(\text{K}_{0.5}\text{Na}_{0.5})\text{NbO}_3$ $-(x)$ $\text{BaFe}_{12}\text{O}_{19}$ (a) KNN, (b) $x = 30$ wt.%, (c) $x = 40$ wt.%, (d) $x = 50$ wt.% composites and (e) BHF	147
Figure 5.6	Frequency dependence of dielectric constant at room temperature for $(1-x)$ $(\text{K}_{0.5}\text{Na}_{0.5})\text{NbO}_3$ $-(x)$ $\text{BaFe}_{12}\text{O}_{19}$ ($x = 30, 40$ and 50 wt.%) composites	149
Figure 5.7	P-E hysteresis loops for $(1-x)$ $(\text{K}_{0.5}\text{Na}_{0.5})\text{NbO}_3$ $-(x)$ $\text{BaFe}_{12}\text{O}_{19}$ (a) KNN, (b) $x = 30$ wt.%, (c) $x = 40$ wt. %, (d) $x = 50$ wt.% composites and (e) BHF obtained at room temperature	150
Figure 5.8	M-H hysteresis loops for (a) BHF, (b) $(1-x)$ $(\text{K}_{0.5}\text{Na}_{0.5})\text{NbO}_3$ $-(x)$ $\text{BaFe}_{12}\text{O}_{19}$ ($x = 30, 40$ and 50 wt.%) composites	153
Figure 5.9	(a) Variation of saturation magnetization (M_s) and coercive field (H_c) and (b) anisotropy field (H_a) of $(1-x)$ $(\text{K}_{0.5}\text{Na}_{0.5})\text{NbO}_3$ $-(x)$ $\text{BaFe}_{12}\text{O}_{19}$ ($x = 30, 40$ and 50 wt.%) composites with BHF wt.%	153
Figure 5.10	ZFC and FC magnetization curves for $(1-x)$ $(\text{K}_{0.5}\text{Na}_{0.5})\text{NbO}_3$ $-(x)$ $\text{BaFe}_{12}\text{O}_{19}$ (a) $x = 30$ wt.%, (b) $x = 40$ wt.%, (c) $x = 50$ wt.% composites and (d) BHF	154
Figure 5.11	Equivalent circuits showing distinct effects including contributions from grain, grain boundaries and surface charge polarization	155
Figure 5.12	Nyquist plots of $(1-x)$ $(\text{K}_{0.5}\text{Na}_{0.5})\text{NbO}_3$ $-(x)$ $\text{BaFe}_{12}\text{O}_{19}$ (a) $x = 30$ wt.%, (b) $x = 40$ wt. %, (c) $x = 50$ wt.% composites 30, 50 and 100 °C and (d) Nyquist plots of composites at room temperature	156
Figure 5.13	Variation of imaginary part (M'') of modulus with frequency for $(1-x)$ $(\text{K}_{0.5}\text{Na}_{0.5})\text{NbO}_3$ $-(x)$ $\text{BaFe}_{12}\text{O}_{19}$ (a) $x = 30$ wt.%, (b) x	158

= 40 wt.% (c) $x = 50$ wt.% composites

- Figure 5.14 Combined plots of imaginary parts of modulus and impedance vs. frequency for $(1-x)$ $(\text{K}_{0.5}\text{Na}_{0.5})\text{NbO}_3$ - x $\text{BaFe}_{12}\text{O}_{19}$ (a) $x = 30$ wt.%, (b) $x = 40$ wt. %, (c) $x = 50$ wt.% composites at room temperature 159
- Figure 5.15 Variation of α_{ME} with DC magnetic field for $(1-x)$ $(\text{K}_{0.5}\text{Na}_{0.5})\text{NbO}_3$ - x $\text{BaFe}_{12}\text{O}_{19}$ (a) $x = 30$ wt.%, (b) $x = 40$ wt. %, (c) $x = 50$ wt.% composites at room temperature 160

Table Captions

Table No.	Title	Page No.
Table 3.1	Lattice parameters, grain sizes and relative densities of (x) $\text{Ni}_{0.2}\text{Co}_{0.8}\text{Fe}_2\text{O}_4-(1-x)$ ($\text{K}_{0.5}\text{Na}_{0.5}$) NbO_3 ($x = 0, 0.10, 0.20, 0.30, 0.40, 0.50$ and 1.0) ME composites	56
Table 3.2	Magnetic parameters of (x) $\text{Ni}_{0.2}\text{Co}_{0.8}\text{Fe}_2\text{O}_4-(1-x)$ ($\text{K}_{0.5}\text{Na}_{0.5}$) NbO_3 ($x = 0.10, 0.20, 0.30, 0.40, 0.50$ and 1.0) composites measured at room temperature	63
Table 3.3	The variation of AC impedance parameters for NCFO/KNN composites at different temperatures	67
Table 3.4	Lattice parameters, grain sizes and relative densities of (x) $\text{CoMn}_{0.2}\text{Fe}_{1.8}\text{O}_4-(1-x)$ ($\text{K}_{0.5}\text{Na}_{0.5}$) NbO_3 ($x = 0, 0.10, 0.20, 0.30, 0.40, 0.50$ and 1.0) ME composites	74
Table 3.5	Calculated values of remnant polarization (P_r), maximum polarization (P_{\max}) and coercive field (E_C) for CMFO/KNN composites	77
Table 3.6	Calculated values of remnant magnetization (M_r), saturation magnetization (M_S), magnetic moment (μ_B) and exchange field (H_E) for CMFO/KNN composites at 5 and 300 K	79
Table 3.7	The variation of AC impedance parameters for CMFO/KNN composites at different temperatures	86
Table 4.1	Magnetic parameters of (x) $\text{Co}_{0.8}\text{Zn}_{0.2}\text{Fe}_2\text{O}_4-(1-x)$ $\text{Bi}_{0.5}\text{Na}_{0.5}\text{TiO}_3$ ($x = 10, 20, 30, 40,$ and 50 wt.%) $\text{Bi}_{0.5}\text{Na}_{0.5}\text{TiO}_3$ composites measured at room temperature	105
Table 4.2	Comparison of α_{ME} for (x) $\text{Co}_{0.8}\text{Zn}_{0.2}\text{Fe}_2\text{O}_4-(1-x)$ $\text{Bi}_{0.5}\text{Na}_{0.5}\text{TiO}_3$ composites with other lead-free composites	108
Table 4.3	Lattice parameters, grain sizes and relative densities of (1-x) $\text{Bi}_{0.5}\text{Na}_{0.5}\text{TiO}_3-(x)$ $\text{CoMn}_{0.2}\text{Fe}_{1.8}\text{O}_4$ ($x = 0.10, 0.20, 0.30, 0.40$ and 0.50) composites	110
Table 4.4	Ferroelectric parameters of (1-x) $\text{Bi}_{0.5}\text{Na}_{0.5}\text{TiO}_3-(x)$ $\text{CoMn}_{0.2}\text{Fe}_{1.8}\text{O}_4$ ($x = 0.10, 0.20, 0.30, 0.40$ and 0.50) composites measured at room temperature	117
Table 4.5	Magnetic parameters of (1-x) $\text{Bi}_{0.5}\text{Na}_{0.5}\text{TiO}_3-(x)$ $\text{CoMn}_{0.2}\text{Fe}_{1.8}\text{O}_4$ ($x = 0.10, 0.20, 0.30, 0.40, 0.50$) composites	118

Table Captions

	measured at room temperature	
Table 4.6	The variation of AC impedance parameters for BNT/CMFO composites measured at different temperatures	122
Table 4.7	Comparison of α_{ME} for $(1-x)$ $\text{Bi}_{0.5}\text{Na}_{0.5}\text{TiO}_3$ - (x) $\text{CoMn}_{0.2}\text{Fe}_{1.8}\text{O}_4$ composites with other lead-free composites	124
Table 4.8	Lattice parameters, grain sizes and relative densities of (x) $\text{Bi}_{0.5}\text{Na}_{0.5}\text{TiO}_3$ - $(1-x)$ $\text{Ni}_{0.2}\text{Co}_{0.8}\text{Fe}_2\text{O}_4$ ($x = 0.30 - 0.80$) composites	126
Table 4.9	Magnetic parameters of (x) $\text{Bi}_{0.5}\text{Na}_{0.5}\text{TiO}_3$ - $(1-x)$ $\text{Ni}_{0.2}\text{Co}_{0.8}\text{Fe}_2\text{O}_4$ ($x = 0.30-0.80$) composites measured at room temperature	133
Table 5.1	Lattice parameters, grain sizes and relative densities of $(1-x)$ $(\text{K}_{0.5}\text{Na}_{0.5})\text{NbO}_3$ - (x) $\text{BaFe}_{12}\text{O}_{19}$ ($x = 30, 40$ and 50 wt.%) ME composites	143
Table 5.2	Magnetic parameters of $(1-x)$ $(\text{K}_{0.5}\text{Na}_{0.5})\text{NbO}_3$ - (x) $\text{BaFe}_{12}\text{O}_{19}$ ($x = 30, 40$ and 50 wt.%) ME composites	152
Table 5.3	Comparison of α_{ME} for $(1-x)$ $(\text{K}_{0.5}\text{Na}_{0.5})\text{NbO}_3$ - (x) $\text{BaFe}_{12}\text{O}_{19}$ composites with other $\text{BaFe}_{12}\text{O}_{19}$ based ME composites	160

CONTENTS

ABSTRACT	i-iv
ACKNOWLEDGEMENTS	v-vi
LIST OF FIGURES	vii-xv
LIST OF TABLES	xvii-xviii
CONTENTS	xix-xxii

Chapter No.	Title	Page No.
Chapter 1	Introduction	1-27
1.1	General Background	1
1.2	Multiferroics	3
1.3	Coupling in Multiferroics	5
1.4	Magnetoelectric (ME) Effect	6
1.5	Magnetoelectric Composites	7
1.6	Electrical Polarization	8
	1.6.1 Dielectrics	9
	1.6.2 Piezoelectrics	9
	1.6.3 Ferroelectrics	9
1.7	Magnetism	10
	1.7.1 Ferromagnetic	11
	1.7.2 Ferrimagnetic	12
	1.7.3 Antiferromagnetic	12
1.8	Magnetic Interactions	13
	1.8.1 Exchange Interaction	13
	1.8.1.1 <i>Direct Exchange</i>	13
	1.8.1.2 <i>Superexchange or Indirect Exchange</i>	14
1.9	Perovskites and Spinel Ferrites	14

Contents

1.9.1	Perovskites	14
1.9.2	Spinel Ferrites	15
1.10	Literature Review	16
1.11	Scope of Thesis	23
1.12	Objectives of the present work	24
1.13	Materials under present study	24
1.14	Organization of the thesis	25
Chapter 2	Synthesis and Characterization Techniques	29-49
2.1	Introduction	29
2.2	Synthesis Techniques	29
2.2.1	Synthesis using Solid State Reaction method	30
2.2.2	Synthesis using Sol-Gel method	32
2.3	Tools used for Characterization of Samples	33
2.3.1	X-ray Diffraction	34
	<i>Operating method of X-ray diffractometer</i>	35
2.3.2	Field Emission Scanning Electron Microscopy (FE-SEM)	36
2.3.3	Energy Dispersive X-ray Spectroscopy (EDX)	39
2.3.4	Vibrating Sample Magnetometer (VSM)	40
2.3.5	Superconducting Quantum Interference Device (SQUID)	42
2.3.6	LCR Meter	45
2.3.7	Polarization-Electric Field (P-E) Hysteresis Loop Tracer	46
2.3.8	Magnetoelectric Coupling Measurement setup	47
Chapter 3	Synthesis and Characterization of $K_{0.5}Na_{0.5}NbO_3$ based Magnetoelectric Composites	51-90
3.1	Introduction	51

3.2	Experimental Details	52
	3.2.1 <i>Synthesis of (x) Ni_{0.2}Co_{0.8}Fe₂O₄-(1-x) (K_{0.5}Na_{0.5})NbO₃ ME composite system with x = 0, 0.10, 0.20, 0.30, 0.40, 0.50 and 1.0</i>	52
	3.2.2 <i>Synthesis of (x) CoMn_{0.2}Fe_{1.8}O₄-(1-x)(K_{0.5}Na_{0.5})NbO₃ ME composite system with x = 0, 0.10, 0.20, 0.30, 0.40, 0.50 and 1.0</i>	53
	3.2.3 <i>Characterizations</i>	53
3.3	Results and Discussions	54
	3.3.1 <i>(x) Ni_{0.2}Co_{0.8}Fe₂O₄-(1-x) (K_{0.5}Na_{0.5})NbO₃ ME composite system with x = 0, 0.10, 0.20, 0.30, 0.40, 0.50 and 1.0</i>	54
	3.3.2 <i>(x) CoMn_{0.2}Fe_{1.8}O₄-(1-x) (K_{0.5}Na_{0.5})NbO₃ ME composite system with x = 0, 0.10, 0.20, 0.30, 0.40, 0.50 and 1.0</i>	72
3.4	Summary	89
Chapter 4	Synthesis and Characterization of Bi_{0.5}Na_{0.5}TiO₃ based Magnetolectric Composites	91-137
4.1	Introduction	91
4.2	Experimental Details	93
	4.2.1 <i>Synthesis of (x) Co_{0.8}Zn_{0.2}Fe₂O₄-(1-x) Bi_{0.5}Na_{0.5}TiO₃ ME composite system with x = 10, 20, 30, 40 and 50 wt. %</i>	93
	4.2.2 <i>Synthesis of (1-x) Bi_{0.5}Na_{0.5}TiO₃-(x) CoMn_{0.2}Fe_{1.8}O₄ ME composite system with x = 0.10, 0.20, 0.30, 0.40 and 0.50</i>	93
	4.2.3 <i>Synthesis of (x) Bi_{0.5}Na_{0.5}TiO₃-(1-x) Ni_{0.2}Co_{0.8}Fe₂O₄ ME composite system with x = 0.30, 0.40, 0.50, 0.60 0.70 and 0.80</i>	94
	4.2.4 <i>Characterizations</i>	95
4.3	Results and Discussions	95
	4.3.1 <i>(x) Co_{0.8}Zn_{0.2}Fe₂O₄-(1-x) Bi_{0.5}Na_{0.5}TiO₃ ME composite system with x = 10, 20, 30, 40 and 50 wt. %</i>	95

Contents

4.3.2	$(1-x) \text{Bi}_{0.5}\text{Na}_{0.5}\text{TiO}_3-x \text{CoMn}_{0.2}\text{Fe}_{1.8}\text{O}_4$ ME composite system with $x = 0.10, 0.20, 0.30, 0.40$ and 0.50	108
4.3.3	$(x) \text{Bi}_{0.5}\text{Na}_{0.5}\text{TiO}_3-(1-x) \text{Ni}_{0.2}\text{Co}_{0.8}\text{Fe}_2\text{O}_4$ ME composite system with $x = 0.30, 0.40, 0.50, 0.60, 0.70$ and 0.80	125
4.4	Summary	136
Chapter 5	Synthesis and Characterization of $\text{BaFe}_{12}\text{O}_{19}$ based Magnetolectric Composites	139-161
5.1	Introduction	135
5.2	Experimental Details	140
5.2.1	<i>Synthesis of $(1-x) (K_{0.5}\text{Na}_{0.5})\text{NbO}_3-x \text{BaFe}_{12}\text{O}_{19}$ novel ME composite system with $x=30, 40$ and 50 wt.%</i>	140
5.2.2	<i>Characterizations</i>	141
5.3	Results and Discussions	142
5.4	Summary	161
Chapter 6	Conclusions and Future Suggestions	163-165
	Bibliography	167-190
	List of Publications	191

Chapter 1

Introduction

1.1 General Background

The controllability of material properties by tailoring the composition and structure of materials through synthesis and processing meet under a vast umbrella, popularly known as Materials science and Engineering (MSE). The terms composition and structure respectively means the chemical makeup of the material and description of its atomic arrangements. The procedure of fabricating new materials or compounds from natural or manmade sources is known as “synthesis”. The framing of synthesized materials or compounds into functional constituents is known as “processing”. The correlation amongst synthesis, processing, structure and properties of materials are highlighted in materials science and transformation of these materials in practical devices comes under the scope of materials engineering [1]. Under the aegis of materials science the materials are divided into distinct group viz. metals, semiconductor, composites and ceramics. Metals comprise of atoms bound by delocalized electrons. Materials having the conductivity amid that of conductor and insulator are usually known as semiconductors. Also distinct materials or phases can be mixed together to form composites, comprising of distinct phases and exhibits the combined properties of the constituent phases. The word ceramic was derived from word “Keramikos” meaning pottery in Greek. It is generally a combination of at least two elements which may include a non metallic elemental solid and metal(s) or non metallic element solids which are synthesized by combined application of pressure and heat. Ceramic materials exhibit many interesting properties including hardness, brittleness, thermal and electrical insulation, chemically stable and resistant to oxidation. The oxide materials constitute a principal class of ceramics owing to their use in production of different materials viz. insulators, semiconductors, dielectrics, ferroelectrics, ferromagnets and magnetoresistive materials. The ceramic oxides procure huge potential for exploiting their use to a wide extent in multifunctional properties including electric, magnetic, magnetoelectric and optical properties. Figure 1.1 represents the schematic of different types of ceramic materials.

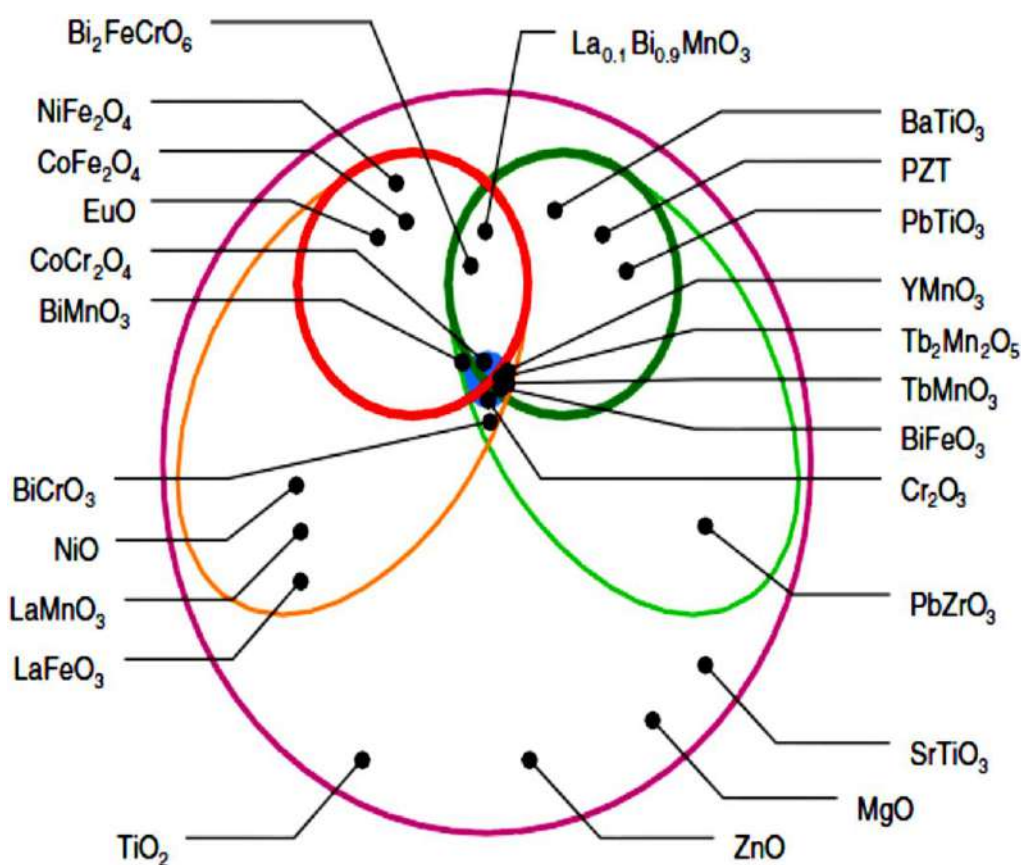


Figure 1.1 Schematic of different type of ceramics

Functional materials execute different tasks when specific physical parameters including magnetic and electric field, pressure, temperature etc. interact with their innate medium. Some oxide materials exhibit multiple functional properties concomitantly and are known as “multifunctional” materials. These oxides include materials such as BiFeO_3 , YMnO_3 etc. which show ferromagnetic and ferroelectric properties concurrently and doped ZnO , TiO_2 etc. which exhibit ferromagnetic and semiconducting properties at the same time. Ferroelectrics are quite useful in designing of electronic components for devices. In order to gain multifunctionality for device operations, combination of magnetic and ferroelectric properties has been the eye catcher for research community in late years. A lot of research is being carried out for synthesis and characterization of these multifunctional materials for exploiting their use for technological applications in miniaturization of electronic devices. On these lines we are motivated to carry out the synthesis and study of structural, dielectric, ferroelectric, magnetic and magnetoelectric properties of composites comprising of ferroelectric and ferrite phase simultaneously.

1.2 Multiferroics

The multifunctional materials which comprise of two or more types of fundamental ferroicities viz. ferroelectricity, ferromagnetism and ferroelasticity simultaneously are known as multiferroics [3]. Currently, the term multiferroic is used to represent the class of materials which exhibit ferroelectric and magnetic (ferro-, ferri- and antiferromagnetic) characteristics simultaneously [4] and even ferrotoroidicity [5]. These materials entice reasonable interest because of their potential for use in novel applications including magnetoelectric random access memories [6, 7], sensors, actuators, energy harvesting, spintronics etc [8-11] Figure 1.2 represents the schematics of multiferroics. The ferromagnetic materials exhibits general hysteresis loops in applied external magnetic field (blue in Figure 1.2), while ferroelectric material exhibit similar hysteresis in applied electric field (yellow in Figure 1.2). The multiferroic materials exhibit electric response on application of magnetic field and vice versa (green in Figure 1.2) [12].

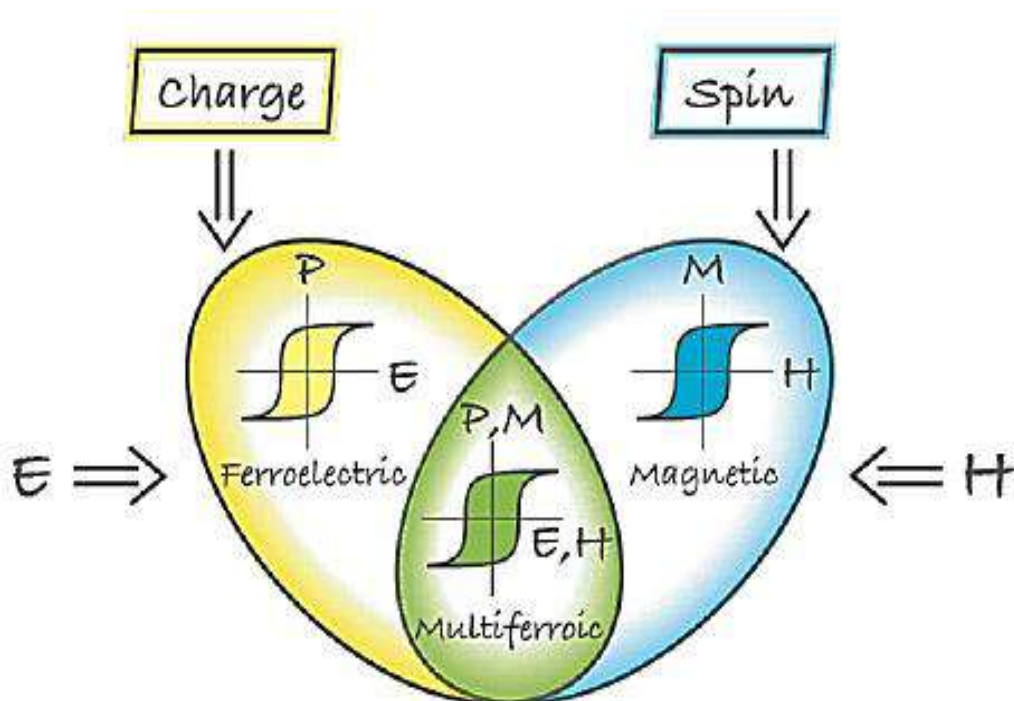


Figure 1.2 Schematic of multiferroics [12]

Ferroelectricity is the phenomenon in which the spontaneous electric polarization of the specimen can be changed through application of an electric field [13]. It is used in analogy with the term ferromagnetism, which was already known before the discovery of ferroelectricity.

Ferromagnetism is the phenomenon involving spontaneous magnetization, which can be altered by the applying of external magnetic field and saturated along the direction of the external magnetic field, below critical temperature [14]. Antiferromagnetism is also included in the definition of multiferroics currently. Materials exhibiting antiferromagnetism, have ordered magnetic moments aligned in regular pattern with neighbours that cancel each other completely with in single magnetic unit cell.

Ferroelasticity is the phenomenon in which the specimen exhibits spontaneous strain by application of stress. When ferroelastic material is subjected to mechanical stress, a phase change occurs from one phase to an equally stable phase having different crystal structure or different orientation, resulting in a spontaneous strain in the material [15].

The first recognized ferroelectric-ferromagnetic material is Nickel Iodine Boracite ($\text{Ni}_3\text{B}_7\text{O}_{13}\text{I}$) [16]. After this many multiferroic boracites compounds were synthesized. The endeavour to combine both ferromagnetic and ferroelectric properties in single system initiated in 1960's by two Russian groups: Smolenskii in St. Petersburg and Venetsev in Moscow [17]. The strategy of substitution of B site d^0 cations by magnetic d^n cations in the ferroelectric perovskites was adopted for development of new ferroelectric-ferromagnetic compounds and with this technique new ferroelectric-antiferromagnetic " $\text{Pb}(\text{Fe}_{1/2}\text{Nb}_{1/2})\text{O}_3$ " and ferroelectric-ferrimagnetic " $\text{Pb}(\text{Fe}_{2/3}\text{W}_{1/3})\text{O}_3$ " were discovered. Two distinct phenomenas viz. ferroelectricity and magnetism, exist simultaneously in the multiferroics. The presence of cross coupling among these two ferroic orders is known as magnetoelectric (ME) coupling, which is of specific importance because it is the most fascinating facet of multiferroics. History of ME effect dates back to year 1894, when Pierre Curie proposed that it is viable to directionally polarize asymmetric crystalline material under impact of externally applied magnetic field. Dzyaloshinskii [18] theoretically proposed this kind of coupling in antiferromagnetic Cr_2O_3 in 1959. Further in 1960, Astrov experimentally established this coupling by estimating the magnetization induced by externally applied electric field in Cr_2O_3 [19]. Rado and Folen also established ME coupling in Cr_2O_3 by measuring electrical signals induced by magnetization in 1961 [20]. There was dwindle in this field for next two decades because of weak ME coupling in all materials studied. The scenario started to change with the theoretical findings of N.A. Hill in the year 2000 [4]. The breakthrough in the field of multiferroics was achieved again with the detection of magnetism induced ferroelectricity in TbMn_2O_5 and TbMnO_3 [21] and hexagonal YMnO_3 [22]. The possibility of electric field control of magnetism and vice

versa is very crucial from application point of view as it leads to device miniaturization and energy efficient devices for magnetic technologies [23].

1.3 Coupling in Multiferroics

Coexistence of two distinct phenomena viz. ferromagnetism and ferroelectricity, where the spontaneous ordering of spin and orbital magnetic moments and of electric dipole moments are responsible for existence of magnetism and ferroelectricity respectively. This leads to the prospect of existence of cross coupling amongst these order parameters in multiferroics. This coupling is commonly known as Magnetolectric (ME) effect and leads to additional functionality. Figure 1.3 exhibits the phase control in distinct type of couplings present amongst different ferroic orders of multiferroics. The control of electric polarization (P) by magnetic field and control of magnetization (M) by external electric field (represented by green arrows in Figure 1.3) is the most fascinating facet in the field of multiferroics. The electric polarization (P), magnetization (M) and strain (ϵ) are controlled by electric field (E), magnetic field (H) and stress (σ) respectively.

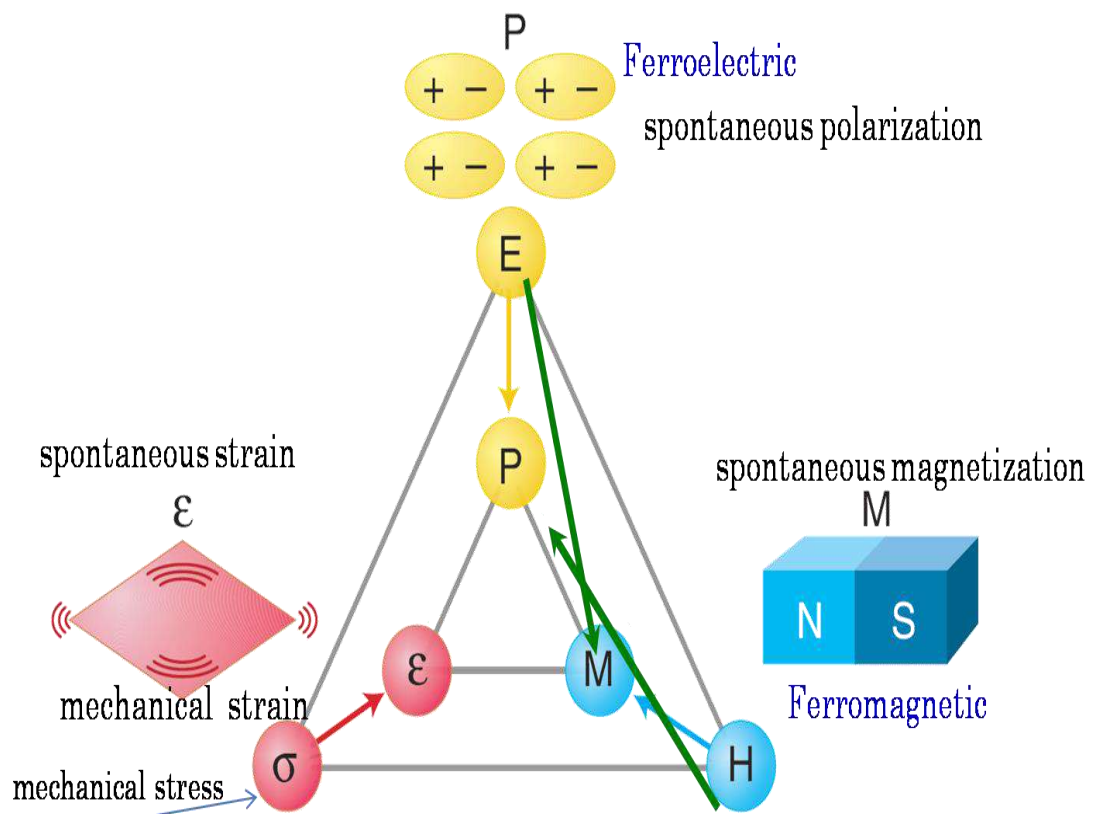


Figure 1.3 The schematic picture and phase control in ferroics and multiferroics [24]

1.4 Magnetoelectric (ME) effect

The ME effect is better understood using free energy expression in Landau theory written in terms an applied electric field, whose i^{th} component is represented by E_i and applied magnetic field with i^{th} component H_i . In an infinite stress free and homogeneous medium the free energy F can be written using Einstein summation convention [25] given by equation 1.1

$$-F(E, H) = \frac{1}{2} \varepsilon_0 \varepsilon_{ij} E_i E_j + \frac{1}{2} \mu_0 \mu_{ij} H_i H_j + \alpha_{ij} E_i H_j + \frac{\beta_{ijk}}{2} E_i H_j H_k + \frac{\gamma_{ijk}}{2} H_i E_j E_k + \dots \quad (1.1)$$

First term on the right hand side represents the contribution arising from the response due to applied electric field, where ε_0 represents the permittivity of free space and ε_{ij} represents the second rank tensor independent of E_i in non-ferroic materials. The second term of equation (1.1) represents the magnetic analogue of first term, here μ_0 represents permeability of free space and μ_{ij} is the relative permeability. The factor α_{ij} in the third term represents describes linear magnetoelectric coupling, which denotes the induction of polarization due to applied magnetic field and magnetization by applied electric field. It is to be noted that higher order magnetoelectric coefficients i.e. the third rank tensors β_{ijk} and γ_{ijk} are also possible, but not so due to their smaller magnitude than the lower order terms. On differentiating equation (1.1) with respect to E_i and then putting $E_i = 0$, along with respect to H_i and putting $H_i = 0$, gives us successive order parameters for polarization and magnetization respectively. We obtain equations (1.2, 1.3):

$$P_i = \alpha_{ij} H_j + \frac{\beta_{ijk}}{2} H_j \quad (1.2)$$

and

$$\mu_0 M_i = \alpha_{ij} E_j + \frac{\gamma_{ijk}}{2} E_j E_k + \dots \quad (1.3)$$

Moreover the ME effect is limited by the equation (1.4):

$$\alpha_{ij}^2 \leq \varepsilon_0 \mu_0 \varepsilon_{ii} \mu_{jj} \quad (1.4)$$

This shows that large ME effect can be obtained in multiferroics which have both ferroelectric and ferromagnetic phases, because ferroelectrics and ferromagnetic materials display large permittivity and permeability respectively. Large magnetoelectric coupling till date has been observed in multiferroics and composites which exhibit magnetoelectric coupling as a product property of piezoelectric and magnetostrictive effects [26]. Magnetoelectric effect in the composites will be discussed later in next section.

1.5 Magnetoelectric Composites

Depending on the constituent materials, the multiferroic magnetoelectric materials are divided into two class viz. single phase multiferroics and composites. Naturally occurring single phase multiferroics exhibiting spontaneous magnetization and polarization are very less in number. Despite displaying intrinsic ME effect, majority of single phase multiferroics either exhibit feeble ME effect at room temperature or exhibit ME effect below room temperature. So there is a big question regarding to their applications due to their low critical temperatures and feeble ME coupling at room temperature, thereby making it necessary to invent alternative materials. This gave rise to development of magnetoelectric composites, produced by combining magnetic and piezoelectric materials. The desirable property viz. ME effect can be obtained from appropriate composition of magnetostrictive and piezoelectric phases or piezoelectric and piezomagnetic phases [27]. ME composites are drawing more interest than single phase multiferroics due to their high value of ME coupling. Composites may either exhibit sum or product properties [27, 28]. The product property is more appealing as it is missing in constituent phases, but is present in composites. ME effect in composites is a product tensor property which was initially put forward by Van Suchtelen [28]. Boomgard et al. [29] formulated some prerequisites to obtain higher ME coupling in the composites which include (i) both the constituent phases of the composites should be in equilibrium with each other, (ii) magnetostriction and piezoelectric coefficients of ferrite and ferroelectric phases should be high and (iii) ferrite phase should have high resistivity in order to avert charge leakage. The ME effect in the composites may be described as product of magnetostrictive (magnetic/mechanical) effect in a ferrite phase and piezoelectric (mechanical/electrical) effect of ferroelectric phase, which is a coupled electrical and magnetic phenomenon via elastic interaction. ME coupling is an extrinsic effect relying upon the microstructure of composites and coupling interaction between interfaces of constituent phases [30]. The ME effect in the composites is basically of two types and described by equation (1.5)

$$\text{Direct ME effect} = \frac{\text{Magnetic}}{\text{Mechanical}} \times \frac{\text{Mechanical}}{\text{Electric}} \quad (1.5 \text{ (a)})$$

$$\text{Converse ME effect} = \frac{\text{Electric}}{\text{Mechanical}} \times \frac{\text{Mechanical}}{\text{Magnetic}} \quad (1.5 \text{ (b)})$$

The induction of electric polarization on application of external magnetic field is known as direct ME effect and vice-versa is known as converse ME effect. In direct ME effect ferrite phase changes its shape magnetostrictively on application of magnetic field, the strain produced in ferrite phase is transferred to ferroelectric phase via elastic interaction resulting in electric polarization due to piezoelectric effect. In converse ME effect, electric field induces strain in the ferroelectric phase ascribed to inverse piezoelectric effect. This strain is then mechanically transferred to ferrite phase, inducing a change in magnetization through piezomagnetic effect [31]. The mechanism of direct ME effect is described in Figure 1.4.

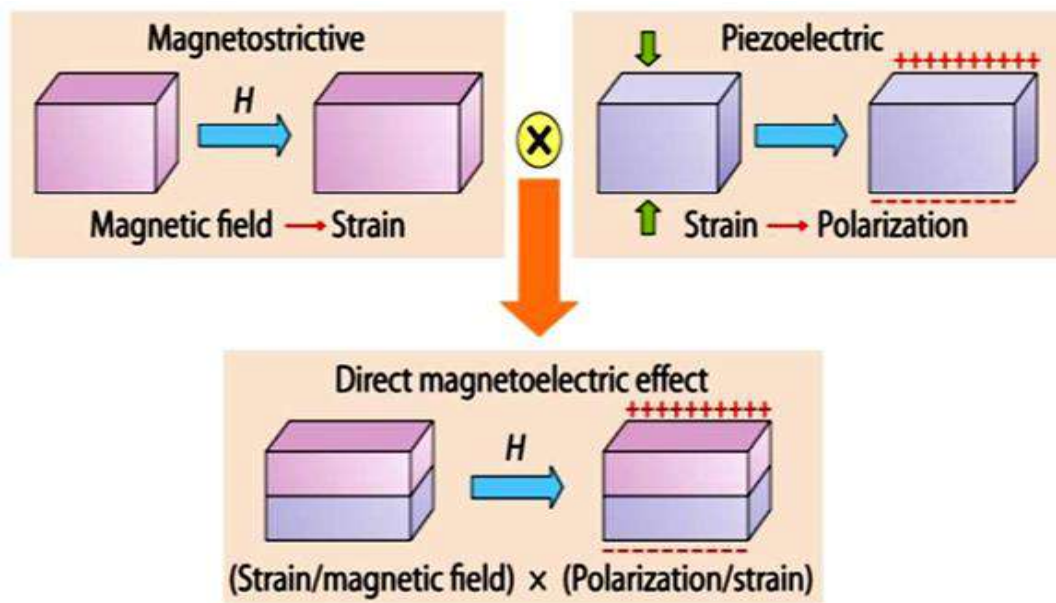


Figure 1.4 Illustration of strain mediated direct ME effect in a composite with an applied magnetic field H having magnetic layer (blue) and ferroelectric layer (pink) [31]

Electrical polarization and magnetism are most important phenomena associated with the multiferroics, composite materials and ME effect. In the next section we will discuss about these electrical and magnetic properties in detail.

1.6 Electrical Polarization

Electric polarization in materials arises due to arrangement of electric dipole moments which is determined by the crystal symmetry of a material, mainly by the lack of centre of inversion symmetry [32, 33]. In the following section we will discuss about the different classes of materials exhibiting electrical polarization.

1.6.1 Dielectrics

Dielectric material is an electrical insulator which becomes polarized with application of electric field. The displacement of positive and negative charges relative to each other produces dipole moment or polar structure [34]. The polarization in an ideal dielectric is independent of temperature and is linearly dependent on applied electric field. Polarization is reduced to zero when the applied electric field is removed. The main mechanisms for polarizations responsible for existence of dipole moment in a dielectric material are: electronic, ionic, dipolar, and space charge polarizations.

1.6.2 Piezoelectrics

The materials which are polarized by application of mechanical stress in addition to electric field are known as piezoelectric materials. Piezoelectric effect is basically divided into two type viz. direct and converse piezoelectric effect. The induction of dipole moment on application of external stress to a piezoelectric material gives rise to direct piezoelectric effect [32, 35]. On the other hand, when we apply external electric field to the piezoelectric material a strain is induced, giving rise to converse piezoelectric effect.

1.6.3 Ferroelectrics

Ferroelectric materials are insulators which exhibit spontaneous polarization in the absence of an external electric field. The materials possess polarization and its direction may be altered by application of external electric field. The polarization reversal on application of electric field is the main characteristic of ferroelectric materials. Presence of hysteresis loops for ferroelectrics unveil that for these materials the electric flux density D is not solely determined by applied electric field but also depends on their previous history as well. Generally in a macroscopic crystal the direction of spontaneous polarization is not the same, rather it comprises of large number of domains. The direction of polarization is specific in each domain, but it varies from one domain to other [37]. Figure 1.5 exhibits the polarization (P) vs. electric field (E) hysteresis loop for a ferroelectric material. Initially in the absence of electric field the overall polarization of a ferroelectric material is zero because sum of vectors corresponding dipole moments of constituent domains disappear. When we apply external electric field to the specimen, the polarization components akin to the domains which are oriented in applied field direction, grow at expense of the anti parallel domains, consequently increasing the polarization (OA). In the region AB the domains which have unfavourable direction of polarization will start

to switch along field direction with increase in magnitude of applied field and a nonlinear increase in polarization is observed. When all the domains of the material are oriented along field direction (BC) the polarization becomes saturated, thereby making the crystal a single domain.

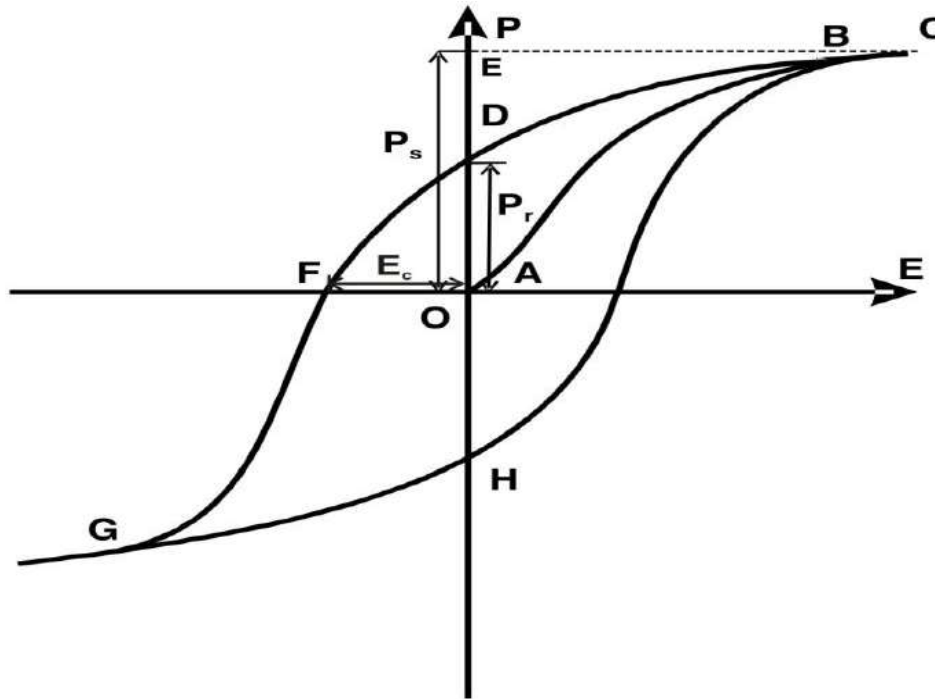


Figure 1.5 Schematic of P-E hysteresis loop for a ferroelectric material [37]

Linear extrapolation of BC to zero field provides the magnitude of saturation polarization P_s (AP). On reducing the magnitude of the field further to zero the polarization also decreases but it is not zero. This remaining polarization is known as remnant polarization P_r (AD). For reducing the polarization to zero, electric field has to be applied in opposite direction. This field is known as coercive fields E_c (OF).

1.7 Magnetism

Magnetism in materials arises mainly due to spin and orbital motion of electrons. Compounds which own partially filled d - or f - orbitals display significant magnetic moment. Depending on the ordering of magnetic moments the magnetic materials are divided into different classes which are either ferromagnetic, ferrimagnetic or antiferromagnetic in nature below a particular critical temperature. We will discuss the characteristics of different magnetic orderings in the upcoming sections.

1.7.1 Ferromagnetic

The materials which possess spontaneous magnetization in absence of magnetic field are known as ferromagnetic materials. Direction of magnetization can be altered by applying external magnetic field. The spontaneous magnetization arises due to internal “Weiss molecular field” of the magnetic ions. Ferromagnetic materials also comprise of arbitrarily oriented domains having spontaneous magnetization analogous to ferroelectrics. Total magnetization of the material is the vector sum of the magnetizations akin to constituent domains. When an external magnetic field is applied to the ferromagnetic material, it leads towards reorientation of magnetic domains resulting in magnetization (M) vs. magnetic field (H) hysteresis loop.

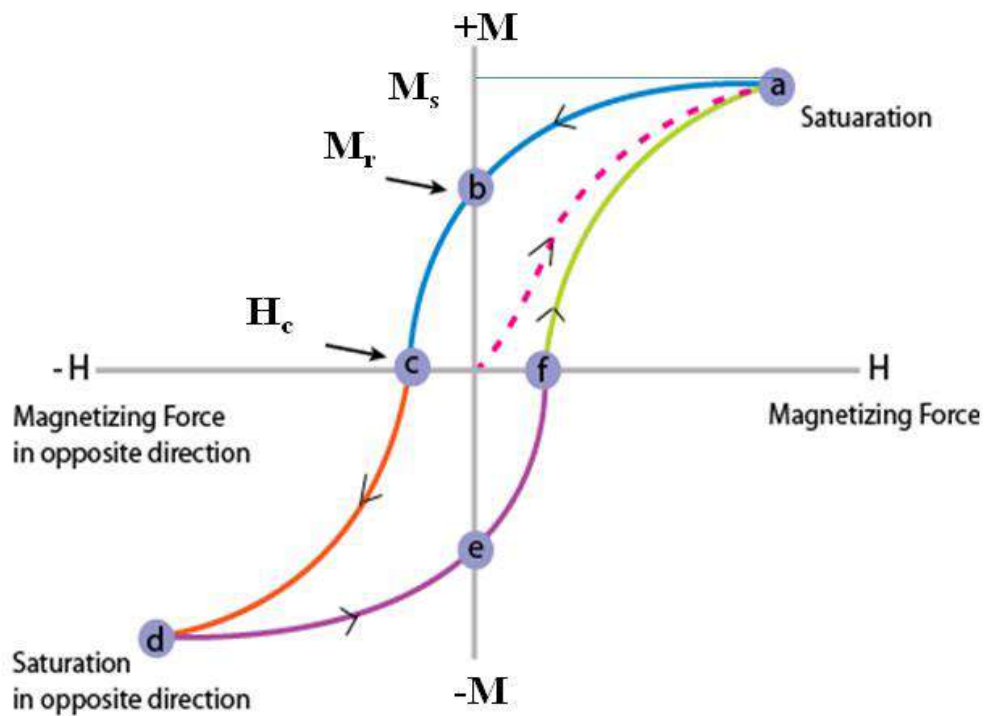


Figure 1.6 Schematic of (M-H) hysteresis loop for a ferromagnetic material [38]

Figure 1.6 exhibits the typical M-H hysteresis loop of a ferromagnetic material. On increasing the magnitude of applied magnetic field, the material gets magnetized in particular direction and saturation magnetization (M_s) is achieved when magnetization attains a highest value. The magnetization will remain finite (remnant magnetization, M_r) when the field is withdrawn. Therefore an extra magnetic field in opposite direction (coercive field, H_c) is necessary for relaxing the magnetization.




Ferromagnetic 	Below T_C , spins are aligned parallel in magnetic domains
Antiferromagnetic 	Below T_N , spins are aligned antiparallel in magnetic domains
Ferrimagnetic 	Below T_C , spins are aligned antiparallel but do not cancel

Figure 1.7 Arrangement of spins in ferro-, ferri- and antiferromagnetic material [39]

1.7.2 Ferrimagnetic

Ferrimagnetic materials act as ferromagnets with non-zero magnetic moment in the absence of magnetic field. The total magnetization results from antiparallel alignment of dissimilar magnetic moments at different sublattices (Figure 1.7). Analogous to ferromagnetic material there exist a critical temperature (T_C) above which the spontaneous magnetization disappears and ferrimagnetic material becomes paramagnetic.

1.7.3 Antiferromagnetic

The internal molecular field in the antiferromagnetic materials aligns the spin at adjacent sites in antiparallel direction. Consequently, no magnetization is observed macroscopically due to complete cancellation of spin moments. The spins can be oriented in antiparallel direction in distinct ways depending upon unit cell symmetry. Distinct kind of antiferromagnetic orderings including G-type, C-type and A-type are exhibited in Figure 1.8. The temperature above which antiferromagnetic ordering disappears is known as Neel temperature (T_N) and material becomes paramagnetic.

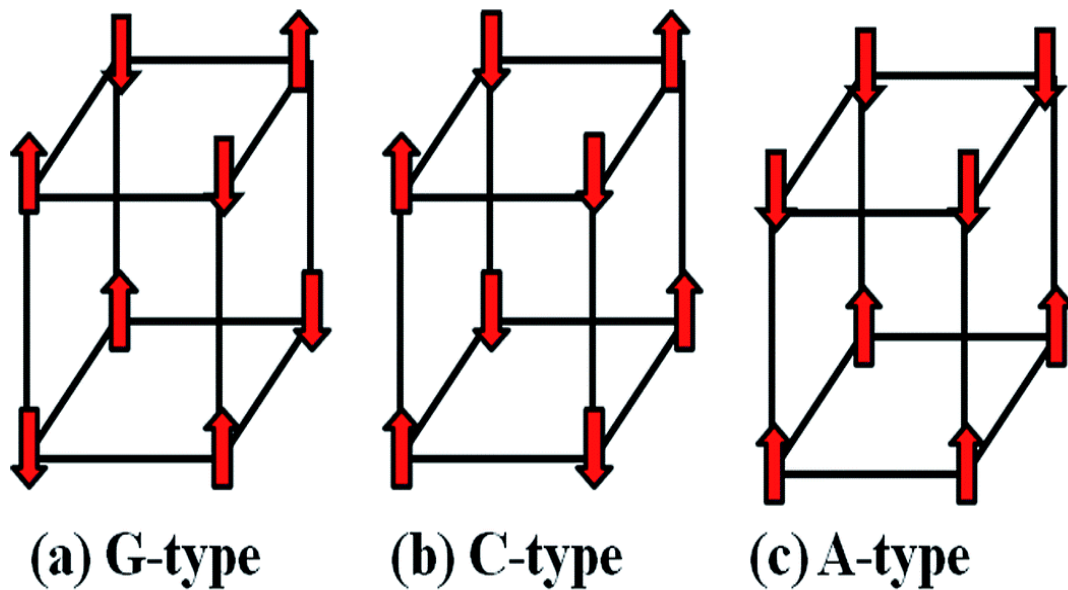


Figure 1.8 Different types of antiferromagnetic ordering present in materials [40]

(a) G-type: Here both intra plane and inter plane orderings are antiferromagnetic.

(b) C-type: Here intra plane ordering is antiferromagnetic while inter plane ordering is ferromagnetic.

(c) A-type: Here intra plane ordering is ferromagnetic while inter plane ordering is antiferromagnetic.

1.8 Magnetic interactions

1.8.1 Exchange interaction

These types of interactions are experienced by localized unpaired electrons. Atoms and ions having fixed magnetic dipoles, exhibit exchange forces due to orbital overlapping. It is a quantum mechanical perspective, allowing spin dependent coulomb interaction amidst adjacent ions. It is of two types viz. direct exchange and indirect or superexchange.

1.8.1.1 Direct Exchange

If the electrons of neighbouring atoms have overlapping orbitals, they interact via exchange interaction. This is called as direct exchange. It is so called because there is no direct or indirect help from non-magnetic atoms or ions. This type of exchange interaction is strong in the metals where magnetic ions are very adjacent to each other.

1.8.1.2 Superexchange or indirect exchange

Long range magnetic ordering is a consequence of the exchange interaction between magnetic moments. If adjacent magnetic moments interact with each other, then it is a direct exchange. If the magnetic moments interact via some midway process then it is called as indirect or superexchange [41].

1.9 Perovskites and Spinel Ferrite

1.9.1 Perovskites

Perovskites are an interesting class of materials. The name comes from mineral CaTiO_3 [42], generally known as perovskite. It was discovered by Gustav Rose in 1839 and was named after L.A. Perovski (1792-1856), a Russian mineralogist who was the first person to characterize the structure. A huge number of perovskites including BaTiO_3 were synthesized and characterized by Goldschmidt during 1924-1926 [43]. Generally, perovskites are solids having general formula ABO_3 where A and B are cations. A is located at the corners of unit cell, B is at the centre of the unit cell and oxygen at the centre of each face of unit cell (Figure 1.9). A and B cations have different charges and in original perovskite (CaTiO_3) A and B are divalent and tetravalent cations respectively.

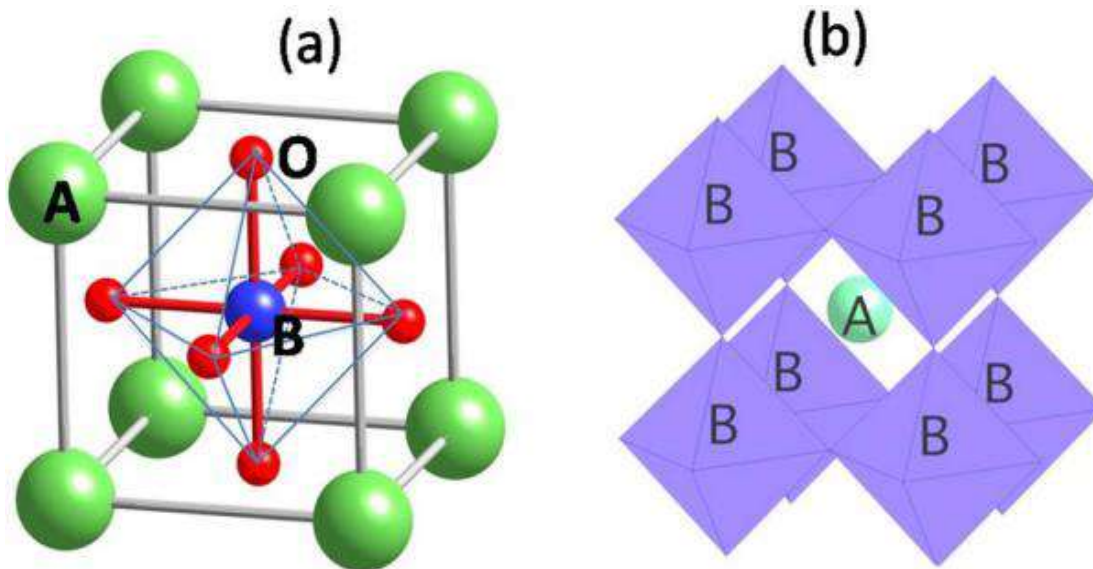


Figure 1.9 Structure of general ABO_3 perovskite

The perovskite structure contains smaller B cations with in oxygen octahedral form BO_6 and larger A cation are 12 fold coordinated by oxygen. Perovskites find their applications in various technical devices including sensors, memory devices, fuel cells etc. which is

accomplished by doping at A and B sites.

Tolerance factor ‘ t ’, has been proposed by Goldschmidt for studying the stability of perovskites which allows us to estimate the degree of distortion. Relative size of both the cations is a major factor for the geometric and thermodynamic stability of perovskites. The Goldschmidt’s tolerance factor is given by equation 1.7:

$$t = \frac{R_A + R_B}{\sqrt{2} (R_B + R_O)} \quad (1.7)$$

Where R_A , R_B and R_O are the ionic radii of cation A, cation B and O^{2-} anion respectively. Magnitude of ‘ t ’ close to one means that the cubic perovskite structure is stable. When the A cation is large and $t > 1$, the hexagonal structure is formed. It has been proposed that, a perovskite structure is expected to be stable for $0.88 \leq t \leq 1.09$. For $t = 1$ we have ideal cubic perovskite. It has been experimentally studied by Goldschmidt that for majority of cubic perovskites $0.8 \leq t \leq 0.9$ and in somewhat wider range for distorted perovskites [44].

1.9.2 Spinel Ferrites

Ferrites are mixed oxides with general formula AB_2O_4 , where A is a divalent metal ion and B is Fe^{3+} ion. The ferrites have structure identical to ‘spinel’ mineral $MgAl_2O_4$ [45]. A usual spinel lattice has a cubic close pack arrangement of oxygen atoms and the metal ions are situated in the interstices (Figure 1.10). The ordering of oxygen ions in FCC structure consists of 8 tetrahedral (A) sites and 16 octahedral B sites. Spinel display a cubic unit cell which is assumed to be made up of eight small cubes commonly known as formula units or octants having formula ‘ $A_8B_{16}O_{32}$ ’. Therefore each unit cell of spinel comprises of 32 oxide ions, 32 octahedral sites and 64 tetrahedral sites. For achieving the charge balance of ions it is necessary that the partial interstitial voids are to be occupied by positive ions. Therefore the metal ions in any stoichiometric spinel occupy only one eighth of tetrahedral and one half of octahedral sites [46]. The unit cell of a spinel compound consists of two types of octants or formula units alternately. The A type octants which are tetrahedrally coordinated by four oxide ions consists of A^{2+} ions which are situated at their centres in such a way that half corners of these cubes are occupied. In the unit cell of spinel, divalent (A^{2+}) ions are located at the corners and face centres. Trivalent (B^{3+}) ions are located at octahedral interstitial sites of B type octants in such a manner that oxide ions occupy half the corners trivalent ions occupy the other half. Depending on cationic

distribution at different crystallographic sites the spinels can be divided into two classes viz. normal spinels and inverse spinels. Normal spinels have $(A^{2+})(B^{3+})O_4$ as its chemical formula in which all divalent A ions and trivalent B ions occupy tetrahedral and octahedral sites respectively. Some examples of normal spinel ferrites are aluminates such as $FeAl_2O_4$, $MgAl_2O_4$ and some transition metal ferrites such as $ZnFe_2O_4$ etc.

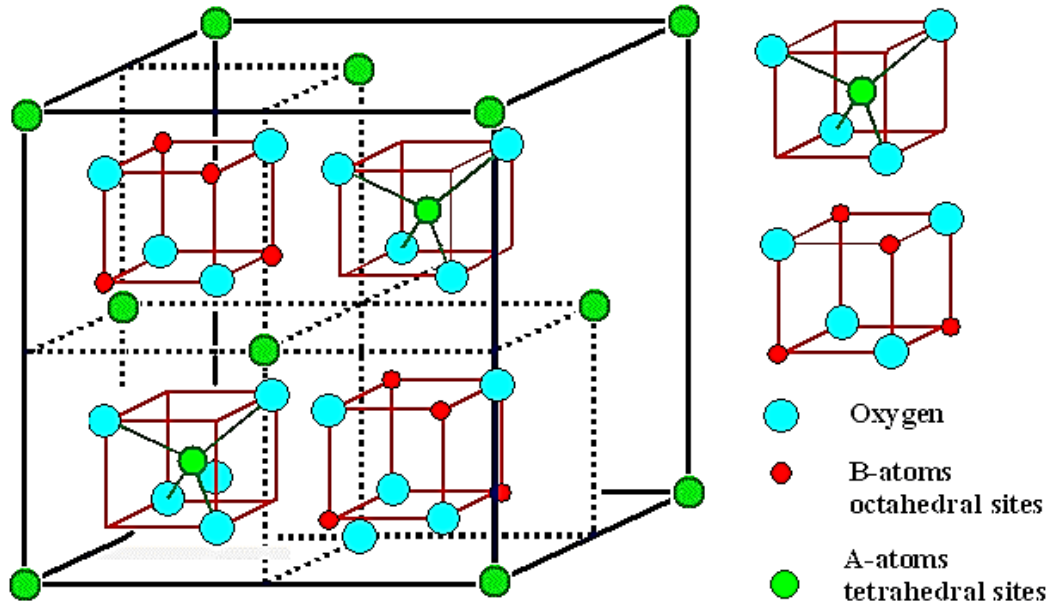


Figure 1.10 Structure of typical AB_2O_4 spinel [47]

Inverse spinel ferrites are generally represented using chemical formula $(A^{2+})(B^{3+})_2O_4$. The divalent A cations and half of trivalent B cations occupy the octahedral sites, while other half of trivalent B cations occupy tetrahedral sites. Majority of transition metal ferrites reside in this structure for eg. $CoFe_2O_4$, $NiFe_2O_4$ etc. Spinel ferrites find their use in high frequency, high power and high field applications for designing generators, motors and power transformers etc.

1.10 Literature Review

Before the discovery of ME composites, the main focus of research were the single phase multiferroics including $BiFeO_3$, $BiMnO_3$, $LuFe_2O_4$, $TbMnO_3$ etc. Out of these $BiFeO_3$ is the most studied and promising single phase multiferroic because it shows multiferroic character above room temperature and is easily synthesized. Bhattacharya et al. [48-49] observed the coupling between ferroelectric and ferromagnetic order parameters in nanoscale $BiFeO_3$. They also observed the presence of room temperature multiferroicity in $LuFeO_3$ [50]. Nath et al. [51] also confirmed multiferroicity of $BiFeO_3$ by studying their

magnetic, dielectric and magnetoedielectric properties. Garg et al. [52-53] established the magnetoelectric coupling in GaFeO_3 crystals by using dielectric and complex modulus analysis. Mitoseriu et al. [54] studied the multiferroic characteristics of double perovskite $\text{Sm}_2\text{NiMnO}_6$. They observed magnetic transitions in ZFC/FC cycle and obtained strong non linearity in its dielectric behaviour thereby confirming its multiferroicity. A.R. James et al. [55] studied the magnetic and magnetoelectric behaviour of polycrystalline four layered material $\text{LaBi}_4\text{FeTi}_3\text{O}_{15}$ which belongs to the Aurivillius family of compounds and obtained a magnetoelectric output of 2.52 mV/cm-Oe for uni-axially pressed samples. Katiyar et al. [56] studied the multiferroic properties of La doped BiFeO_3 and observed enhanced ferroelectric and ferromagnetic response with La doping. Intrinsic ME response have been widely studied in the single phase multiferroics. Despite displaying intrinsic ME effect, majority of single phase multiferroics exhibit very low ME effect at room temperature. It is a big hindrance regarding to their applications due to their low ME coupling at room temperature, thereby making it necessary to invent alternative materials. Therefore, multiferroic ME composites come into the picture. The huge development in the field of ME composites started soon after the development of ME effect as a product property in the composites as suggested by J. Van Suchetelene [57]. In ME composites mechanical connectivity is an important parameter since it involves transfer of mechanical deformation from one phase to the other. Depending on the types of connectivity schemes the composites are classified into three different categories including 0-3, 2-2 and 1-3 connectivities. In 0-3 scheme, particles of one phase with zero connectivity to itself are dispersed in other phase with connectivity to itself in all directions. 2-2 scheme comprises of alternating layers of two individual phases. Finally 1-3 connectivity scheme comprises of nanopillars of one phase in a host matrix of second phase [58]. Boomgaard et al. first synthesized bulk ME composite of CoFe_2O_4 (CFO) and BaTiO_3 (BT) and obtained very high ME voltage coefficient ($\partial E/\partial H$) of 0.13 V/cm-Oe [59]. It was obtained by unidirectional solidification of eutectic composition in quinary Fe-Co-Ti-B-O system. Despite having large ME voltage coefficient but due to complexity of this unidirectional solidification this composite didn't attract much attention. In 1990's two Russian groups: Lisnevskaya's [60, 61] and Newnham's group [62] synthesized the composites comprising of ferrites and $\text{Pb}(\text{Zr},\text{Ti})\text{O}_3$ or BaTiO_3 as ferroelectric phase using conventional sintering process. Although these composites were synthesized easily as compared to Boomgaard et al. but they exhibited lower ME effect thereby suppressing the growth in this field. The breakthrough in this field was achieved in the year 2000 with the development of PZT

based composites by Ryu et al. [63, 64] and PVDF by Mori et al. [65] having large ME effect. Majority of multiferroic ME composites initially studied, comprised of lead based ferroelectric phase and BiFeO₃ as ferrite phase. Garg et al. [66] synthesized solid solutions of BiFeO₃ and PbTiO₃ and studied their multiferroic properties. Ranjan et al. [67, 68] synthesized solid solutions of BiFeO₃ and Pb(Zr_{0.52}Ti_{0.48})O₃ and observed improved multiferroic properties with addition of Pb(Zr_{0.52}Ti_{0.48})O₃. They confirmed the magnetoelectric coupling in the solid solutions by measuring the variation of dielectric constant in presence of magnetic field indicating their small ME response. Nath et al. [69] studied the magnetoelectric coupling of PbZr_{0.53}Ti_{0.47}O₃-Ni_{0.65}Zn_{0.35}Fe₂O₄ multiferroic composites by studying their dielectric, ferroelectric and magnetic properties. Chatterjee et al. [70] directly measured the magnetoelectric coefficient (α) for the BiFeO₃-PbTiO₃ composite with La substitution. They obtained maximum α of 0.88 mV/cm-Oe, for 50:50 La substitution in BiFeO₃. Mitoseriu et al. [72] studied the PZT-Cobalt ferrite based particulate composite synthesized by fast sintering process to obtain dense microstructures and obtained highest magnetoelectric coefficient of 1.56 mV/cm-Oe. Nath et al. [73, 74] observed multiferroicity in La_{0.7}Sr_{0.3}MnO₃-ErMnO₃ composites by measuring their ferroelectric and magnetic response and studied their magnetically tunable alternating current electrical properties. Chatterjee et al. [75] observed maximum magnetoelectric coefficient of 122 mV/cm-Oe for Mn and Zn doped CoFe₂O₄-PbZr_{0.52}Ti_{0.48}O₃ particulate composite. Mitoseriu et al. [76] synthesized the BaTiO₃-Fe₂O₃ core shell structure and studied their multiferroic properties. Shannigarhi et al. [77] studied the multiferroic properties of PZT-NZF composite film and obtained an improved ferroelectric response on poling the samples in magnetic field of 1 T indicating the presence of magnetoelectric coupling. The nanocomposite thin films of BaTiO₃/CoFe₂O₄ have been synthesized by Zheng et al. [78]. Tan et al. [79] have synthesized (x) MgFe₂O₄-(1- x) BaTiO₃ multiferroic composites by solid state reaction method. The maximum ME voltage coefficient of 50.2 mV/cm-Oe was observed for $x = 0.60$ composite. The magnetodielectric (MD) effect was also studied by measuring the variation of dielectric constant under applied magnetic field of 7 kOe and MD (%) was found to be maximum for the composition with $x = 0.50$. Zhou et al. [80] synthesized the NiFe₂O₄-BaTiO₃ ME composites using hydrothermal method. The observed dielectric anomaly signifies the presence of ME coupling in the composites which was finally confirmed from ME measurements. Juneja et al. [81] synthesized (x) Ni_{0.8}Zn_{0.2}Fe₂O₄-(1- x) Ba_{0.9}Sr_{0.1}Zr_{0.04}Ti_{0.96}O₃ for $x = 0-0.15$ and obtained highest ME voltage coefficient of 1.6 mV/cm-Oe for $x = 0.10$ composition. The ME composites having

$\text{Ba}_{0.8}\text{Pb}_{0.2}\text{Zr}_{0.8}\text{Ti}_{0.2}\text{O}_3$ as ferroelectric phase with $\text{Ni}_{0.5}\text{Zn}_{0.5}\text{Fe}_2\text{O}_4$ and $\text{Ni}_{0.2}\text{Co}_{0.8}\text{Fe}_2\text{O}_4$ as ferrite phase were synthesized by Bammannavar et al. [82, 83] using double sintering method. For both the ME composites the ME voltage coefficient was measured as a function of DC magnetic field. The composites show maximum ME voltage coefficients of 536 and 698 $\mu\text{V}/\text{cm-Oe}$ for 15 % $\text{Ni}_{0.2}\text{Co}_{0.8}\text{Fe}_2\text{O}_4$ and 30 % $\text{Ni}_{0.5}\text{Zn}_{0.5}\text{Fe}_2\text{O}_4$ respectively. R.P. Tandon et al. [84] investigated $(1-x) \text{Ba}_{0.95}\text{Sr}_{0.05}\text{TiO}_3-(x) \text{Ni}_{0.8}\text{Co}_{0.2}\text{Fe}_2\text{O}_4$ ME composites and obtained maximum ME voltage coefficient of 0.711 $\text{mV}/\text{cm-Oe}$ for $x = 0.15$ composition. C.M. Kanamadi et al. [85] investigated the dielectric and magnetic properties of $(x) \text{CoFe}_2\text{O}_4-(1-x) \text{Ba}_{0.9}\text{Sr}_{0.1}\text{TiO}_3$ ME composites synthesized using conventional solid state reaction method and found the maximum ME voltage coefficient of 0.826 $\text{mV}/\text{cm-Oe}$ for $x = 0.15$ composition. Hemeda et al. [86] synthesized $(x) \text{BaTiO}_3 - (1-x) \text{Ni}_{0.8}\text{Zn}_{0.2}\text{Fe}_2\text{O}_4$ ME composites using double sintering method. They found a shift in transition temperature of BT with addition of ferrite and found a maximum ME voltage coefficient of 2.37 $\text{mV}/\text{cm-Oe}$ for $x = 0.60$ composition. The multiferroicity and ME properties of $\text{CoFe}_2\text{O}_4-\text{Pb}_{0.7}\text{Ca}_{0.3}\text{TiO}_3$ composites synthesized using metallo-organic decomposition have been investigated by Sharma et al. [87]. Mandal et al. [88] found ME response of 0.35-0.60 % at 50 kHz by varying the DC magnetic field in the range 5 - 8 T in $\text{Co}_{0.65}\text{Zn}_{0.35}\text{Fe}_2\text{O}_4-\text{PbZr}_{0.52}\text{Ti}_{0.48}\text{O}_3$ ME composites. Nath et al. [89] again investigated $\text{Co}_{0.65}\text{Zn}_{0.35}\text{Fe}_2\text{O}_4-\text{PbZr}_{0.52}\text{Ti}_{0.48}\text{O}_3$ ME composites synthesized using microwave assisted process and obtained an enhanced magnetocapacitance and dielectric property and obtained ME response of 1.02 % at a frequency of 100 kHz at 2 T. Gupta et al. [90] have synthesized $\text{BaTiO}_3-\text{Co}_{0.6}\text{Zn}_{0.4}\text{Fe}_{1.7}\text{Mn}_{0.3}\text{O}_4$ ME composite and investigated their multiferroic properties. They obtained maximum ME voltage coefficient of 73 $\text{mV}/\text{cm-Oe}$ for 50 % composition. Sodium niobate based ME composite viz. $\text{NaNbO}_3-\text{NiFe}_2\text{O}_4$ was synthesized by Ren et al. [91] using solid state method. Observation of MD effect was confirmed through increase of dielectric constant in presence of magnetic field and maximum MD coefficient of 1.27 % was obtained. Krishnaiah et al. [92] synthesized $(1-x) \text{Na}_{0.5}\text{Bi}_{0.5}\text{TiO}_3-(x) \text{CoFe}_2\text{O}_4$ particulate ME composites using solid state reaction method and studied the influence of mole % of CoFe_2O_4 on the ferroelectric, magnetic properties as well as on magnetostriction and piezoelectric coefficients and in turn their effect on ME voltage coefficient. They obtained a maximum ME voltage coefficient of 0.50 $\text{mV}/\text{cm-Oe}$ for $x = 0.35$ composite. Kanamadi et al. [93] synthesized $(x) \text{CoFe}_2\text{O}_4-(1-x) \text{Ba}_{0.8}\text{Sr}_{0.2}\text{Fe}_2\text{O}_4$ ME composites examined their dielectric and magnetic properties and obtained highest ME voltage coefficient of 0.761 $\text{mV}/\text{cm-Oe}$ for $x = 0.15$ composition. Pahuja et al. [94]

synthesized $\text{Ba}_{0.95}\text{Sr}_{0.05}\text{TiO}_3\text{-Ni}_{0.8}\text{Co}_{0.2}\text{Fe}_2\text{O}_4$ ME composite system in which ferrite phase was synthesized using three different methods and investigated the multiferroic properties of the combined system. The highest ME voltage coefficient of $\sim 0.720 \mu\text{V}/\text{cm-Oe}$ was obtained for composite system in which ferrite phase was synthesized using solid state reaction method. S.N. Babu et al. [95] investigated the magnetoelectric response of $(1-x)\text{Na}_{0.5}\text{Bi}_{0.5}\text{TiO}_3\text{-(}x\text{)NiFe}_2\text{O}_4$ composites synthesized using sol-gel method and found an optimal ME response of 0.14 % for $x = 0.67$ composition. Kadam et al. [96] investigated the electrical and magnetoelectric properties of $(x)\text{Ba}_{0.8}\text{Pb}_{0.2}\text{TiO}_3\text{-(}1-x\text{)Ni}_{0.75}\text{Co}_{0.25}\text{Fe}_2\text{O}_4$ ME composites synthesized using standard ceramic method. The variation of resistivity and thermoemf of the composites was studied with temperature. The maximum ME voltage coefficient of $140 \mu\text{V}/\text{cm-Oe}$ is obtained. Kumar et al. [97] synthesized $(x)\text{Ni}_{0.75}\text{Co}_{0.25}\text{Fe}_2\text{O}_4\text{-(}1-x\text{)BiFeO}_3$ nanocomposites using sol-gel method and investigated their magnetoelectric properties. Addition of ferrite was found to significantly affect the dielectric and magnetic properties. The maximum ME voltage coefficient of $3.09 \text{ mV}/\text{cm-Oe}$ was obtained for $x = 0.30$ composition. Miah et al. [98] investigated $(x)\text{Ba}_{0.95}\text{Sr}_{0.05}\text{TiO}_3\text{-(}1-x\text{)BiFe}_{0.9}\text{Gd}_{0.1}\text{O}_3$ multiferroic composites synthesized using conventional ceramic method and studied their dielectric, magnetic and magnetoelectric properties. The frequency dependent high temperature dielectric measurements exhibit the presence of relaxor ferroelectric behaviour of the composites and addition of $\text{Ba}_{0.95}\text{Sr}_{0.05}\text{TiO}_3$ was found to enhance the electrical conductivity of the composites. The maximum ME voltage coefficient of $1.67 \text{ mV}/\text{cm-Oe}$ was obtained for $x = 0.25$ composition. Mazumdar et al. [99] investigated the $(1-y)\text{Bi}_{0.8}\text{Dy}_{0.2}\text{FeO}_3\text{-(}y\text{)Ni}_{0.5}\text{Zn}_{0.5}\text{Fe}_2\text{O}_4$ synthesized using solid state reaction method and tuned the ME coupling of the composites with addition of ferrite. They showed the contribution of grain and grain boundary to the total resistance using complex impedance spectroscopy and also showed the enhancement in magnetization with an increase in ferrite content. They also tuned the percentage of ferrite to obtain maximum ME voltage coefficient and found maximum ME voltage coefficient of $66 \text{ mV}/\text{cm-Oe}$ for $y = 40\%$ composition. Kamble et al. [100] synthesized ME composites comprising of $\text{BaZr}_{0.08}\text{Ti}_{0.92}\text{O}_3$ as the ferroelectric phase and $\text{Co}_{1.2-y}\text{Mn}_y\text{Fe}_{1.8}\text{O}_4$ ($y = 0.0\text{-}0.40$) as the ferrite phase using conventional ceramic method. Usual dielectric dispersion was observed for the frequency dependent dielectric studies. They also observed the decrease in phase transition temperature of the ferrite phase with increase in Mn concentration. The maximum ME voltage coefficient of $2.34 \text{ mV}/\text{cm-Oe}$ was obtained for 25% $\text{CoMn}_{0.2}\text{Fe}_{1.8}\text{O}_4\text{-}75\%$ $\text{BaZr}_{0.08}\text{Ti}_{0.92}\text{O}_3$ composition. Manjusha et al. [101] synthesized $(x)\text{Bi}_{0.5}\text{Na}_{0.5}\text{TiO}_3\text{-(}1-x\text{)}$

MgFe₂O₄ multiferroic composites using solid state reaction method and investigated their multiferroic properties and obtained strained mediated ME effect in the composites. A dielectric anomaly was observed in the vicinity of phase transition temperature of Bi_{0.5}Na_{0.5}TiO₃. Significant decrease in the magnetic properties of the composites was also observed with increase of BNT content. The highest ME voltage coefficient of 4.793 mV/cm-Oe for $x = 0.80$ composition. Chavan et al. [102] investigated the ME composites based on Ba_{1-x}Sr_xTiO₃ ($x = 0.20$ and 0.30) and Co_{0.9}Ni_{0.1}Fe₂O₄ and studied their dielectric, ferroelectric, magnetodielectric and magnetoelectric properties. They obtained a maximum value of magnetocapacitance -6 % for (0.20)Co_{0.9}Ni_{0.1}Fe₂O₄-(0.80)Ba_{0.8}Sr_{0.2}TiO₃ composition while a maximum ME voltage coefficient of 5 mV/cm-Oe is obtained for (0.20)Co_{0.9}Ni_{0.1}Fe₂O₄-(0.80)Ba_{0.7}Sr_{0.3}TiO₃ composition. Rakhikrishna et al. [103] synthesized (x) (Na_{0.5}K_{0.5})_{0.94}Li_{0.06}NbO₃-(1- x) NiFe₂O₄ ME composites synthesized using solid state reaction involving co-precipitation and investigated their multiferroic properties. The effect of poling on the dielectric properties of the composites was investigated and they were found to decrease after poling. They also studied the magnetodielectric effect in the composites and obtained MD (%) coefficients of 0.8 and 1.1 for $x = 0.15$ and 0.20 compositions respectively. Highest ME voltage coefficient of 2.43×10^{-2} V/cm-Oe was obtained for $x = 0.85$ composition. Raina et al. [104] investigated the 0.1Ni_{0.8}Zn_{0.2}Fe₂O₄-0.9Pb_{1-3x/2}Sm_xZn_{0.65}Ti_{0.35}O₃ ME composites and confirmed their multiferroicity by studying magnetic (M-H) and polarization (P-E) hysteresis loops. They obtained maximum ME voltage coefficient of 22.5 mV/cm-Oe for $x = 0.03$ composition. Zhang et al. [105] synthesized BaTiO₃/(Ni_{0.5}Zn_{0.5})Fe₂O₄ multiferroic composites using in-sol precursor hybrid processing route. They have investigated the multiferroicity of the composites by measuring the P-E and M-H hysteresis loops. The composites also exhibit excellent dielectric and magnetic properties in the wide frequency range indicating the combination of high permeability and permittivity in with low losses. Yu et al. [106] synthesized (1- x) BaTiO₃-(x) (Ni_{0.3}Zn_{0.7})Fe_{2.1}O₄ ME composites and analysed the effect of ferrite addition on dielectric behaviour of the composites. Huang et al. [107] synthesized ME composite comprising of Ni_{0.55}Zn_{0.45}Fe_{2.03}O₄ as a ferrite phase and BaTiO₃ as the ferroelectric phase. They observed a maximum value of 1.27 % for MD coefficient and the composites exhibit the excellent magnetic and dielectric properties after certain amount of ferrite concentration was achieved. Song et al. [108] synthesized Ni_{0.83}Co_{0.15}Cu_{0.02}Fe_{1.9}O_{4- δ} -Na_{0.5}Bi_{0.5}TiO₃ multiferroic composites using spark plasma sintering in addition to ball milling. They investigated the multiferroic properties by measuring P-E and M-H

hysteresis loops for the composites. The composites were found to exhibit excellent combination of magnetization and coercivity. The composites were found to have large ME voltage sensitivity having maximum ME voltage coefficient of 663 mV/cm-Oe at an applied DC magnetic field of 5 kOe. Testino et al. [109] prepared multiferroic composites comprising of BaTiO₃ as ferroelectric and Ni_{0.5}Zn_{0.5}Fe₂O₄ as ferrite phase by solid state reaction and co precipitation method and obtained higher density and uniform microstructures with latter process. They investigated the dielectric and magnetic properties indicating the presence of ME coupling in the composites and obtained a dilution in magnetic properties with addition of BaTiO₃. The composites exhibit a ferroelectric – paraelectric phase transition due to BaTiO₃ phase indicating the presence of ferroelectric order at room temperature. R.K. Kotnala et al. [110] synthesized (1-x) BiFeO₃-(x) BaTiO₃ ME composites using sol-gel method and investigated their dielectric, magnetic and calorimetric properties. Sol-gel method provided the large surface area required for effective ME coupling. They confirmed the presence of ME coupling using dynamic method and obtained maximum ME voltage coefficient of 2.74 mV/cm-Oe for x = 0.10 composition. E.V. Ramana et al. [111] synthesized (1-x) Na_{0.5}Bi_{0.5}TiO₃-(x) BiFeO₃ multiferroic composites using acetic assisted sol-gel method and studied their ME properties using magnetometry and piezoresponse force microscopy (PFM). PFM indicated an improved polarization. Magnetic studies indicated the room temperature weak ferromagnetic characteristics in all the compositions. Maximum ME voltage coefficient of 9 mV/cm-Oe was obtained for x = 0.60 composition. A.S. Priya et al. [112] synthesized BiFeO₃-BaTiO₃ composites with doped BiFeO₃ using solid state reaction method and investigated their multiferroic properties. They synthesized 0.85Bi_{0.95}Dy_{0.05}Fe_{0.98}Cu_{0.02}O₃-0.15BaTiO₃ (BDFCO-BT) and 0.85Bi_{0.95}Dy_{0.05}FeO₃-0.15BaTiO₃ (BDFO-BT). They observed improved magnetic and ME properties as compared to undoped BiFeO₃. They obtained maximum ME voltage coefficient of 3.2x10⁻³ mV/cm-Oe for BDFCO-BT composite. Chen et al. [113] synthesized crystalline solutions of 0.57(Bi_{1-x}La_x)FeO₃-0.43PbTiO₃ for (x = 0, 0.10, 0.20 and 0.30) using solid state reaction method and studied their multiferroic properties. They found enhanced dielectric, magnetic and ferroelectric properties with La substitution. Liu et al. [114] synthesized (x) CoFe₂O₄-(1-x) BiFeO₃ mixed spinel perovskite nanocomposites using sol-gel method. They studied the effects of annealing temperature and concentration of CoFe₂O₄ on the magnetic and magnetoelectric properties of the composites. The effect of DC magnetic field and frequency of applied AC field on the ME coupling of the composites was also analyzed and they obtained ME

voltage coefficient of 285 mV/cm-Oe for 0.30CoFe₂O₄-0.70BiFeO₃ composite at applied field frequency of 50 kHz.

1.11 Scope of the thesis

The composites based on ferroelectrics and ferrites have allured considerable recognition over the previous decades because of their multifunctionalities with tunable electric and magnetic properties. Presence of high magnetoelectricity in these multiferroic composites as compared to single phase multiferroics has compelled the researchers to shift their focus towards these composites and explore in them the ways to achieve higher magnetoelectricity.

Ferroelectric ceramics came into light circa 1940's with the discovery of ferroelectricity as the source of peculiar large dielectric constant in barium titanate (BaTiO₃) capacitors. Since then the ferroelectrics have been widely used in distinct applications including piezoelectric transducers, high dielectric constant capacitors, positive temperature coefficient devices etc. Ferroelectric materials based on two compounds viz. barium titanate and lead zirconate titanate, have controlled the field of ferroelectricity since its inception. Till date Barium Titanate is widely used in different applications and many multiferroic composites have been synthesized using it as their ferroelectric phase. On the other hand taking into account the toxicity of lead based compounds, their harmful effects on the human health and possibility of environmental pollution over their use in the long run limit their use in distinct applications. Keeping these facts in mind we were motivated to synthesize the multiferroic composites which have their ferroelectric phase other than the materials discussed above. Bismuth sodium titanate, (Bi_{0.5}Na_{0.5})TiO₃ (BNT) has ABO₃ perovskite structure and is a well established ferroelectric material having excellent dielectric and piezoelectric properties. Potassium sodium niobate, (K_{0.5}Na_{0.5})NbO₃ (KNN) is also regarded as good prospect for ferroelectric ceramics. It shows large piezoelectric longitudinal response, high planar coupling coefficient, large remnant polarization and coercive field.

From the viewpoint of specific applications of the ME composites, it becomes necessary to understand the different phenomena related to individual ferroelectric and ferrite phases constituting the ME composites. To execute this, it is necessary to extract as many distinct experimental data possible by using different experimental techniques. Along the lines of advancement made till now in the field of ME composites as discussed

in the earlier sections, this thesis discusses about the synthesis and characterizations of BNT and KNN based ME composites with $\text{Ni}_{0.2}\text{Co}_{0.8}\text{Fe}_2\text{O}_4$, $\text{Co}_{0.8}\text{Zn}_{0.2}\text{Fe}_2\text{O}_4$, $\text{CoMn}_{0.2}\text{Fe}_{1.8}\text{O}_4$ and $\text{BaFe}_{12}\text{O}_{19}$. The structural, dielectric, magnetic, ferroelectric, electric and magnetoelectric properties of the composites have been examined using various characterization techniques.

1.12 Objectives of the present work

The main objective of our research work is to synthesize and perform the systematic characterizations in order to tune the magnetoelectric response of different lead-free multiferroic composites comprising of different ferroelectric and ferrite phases.

For achieving these objectives the following steps are adopted:

- Synthesis of $(\text{K}_{0.5}\text{Na}_{0.5})\text{NbO}_3$ (KNN) based multiferroic composites viz. $(\text{K}_{0.5}\text{Na}_{0.5})\text{NbO}_3\text{-Ni}_{0.2}\text{Co}_{0.8}\text{Fe}_2\text{O}_4$ and $(\text{K}_{0.5}\text{Na}_{0.5})\text{NbO}_3\text{-CoMn}_{0.2}\text{Fe}_{1.8}\text{O}_4$
- Synthesis of $\text{Bi}_{0.5}\text{Na}_{0.5}\text{TiO}_3$ (BNT) based multiferroic composites viz. $\text{Bi}_{0.5}\text{Na}_{0.5}\text{TiO}_3\text{-Co}_{0.8}\text{Zn}_{0.2}\text{Fe}_2\text{O}_4$, $\text{Bi}_{0.5}\text{Na}_{0.5}\text{TiO}_3\text{-CoMn}_{0.2}\text{Fe}_{1.8}\text{O}_4$ and $\text{Bi}_{0.5}\text{Na}_{0.5}\text{TiO}_3\text{-Ni}_{0.2}\text{Co}_{0.8}\text{Fe}_2\text{O}_4$.
- Synthesis of Barium hexaferrite ($\text{BaFe}_{12}\text{O}_{19}$) based composites viz. $\text{BaFe}_{12}\text{O}_{19}\text{-}(\text{K}_{0.5}\text{Na}_{0.5})\text{NbO}_3$.
- Investigation and analysis of phase formation, dielectric, ferroelectric, magnetic and magnetoelectric properties of the synthesized multiferroic composites.

1.13 Materials under present study

In the investigations presented in this thesis work, the following polycrystalline multiferroic composites have been synthesized and subsequently their structural, microstructural, dielectric, magnetic, ferroelectric and magnetoelectric properties have been studied. The value of x has been chosen in such a way that no structural deformation takes place.

Group I

(a) $x \text{ Ni}_{0.2}\text{Co}_{0.8}\text{Fe}_2\text{O}_4\text{-}(1-x) (\text{K}_{0.5}\text{Na}_{0.5})\text{NbO}_3$ where $x = 0, 0.10, 0.20, 0.30, 0.40$ and 0.50

(b) $x \text{ CoMn}_{0.2}\text{Fe}_{1.8}\text{O}_4\text{-}(1-x) (\text{K}_{0.5}\text{Na}_{0.5})\text{NbO}_3$ where $x = 0, 0.10, 0.20, 0.30, 0.40$ and 0.50

Group II

- (a) $(1-x) \text{Bi}_{0.5}\text{Na}_{0.5}\text{TiO}_3-x \text{Co}_{0.8}\text{Zn}_{0.2}\text{Fe}_2\text{O}_4$ where $x = 0, 0.10, 0.20, 0.30, 0.40$ and 0.50
- (b) $(1-x) \text{Bi}_{0.5}\text{Na}_{0.5}\text{TiO}_3-x \text{CoMn}_{0.2}\text{Fe}_{1.8}\text{O}_4$ where $x = 0, 0.10, 0.20, 0.30, 0.40$ and 0.50
- (c) $x \text{Bi}_{0.5}\text{Na}_{0.5}\text{TiO}_3-(1-x) \text{Ni}_{0.2}\text{Co}_{0.8}\text{Fe}_2\text{O}_4$ where $x = 0, 0.10, 0.20, 0.30, 0.40, 0.50, 0.60, 0.70$ and 0.80 .

Group III

- (a) $(1-x) (\text{K}_{0.5}\text{Na}_{0.5})\text{NbO}_3-x \text{BaFe}_{12}\text{O}_{19}$ where $x = 0, 0.30, 0.40, 0.50$ and 1.0

1.14 Organization of the thesis

The thesis work is presented in six chapters followed by a bibliography. A brief outline of the work done chapter wise is described below.

The current **chapter 1** consists of an introduction to the backdrop and main motivation along with the scope of the research work. The same is assisted by pertinent literature survey to set the blueprint of the thesis work. Moreover this chapter also gives a brief insight and fundamental aspects of ferroelectrics, perovskites and spinel structure, magnetoelectric coupling and multiferroics (single phase and magnetoelectric composites).

Chapter 2 describes the experimental techniques, principles and equipments used in the research work. The main experimental techniques utilized for the characterization of synthesized composites were X-ray diffractometer (XRD), Field emission scanning electron microscopy (FE-SEM), Superconducting quantum interference devices (SQUID), vibrating sample magnetometer (VSM), LCR meter for dielectric and complex impedance spectroscopy measurement, Polarization-Electric field (P-E) hysteresis loop and magnetoelectric coupling measurement.

In **Chapter 3** we present a systematic study on synthesis and characterizations of two different magnetoelectric composites comprising of $\text{K}_{0.5}\text{Na}_{0.5}\text{NbO}_3$ as their ferroelectric phase and $\text{Ni}_{0.2}\text{Co}_{0.8}\text{Fe}_2\text{O}_4$ and $\text{CoMn}_{0.2}\text{Fe}_{1.8}\text{O}_4$ as ferrite phases which are discussed below:

- (i) $x \text{Ni}_{0.2}\text{Co}_{0.8}\text{Fe}_2\text{O}_4-(1-x) (\text{K}_{0.5}\text{Na}_{0.5})\text{NbO}_3$ with $x = 0, 0.10, 0.20, 0.30, 0.40$ and **0.50**

- (ii) (x) $\text{CoMn}_{0.2}\text{Fe}_{1.8}\text{O}_4-(1-x) (\text{K}_{0.5}\text{Na}_{0.5})\text{NbO}_3$ with $x = 0, 0.10, 0.20, 0.30, 0.40$ and **0.50**

The first and second sections of this chapter deals with synthesis and characterization of ME composites with general formula (x) $\text{Ni}_{0.2}\text{Co}_{0.8}\text{Fe}_2\text{O}_4-(1-x) (\text{K}_{0.5}\text{Na}_{0.5})\text{NbO}_3$ ($x = 0, 0.10, 0.20, 0.30, 0.40, 0.50$) and (x) $\text{CoMn}_{0.2}\text{Fe}_{1.8}\text{O}_4-(1-x) (\text{K}_{0.5}\text{Na}_{0.5})\text{NbO}_3$ ($x = 0, 0.10, 0.20, 0.30, 0.40, 0.50$) respectively, synthesized using solid state reaction method. We have investigated and reported the structural, dielectric, ferroelectric, magnetic, complex impedance spectroscopy and magnetoelectric properties of the synthesized composites. In addition to this we have investigated and discussed the effect of addition of ferrite phase on the dielectric, magnetic, ferroelectric impedance and magnetoelectric properties of the synthesized composites.

Chapter 4 presents a systematic study on synthesis and characterizations of ME composites having $\text{Bi}_{0.5}\text{Na}_{0.5}\text{TiO}_3$ as the ferroelectric phase and $\text{Co}_{0.8}\text{Zn}_{0.2}\text{Fe}_2\text{O}_4$, $\text{CoMn}_{0.2}\text{Fe}_{1.8}\text{O}_4$ and $\text{Ni}_{0.2}\text{Co}_{0.8}\text{Fe}_2\text{O}_4$ as their ferrite phases which are discussed below:

- (i) $(1-x) \text{Bi}_{0.5}\text{Na}_{0.5}\text{TiO}_3-(x) \text{Co}_{0.8}\text{Zn}_{0.2}\text{Fe}_2\text{O}_4$ with $x = 0.10, 0.20, 0.30, 0.40$ and **0.50**
(ii) $(1-x) \text{Bi}_{0.5}\text{Na}_{0.5}\text{TiO}_3-(x) \text{CoMn}_{0.2}\text{Fe}_{1.8}\text{O}_4$ with $x = 0.10, 0.20, 0.30, 0.40$ and **0.50**
(iii) (x) $\text{Bi}_{0.5}\text{Na}_{0.5}\text{TiO}_3-(1-x) \text{Ni}_{0.2}\text{Co}_{0.8}\text{Fe}_2\text{O}_4$ with $x = 0.30, 0.40, 0.50, 0.60, 0.70$ and **0.80**

In the first, second and third section of this chapter we deal with the synthesis and characterizations of the distinct lead-free ME composites with general formula $(1-x) \text{Bi}_{0.5}\text{Na}_{0.5}\text{TiO}_3-(x) \text{Co}_{0.8}\text{Zn}_{0.2}\text{Fe}_2\text{O}_4$, $(1-x) \text{Bi}_{0.5}\text{Na}_{0.5}\text{TiO}_3-(x) \text{CoMn}_{0.2}\text{Fe}_{1.8}\text{O}_4$ and (x) $\text{Bi}_{0.5}\text{Na}_{0.5}\text{TiO}_3-(1-x) \text{Ni}_{0.2}\text{Co}_{0.8}\text{Fe}_2\text{O}_4$ respectively, synthesized using solid state reaction method. In the respective sections we have studied and reported the structural, dielectric, magnetic, ferroelectric, complex impedance spectroscopy and magnetoelectric properties of the respective composites. Further, we have also investigated and discussed the effect of ferrite or ferroelectric phases in the respective sections on the dielectric, magnetic, ferroelectric, impedance and magnetoelectric properties of the synthesized composites.

Chapter 5 presents a systematic study on synthesis and characterizations of ME composites with general formula $(1-x) (\text{K}_{0.5}\text{Na}_{0.5})\text{NbO}_3-(x) \text{BaFe}_{12}\text{O}_{19}$ ($x = 0, 0.30, 0.40, 0.50$ and 1.0) comprising of $(\text{K}_{0.5}\text{Na}_{0.5})\text{NbO}_3$ as ferroelectric and $\text{BaFe}_{12}\text{O}_{19}$ as ferrite phase

synthesized using hybrid processing route. We have investigated and reported the structural, dielectric, magnetic, ferroelectric, impedance and magnetoelectric properties of the synthesized composites and analyzed the effect of addition of BaFe₁₂O₁₉ on the respective properties.

Chapter 6 provides a comprehensive summary of the work done for the thesis, which largely deals with synthesis and organized study of structural, dielectric, magnetic, electric and magnetoelectric properties of lead-free ME composites under inspection. The room temperature structural study of lead-free ME composites based on distinct ferroelectric and ferrite phases have been done using powder diffraction technique and FE-SEM to confirm the phase purity and structure of synthesized composites. Furthermore, we performed organized and comprehensive studies of electrical (dielectric constant, loss, P-E loops and complex impedance spectroscopy), magnetic and magnetic field induced electric polarization (magnetoelectric) properties of abovementioned lead-free ME composites under inspection. These studies have provided useful insights about their multiferroic properties and magnetoelectric coupling.

Chapter 2

Synthesis and Characterization Techniques

2.1 Introduction

Materials science plays a pivotal role in the development of society. Characterization is the major step for designing and developing the different varieties of new materials. The use of high purity raw materials including ceramics, polymers and composites etc. is necessary for chemical processing and synthesis of high technological components, industrial applications and research. Since nowadays particle size of the materials is reduced to nano regime, therefore the characterization techniques involved are to be employed with better resolution in order to obtain the information about the material at the atomic level. The studied properties of the materials depend on the range of size over which they are measured. While studying the bulk materials the microscopic details become averaged. Distinct properties of the materials including ferroelectric, mechanical and ferromagnetic are changed when these are measured in micrometer or nanometer range [115, 116]. Nanoparticles have gained interest of research fraternity because they act as a bridge between bulk materials and molecular or atomic structure. A bulk material exhibits physical properties which remain constant regardless of the size. But this is not true at nanoscale because the size dependent properties are generally observed. Hence, as the size of the material approaches to nanoscale, the number of atoms present at the surface becomes significant. The huge driving force for diffusion of nanoparticles is imparted by the large surface area to volume ratio at high temperatures. Therefore, nanoparticles can be sintered at low temperatures over a short period of time as compared to large particles.

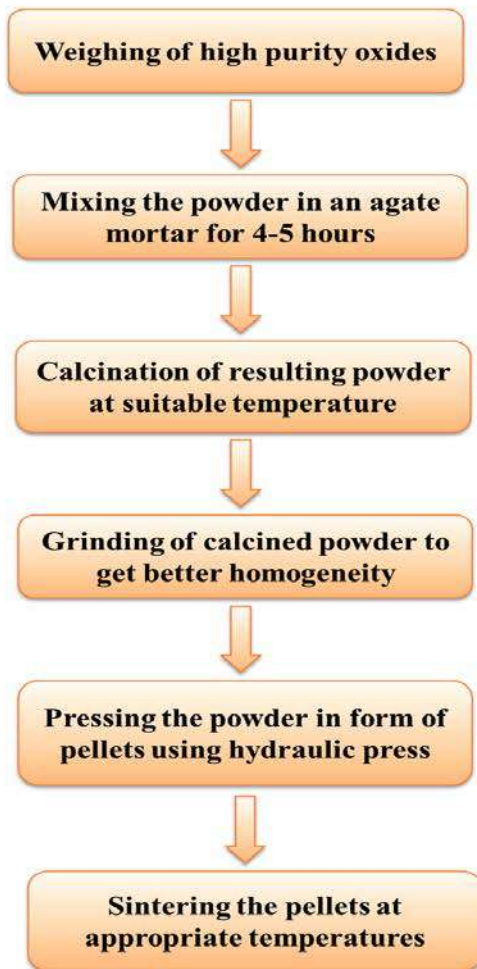
The main aim of current thesis work is directed towards the exploration to synthesize and characterize magnetoelectric composite materials. So, in this chapter we will discuss the relevant experimental tools and techniques to be utilized for the observation made in the upcoming chapters.

2.2 Synthesis Techniques

In this section we will discuss about the two synthesis techniques, namely solid state reaction and sol-gel method, which are exploited for the preparation of the different composites under study. A flow chart of the different stages and steps involved in the two

synthesis methods are shown in Figure 2.1.

Solid state reaction method



Sol gel process

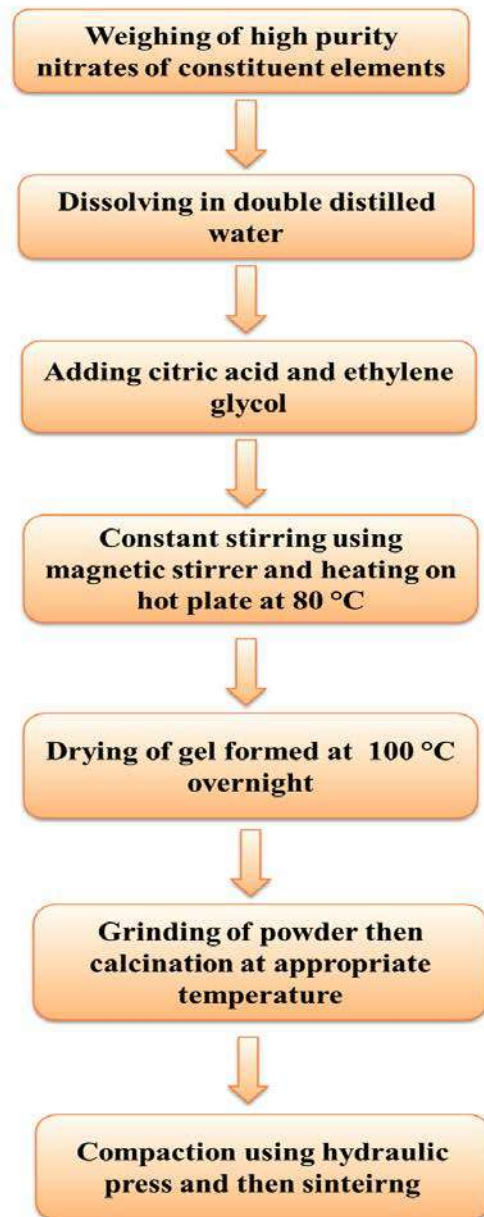


Figure 2.1 General Flowchart of ceramic processing

2.2.1 Synthesis using Solid State Reaction method

It is the most usual method taken into account for synthesis of polycrystalline solids from oxides, carbonates, sulphates and other metal salts. This method is also known as “dry media reaction” because no solvents are used in chemical reaction. The advantage of this method is that due to powder reaction involved, the products have less cost. Further it is also eco-friendly because at the end of reaction there is no waste to eliminate as the

solvents are not involved. This method requires heat treatment given to solid reactants for production of new phase. The sequential steps involved in this method are discussed below with brief description:

Raw materials selection

Usually, the raw materials used in this process are generally oxides and carbonates. So, this process is also known as oxide mixing method.

Weighing of raw materials

This step involves weighing of the raw materials using electronic balance. The amount of raw materials to be used is obtained from the reaction formula.

Mixing of raw materials

After weighing the required materials in the stoichiometric proportions the mixing of these materials is carried out using agate mortar and pestle, which involves the breaking up of agglomerates and should end up with intimate mixing of constituents.

Calcination

After mixing the powder thoroughly the calcination is carried out to form the desired single phase. During the course of calcination the thermochemical reaction takes place amongst the constituents, giving rise to the desired phase. Generally, the calcination temperature should be kept high enough in order to complete the thermochemical reaction and low enough in order to avert any losses of the constituents. Calcination temperature is an important parameter because it affects the density and homogeneity of final phase.

Binder addition and Shaping

The pelletization of the powder is achieved by mixing 2 % polyvinyl alcohol (PVA) as a binder in the powder of composites. Using movable top and bottom punches dry pressing is carried out using hydraulic press. The granulated powder is filled in the cavity of bottom punch which is then compressed in form of cylindrical pellets.

Sintering

Sintering is done by heating the pellets up to a temperature below melting points of its constituents and the same results in chemical reaction between precursor materials [117].

It is done to achieve high density. It is the process of converting a ceramic green body into a compact solid by heating it at high temperature. Sintering comprises of mass transfer process which deforms the ceramic powder thereby filling inter-particle voids causing overall shrinkage in the sample. Sintering is basically a thermally activated process controlled by diffusion. Densification of the sample occurs when the atoms diffuse from grain boundaries to the void surface thereby filling it up. Grain boundaries are atomically loose and give rise to fast diffusion. Since matter is separated from grain boundaries the powder particles approach giving rise to densification. After sintering, the sample is transformed into a more dense structure in which the crystallites are joined together by grain boundaries.

Electroding

Conductive electrodes are necessary for measuring the electric properties of the samples. These electrodes are made by applying a layer of metallic silver made in dispersed liquid or in form of paste. After this the samples are sintered at 200 °C to form a sustained conductive layer on the sample surface. Silver is generally used because it strongly adheres to the sample surface, has zero electrical resistance, excellent chemical and physical durability.

2.2.2 Synthesis using Sol-Gel method

Sol-gel method is the widely used wet chemical technique in the area of materials sciences. In this method the required product materials are obtained from solution via gelation. It is possible to obtain unique product materials due to high homogeneity of constituent elements and medium preparation temperatures which is not attainable with other methods. This process mainly involves a transition of the material from liquid sol into highly viscous mass (gel). This process has a number of advantages. High purity materials can be synthesized due to ease of purification of liquids. Mixing takes place at molecular level, thereby guaranteeing good chemical homogeneity. The materials obtained using this process has low calcination temperature as compared to materials produced by solid state reaction method. This process also has some disadvantages. The raw materials used are a bit expensive. Further, due to problem of conventional drying of materials prepared using sol-gel process, they are not usually used for production of monolithic ceramics. Rather they are used for fabrication of thin films, nanopowders etc [118]. The major steps involved in this method are as follows:

Raw materials selection

For preparation of sol the starting raw materials used are usually inorganic metal salts such as nitrates, acetates etc.

Weighing

The raw materials required are then weighed according to the amounts estimated from the reaction formula.

Dissolution

In order to form a colloidal sol, the precursors used in this process undergo a chain of polymerization reactions and hydrolysis. Starting with a solution of metal-organic compounds the production of gelled material in many cases is acquainted with network of polymer chains or the gel material comprising of identifiable joint colloidal particles in form of networks through surface forces.

Constituent mixing and drying

The precursor solution was stirred at 80 °C until a gel is formed. The obtained gel was then dried at 100 °C in an oven overnight to obtain the required powder.

2.3 Tools used for Characterization of Samples

The organized use of various instruments for material characterizations is the main step in experimental research. Different techniques are employed for the characterization of materials. The various characterization tools and techniques used in our research work are given below and followed with their brief descriptions in next sections.

- (a) X-ray diffraction (XRD) for structural and phase analysis.
- (b) Field Emission Scanning Electron Microscopy (FE-SEM) for microstructural analysis.
- (c) Energy Dispersive X-ray Spectrometry for compositional analysis.
- (d) Vibrating Sample Magnetometer (VSM) and Superconducting Quantum Interference Device (SQUID) for magnetic measurements.
- (e) LCR meter for capacitance measurements.

(f) P-E hysteresis loop tracer

(g) Magnetoelectric coupling measurement system.

In the following sections we have discussed the functionality of the above mentioned tools which are used to characterize the magnetoelectric composites under study.

2.3.1 X-ray diffraction (XRD)

It is one of the most widely used, powerful and non-destructive technique for characterizing the crystalline materials. This method is used from long time for determination of crystal structure, phase analysis, lattice constants, crystallite size and structural imperfections in addition to other structural properties of crystalline materials. It is possible to identify phases in the polycrystalline bulk materials and their relative amounts from intensity of diffraction peaks can be determined. The standard X-ray diffraction patterns for many inorganic structures and minerals, have been produced by an organization named as J. C. P. D. S (Joint Committee on Powder Diffraction Standards). The X-ray diffraction phenomenon in crystals results from diffraction phenomena in which electrons of atoms diffract the X-rays without changing its wavelength [98]. X-rays are electromagnetic radiations discovered by Roentgen in the year 1895. Their exact nature was established in the year 1912, when X-ray diffraction phenomena in crystals was discovered by Max Van Loue [119]. When an electromagnetic radiation falls on a periodic structure having the length scale of the order of its wavelength then diffraction phenomena is observed. To generate the diffraction conditions in an easy way W. H. Bragg and W. L. Bragg devised a model in 1912 [120]. They proposed that crystal lattice comprises of different sets parallel rows of atoms. The wavelength of X-rays with photon energies lying in the range 3–8 keV corresponds to interatomic distances in crystals. Therefore, when the crystal lattice is irradiated with X-rays then atoms scatter such rays in all the viable directions. In certain directions the scattered rays can be completely in the same phase thereby giving rise to constructive interference (Figure 2.2), while in certain other directions they will be entirely out of phase resulting in destructive interference. The condition for constructive interference when a beam of monochromatic X-rays fall on a crystal lattice is governed by Bragg's law [120]:

$$2d \sin\theta = n\lambda \quad (2.1)$$

Where λ is the wavelength of X-rays used, n is an integer exhibiting the order of diffraction

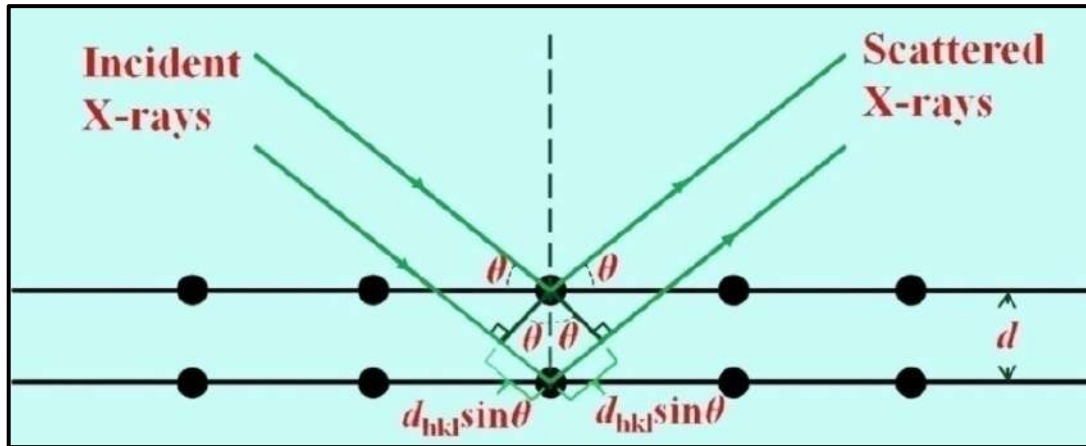


Figure 2.2 Schematic diagram of diffraction of X-rays from parallel planes in crystal

d is the interplanar spacing and θ is the Bragg's angle which is defined as the angle between incident ray and scattering plane. The Bragg's law for X-ray diffraction is shown in Figure 2.2.

Operating method of X-ray diffractometer

The powder diffraction technique is adopted in the investigations for structural characterization and phase analysis. Bruker D8 Advance powder diffractometer using CuK_α radiation of wavelength $\lambda = 1.54056 \text{ \AA}$, operating at 40 kV and 30 mA has been used for the present analysis (Figure 2.3).



Figure 2.3 Bruker D8 Advance powder X-ray diffractometer

The X-ray diffractometer shows a geometry in which the sample is rotated in the path of collimated X-ray beam at an angle θ , however the detector used to collect the diffracted X-rays rotates at an angle 2θ . The instrument which is employed in the rotation of sample to a precise angular position is known as *goniometer*. The orientation of setup is made in such a way that the beam incident at an angle θ with respect to lattice plane is collected at an angle 2θ when reflected. This scan is generally known as θ - 2θ scan which is shown in Figure 2.4. Proportional counter or scintillation counter is used as X-ray detector to measure the diffracted beam positions in powder diffractometer.

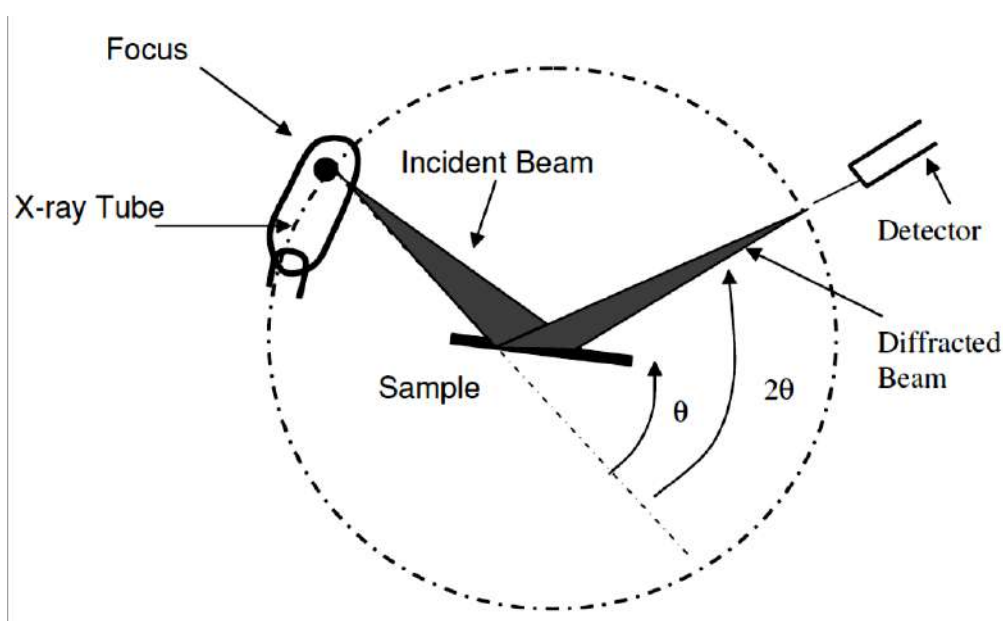


Figure 2.4 Schematic diagram of X-ray diffractometer

The crystallographic information is obtained by evaluating d values and indices of reflection (hkl). Whether the sample is in pure form or it is present as one of the constituents in a mixture, the characteristic diffraction pattern can always be obtained. The obtained X-ray diffraction pattern is characterized by a set of relative intensities (I) and peak positions (2θ). The material's crystallinity can be analysed from peak intensities and cell parameters are evaluated from peak positions. Every peak obtained in the diffraction pattern has its own indices. The information about location of planes in the crystal lattice is presented by peak positions and corresponding d spacing.

2.3.2 Field Emission Scanning Electron Microscopy (FE-SEM)

Scanning electron microscopy is a powerful technique to examine and analyze the surface morphology and chemical composition. Electron beam is produced at the top of

microscope by heating the metallic filament. This electron beam follows a vertical path, which is focussed and directed by electromagnetic lenses through column of microscope. When this electron beam is allowed to fall on the specimen, it undergoes a number of interactions with the electrons of atoms inside the specimen. These interactions may be either elastic or inelastic. In elastic scattering the electrons of the incident beam are either deflected either by the similar energy electrons of the outer shell or atomic nucleus. Electrons scattered elastically lose no energy and only their direction is changed. The electrons scattered at an angle more than 90° are known as “back scattered electrons” (BSE). When the scattering is inelastic a considerable amount of energy is transferred to the atoms of the specimen from the primary electron beam in distinct ways. This transferred energy may lead to several processes including excitation of free electrons, ionization or excitation of bound electrons or heating of the specimen [121]. As a result number of signals are produced which comprise of secondary electrons, Auger electrons, characteristic X-rays emission, cathodoluminescence and photons of different energies. These different signals are used to study the different characteristics of the specimen. The major interactions occurring when an electron beam strikes the sample surface are shown in Figure 2.5.

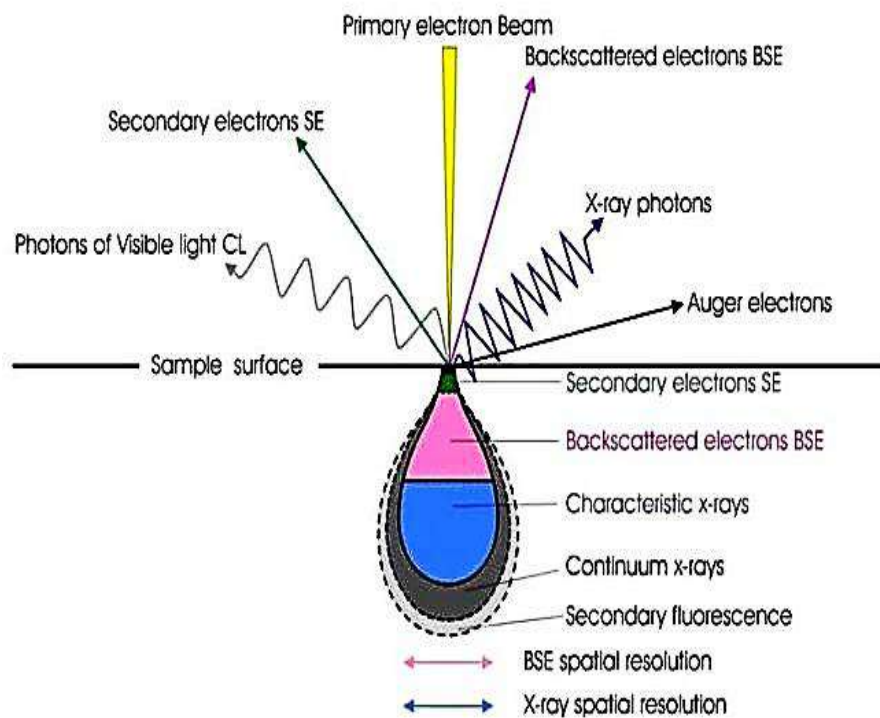


Figure 2.5 Schematic diagram showing various interactions of an electron beam with specimen

Field emission scanning electron microscope (FE-SEM) is much better than traditional scanning electron microscope (SEM) because the emission gun provides better spatial resolution up to 1.5 nm (3-6 times greater in comparison to traditional SEM). In FE-SEM a high voltage is applied between the pointed cathode and (made using single crystal tungsten wire having diameter of tip between 100 to 1000 Å) and a plate anode, which allows current to flow. A very large vacuum is necessary for field emission because the work function of the metal could be affected by the adsorbed gases. The block diagram of FE-SEM is shown in Figure 2.6 (a)

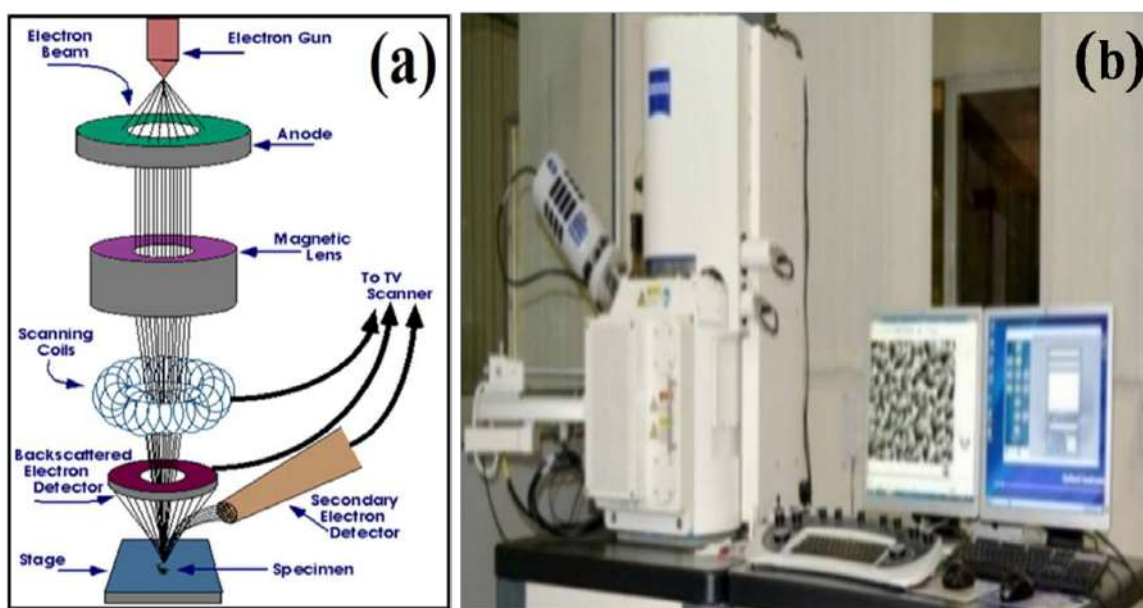


Figure 2.6 (a) Schematic diagram of scanning electron microscope and (b) Carl Zeiss Ultra Plus model of FE-SEM

The electrons get accelerated by an applied voltage in the range of some hundred volts to 50 kV and are aimed at the center of an electrical optical column. The divergent electron beam is focussed into a very fine focal spot size electron beam using condenser lens and is allowed to fall on the sample, then it is made to scan the surface in the raster form with the help of deflection system. Each point on the sample where the electron beam falls on the sample gives rise to emission of secondary or back scattered electrons which are then collected by the detector. The collected electrons are converted to signals by the detector which is then send to viewing screen thereby producing image analogous to an ordinary television. The samples which have higher atomic number produce secondary electrons in a large number thereby giving rise to images having higher intensity.

In the present research work field emission scanning microscope (Carl Zeiss Ultra Plus model) (Figure 2.6 (b)) with resolution < 0.8 nm @ 30 kV- High vacuum and up to 100,000X magnification, accelerating voltage ~ 200 V-30 kV and maximum probe current-100 nA (2 pA-110 nA) is used to study the morphology of the materials.

2.3.3 Energy Dispersive X-ray Spectrometry (EDX)

EDX attached with FE-SEM is an analytical tool which is used for chemical characterization of the specimens. EDX spectrum exhibits the peaks akin to energy levels which emit maximum X-rays. Each of these peaks corresponds to single element and is unique to an atom. The intensity and energy analysis of emitted X-rays is carried out, where the intensity signifies how much an element is present in a specimen and energy signifies the element which emits it. The intensity of the peak in the spectrum is proportional to the concentration of element in the specimen. The X-ray spectrum emitted by a solid specimen is detected using a detector which comprises of silicon chip with diffused with lithium ions on which Au layer has been evaporated to make thin contacts. The X-rays emitted from the specimen reach to the detector through a collimator and confirms that only those X-rays are taken into account which comes from the area that interacts with electrons and other stray X-rays are excluded. The X-rays emitted from the specimen enter the semiconductor Si crystal in which Lithium is drifted to compensate the minor levels of impurities. In the EDX detectors, Si (Li) was the first materials used [119]. It is the most common material used till date. This detector converts particular energy of X-rays into electric charge of proportional size through ionization. The X-rays entering the detector create large number of electron-hole pair due to absorption of energy. Each X-ray reduces its energy by ionizing silicon atoms and producing the photoelectrons. Each ionization requires 3.8 eV of energy. Therefore number of electrons and ionized Si atoms produced are equal to X-ray energy divided by 3.8. A high bias voltage is applied between electrical contacts on the front and back face of the crystal to collect the electrons. The collection of electrons gives rise to a charge signal proportional to incident X-ray energy. This charge signal is then converted into voltage by using integrated field effect transistor preamplifier. EDX detectors are designed for conversion of X-ray energy into voltage signal as accurate as possible. In the present work EDX attached to FE-SEM (Carl Zeiss Ultra Plus model) procured from Carl Zeiss company, Germany was used to study the chemical composition of the materials.

2.3.4 Vibrating Sample Magnetometer (VSM)

VSM was introduced by S. Foner [122]. It is the simple and effective technique for determining the magnetic moment of the magnetic materials. The magnetic properties are determined by VSM according to applied magnetic field and temperature. VSM usually can measure magnetic moment up to 5×10^{-5} emu. VSM works on Faraday's law of electromagnetic induction, in which a time varying magnetic flux induces an e.m.f in a conductor [123]. By measuring the induced e.m.f we can get information about change in magnetic field. Here sample is kept in a uniform magnetic field produced amidst poles of electromagnet. The specimen gets magnetized in the presence of fixed magnetic field by aligning the individual magnetic spins or domains in the field direction. This induces a dipole moment which is proportional to product of applied field and susceptibility of the specimen. A magnetic stray field is created because of the induced magnetic moment. The specimen is then made to undergo sinusoidal motion at small constant amplitude, which changes the stray magnetic flux as a function of time, thereby inducing an electrical signal in the stationary coils (Figure 2.7). This signal produced is proportional to magnetic moment, amplitude and frequency of vibration.

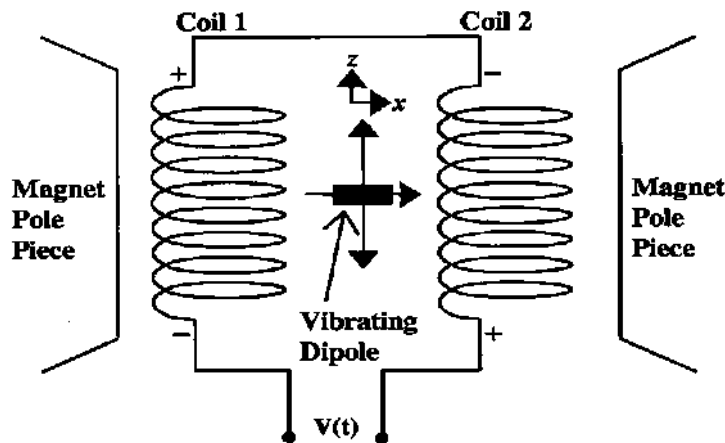


Figure 2.7 Schematic diagram showing working principle of Vibrating sample magnetometer [123]

The voltage $V(t)$ induced at a point r inside the detection coils as a result of changing magnetic field $\partial B(t)$ [123] is given by equation (2.2):

$$V(t) = \sum_n \int_A \frac{\partial B(t)}{\partial t} \cdot dA \quad (2.2)$$

Where A is the area vector of a single turn of the coil summed over n turns. Furthermore $V(t)$ is a measure of magnetic moment of the specimen.

Figure 2.8 (a) exhibits the block diagram of VSM [124]. The specimen under observation is inserted in the sample holder placed amidst poles of electromagnet. The signal obtained from the lock in amplifier is directly proportional to the magnetic moment of the specimen. A set of pickup coils is placed in the vicinity of the specimen amidst the magnetic poles. The sample holder is organized with the help of sample rod in a transducer assembly which passes through the centre of driving coil. A permanent magnet is also connected to sample holder. The power amplifier drives the transducer which is controlled by an oscillator. A vibration exciter is connected to the sample holder rod.

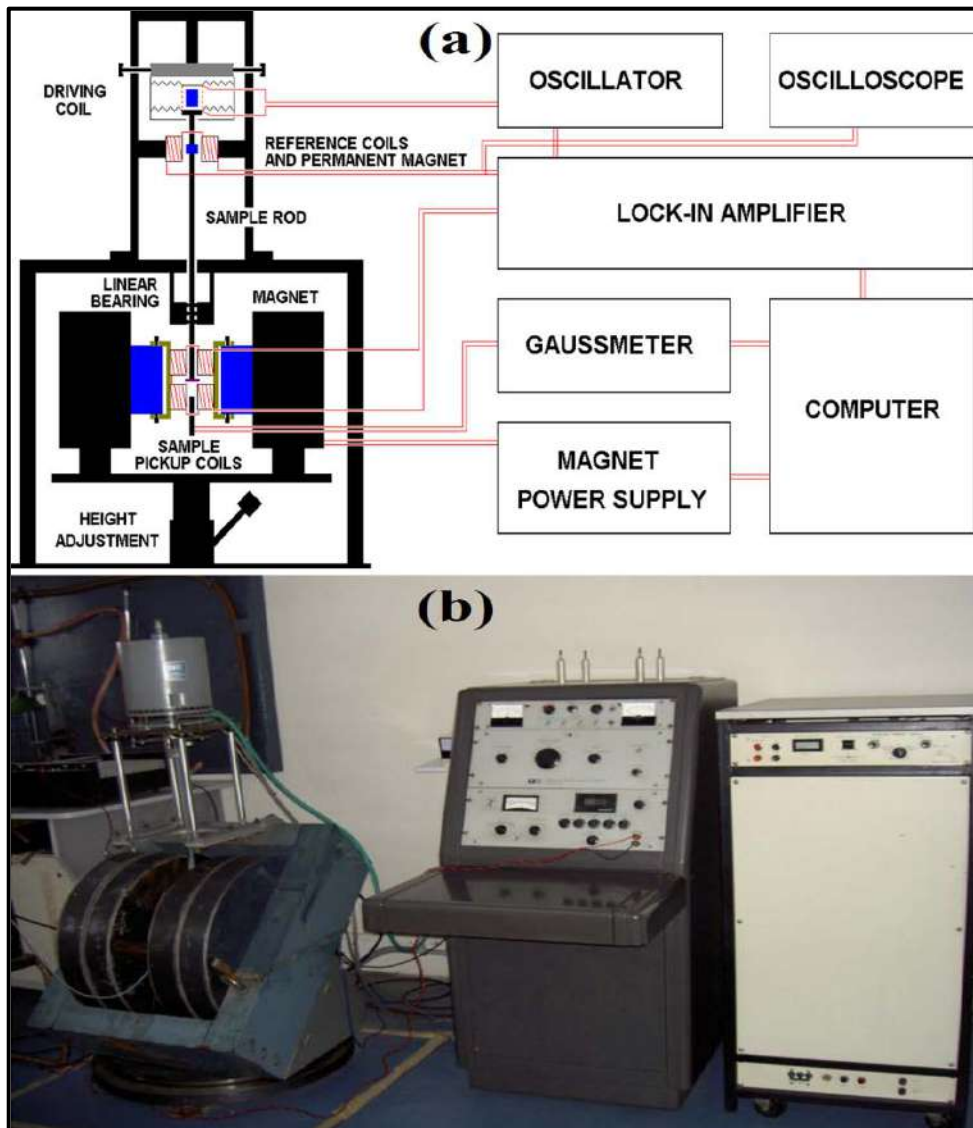


Figure 2.8 (a) Block diagram of Vibrating sample magnetometer [124] and (b) Setup of Vibrating sample magnetometer

The specimen is moved sinusoidally at a frequency of 85 Hz and is restricted to vibrate only in vertical direction. As the sample vibrates, a pair of stationary coils picks up the induced *ac* signal. The output of sample coil is fed to the differential input of the lock in amplifier and its reference input comes from the sine wave oscillator. The signal obtained from the lock in amplifier is directly proportional to the magnetic moment of the specimen. The signal of pure Ni standard placed in the saddle point is used for calibration of VSM because magnetic moment of Ni is known. Figure 2.8 (b) shows setup of VSM used to measure magnetic properties of the samples under study.

2.3.5 Superconducting Quantum Interference Device (SQUID)

SQUID is the world's most sensitive instrument to detect the magnetic flux. It can detect small magnetic moment of the order of 10^{-9} emu. It takes into account the phenomenon of flux quantization [125] and Josephson tunnelling. SQUID magnetometers are of two types: radio frequency (RF) SQUID and direct current (DC) SQUID. RF SQUID is based on one Josephson junction and are less sensitive for detection of magnetic moments. However, DC SQUID is based on two Josephson junctions, therefore they are highly sensitive and can measure weakest magnetic signals. To understand the mechanism of SQUID it is necessary to understand the theory of flux quantization and Josephson junction. The basis of great sensitivity of SQUIDs is the measurement of change in magnetic field associated with one flux quantum. One important fact linked with Josephson junction was that in a closed superconducting loop the flux is quantized in units of flux quantum $\phi_0 = \frac{h}{2e} \approx 2.07 \times 10^{-15}$ *Wb*, where *e* is electron's charge and *h* is the Planck's constant [126].

Josephson junction: The current in superconductors is carried by pairs of electrons known as Cooper pairs. Cooper pair is generally a pair of electrons which have opposite spins and are bound together. Each pair is considered as a single particle having mass and charge twice of the single electron. Electrons in the normal conductors get scattered and have short wavelength, while in case of superconductors the Cooper pairs are not scattered and their wave functions remain coherent over large distances. Each Cooper pair can be represented by wavefunction having form $\varphi = \varphi_0 e^{2\pi i(\mathbf{p}\cdot\mathbf{r})/h}$. *p* being the net momentum of the pair having its center of mass at '*r*'. All electrons have same wavelength and uniform current density and a single wave of same wavelength is produced by superposition of these coherent waves. Thus all the electron pairs can be represented by a single wave

function of the form $\psi_p = \psi e^{2\pi i(p.r)/h}$, the electron pairs in two superconducting regions will have unrelated phases if these regions are isolated. But if the regions are brought together the electron pairs will tunnel across the gap and there will be coupling between two electron pair waves. The coupling strength increases with decrease in the separation. B. D. Josephson argued that a superconducting current is carried by electron pairs tunnelling across the gap which is known as “Josephson tunnelling” [127]. The superconductors separated by a weak link is known as “Josephson junction” (Figure 2.9). Usually the layer is insulating in nature. The Cooper pairs can tunnel quantum mechanically through the barrier without breaking up the pair and forms supercurrent if the layer is thin enough. The current flowing through the junction in absence of applied voltage is known as DC Josephson effect. If the voltage is applied across the junction the Josephson junction will oscillate with a frequency which is proportional to the voltage across the junction. This effect is commonly known as AC Josephson effect.

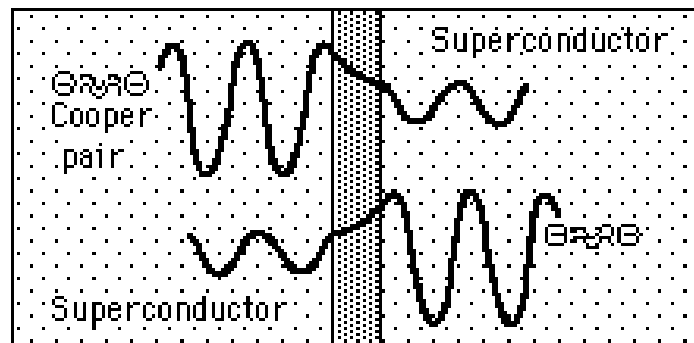


Figure 2.9 Schematic representation of a Josephson junction

Usually the SQUID comprises of two Josephson junctions (DC SQUID) as shown in Figure 2.10 (a) connected in parallel and form a ring with two weak links. The magnetic coil placed in the interior of the ring produces the flux across the loop. In the absence of magnetic field the current is divided evenly between the two junctions and the phase difference among the junctions is same. When the magnetic field is applied the phase difference no longer remains the same. The current flowing across the junction due to phase difference between the phases φ_1 and φ_2 [128] is given by equation 2.3:

$$I = I_c \text{Sin}\delta \quad (2.3)$$

where I_c is the critical current flowing across the junction and $\delta = \varphi_1 - \varphi_2$ is the phase difference. The SQUID is operated at constant biasing current greater than I_c . The periodic relation between voltage and applied magnetic flux is having a period of one flux measured

measured voltage oscillates with the changes in phase at the two junctions if a fixed biasing current is maintained, which further depends on the change in magnetic flux. The quantum ϕ_0 is shown in Figure 2.10 (b). The subsequent flux change can be evaluated by counting oscillations. For the present research work measurements are done using Quantum Design Evercool XL DC SQUID magnetometer (Figure 2.11) having temperature range for the measurement from 4 K – 400 K and sensitivity $\sim 10^{-8}$ emu.

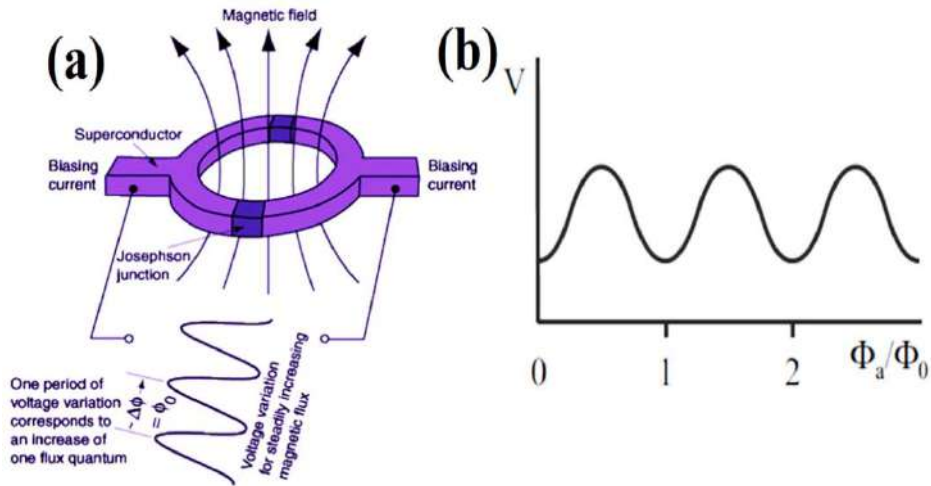


Figure 2.10 (a) Schematic of DC SQUID and (b) Periodic relationship between voltage across the SQUID and the applied magnetic flux having a period of one flux quantum ϕ_0 , where $\phi_a = n\phi_0$ [128]



Figure 2.11 Quantum Design MPMS Evercool with integrated Cryocooler Dewar system

2.3.6 LCR Meter

LCR meter is used to compute the inductance (L), capacitance (C) and resistance (R) of a specimen. Impedance measurement is carried out internally by LCR meter and the corresponding values of inductance and capacitance are displayed. LCR meters based on “alternating current (AC) bridges” are of major importance for calculation of inductance, capacitance, resistance and dissipation factor. AC bridges are an improved version of Wheatstone bridge comprising of a detector, which is sensitive to tiny alternating potential differences and a source of excitation. Schering bridge is one type of AC bridge which is commonly used for measurement of unknown capacitance and its dissipation factor, where dissipation factor is the ratio its resistance to its capacitive reactance. Schering bridge comprises of four arms and the measurement depends basically on balancing the loads on its arms. The circuit diagram of Schering bridge is shown in Figure 2.12.

One arm of the bridge comprises of a fixed capacitor C_1 which is connected in parallel to a variable resistance R_1 and is used as one of the variable arm of the bridge. Resistors R_1 and R_2 have known values, but R_3 is unknown. Similarly the capacitance value C_3 is not known and it is to be calculated, however C_1 and C_2 are known. Calculation of R_3 and C_3 is done by keeping R_2 and C_2 fixed, but adjusting the values of R_1 and C_1 , until the voltages at points A and B are same and current amidst these points through ammeter becomes null. In this stage bridge is said to be ‘balanced’. For the bridge to be balanced, we obtain the following relation (2.4)

$$\frac{Z_1}{C_2} = \frac{R_2}{Z_3} \quad (2.4)$$

Here Z_1 is the impedance of C_1 in parallel with R_1 and Z_3 is the impedance of C_3 in series with R_3 . On solving equation (2.4) we get equation (2.5) and (2.6):

The positive and negative reactive components are equal and cancel out during balancing of bridge and we obtain equation (2.5):

$$R_3 = \frac{C_1 R_2}{C_2} \quad (2.5)$$

Similarly the purely resistive elements are equal during balancing of bridge and we obtain equation (2.6):

$$C_3 = \frac{R_1 C_2}{R_2} \quad (2.6)$$

Using this method unknown capacitance and resistance are measured. The dielectric and impedance measurements are studied using computer controlled HIOKI 3532-50 Hi-Tester LCR meter (Figure 2.13) from room temperature to 500 °C (100 Hz – 1 MHz), with step temperature being 5 °C.

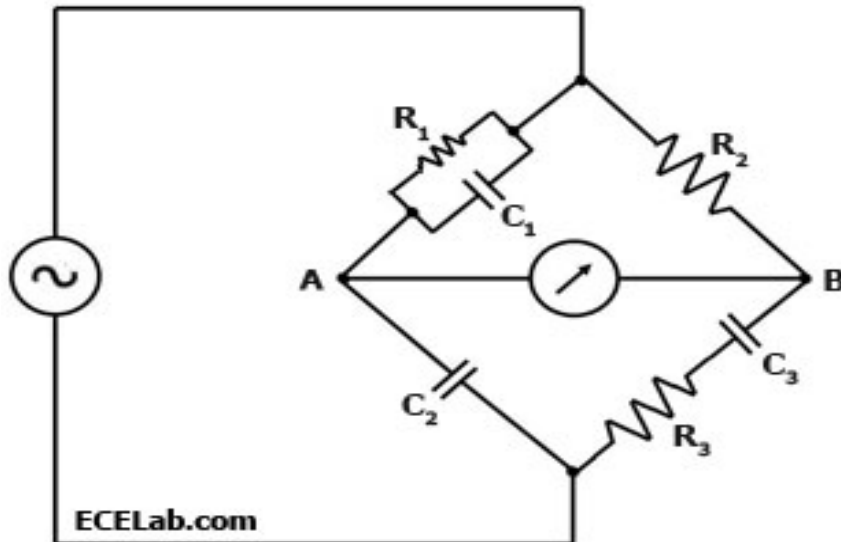


Figure 2.12 Schematic representation of Schering bridge

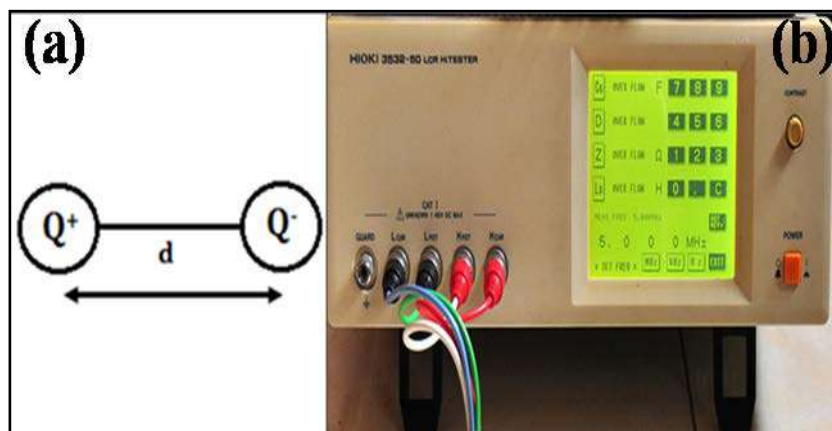


Figure 2.13 Photograph of HIOKI 3532-50 LCR Hi Tetser

2.3.7 Polarization-Electric Field (P-E) Hysteresis Loop Tracer

P-E hysteresis loop is one of the major feature and significant electrical characteristic of ferroelectric materials. Concept of domain is explained using phenomenon of hysteresis. The Sawyer-Tower method shown in Figure 2.14 is the most commonly used method for measuring the P-E hysteresis loop. Setup used for P-E hysteresis loop measurement is computer controlled and standard P-E measurement parameters are automatically determined. In Figure 2.13, C is the capacitance of specimen placed in series with reference capacitor C_0 and V is the applied ac signal. The capacitance of reference

capacitor should be 100 to 1000 times greater than capacitance of specimen. For saturation of polarization the voltage across C should be sufficiently large. In this configuration the voltage V_0 across C_0 is proportional to polarization charge of specimen which is given by $V_0 = AP/C_0$, where A is the specimen's area. Therefore, the applied field across the specimen is given as $F = V_c/d = (V - V_0)/d$ [37]. The polarization appears across the vertical plates of the oscilloscope. An immediate huge change in polarization leads to initial dielectric breakdown. In the present research work the P-E hysteresis loops of the samples were measured using a modified Sawyer-Tower circuit (Automatic P-E loop tracer system, Marine India Electr. Pvt. Ltd.)

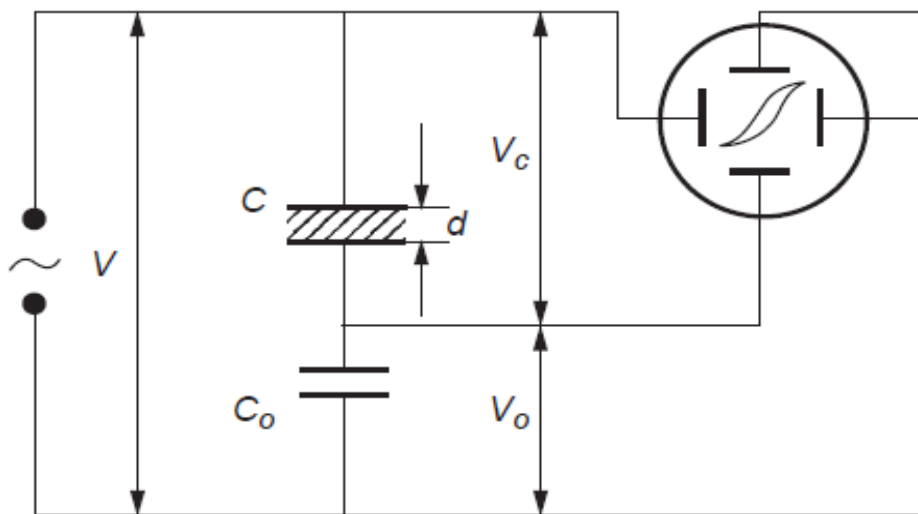


Figure 2.14 Schematic of Sawyer-Tower circuit for P-E loop measurement [37]

2.3.8 Magnetoelectric Coupling Measurement setup

Magnetoelectric voltage coefficient (α) was calculated using dynamic method using an in-house built measurement setup at CSIR-National Physical Laboratory. The experimental setup for studying the ME effect using lock in technique is shown in Figure 2.15. Before the measurement the sample pellets were poled normal to its plane at an applied electric field of 0.5–1 kV/cm for 1 h at 100 °C and cooled back to room temperature, to polarize them adequately.

A biased DC magnetic field of 10 kOe is produced using an electromagnet. The time varying DC magnetic field is obtained using a programmable DC power source. A Hall probe is employed to measure the DC magnetic field. In addition to this, an AC magnetic field up to 10 Oe having frequency in the range of 1 to 10 kHz is superposed on to DC

magnetic field. This AC magnetic field is generated using a Helmholtz coil having 100 turns with a diameter of 50 mm. This coil is driven by an AC current generated using a function generator. The magnitude of AC field is calculated from driving current that is measured using multimeter. The specimen is placed in magnetic field having its surface parallel or perpendicular to the field direction, for longitudinal and transverse measurement respectively. The ME signal was measured using a lock-in amplifier [129]

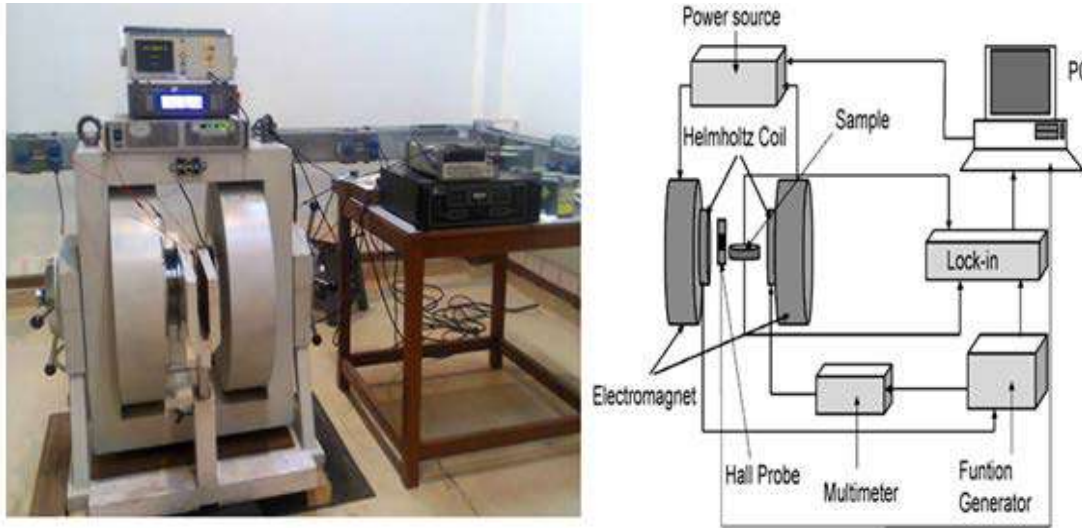


Figure 2.15 Schematic diagram of Magnetolectric measurement setup [108]

In our present research work, ME voltage coefficient a 5 Oe AC magnetic field of frequency 999 Hz was applied in tandem with a sweeping DC magnetic field from 0 – 8500 Oe and field orientation was longitudinal with respect to the sample plane to obtain ME voltage coefficient using the equation 2.7:

$$\alpha = \frac{V_{out}}{d * H_{ac}} \quad (2.7)$$

Where V_{out} , d and H_{ac} are induced output voltage, thickness of sample and magnitude of applied AC field respectively.

The fundamental equation necessary to evaluate ME coefficients from the voltage is discussed as follows. When a DC magnetic field is applied, the ME output voltage (V) in a material showing second order effect is given as

$$V \propto (\alpha H + \beta. H.H) \quad (2.8)$$

where α and β are respectively the coefficients of linear and quadratic components of ME sample. If an ac field h_0 is superimposed over the dc field H_0 , the effective field is,

$$H = H_0 + h_0 \sin(\omega t) \quad (2.9)$$

A lock in amplifier tuned to the frequency ω ($\omega=2\pi f$) would measure the output emf giving the ME output. Then, we can write,

$$V \propto (\alpha + \beta H_0) h_0 = \alpha^*(H_0) h_0 \quad (2.10)$$

When H_0 is zero, it is possible to find out the linear term α and hence the second order term β is evaluated in the presence of a dc magnetic field [130].

Chapter 3

Synthesis and Characterization of $K_{0.5}Na_{0.5}NbO_3$ based Magnetolectric Composites

This chapter has been published in the form of following papers

- (1) Study of structural, dielectric, electric, magnetic and magnetolectric properties of $K_{0.5}Na_{0.5}NbO_3$ - $Ni_{0.2}Co_{0.8}Fe_2O_4$ composites, Yogesh Kumar, K.L. Yadav, Manjusha, Jyoti Shah, R.K. Kotnala, **Ceramics International** **43** (2017) **13438-13446**.
- (2) Synthesis and study of structural, dielectric, magnetic and magnetolectric properties of $K_{0.5}Na_{0.5}NbO_3$ - $CoMn_{0.2}Fe_{1.8}O_4$ composites, Yogesh Kumar and K.L. Yadav, **Journal of Materials Science: Materials in Electronics** (2018) **29**: **8923-8936**.

3.1 Introduction

Lead-free magnetolectric composites comprising of ferroelectric (piezoelectric) and ferrite (magnetic) phases have attracted remarkable attention in late years owing to their multifunctionality, due to ME coupling between both the constituent phases giving rise to large ME response at room temperature [131-132]. These ME composites find their fair share of applications in magnetic probes, sensors, actuators, phase shifters, transducers, memory applications etc. [4, 7, 133]. Single phase materials exhibit very low ME effect thereby restraining their use in technological applications. This limitation is overcome by synthesis of composites involving ferroelectric (piezoelectric) and ferrite (magnetostrictive) phase. In order to obtain substantial value of ME output from the composites, Boomgard et al. [29] formulated some requirements which are summarized as: (i) both the ferroelectric and ferrite phases should be in equilibrium with each other, (ii) both ferrite and ferroelectric phases should have high magnetostrictive and piezoelectric coefficient respectively, (iii) ferrite phase should have high resistivity in order to avert leakage of charges.

Distinct lead-free ME composites including $NiFe_2O_4$ - $BaTiO_3$ [134], $NiFe_2O_4$ - $Bi_{0.5}Na_{0.5}TiO_3$ [95], $Bi_{0.5}Na_{0.5}TiO_3$ - $CoFe_2O_4$ [92], $(Na_{0.5}K_{0.5})_{0.94}Li_{0.06}NbO_3$ - $NiFe_2O_4$ [103], $CoMn_{0.2}Fe_{1.8}O_4$ - $BaZr_{0.08}Ti_{0.92}O_3$ [100], $(Na_{0.5}K_{0.5})_{0.94}Li_{0.06}NbO_3$ - $CoFe_2O_4$ [135] etc. have been studied in past years. Co^{2+} doped nickel ferrite is a soft ferromagnetic material having high electrical resistivity, saturation magnetization, magnetostriction coefficient and high Curie temperature. $Ni_{0.2}Co_{0.8}Fe_2O_4$ has high electrical resistivity [136]

and high magnetostriction coefficient [137]. $(K_{0.5}Na_{0.5})NbO_3$ (KNN) is considered as outstanding lead free piezoelectric ceramic owing to its improved ferroelectric, dielectric and piezoelectric properties. KNN has large piezoelectric longitudinal response ($d_{33}\sim 160$ pC/N) and a high planar coupling coefficient ($k_p\sim 45\%$) [138-139]. Moreover it also shows large remnant polarization ($P_r = 20 \mu C/cm^2$) and coercive field ($E_C = 8$ kV/cm) [140]. Pristine $CoFe_2O_4$ exhibits higher magnetostriction as compared to other ferrites [141]. It also has high Curie temperature (T_C) and magnetocrystalline anisotropy. In order to reduce magnetocrystalline anisotropy and T_C , manganese substitution can be very effective [142-143]. Keeping in mind the abovementioned properties and characteristics of distinct ferroelectric and ferrite phases and to achieve substantial ME coupling we synthesized two phase lead free $(x) Ni_{0.2}Co_{0.8}Fe_2O_4-(1-x) (K_{0.5}Na_{0.5})NbO_3$ (NCFO/KNN) and $(x) CoMn_{0.2}Fe_{1.8}O_4-(1-x) (K_{0.5}Na_{0.5})NbO_3$ (CMFO/KNN) ME composites.

In the first section of this chapter we present the synthesis and organized study of structural, dielectric, magnetic and magnetolectric properties of $(x) Ni_{0.2}Co_{0.8}Fe_2O_4-(1-x) (K_{0.5}Na_{0.5})NbO_3$ ME composites comprising of KNN and NCFO as their ferroelectric and ferrite phase respectively.

In the second section of this chapter we focused on $(x) CoMn_{0.2}Fe_{1.8}O_4-(1-x) (K_{0.5}Na_{0.5})NbO_3$ ME composites having KNN and CMFO as their ferroelectric and ferrite phases respectively and presented a systematic study of their structural, multiferroic and magnetolectric properties.

3.2 Experimental Details

3.2.1 Synthesis of $(x) Ni_{0.2}Co_{0.8}Fe_2O_4-(1-x) (K_{0.5}Na_{0.5})NbO_3$ ME composite system with $x = 0, 0.10, 0.20, 0.30, 0.40, 0.50$ and 1.0

The ME composites $Ni_{0.2}Co_{0.8}Fe_2O_4/(K_{0.5}Na_{0.5})NbO_3$ (NCFO/KNN) having two distinct phases were synthesized using solid state reaction (SSR) method. Individual ferrite phase NCFO was prepared using SSR method. The stoichiometric amounts of high purity AR grade NiO (97.2 %, Himedia, India), Co_3O_4 (98.5 %, Himedia, India) and Fe_2O_3 (98 %, Himedia, India) were weighed, mixed and grounded in acetone medium for 3 h. The well mixed and grounded powder was dried and calcined at 1273 K for 3 h in air atmosphere to obtain the desired NCFO phase. The ferroelectric phase KNN was also synthesized using SSR method by taking stoichiometric amounts of K_2CO_3 (99.0 %, Himedia, India), Na_2CO_3 , (99.0 %, Qualigens, India) and Nb_2O_5 (99.9 %, Himedia, India)

and grounding them in acetone medium for 3 h. An extra amount of 5 wt.% of K_2CO_3 and Na_2CO_3 were initially added to the mixture for compensating the Potassium (K) and Sodium (Na) losses during heat treatment. The well mixed and grounded powder was calcined at 1123 K for 3 h in air atmosphere to obtain the desired KNN phase. The obtained powders of KNN and NCFO were mixed in five different mass ratios viz. 10/90, 20/80, 30/70, 40/60, 50/50 respectively to obtain the $(x) Ni_{0.2}Co_{0.8}Fe_2O_4-(1-x) (K_{0.5}Na_{0.5})NbO_3$ ($x = 0, 0.10, 0.20, 0.30, 0.40, 0.50$ and 1.0) ME composites. The homogeneous powders of the obtained compositions were dried and pelletized into pellets of 10 mm diameter and thickness of about 1-2 mm. We used 2 % of poly vinyl alcohol (PVA) (86.5–89.0 mol % Himedia, India) as a binder in the compositions for pelletization. The obtained pellets of different compositions were then sintered at 1323 K for 3 h in air atmosphere.

3.2.2 Synthesis of $(x) CoMn_{0.2}Fe_{1.8}O_4-(1-x) (K_{0.5}Na_{0.5})NbO_3$ ME composite system with $x = 0, 0.10, 0.20, 0.30, 0.40, 0.50$ and 1.0

The lead-free ME composites $CoMn_{0.2}Fe_{1.8}O_4/(K_{0.5}Na_{0.5})NbO_3$ (CMFO/KNN) constituting CMFO as ferrite and KNN as ferroelectric phase were synthesized using conventional SSR method. Individually, ferrite phase CMFO was also synthesized using SSR method using high purity AR grade powders of Co_3O_4 (98.5 %, Himedia, India), Mn_2O_3 (98.5 %, Qualigens, India) and Fe_2O_3 (98 %, Himedia, India). These powders were weighed in appropriate stoichiometric ratio, then mixed and grounded thoroughly in acetone medium for 3-4 h. The well mixed and grounded powder was dried and calcined at 1273 K for 3 h. This calcined powder was again grounded to get homogeneous CMFO powder. KNN was synthesized by same methodology as discussed in section 3.2.1. The obtained powders of CMFO and KNN were mixed thoroughly in different weight ratios 10:90, 20:80, 30:70, 40:60 and 50:50 to obtain $(x) CoMn_{0.2}Fe_{1.8}O_4-(1-x) (K_{0.5}Na_{0.5})NbO_3$ (where $x = 0, 0.10, 0.20, 0.30, 0.40, 0.50$ and 1.0) ME composites. The pelletization was done in accordance with the same technique as described in section 3.2.1 and the obtained pellets were finally sintered at 1373 K for 3 h in air atmosphere to obtain the desired ME composites.

3.2.3 Characterizations

The structural analysis of the synthesized samples was carried out using X-ray diffractometer (Bruker D8 Advance) over wide Bragg angle range ($20^\circ \leq 2\theta \leq 60^\circ$) with a

scanning speed of 1°/min using Cu (K_{α}) ($\lambda=1.5432$ Å) radiation. Microstructural analysis was executed using field emission scanning electron microscope (FE-SEM; Carl Zeiss) operating at an accelerating voltage of 15 kV for analyzing the grain size distribution in the samples. Electrical measurements were obtained after polishing both the flat sides of pellets with high purity silver paste and drying them at 150 °C. The dielectric measurements including dielectric constant (ϵ') and dielectric loss ($\tan \delta$) and complex impedance analysis of the samples was carried out using an automated HIOKI – 3532-50 Hi tester LCR meter in the temperature range 30–500 °C. The magnetic properties including the M-H hysteresis loops and temperature dependent field cooled (FC) and zero field cooled (ZFC) magnetization curves were studied using superconducting quantum interference device (SQUID). The ferroelectric hysteresis (P-E) loops of the composites were measured using modified Sawyer-Tower circuit (Automatic P-E loop tracer system, Marine India Electr. Pvt. Ltd.) ME voltage coefficient (α_{ME}) was determined by dynamic field method using an in house built measurement setup [144].

3.3 Results and Discussions

3.3.1 (x) $Ni_{0.2}Co_{0.8}Fe_2O_4-(1-x)$ ($K_{0.5}Na_{0.5}$) NbO_3 ME composite system with $x = 0, 0.10, 0.20, 0.30, 0.40, 0.50$ and 1.0

The X-ray diffraction patterns (XRD) of (x) $Ni_{0.2}Co_{0.8}Fe_2O_4-(1-x)$ ($K_{0.5}Na_{0.5}$) NbO_3 ($x = 0.10, 0.20$ and $0.30, 0.40$ and 0.50) ME composites along with the constituent phases NCFO and KNN are shown in Figure 3.1. All the XRD peaks could be identified for both the spinel (ferrite) and perovskite (ferroelectric) phase. XRD peak indexing of the composites is in agreement with reported values of KNN [145] and NCFO [146]. The ferrite phase NCFO shows cubic spinel structure, having lattice parameter $a = 8.358$ Å whereas the ferroelectric phase KNN shows orthorhombic structure having lattice parameters $a = 5.616$ Å, $b = 5.590$ Å and $c = 3.930$ Å. The lattice parameters obtained for the constituent phases of the composites are tabulated in Table 3.1. It is evident from Figure 3.1 that the intensity of ferrite phase NCFO increases with addition of NCFO and vice versa.

Figure 3.2 (a)-(g) depicts the FE-SEM micrographs of the NCFO/KNN composites with $x = 0, 0.10, 0.20, 0.30, 0.40, 0.50$ and 1.0 indicating their surface morphology. The FE-SEM micrographs indicate that all the composite samples are found to be well sintered and dense. It is also evident that the grains of the constituent phases are randomly oriented

and distributed over entire sample having certain amount of inter granular porosity. The average grain size of the composites was computed using linear interception method and the obtained values are given in Table 3.1. The grain growth of the composites is attributed to migration of pores in the solid solutions to the grain boundaries [147]. In sintered composites internal stress arises because of the differences in the densification rates and thermal expansion coefficients of the separate phases. The change in the grain morphology implies an evident lattice distortion and stress in the sintered composites [148]. The theoretical density was calculated from the molecular weight and lattice parameters derived using XRD from equation 3.1 and experimental density is calculated using Archimedes method. The relative density was then obtained from experimental and theoretical densities using equation 3.2, which is given in Table 3.1.

$$\rho_{\text{theor}} = \frac{\text{Molecular weight} \times \text{No. of molecules per unit cell}}{\text{Avogadro's number} \times \text{volume of unit cell}} \quad (3.1)$$

$$\rho_{\text{rel}} (\%) = \frac{\rho_{\text{exp}}}{\rho_{\text{theor}}} \times 100 \quad (3.2)$$

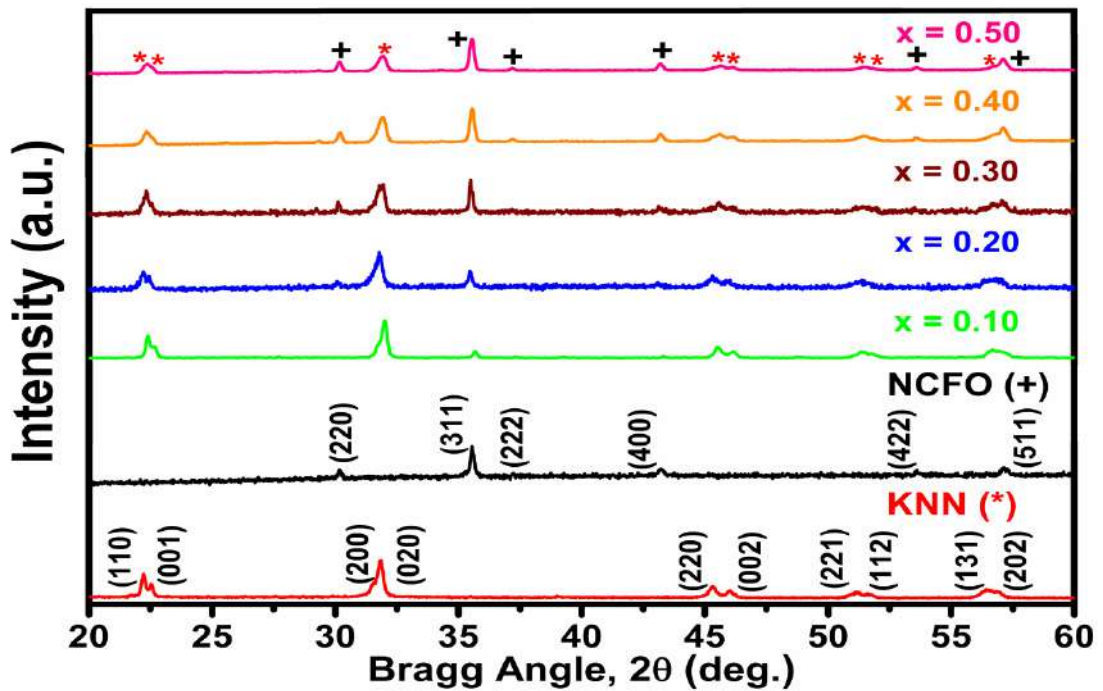


Figure 3.1 XRD patterns of $(x) Ni_{0.2}Co_{0.8}Fe_2O_4-(1-x) (K_{0.5}Na_{0.5})NbO_3$ ($x = 0.10, 0.20, 0.30, 0.40$ and 0.50) composites along with individual KNN and NCFO phases where (asterisk, *) represents KNN and (plus, +) represents the NCFO phase

Table 3.1 Lattice parameters, grain sizes and relative densities of $(x) Ni_{0.2}Co_{0.8}Fe_2O_4-(1-x) (K_{0.5}Na_{0.5})NbO_3$ ($x = 0, 0.10, 0.20, 0.30, 0.40, 0.50$ and 1.0) ME composites

Compositions (x)	Lattice Parameters (Å)				Average	
	NCFO		KNN		grain size (nm)	ρ_{rel} (%)
	a	a	b	c		
0.0	-	5.616	5.515	3.390	632	87.45
0.10	8.333	5.620	5.583	3.319	695	89.21
0.20	8.381	5.686	5.622	3.356	728	85.64
0.30	8.372	5.688	5.608	3.547	758	87.49
0.40	8.361	5.670	5.598	3.548	787	88.52
0.50	8.364	5.678	5.596	3.945	813	86.58
1.0	8.358	-	-	-	974	90.32

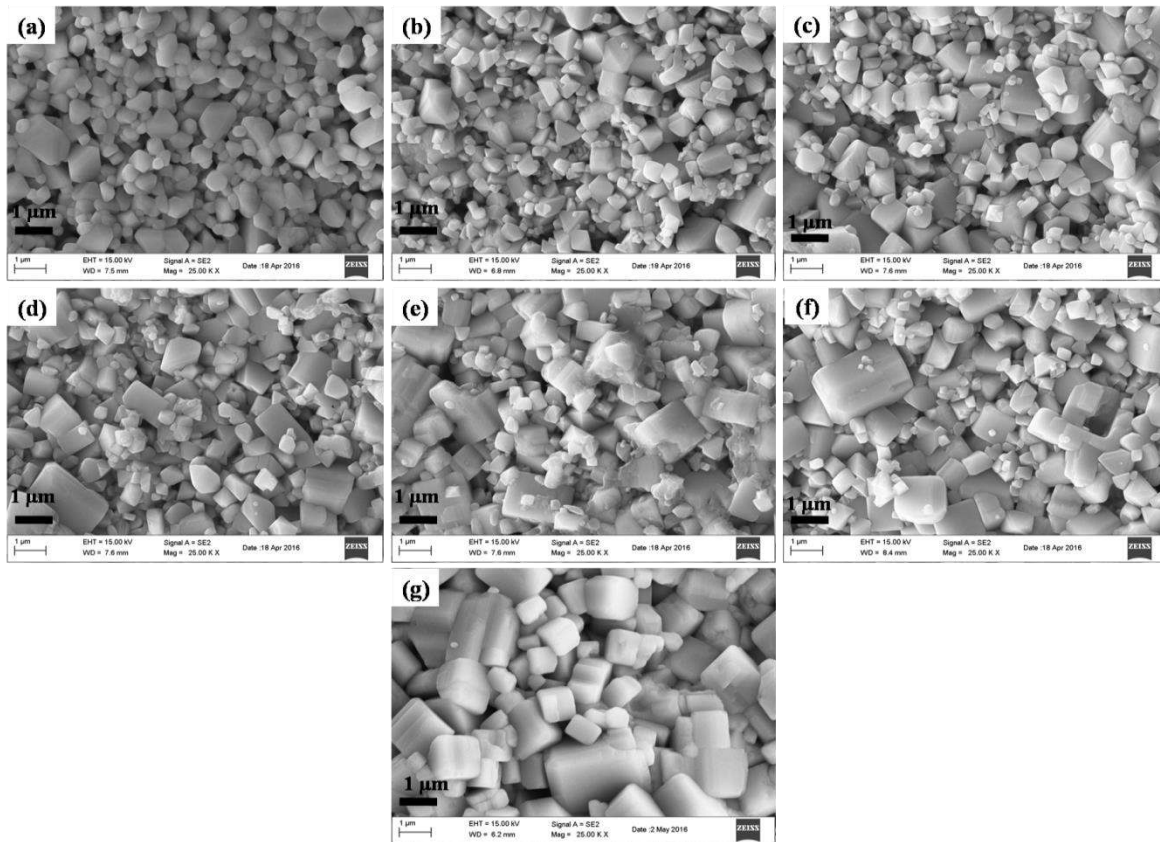


Figure 3.2 FE-SEM micrographs of $(x) Ni_{0.2}Co_{0.8}Fe_2O_4-(1-x) (K_{0.5}Na_{0.5})NbO_3$ composites
 (a) $x = 0$, (b) $x = 0.10$, (c) $x = 0.20$, (d) $x = 0.30$, (e) $x = 0.40$, (f) $x = 0.50$ and
 (g) $x = 1.0$

The compositional analysis for $(x) Ni_{0.2}Co_{0.8}Fe_2O_4-(1-x) (K_{0.5}Na_{0.5})NbO_3$ with $x = 0.10, 0.30$ and 0.50 is depicted in Figure 3.3 (a)-(c). It provides an insight into the quantitative chemical analysis of the synthesized composites. The phase formation, purity, effective synthesis and chemical homogeneity of the composites is revealed from the presence of expected elements (K, Na, Nb, Ni, Co, Fe and O) in the EDAX spectrum.

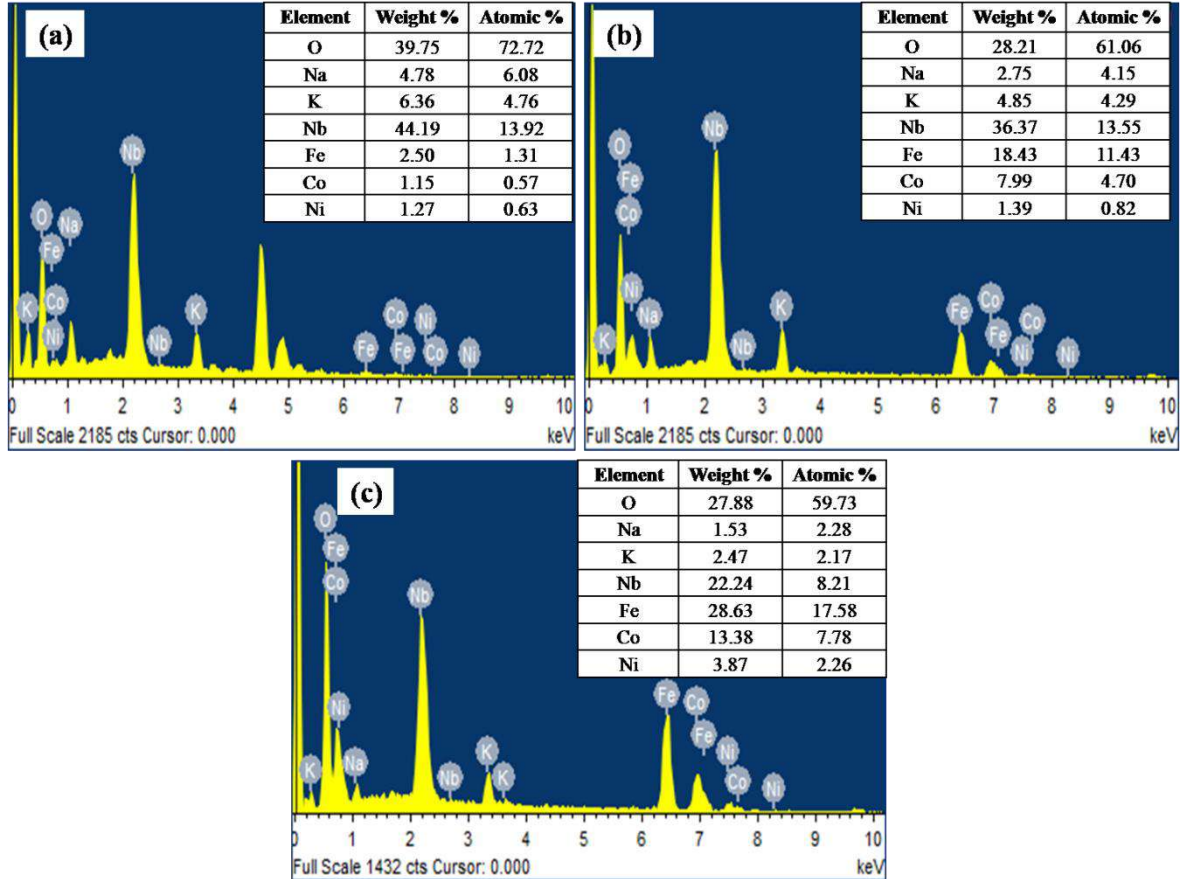


Figure 3.3 EDAX images of $(x) Ni_{0.2}Co_{0.8}Fe_2O_4-(1-x) (K_{0.5}Na_{0.5})NbO_3$ (a) $x = 0.10$, (b) $x = 0.30$ and (c) $x = 0.50$ composites

Figure 3.4 shows elemental mapping in $(x) Ni_{0.2}Co_{0.8}Fe_2O_4-(1-x) (K_{0.5}Na_{0.5})NbO_3$ composites for $x = 0.30$ composition sintered at 1323 K. It shows uniform distribution of constituent elements of the individual ferrite phase viz. Ni, Co, Fe and O and ferroelectric phase viz. K, Na, Nb and O without any impurity trace, thereby indicating the purity and effective synthesis of the prepared composites.

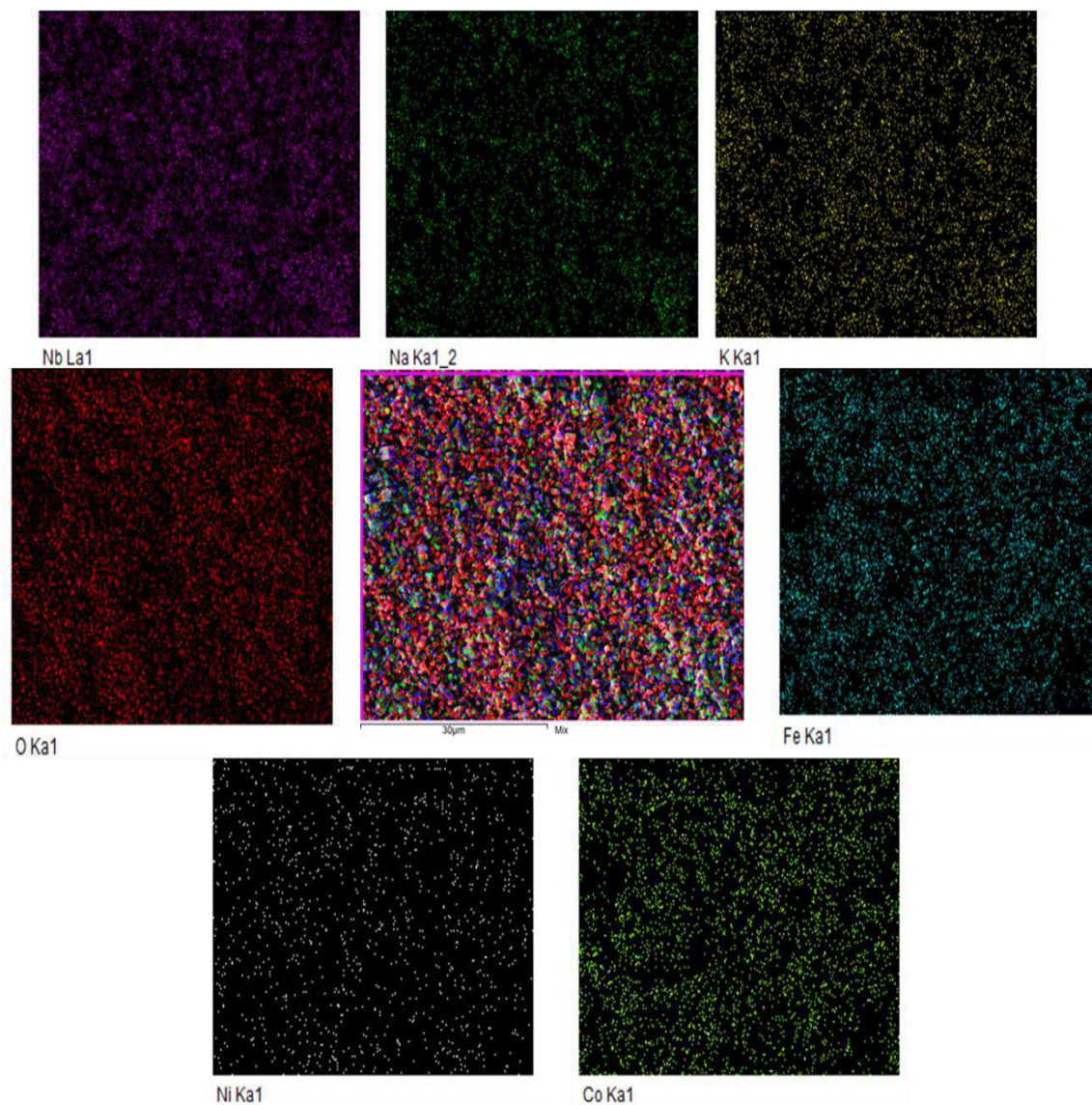


Figure 3.4 Elemental mapping showing distribution of constituent elements in $0.30Ni_{0.2}Co_{0.8}O_4-0.70(K_{0.5}Na_{0.5})NbO_3$ composite

The temperature dependence of the dielectric constant (ϵ') and dielectric loss ($\tan \delta$) of $(x) Ni_{0.2}Co_{0.8}Fe_2O_4-(1-x) (K_{0.5}Na_{0.5})NbO_3$ ($x = 0, 0.10, 0.20, 0.30, 0.40$ and 0.50) measured at three different frequencies is shown in Figure 3.5. Two distinct transitions have been observed for individual KNN phase and different compositions. As seen from Figure 3.5, KNN undergoes two phase transitions, one from orthorhombic to tetragonal phase (T_{O-T}) at $190\text{ }^\circ\text{C}$ and other from tetragonal to cubic phase (T_C) at $420\text{ }^\circ\text{C}$. The composites also exhibit the similar phase transitions at different T_{O-T} and different T_C . There is no systematic change in T_{O-T} and T_C . It is evident from Figure. 3.5 that T_C varies in the range $420\text{--}440\text{ }^\circ\text{C}$ and T_{O-T} varies in the range $190\text{--}225\text{ }^\circ\text{C}$. This may be due to presence of different factors including structural transitions and enhancement in the

movement of charge carriers to the interface of polycrystalline materials [149]. For all the compositions, an anomaly has been observed in the dielectric constant close to T_C of KNN. The dielectric properties of the composites are modified with addition of NCFO. Both dielectric constant and loss are found to enhance with addition of NCFO because the conduction contribution of NCFO towards dielectric constant becomes notable. The conduction mechanism is analogous to polarization mechanism in ferrites. Conduction phenomenon in ferrites is described on the basis of Verwey de Bohr mechanism. This involves electron exchange between ions of same element existing in different valence states. Electron hopping between Fe^{2+} and Fe^{3+} ions causes conduction. The increase in dielectric constant may be attributed to presence of heterogeneity in the composites [83]. Heterogeneities in the composites refer to the interfaces between the ferroelectric and ferrite phases, which produce space charge polarization. In presence of electric field the space charges dispensed due to ferrite phase assemble at interfaces due to difference in permittivities and conductivities of individual phases [150], resulting in space charge polarization. As ferrite concentration increases, the amount of space charges provided by NCFO also increases, resulting in higher value of dielectric constant.

It has also been observed that dielectric constant increases with temperature up to a definite temperature commonly known as transition temperature. After transition temperature, it starts decreasing. This may be due to the hopping of electrons between Fe^{2+} and Fe^{3+} ions present on the octahedral sites, which in turn is thermally activated with increasing temperature. This is the cause for local displacement in the direction of applied field giving rise to dielectric polarization. As the temperature increases beyond transition temperature, the motion of electrons and ions is increased. Therefore, it is difficult for them to orient themselves along the direction of field which is responsible for decrease in dielectric constant [151]. Moreover, dielectric constant arises due to combination of dipolar, electronic, ionic and interfacial polarizations. Dipolar and interfacial polarization dominate at lower frequencies, and electronic polarization dominates at higher frequencies. Consequently, we get higher value of dielectric constant at 1 kHz as compared to 10 kHz. Variation of dielectric loss with temperature is shown in inset of Figure 3.5. It is found to increase considerably with addition of NCFO. The increase in dielectric loss with addition of NCFO signals about space charge conduction which is related with the transport of defects like oxygen vacancies to dielectric-electrode interface [152].

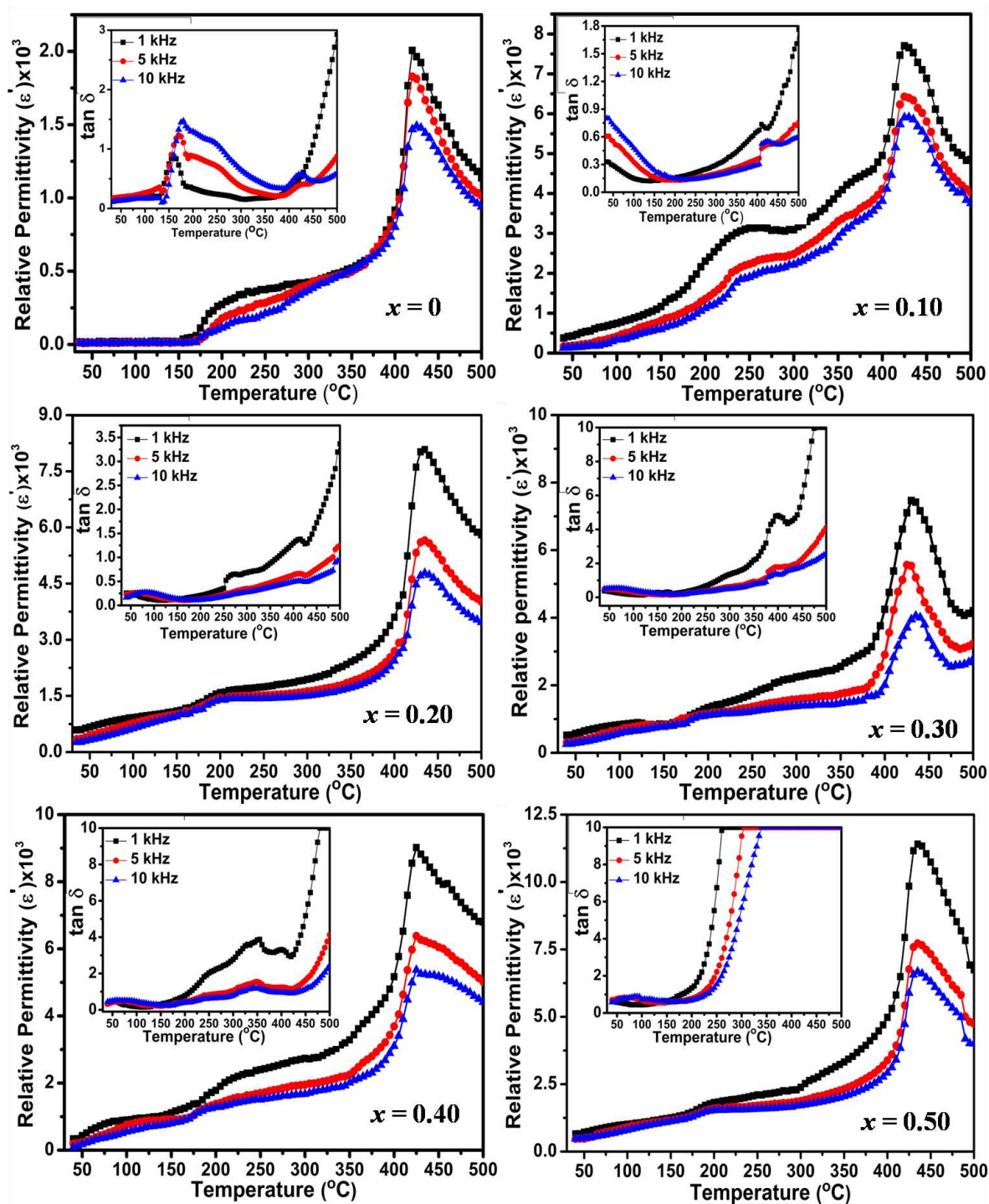


Figure 3.5 Temperature dependence of dielectric constant (ϵ') and dielectric loss ($\tan \delta$) at various frequencies for (x) $Ni_{0.2}Co_{0.8}Fe_2O_4-(1-x)$ $(K_{0.5}Na_{0.5})NbO_3$ ($x = 0, 0.10, 0.20, 0.30, 0.40$ and 0.50) composites

Figure 3.6 exhibits the Polarization vs. Electric field (P-E) hysteresis loops for (x) $Ni_{0.2}Co_{0.8}Fe_2O_4-(1-x)$ $(K_{0.5}Na_{0.5})NbO_3$ ($x = 0, 0.10, 0.20, 0.30, 0.40$ and 0.50) composites measured at room temperature and frequency of 50 Hz. As percentage of NCFO increases in the composites, the P-E loops become slightly narrower, indicating that

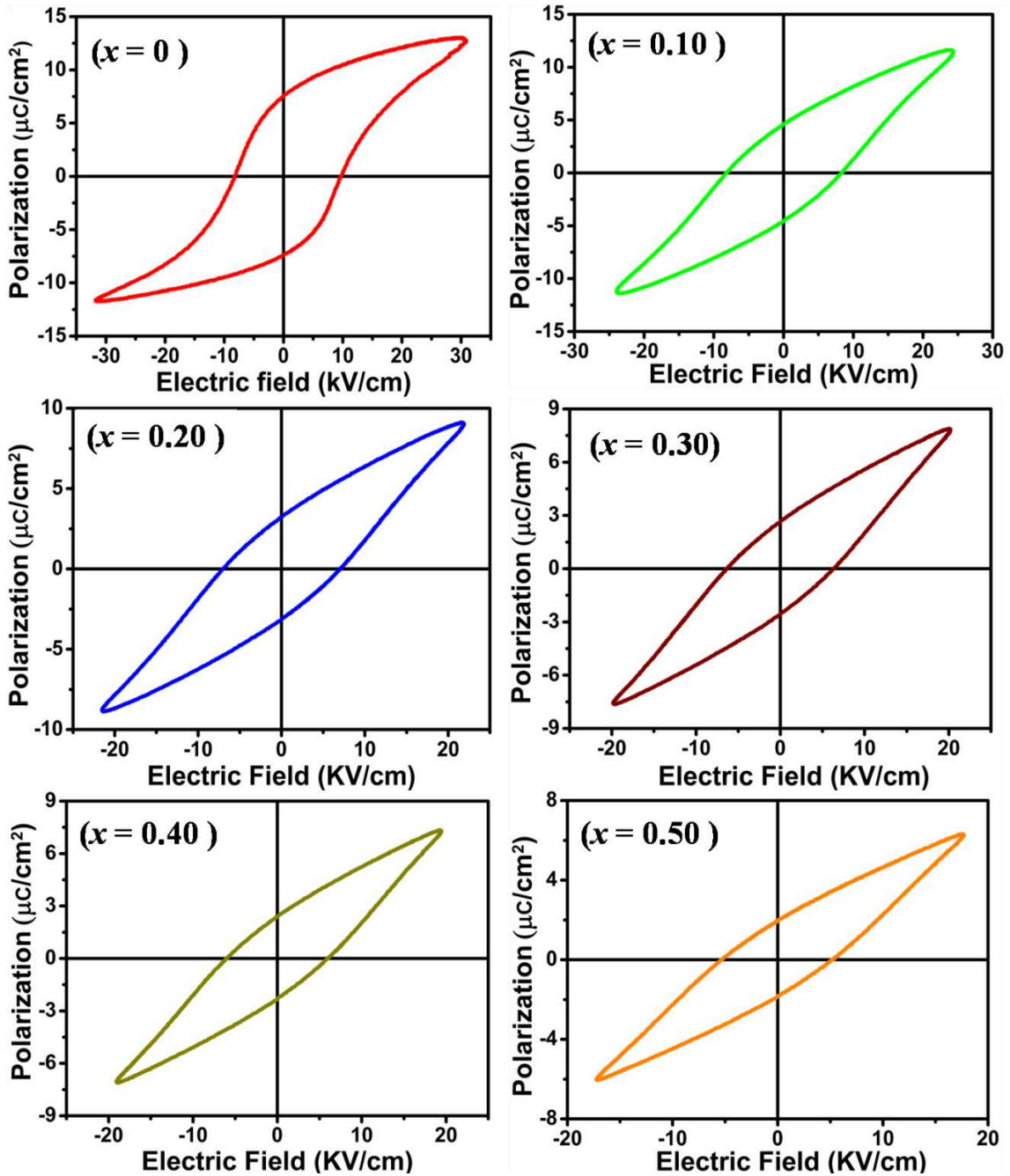


Figure 3.6 P-E hysteresis loops of $(x) Ni_{0.2}Co_{0.8}Fe_2O_4-(1-x) (K_{0.5}Na_{0.5})NbO_3$ ($x = 0, 0.10, 0.20, 0.30, 0.40$ and 0.50) composites

ferroelectric order of KNN is disturbed by adding NCFO. Figure 3.7 shows the variation of remnant polarization ($2P_r$) and coercivity ($2E_c$) with NCFO content and both of them are found to decrease with addition of NCFO. The possible reason for this may be the increase of leakage current in the system. The microstructure of the composites play important role in their observed ferroelectric behaviour. The coupling between grain boundaries and domain walls is stronger in fine grained ceramics as compared to coarse grained ceramics [153]. This strong coupling accounts for a decrease in domain wall mobility and their

alignment. This in turn causes a decrease in the polarization of the composites. Coercive field also decrease with increase in ferrite content by effecting the switching of ferroelectric domains with change in charge carrier concentration which leads to domain pinning [154].

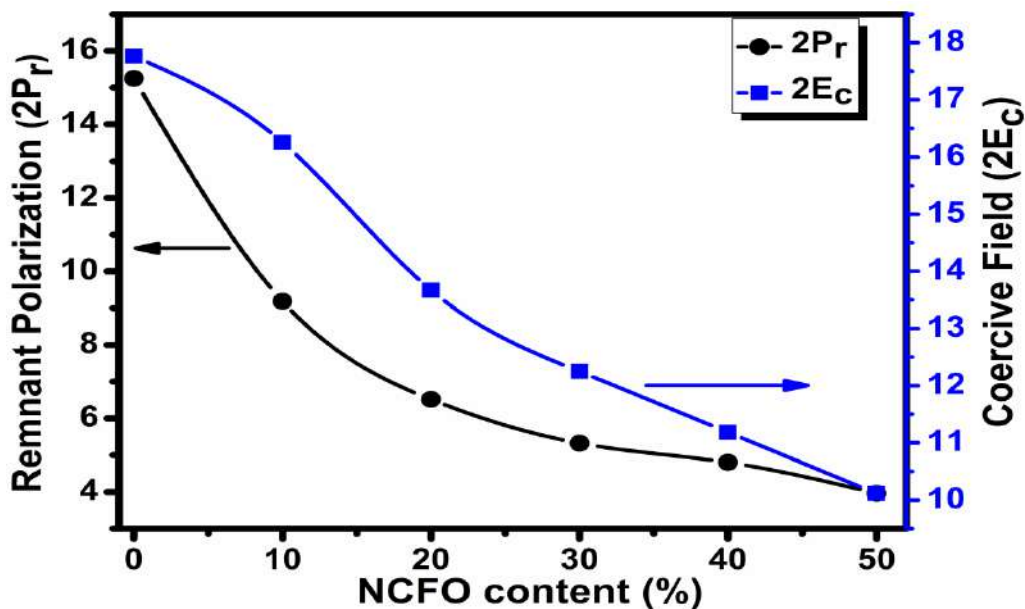


Figure 3.7 Variation of remnant polarization ($2P_r$) and coercive field ($2E_c$) with NCFO content

The magnetic properties including the magnetization vs. magnetic field (M-H) hysteresis loops of $(x) Ni_{0.2}Co_{0.8}Fe_2O_4-(1-x) (K_{0.5}Na_{0.5})NbO_3$ ($x = 0.10, 0.20, 0.30, 0.40, 0.50$ and 1.0) composites are studied at room temperature using VSM with magnetic field in the range $-10 \text{ kOe} \leq H \leq 10 \text{ kOe}$. The M-H hysteresis loops of the composites are presented in Figure 3.8 (a). It is evident that all the composites show ferromagnetic behaviour as shown by NCFO and values of saturation magnetization (M_s), remnant magnetization (M_r) increase with addition of NCFO which is evident from Figure 3.8 (b). The magnetic moment in terms of Bohr magneton is calculated using the equation (3.3):

$$\mu_B = \frac{M \times M_s}{5582} \quad (3.3)$$

Where M is the molecular weight, M_s is the saturation magnetization per gram mole of the composites and 5582 is the magnetic factor [155]. The value of magnetic moment in terms of Bohr magneton (μ_B), saturation magnetization (M_s) and remnant magnetization (M_r) are listed in Table 3.2. The increase in magnetization of the composites may be attributed to

enhancement in concentration of Fe^{3+} ions with addition of NCFO. In $Ni_{0.2}Co_{0.8}Fe_2O_4$, Ni^{2+} and Co^{2+} ions preferably occupy octahedral (B) sites, while Fe^{3+} ions are equally distributed across tetrahedral (A) as well as octahedral sites. The magnetization depends on the distribution of the cation in the spinel network. In a cubic system of ferromagnetic spinels magnetic order is due to super exchange interaction mechanism occurring between metal ions in A and B-sublattices [156]. With addition of NCFO, concentration of Fe^{3+} ions increase in the composites thereby increasing the exchange interaction between A and B sites. This in turn is responsible for increase in magnetization.

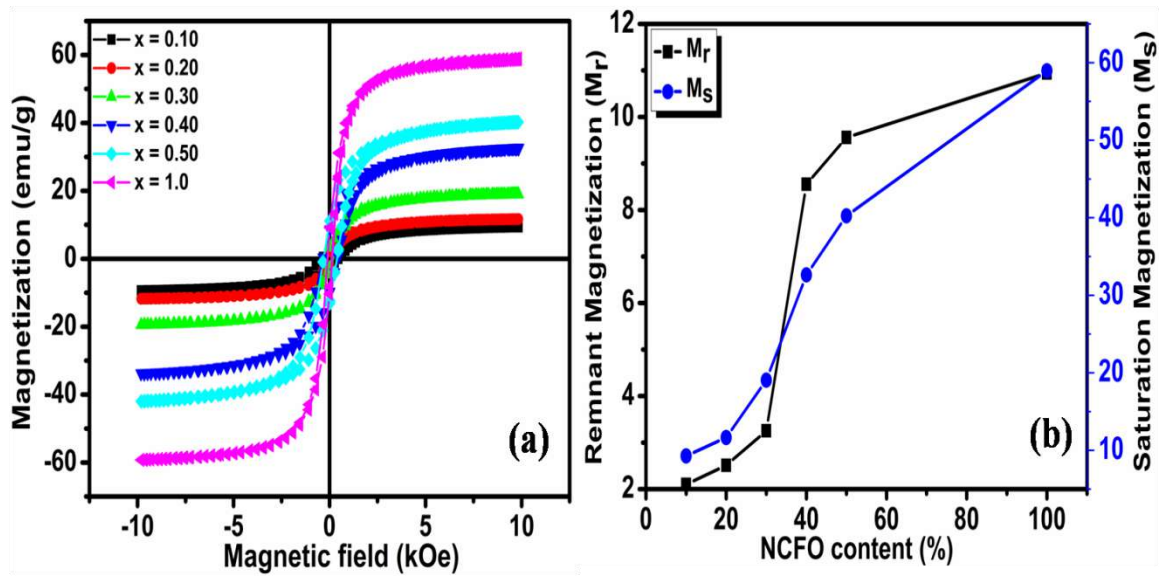


Figure 3.8 (a) M-H loops of $(x) Ni_{0.2}Co_{0.8}Fe_2O_4-(1-x) (K_{0.5}Na_{0.5})NbO_3$ ($x = 0.10, 0.20, 0.30, 0.40, 0.50$ and 1.0) composites and (b) Variation of saturation magnetization (M_s) and remnant magnetization (M_r) with NCFO content

Table 3.2 Magnetic parameters of $(x) Ni_{0.2}Co_{0.8}Fe_2O_4-(1-x) (K_{0.5}Na_{0.5})NbO_3$ ($x = 0.10, 0.20, 0.30, 0.40, 0.50$ and 1.0) composites measured at room temperature

Composition (x)	M_r (emu/g)	M_s (emu/g)	Magnetic moment (μ_B)
0.10	2.102	9.283	0.296
0.20	2.510	11.657	0.385
0.30	3.254	19.055	0.650
0.40	8.552	32.629	1.151
0.50	9.558	40.255	1.465
1.0	10.944	58.955	2.476

In order to get more information about magnetic ordering, the temperature dependent zero field cooled (ZFC) and field cooled (FC) magnetization curves are measured. The FC-ZFC curves are shown in Figure 3.9.

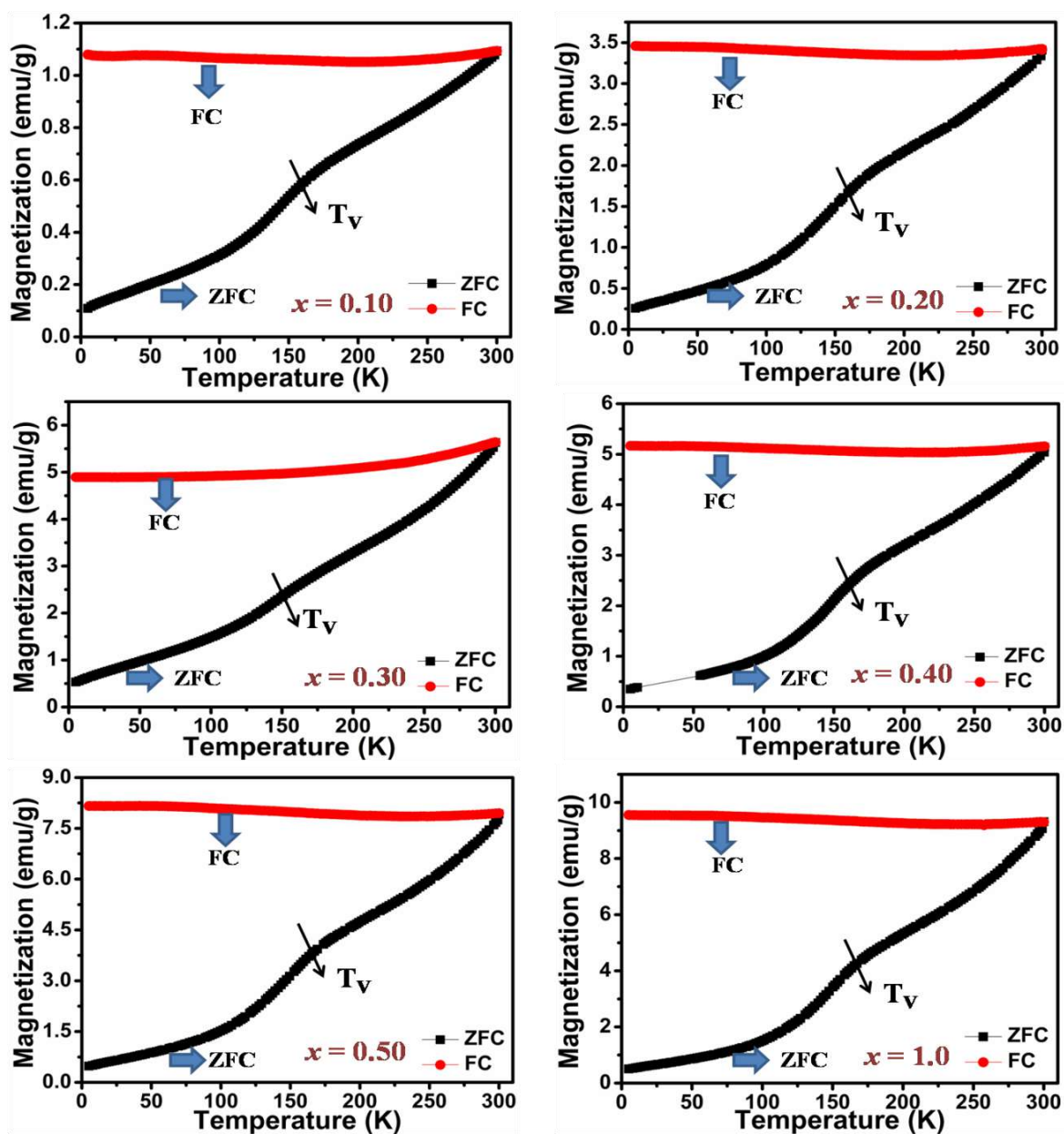


Figure 3.9 FC and ZFC temperature dependent magnetization curves for (x) $Ni_{0.2}Co_{0.8}Fe_2O_4-(1-x)(K_{0.5}Na_{0.5})NbO_3$ ($x = 0.10, 0.20, 0.30, 0.40, 0.50$ and 1.0) composites

These magnetization curves are measured at an applied magnetic field, $H = 500$ Oe in the temperature range 5–300 K. In ZFC magnetization measurement, the sample was cooled in absence of magnetic field from 300 K to 5 K. After this magnetization was measured by heating the sample from 5–300 K. In FC measurement, the sample

was cooled from 300 K to 5 K in presence of magnetic field (500 Oe) and then magnetization was measured on heating the sample from 5–300 K. The FC magnetization curve shows nearly a constant trend which means magnetization is temperature independent. This unvarying tendency of FC magnetization can be attributed to the presence of strong inter-particle interaction which induces magnetic ordered state [157]. The ZFC magnetization curve goes through the transition near 140–145 K, where a substantial change in the slope of magnetization curve has been observed. This transition can be attributed to Verwey transition or charge ordering, metal-insulator transition. At Verwey transition, material goes through a structural transformation from cubic to orthorhombic structure. This observed decrease in magnetization near Verwey transition can be described with the help of magneto-electronic model devised by Belov [158]. In this model the hopping (valence) electrons interact with the fixed (inner) electrons of ferromagnetic materials by means of Vonsovskii type of exchange. When sample cools down through Verwey transition (T_V), the hopping electrons are magnetically ordered with the magnetic cations by means of Vonsovskii exchange interaction, forming an electron sublattice. This electron sublattice has magnetic moment antiparallel to the net magnetic moment of A and B sublattices. Accordingly, we observe decrease in the magnetization for $T < T_V$. For $T > T_V$, the thermal energy wreck the electron sublattice or magnetic ordering of hopping electrons. Hence observed decrease in magnetization of ZFC curve near 140–145 K is due to Verwey transition.

The electrical behaviour of the composites has been studied using complex impedance spectroscopy (CIS) in view of their capability of correlating the sample's electrical behaviour to its microstructure [159]. CIS provide important information about the frequency dependent properties of the composites. The variation of imaginary part (Z'') versus real part (Z') of the complex impedance spectra for different temperatures is known as Nyquist plots. Figure 3.10 exhibits the Nyquist plots of (x) $Ni_{0.2}Co_{0.8}F_2O_4-(1-x)$ ($K_{0.5}Na_{0.5}NbO_3$) ($x = 0, 0.10, 0.20, 0.30, 0.40$ and 0.50) composites taken over a wide frequency range (100 Hz–1 MHz) at different temperatures. Complex impedance can be ideally described by Debye equation whose response is simulated by parallel circuit with a resistor (R) and ideal capacitor (C) related by:

$$Z^* = (R_b^{-1} + i\omega C_b)^{-1} + (R_{gb}^{-1} + i\omega C_{gb})^{-1} \quad (3.4)$$

Evaluating equation 3.4 we will get real and imaginary parts of complex impedance as

$$Z' = R_b/[1+(\omega R_b C_b)^2] + R_{gb}/[1+(\omega R_{gb} C_{gb})^2] \quad (3.5)$$

$$Z'' = \omega R_b^2 C_b/[1+(\omega R_b C_b)^2] + \omega R_{gb}^2 C_{gb}/[1+(\omega R_{gb} C_{gb})^2] \quad (3.6)$$

Where $\omega = 2\pi f$ is the frequency of the applied electric field, R_b , R_{gb} and C_b , C_{gb} represents grain (bulk) resistance, grain boundary resistance and respective capacitances respectively.

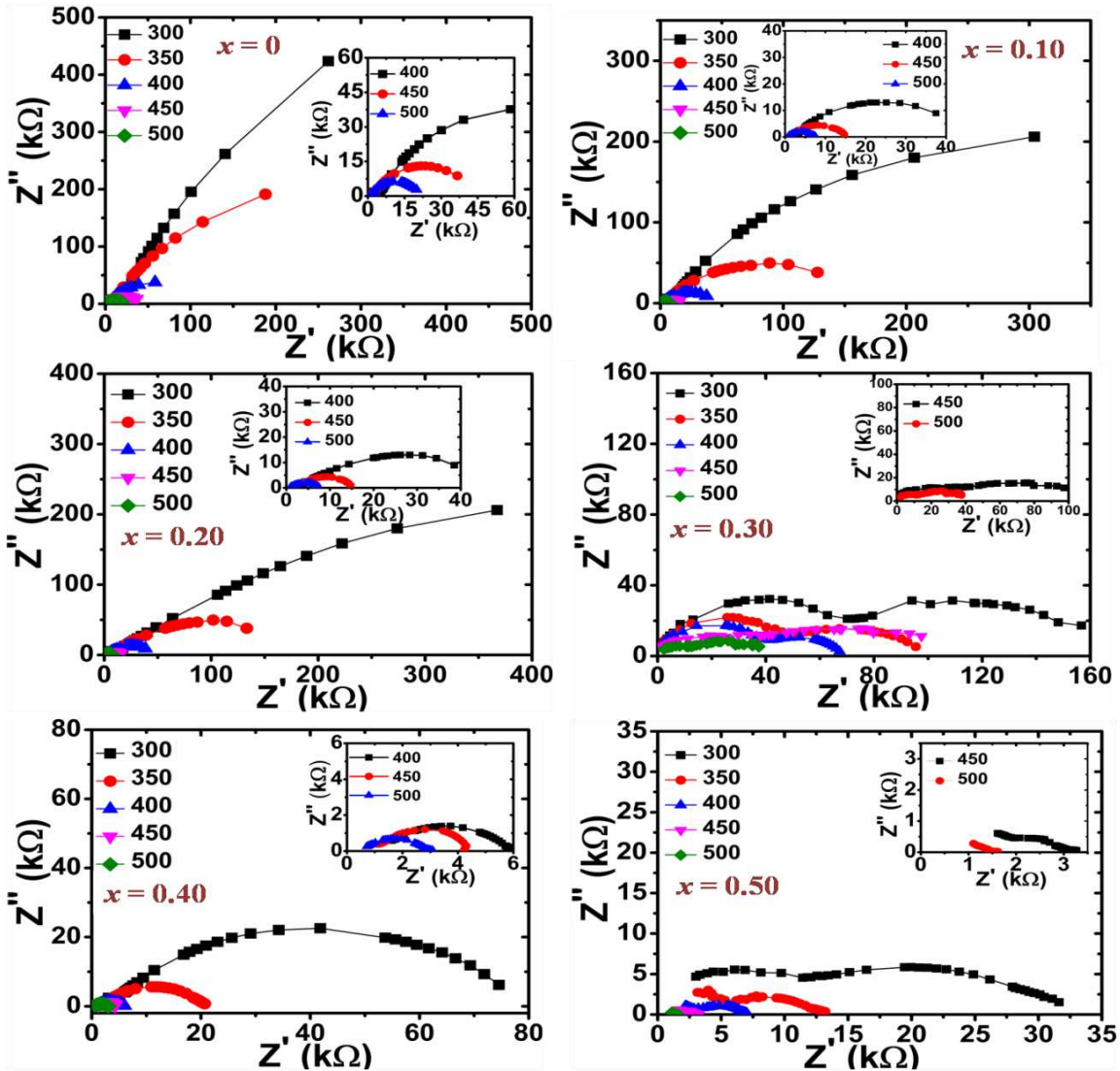


Figure 3.10 Nyquist plots for $(x) Ni_{0.2}Co_{0.8}Fe_2O_4-(1-x) (K_{0.5}Na_{0.5})NbO_3$ ($x = 0, 0.10, 0.20, 0.30, 0.40$ and 0.50) composites at $300, 350, 400, 450$ and 500 °C

The complex impedance spectra show the formation of semicircular arc within the temperature range $300-500$ °C, which depends upon the strength of relaxation and available frequency range. The Nyquist plots of individual KNN phase and $(x) Ni_{0.2}Co_{0.8}Fe_2O_4-(1-x)(K_{0.5}Na_{0.5})NbO_3$ ($x \leq 0.20$) composites comprise of single semicircular arc within the temperature range $300-500$ °C. But for composites with $x > 0.20$ we have two semicircular arcs of different radii corresponding to high and low frequency regions.

Table 3.3 The variation of AC impedance parameters for NCFO/KNN composites at different temperatures

Composition (x)	300 °C	350 °C	400 °C	450 °C	500 °C	
x = 0.10	R _b (kΩ)	695.62	227.09	59.28	19.98	10.65
	C _b (nF)	2.29	2.34	5.37	1.66	1.49
	R _{gb} (kΩ)
	C _{gb} (nF)
x = 0.20	R _b (kΩ)	637.5	211.76	49.03	18.44	7.67
	C _b (nF)	1.90	2.51	6.49	2.88	2.08
	R _{gb} (kΩ)
	C _{gb} (nF)
x = 0.30	R _b (kΩ)	75.55	65.45	51	40.23	20.64
	C _b (nF)	0.035	0.024	0.031	0.014	0.026
	R _{gb} (kΩ)	142.22	109.09	70	65.42	49.68
	C _{gb} (nF)	0.56	0.073	1.14	1.52	1.60
x = 0.40	R _b (kΩ)	20	9.38	4	2.62	1.96
	C _b (nF)	0.079	0.034	0.099	0.020	1.62
	R _{gb} (kΩ)	78.89	22.18	6.60	4.69	2.26
	C _{gb} (nF)	1.01	0.80	1.33	1.69	7.81
x = 0.50	R _b (kΩ)	15.62	6.58	3.76	2.48
	C _b (nF)	0.085	0.078	0.084	0.052
	R _{gb} (kΩ)	33.52	13.08	7.51	3.85	1.68
	C _{gb} (nF)	1.21	1.02	0.89	1.41	0.71

These higher and lower frequency semicircular arcs may be ascribed as parallel combination of bulk resistance (R_b), bulk capacitance (C_b) and grain boundary resistance (R_{gb}), grain boundary capacitance (C_{gb}) respectively, which corresponds to contribution from bulk material (intergranular properties) and grain boundaries respectively, so they relax in different frequency region [160]. The intercepts of these two semicircular arcs with real axis (Z') gives us an estimate of bulk (R_b) and grain boundary (R_{gb}) resistance of the material. The capacitance corresponding to the bulk and grain boundary is computed by determining the frequency for the peak maxima of semicircular arcs and then using the relations:

$$\omega_{\max}R_bC_b = 1 \quad (3.7)$$

$$\omega_{\max}R_{gb}C_{gb} = 1 \quad (3.8)$$

The obtained values of R_b , R_{gb} , C_b and C_{gb} for the composite samples from the Nyquist plots are tabulated in Table 3.3. It is evident from Table 3.3 that R_b and R_{gb} are found to decrease with increase in temperature indicating the negative temperature coefficient of resistance (NTCR) behaviour of the composites analogous to semiconductors [161]. It is also evident from the Nyquist plots shown in Figure 3.10 that the semicircles exhibit some degree of depression indicating that centre of the semicircles lies below (Z') axis signalling the presence of non-Debye type of relaxation in the composites. With an increase in temperature, the semicircular arcs become smaller and depression angle decreases. This may be attributed to presence of distributed elements in the material-electrode system [162].

The impedance loss spectra has been used to evaluate the relaxation time (τ) of the charge carriers by using the relation, $\omega_{\max}\tau = 2\pi f_{\max}\tau = 1$. The relaxation time basically gives an estimation of the dynamics of the electrical relaxation process occurring in the material. Figure 3.11 exhibits the plots of $\ln \tau$ vs. inverse of absolute temperature ($10^3/T$) for different compositions of NCFO/KNN composites. It is found that higher the value of τ , slower is the electrical relaxation process, and vice-versa. The nature of variation of τ with temperature follows the Arrhenius relation given by equation (3.9)

$$\tau = \tau_0 \exp(-E_a/K_B T) \quad (3.9)$$

Where τ_0 is pre exponential factor, E_a is activation energy, K_B is Boltzmann constant

and T is the absolute temperature. The values of the activation energies of the samples evaluated from the linear fit to $\ln \tau$ vs. $10^3/T$ plots are 0.93, 0.87, 0.50, 0.77 and 0.66 eV for $x = 0.10, 0.20, 0.30, 0.40$ and 0.50 , respectively.

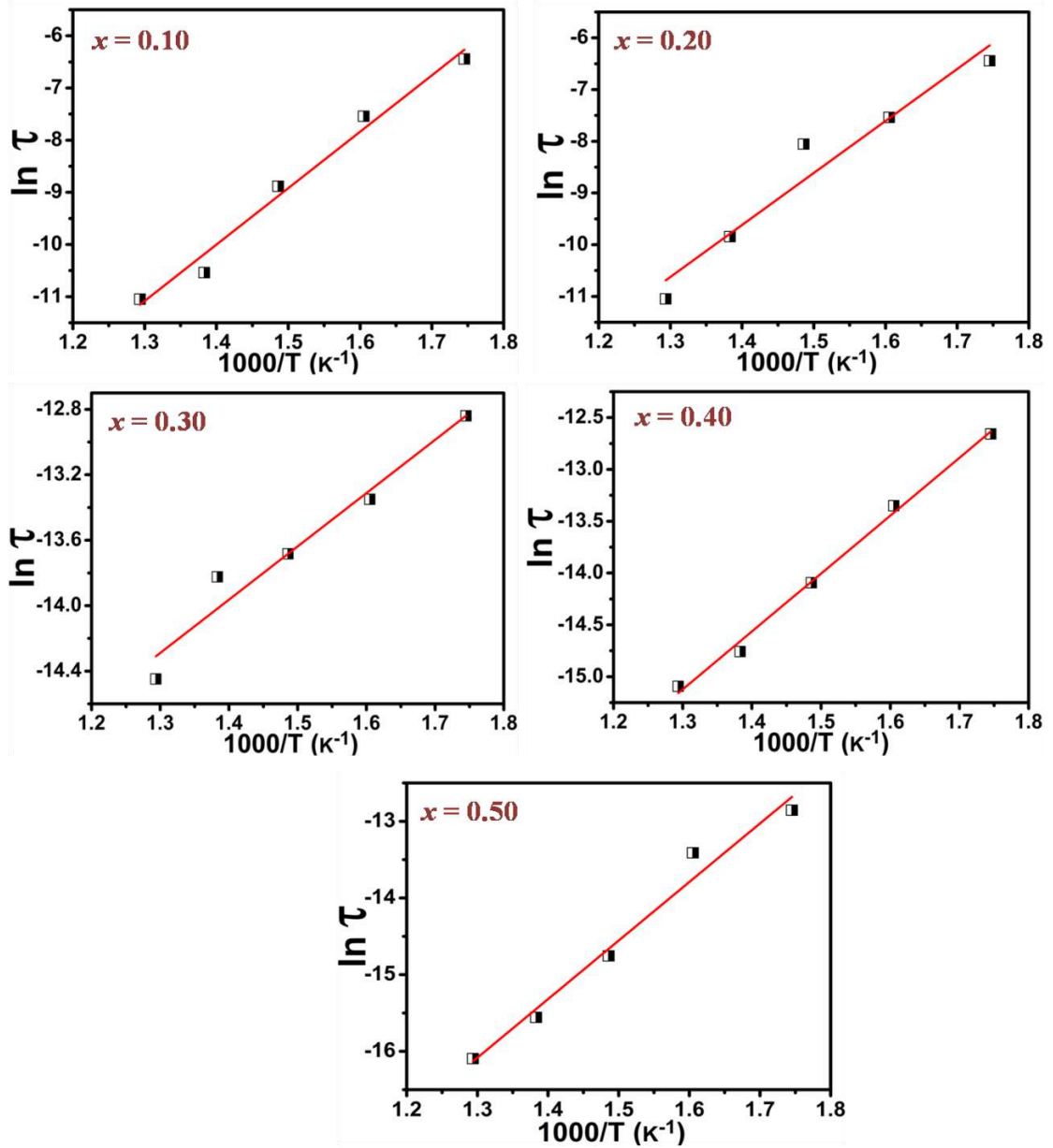


Figure 3.11 Variation of relaxation time ($\ln \tau$) with $10^3/T$ for (x) $Ni_{0.2}Co_{0.8}Fe_2O_4-(1-x)$ $(K_{0.5}Na_{0.5})NbO_3$ ($x = 0.10, 0.20, 0.30, 0.40$ and 0.50) composites

The coexistence of ferroelectric and ferrite phases in the particulate composites gives rise to ME effect. The ME effect is an outcome of interaction among the distinct orderings of constituent phases in the composite. This effect is basically an interface coupled electric and magnetic ordering through elastic interaction between the piezoelectric and piezomagnetic phases [30]. In order to establish the ME coupling between ferroelectric and

ferrite phases in $(x) Ni_{0.2}Co_{0.8}Fe_2O_4-(1-x) (K_{0.5}Na_{0.5})NbO_3$ composites, ME voltage coefficient (α_{ME}) has been determined by dynamic method [144] using an in-house setup. Figure 3.12 (a-e) shows the variation of α_{ME} with DC bias magnetic field for $(x) Ni_{0.2}Co_{0.8}Fe_2O_4-(1-x) (K_{0.5}Na_{0.5})NbO_3$ ($x = 0.10, 0.20, 0.30, 0.40$ and 0.50) composites.

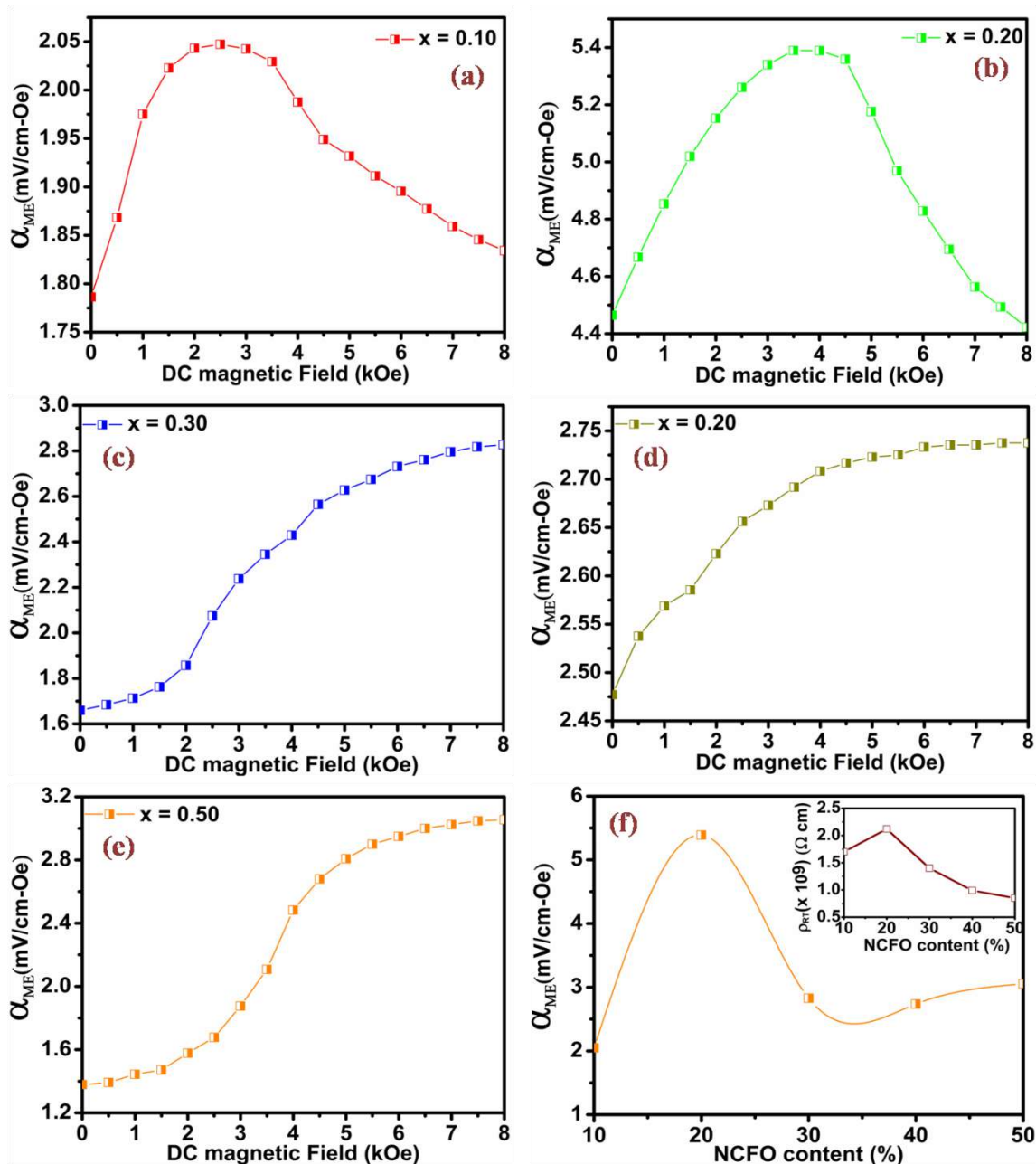


Figure 3.12 Variation of α_{ME} with DC magnetic field for $(x) Ni_{0.2}Co_{0.8}Fe_2O_4-(1-x) (K_{0.5}Na_{0.5})NbO_3$ (a) $x = 0.10$, (b) $x = 0.20$, (c) $x = 0.30$, (d) $x = 0.40$, (e) $x = 0.50$ composites and (f) variation of α_{ME} with NCFO content, inset shows variation of resistivity with NCFO content

Before measuring α_{ME} samples were poled at an applied electric field of 1 kVcm^{-1} for 30

minutes at 80 °C. While measuring α_{ME} , we applied AC magnetic field of 5 Oe having frequency 999 Hz in tandem with a sweeping DC magnetic field from 0–8 kOe. The ME voltage coefficient, α_{ME} , was determined using the following relation:

$$\alpha_{ME} = \frac{V_{out}}{d \times H} \quad (3.10)$$

Here V_{out} , d and H are the induced output voltage, thickness of sample and applied AC magnetic field respectively [163].

We found the highest value of $\alpha_{ME} = 5.389$ mV/cm-Oe for $x = 0.20$ bulk composite. It is evident from Figure 3.12 (b) for $x = 0.20$ that ME voltage coefficient (α_{ME}) increases with increase in magnetic field up to 4 kOe and thereafter decreases because magnetostriction coefficient ‘ λ ’ increases with increasing magnetic field and reaches its saturation value. Due to this the strain generated in the ferrite phase produces an unvarying electric field in the piezoelectric phase. Once the magnetostriction ‘ λ ’ achieves saturation, the piezomagnetic coupling coefficient $q = \delta\lambda/\delta H_{Bias}$ starts decreasing with increment in magnetic field consequently reducing the piezomagnetic coupling which is responsible for decrease of α_{ME} [164]. For other compositions the value of α_{ME} has been found to increase with applied magnetic field and then remains nearly constant at higher magnetic field. This can be attributed to enhancement in the magnetostrictive properties and in turn the piezomagnetic coefficient of the composites. Figure 3.12 (f) shows the variation of α_{ME} with NCFO content. It is found that α_{ME} is maximum for $x = 0.20$ and then decreases thereafter. Magnetolectric coupling coefficient, α_{ME} depends on a number of factors including resistivity, piezoelectric coefficient, piezomagnetic coefficient and mechanical coupling [165] in composites which comprises piezoelectric and piezomagnetic phases as their constituents. To study the variation in the α_{ME} , we measured the room temperature DC resistivity of the prepared composites and the variation of resistivity with ferrite content is shown in inset of the Figure 3.12 (f). The effective α_{ME} can be significantly affected by the resistivity of the composites. Low resistivity leads to leakage of charges produced in the ferroelectric phase through the neighbouring ferrite grains, consequently decreasing the α_{ME} . It is observed that resistivity increases up to $x = 0.20$ composition and decreases thereafter. The maximum value of the resistivity was observed for $x = 0.20$ composition which is having the highest value of α_{ME} . This may be attributed to its higher resistivity as compared to other compositions. The obtained α_{ME} for the NCFO/KNN composites is larger than observed for other particulate ME composites [93-95].

3.3.2 (x) $CoMn_{0.2}Fe_{1.8}O_4-(1-x)$ ($K_{0.5}Na_{0.5}$) NbO_3 ME composite system with $x = 0, 0.10, 0.20, 0.30, 0.40, 0.50$ and 1.0

Figure 3.13 depicts the X-ray diffraction patterns for (x) $CoMn_{0.2}Fe_{1.8}O_4-(1-x)$ ($K_{0.5}Na_{0.5}$) NbO_3 ($x = 0.10, 0.20, 0.30, 0.40, 0.50$) ME composites along with their constituent phases. All the peaks in the composites can be identified for both $CoMn_{0.2}Fe_{1.8}O_4$ (CMFO) and ($K_{0.5}Na_{0.5}$) NbO_3 (KNN) phases. The XRD peak indexing of the composites is in agreement with reported values of CMFO [166] and KNN [145]. The XRD patterns show that the single phase perovskite orthorhombic structure for KNN and cubic spinel structure of CMFO has been synthesized successfully. No impurity traces are found in the XRD patterns of the composites. This confirms that both constituent phases have retained their identity in the composites. The peak intensity akin to CMFO increases with incorporation of ferrite in the composites. The values of the lattice parameters for composites along with their constituent phases are listed in Table 3.4. The relative density of the composites is obtained using equation 3.2 and is given in Table 3.4.

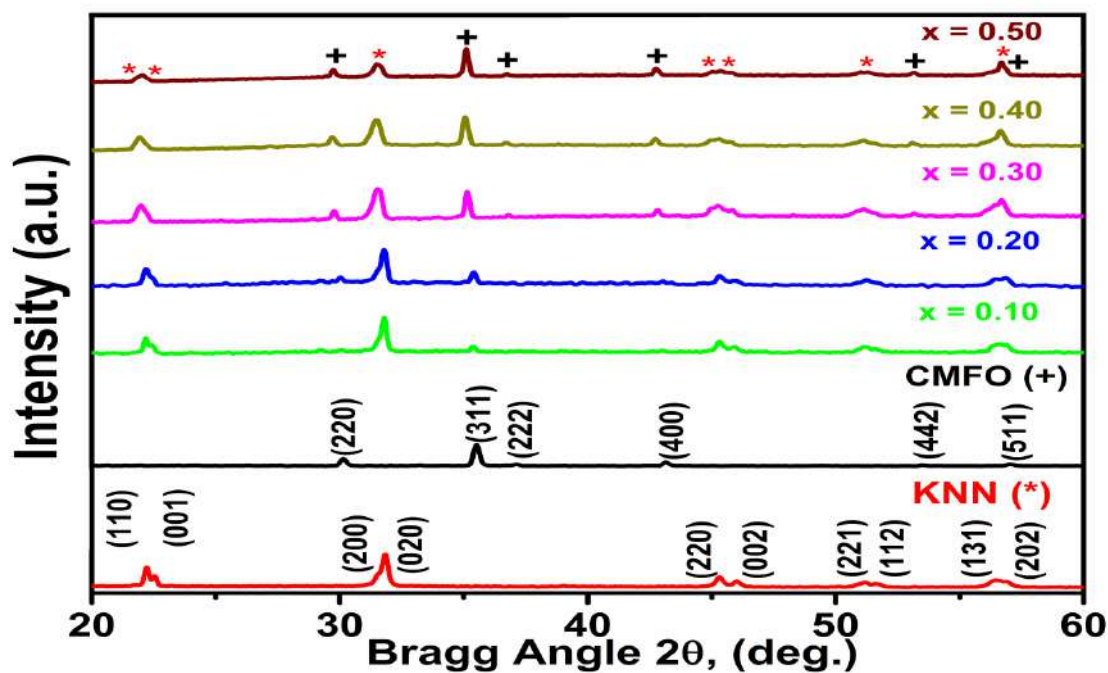


Figure 3.13 XRD patterns of (x) $CoMn_{0.2}Fe_{1.8}O_4-(1-x)$ ($K_{0.5}Na_{0.5}$) NbO_3 ($x = 0.10, 0.20, 0.30, 0.40$ and 0.50) composites along with individual KNN and CMFO phases where (asterisk, *) represents KNN and (plus, +) represents the CMFO phase

Surface morphology of the composite samples has been investigated using field emission scanning electron microscopy (FE-SEM). Figure 3.14 depicts the FE-SEM micrographs of

(x) $CoMn_{0.2}Fe_{1.8}O_{4-(1-x)}(K_{0.5}Na_{0.5})NbO_3$ ($x = 0.0, 0.10, 0.20, 0.30, 0.40, 0.50$ and 1.0) composites. All the composites exhibit homogeneous microstructure. Average grain size of the composites was computed using linear interception technique and obtained values are listed in Table 3.4. The average grain size was found to decrease with incorporation of ferrite. This is because the CMFO/KNN composites consist of ferrite (CMFO) phase distributed among ferroelectric (KNN) phase matrix. Also grain size of pure CMFO phase is smaller than that of KNN phase. Hence decrease in average grain size of composites is a consequence of addition of smaller grain sized CMFO phase in larger grain sized KNN phase matrix.

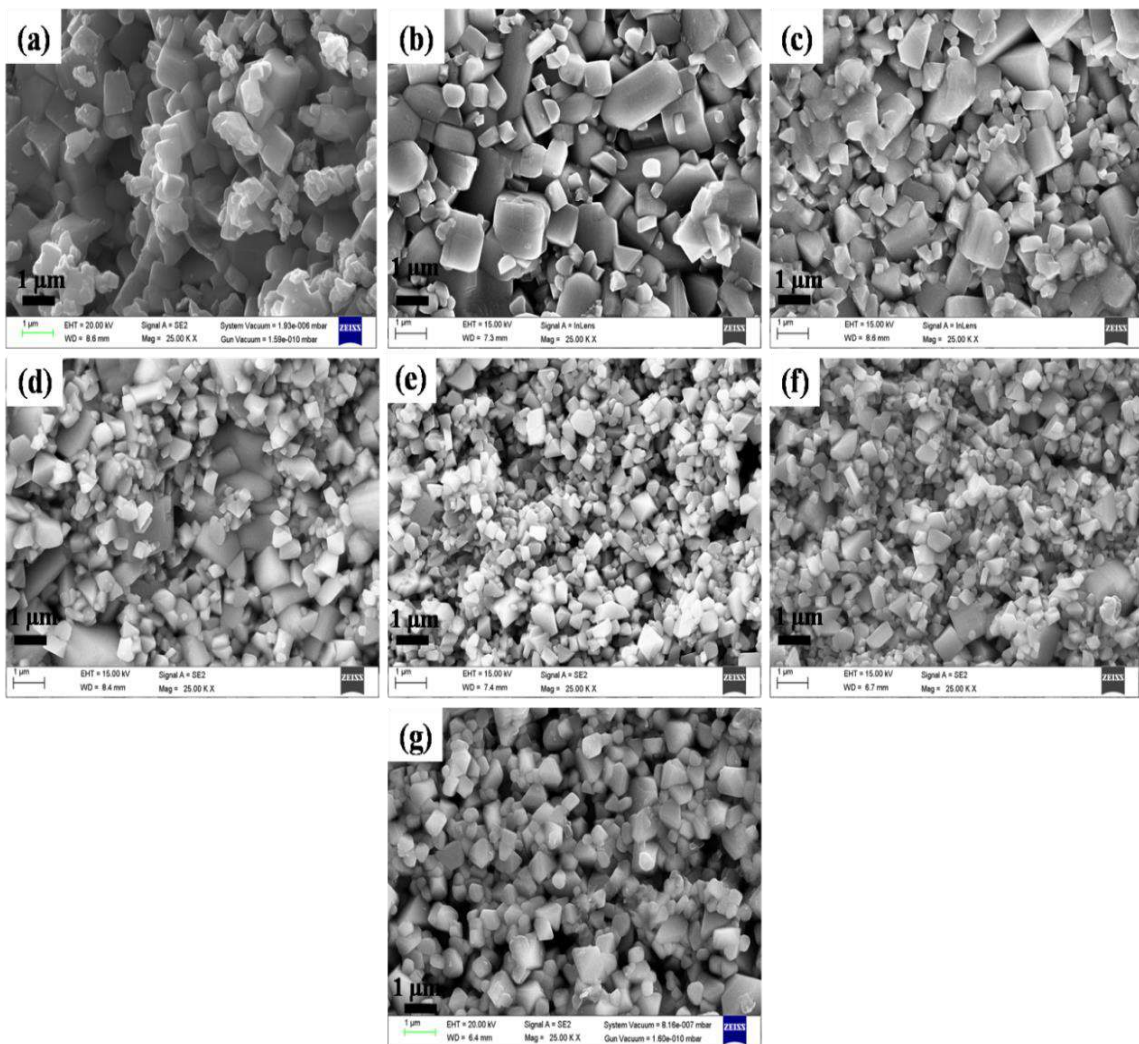


Figure 3.14 FE-SEM micrographs of (x) $CoMn_{0.2}Fe_{1.8}O_{4-(1-x)}(K_{0.5}Na_{0.5})NbO_3$ composites (a) $x = 0$, (b) $x = 0.10$, (c) $x = 0.20$, (d) $x = 0.30$, (e) $x = 0.40$, (f) $x = 0.50$ and (g) $x = 1.0$

Table 3.4 Lattice parameters, grain sizes and relative densities of (x) $CoMn_{0.2}Fe_{1.8}O_4$ -(1-x) $(K_{0.5}Na_{0.5})NbO_3$ (x = 0, 0.10, 0.20, 0.30, 0.40, 0.50 and 1.0) ME composites

Compositions (x)	Lattice Parameters (Å)				Average grain size (nm)	ρ_{rel} (%)
	CMFO		KNN			
	a	a	b	c		
0.0	-	5.707	5.626	3.390	910	88.54
0.10	8.424	5.717	5.634	3.319	883	87.62
0.20	8.414	5.707	5.636	3.356	736	88.52
0.30	8.477	5.774	5.680	3.547	642	86.23
0.40	8.497	5.783	5.688	3.548	479	85.46
0.50	8.484	5.735	5.688	3.945	474	87.63
1.0	8.391	-	-	-	512	85.53

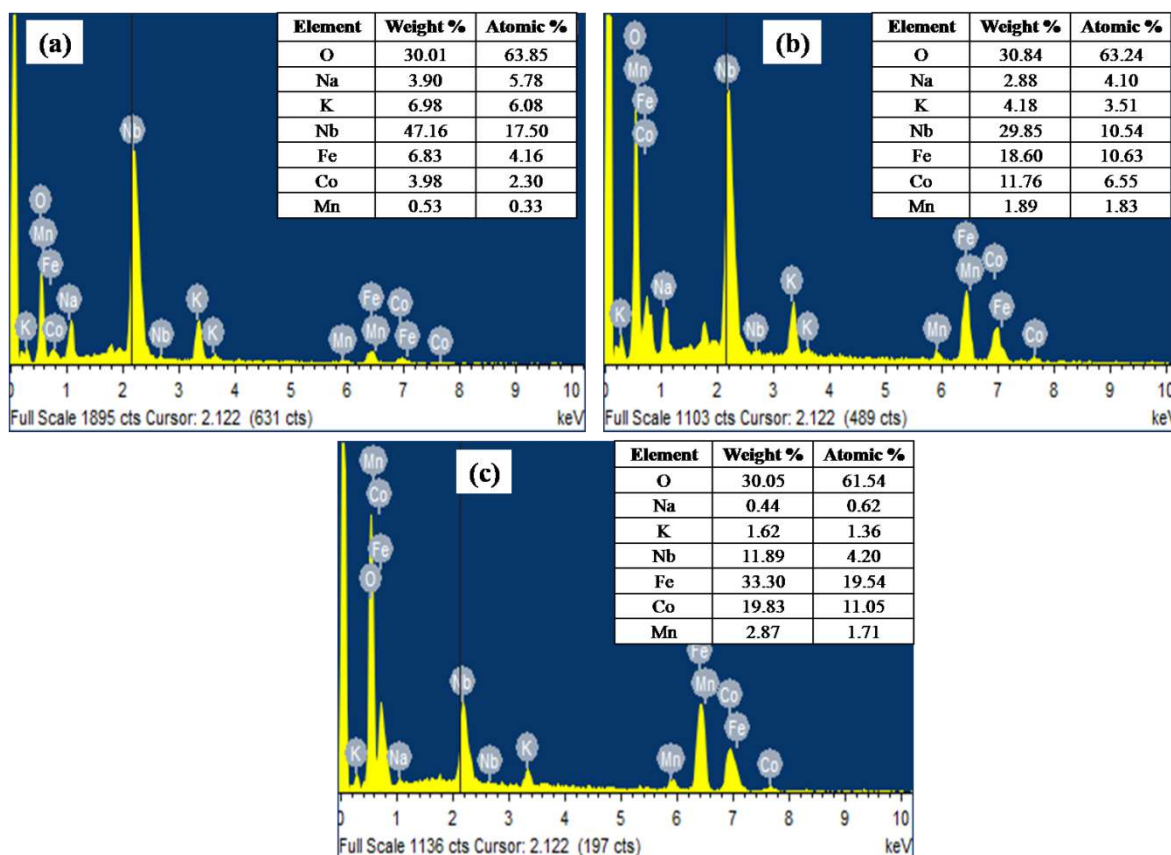


Figure 3.15 EDAX images of (x) $CoMn_{0.2}Fe_{1.8}O_4$ -(1-x) $(K_{0.5}Na_{0.5})NbO_3$ (a) $x = 0.10$, (b) $x = 0.30$ and (c) $x = 0.50$ composites

The compositional analysis for $(x) CoMn_{0.2}Fe_{0.8}O_4-(1-x) (K_{0.5}Na_{0.5})NbO_3$ with $x = 0.10, 0.30$ and 0.50 is done using Energy dispersive X-ray analysis (EDAX) as shown in Figure 3.15 (a)-(c). It provides an insight into the quantitative chemical analysis of the synthesized composites. The phase formation, purity, effective synthesis and chemical homogeneity of the composites is revealed from the presence of expected elements (K, Na, Nb, Mn, Co, Fe and O) in the EDAX spectrum.

Variation of dielectric constant (ϵ') and dielectric loss ($\tan \delta$) with temperature has been studied for $(x) CoMn_{0.2}Fe_{1.8}O_4-(1-x) (K_{0.5}Na_{0.5})NbO_3$ composites at three different frequencies (1, 5 and 10 kHz) and is presented in Figure 3.16. Two dielectric peaks have been observed for pure KNN phase and different composites. First dielectric peak is observed in the temperature range 190–220 °C corresponding to orthorhombic - tetragonal phase transition (T_{O-T}) for KNN phase. The second dielectric peak occurring on the high temperature side in the range 420–440 °C corresponds to tetragonal - cubic phase transition (T_C) for KNN phase. Dielectric constant is found to enhance with addition of CMFO. This can be attributed to presence of heterogeneity in the composites [83]. Heterogeneities correspond to interfaces in between ferroelectric and ferrite phase of composites, which produce space charge polarization. On application of electric field, the space charges produced by the ferrite phase accumulate at constituent phases interface due to the difference in their conductivities and permittivities [150], resulting in space charge polarization. With addition of CMFO, the number of space charges produced by CMFO increases resulting in higher value of dielectric constant. It has also been observed that dielectric constant increases steadily up to transition temperature (T_C) and then decreases afterwards. This may be attributed to electron hopping between Fe^{2+} and Fe^{3+} ions present on the octahedral sites. The hopping is thermally triggered with an increase in temperature. The hopping initiates localized displacement in the applied electric field direction, which encompasses the dielectric polarization in ferrites. Increase in temperature enhances the ac conductivity, which is attributed to increase in the drift mobility of thermally activated charge carriers [149]. Consequently, the dielectric polarization increases which accounts for increase in dielectric constant. Further, increase in temperature beyond T_C , enhances the arbitrary vibrational motion of electrons and ions, making them less receptive to orient themselves in applied field direction, thereby decreasing the dielectric constant. The decrease in dielectric constant after T_C may also be attributed to disappearance of domains [167].

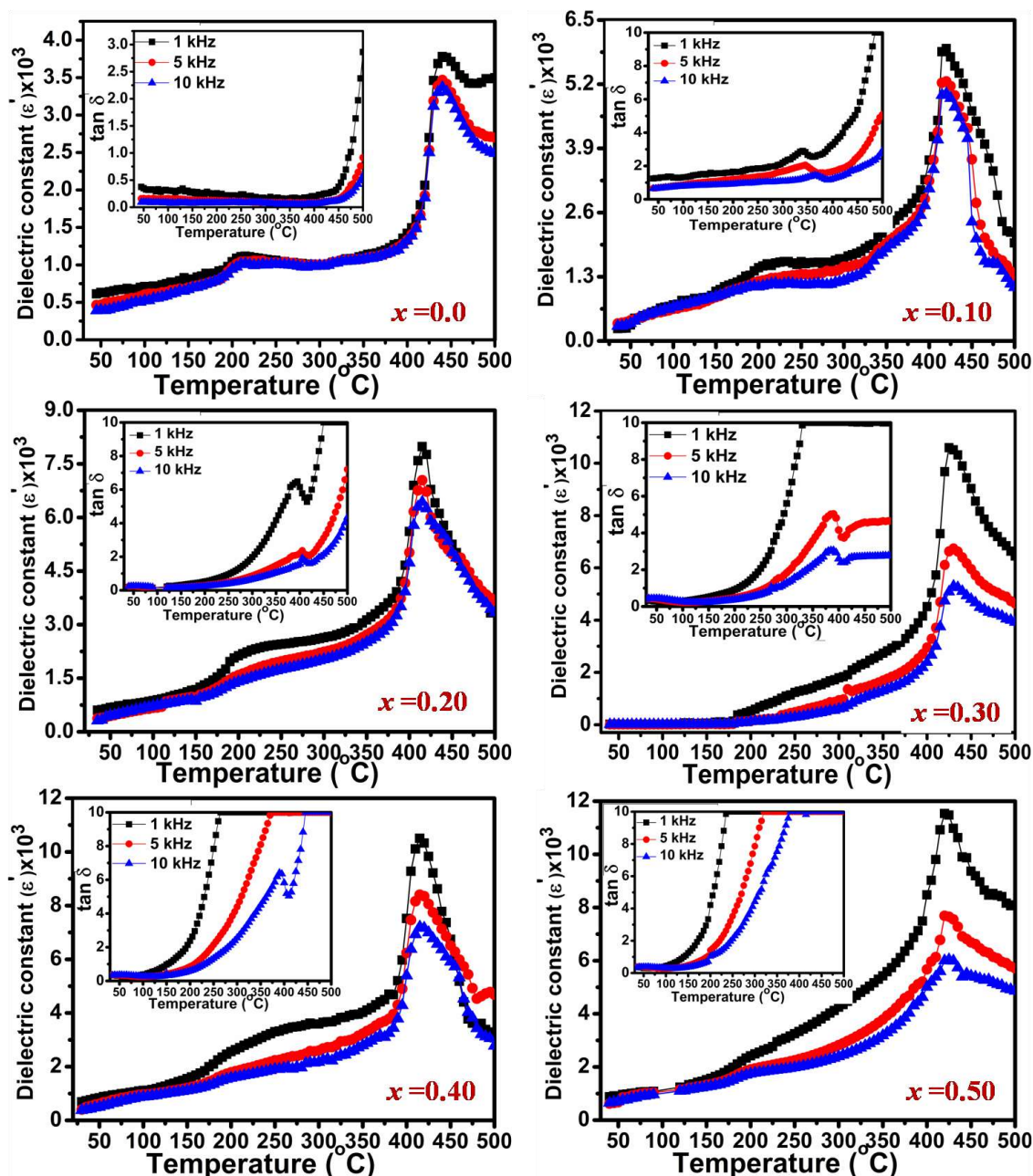


Figure 3.16 Temperature dependence of dielectric constant (ϵ') and dielectric loss ($\tan \delta$) at 1, 5 and 10 kHz frequencies for (x) $\text{CoMn}_{0.2}\text{Fe}_{1.8}\text{O}_4-(1-x)$ $(\text{K}_{0.5}\text{Na}_{0.5})\text{NbO}_3$ ($x = 0, 0.10, 0.20, 0.30, 0.40$ and 0.50) composites

The temperature dependence of dielectric loss factor for the CMFO/KNN composites is shown in inset of Figure 3.16. Dielectric loss peaks are evident from the plots of $\tan \delta$ vs. temperature. The origin of peaks may be attributed to dielectric relaxation phenomenon. Dielectric relaxation is the momentary delay or lag in the dielectric constant of the material. It usually occurs when polarization does not follow the externally applied AC field. Due to dielectric relaxation dielectric constant decreases, and dielectric loss shows

peaks at particular frequencies. Dielectric loss is found to increase with incorporation of ferrite in the composites. Enhancement in dielectric loss may be attributed to space charge conduction which is related to transport of defects like oxygen vacancies to dielectric electrode interface [152].

The significant increase in dielectric constant and strong frequency dependence are typical of that expected for a Maxwell-Wagner conduction mechanism [168]. At lower frequencies dielectric constant is dominated by electronic, ionic, atomic and interfacial polarizations. With further increase in frequency the contributions of ionic and orientational polarizations to dielectric properties diminish. Furthermore, a decrease in dielectric properties with increasing frequency is caused by the inability of different polarization contributions to follow the frequency change of the applied electric field, resulting in lower values of dielectric constant and loss at higher frequencies.

Figure 3.17 represents the P-E hysteresis loops of the (x) $CoMn_{0.2}Fe_{1.8}O_{4-(1-x)}$ ($K_{0.5}Na_{0.5}$) NbO_3 ($x = 0, 0.10, 0.20, 0.30, 0.40$ and 0.50) composites obtained at room temperature and at a frequency of 50 Hz. Addition of ferrite phase CMFO has significant effect on the shape and size of the P-E loops. All composites exhibit regular P-E hysteresis loops signifying the presence of ferroelectric ordering at room temperature. The observed ferroelectric parameters including remnant polarization (P_r) and coercive field (E_C) are listed in Table 3.5.

Table 3.5 Calculated values of remnant polarization (P_r), maximum polarization (P_{max}) and coercive field (E_C) for CMFO/KNN composites

Composition (x)	P_r ($\mu C/cm^2$)	P_{max} ($\mu C/cm^2$)	E_C (kV/cm)
0.0	13.314	22.640	11.179
0.10	8.899	17.505	9.707
0.20	6.535	16.373	9.589
0.30	6.237	15.573	9.364
0.40	6.002	13.819	7.859
0.50	5.038	10.297	6.194

Both P_r and E_C are found to decrease with addition of CMFO. The decrease in polarization can be due to enhancement in the conductivity of the composites leading to increase in leakage current [169]. The observed decrease in E_C may be attributed to switching of

ferroelectric domains due to change in charge carrier concentration which leads to domain pinning [170].

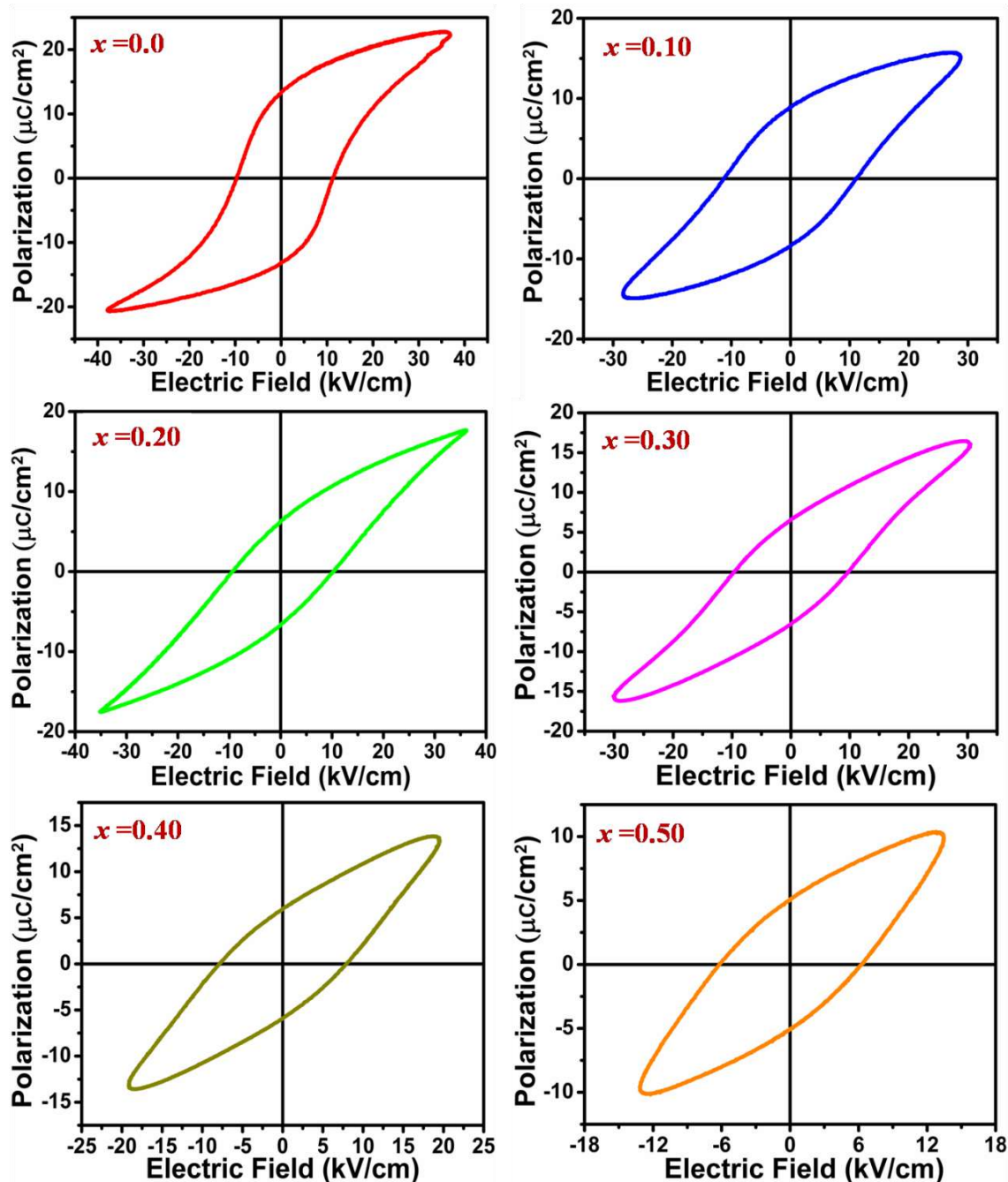


Figure 3.17 P-E hysteresis loops of (x) $CoMn_{0.2}Fe_{1.8}O_{4-(1-x)}(K_{0.5}Na_{0.5})NbO_3$ ($x = 0.0, 0.10, 0.20, 0.30, 0.40$ and 0.50) composites.

The magnetic characteristics of the composites are studied by measuring the M-H hysteresis loops at 300 K and 5 K with an applied magnetic field of $-50 \text{ kOe} \leq H \leq 50 \text{ kOe}$. Figure 3.18 shows the M-H hysteresis loops of the (x) $CoMn_{0.2}Fe_{1.8}O_{4-(1-x)}K_{0.5}Na_{0.5}NbO_3$ ($x = 0.10, 0.20, 0.30, 0.40, 0.50$ and 1.0) composites at 300 and 5 K. The composites are

found to exhibit regular hysteresis loops indicating the presence of long range ferromagnetic ordering [166]. The magnetic moment in Bohr Magneton has been calculated using equation 3.3. The observed magnetic parameters including remnant magnetization (M_r), saturation magnetization (M_s) and magnetic moment (μ_B) at 300 K and 5 K are calculated from M-H hysteresis loops shown in Figure 3.18 and are listed in Table 3.6. From Table 3.6 it is evident that magnetic parameters are enhanced at 5 K as compared to 300 K due to the orientations of spins [95]. Figure 3.19 shows the variation of obtained magnetic parameters with ferrite content at 5 and 300 K respectively. The observed magnetic parameters are found to increase with addition of ferrite in the composites.

Table 3.6 Calculated values of remnant magnetization (M_r), saturation magnetization (M_s), magnetic moment (μ_B) and exchange field (H_E) for CMFO/KNN composites at 5 and 300 K

Composition (x)	M_r (emu/g)		M_s (emu/g)		Mag. Moment (μ_B)		H_E (Oe)	
	5 K	300 K	5 K	300 K	5 K	300 K	5 K	300 K
0.10	7.760	2.950	11.411	9.755	0.364	0.311	-423	2.49
0.20	16.964	5.529	23.123	19.887	0.764	0.657	-73.61	2.64
0.30	23.494	6.420	31.586	27.476	1.078	0.938	-275.24	4.78
0.40	30.323	9.724	41.187	34.884	1.452	1.230	-80.64	8.50
0.50	34.331	12.692	52.282	45.091	1.902	1.640	-50	9.65
1.0	58.178	16.670	92.711	78.965	3.892	3.315	-1	0.50

The inset of Figure 3.18 shows the magnified image of M-H hysteresis loops for the CMFO/KNN composites. It is evident that the loops are slightly asymmetric from which we measured the exchange bias field (H_E) which is presented in Table 3.6.

In order to get more information about magnetic ordering in the CMFO/KNN composites, the magnetization measurements as a function of temperature are carried out. We measured the variation of magnetization with temperature in the zero field cooled (ZFC) and field cooled (FC) modes at an applied magnetic field of 500 Oe and in the temperature range 5–300 K. In ZFC mode the samples were cooled in absence of magnetic field from room temperature to 5 K and then magnetic field of 500 Oe was applied. Then magnetization was measured while heating the samples from 5 K to room temperature.

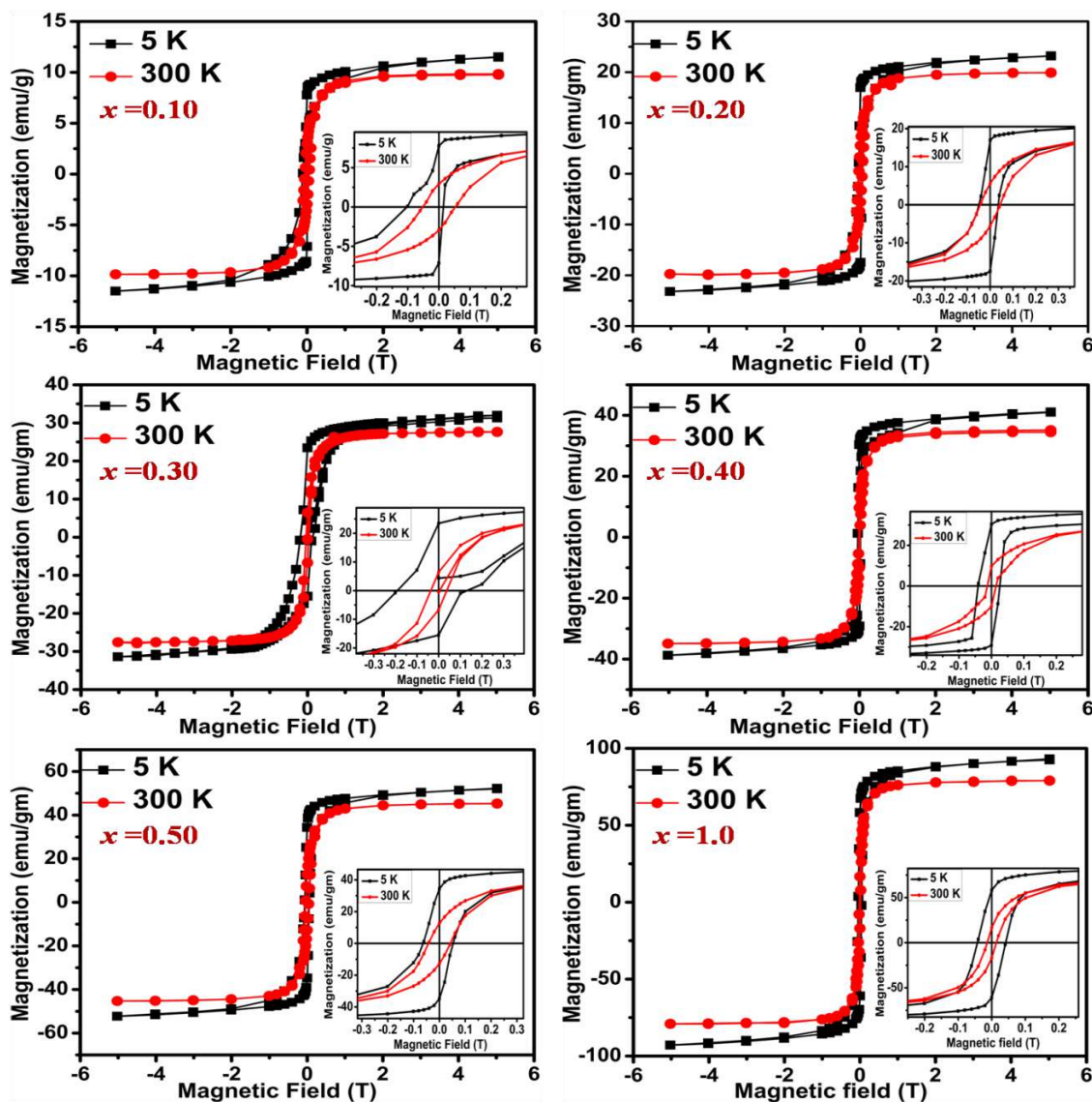


Figure 3.18 M-H hysteresis loops of (x) $CoMn_{0.2}Fe_{1.8}O_4-(1-x)$ $(K_{0.5}Na_{0.5})NbO_3$ ($x = 0.10, 0.20, 0.30, 0.40, 0.50$ and 1.0) composites at 300 and 5 K respectively with magnified images shown in the inset

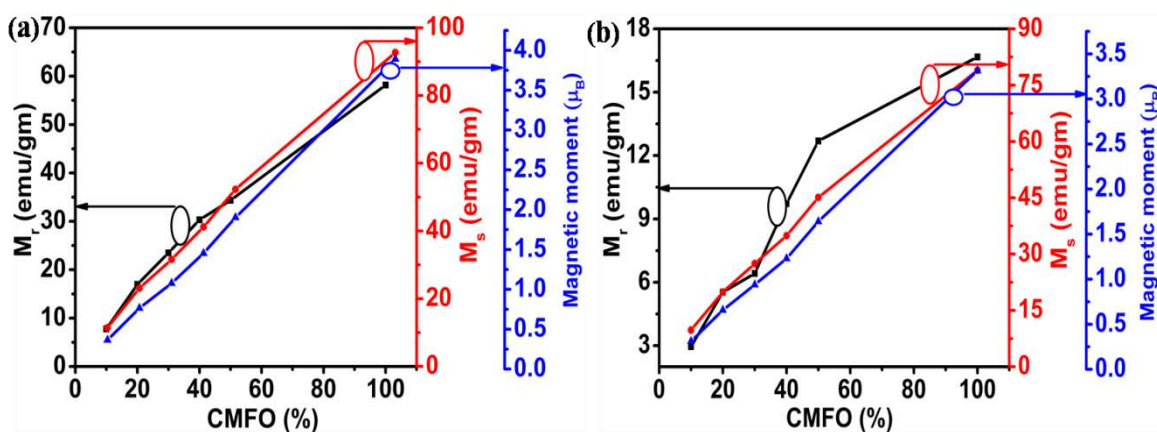


Figure 3.19 Variation of magnetic parameters with CMFO content at (a) 5 and (b) 300 K

In FC mode, the samples were cooled in presence of applied field of 500 Oe from room temperature to 5 K and then magnetization was measured while heating the sample in the same field. Figure 3.20 shows the variation of magnetization with temperature in the zero field cooled (ZFC) and field cooled (FC) modes at an applied magnetic field of 500 Oe.

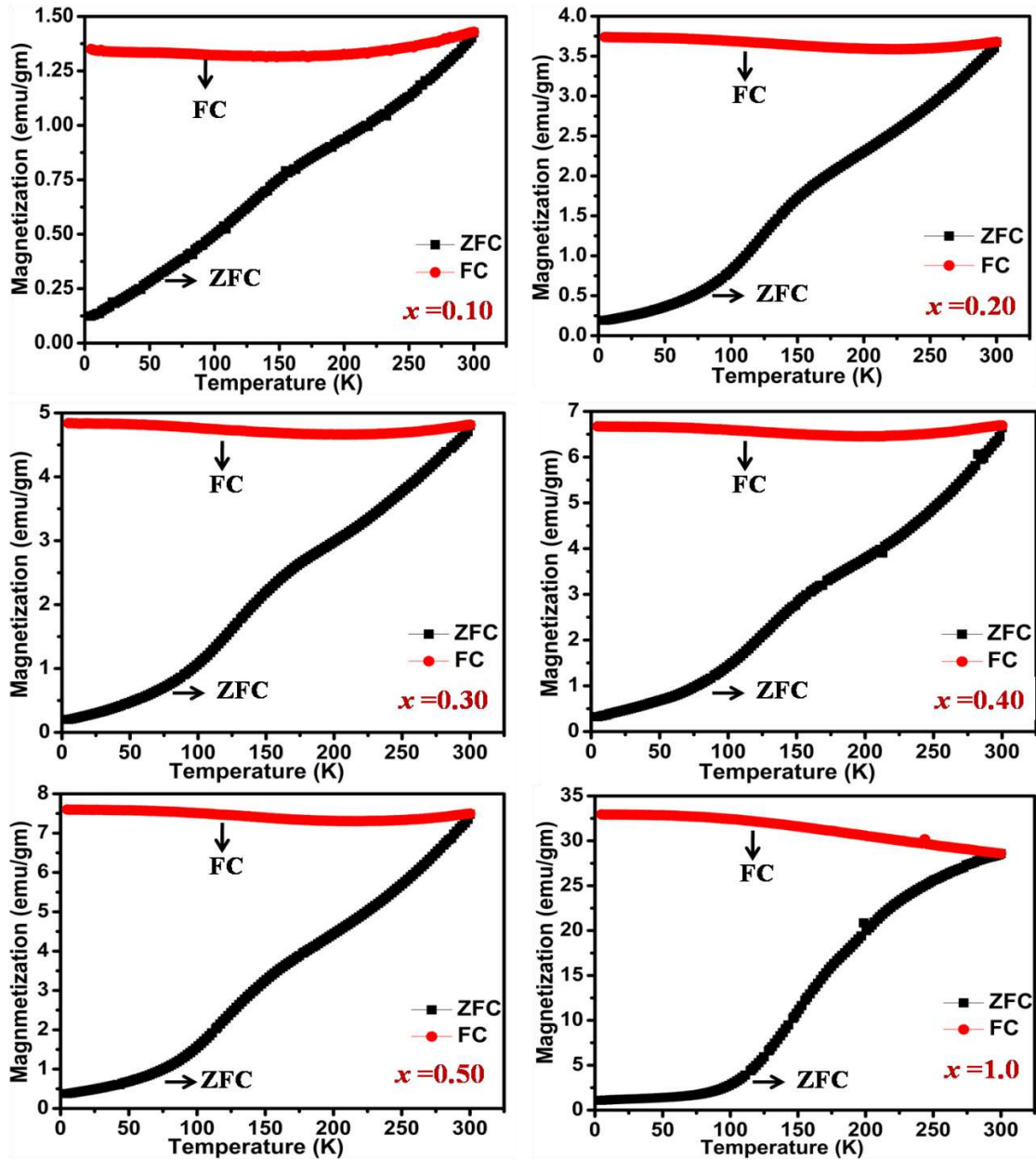


Figure 3.20 FC-ZFC temperature dependent magnetization curves of (x) $CoMn_{0.2}Fe_{1.8}O_4-(1-x)$ $(K_{0.5}Na_{0.5})NbO_3$ ($x = 0.10, 0.20, 0.30, 0.40, 0.50$ and 1.0) composites

It is evident from Figure 3.20 that FC magnetization of the composites remains almost independent of temperature. While ZFC magnetization shows a decreasing trend with decrease in temperature. The observed temperature independent behaviour of FC

magnetization may be due to presence of strong inter-particle interaction, which induces the magnetically ordered state [157]. Also we observe a large bifurcation between FC and ZFC magnetizations, which signals about the presence of strong irreversibility and magnetic relaxation in the composites [171]. Also the observed behaviour of M-T curves in ZFC and FC mode for the composites may be interpreted in terms of different factors which may include (i) structural changes due to increased CMFO content, (ii) change in particle size, (iii) change in magnetic anisotropy and (iv) spin glasses etc. [172].

Figure 3.21 exhibits the variation of real part of impedance (Z') in the frequency range of 100 Hz–1 MHz at different temperatures for CMFO/KNN composites.

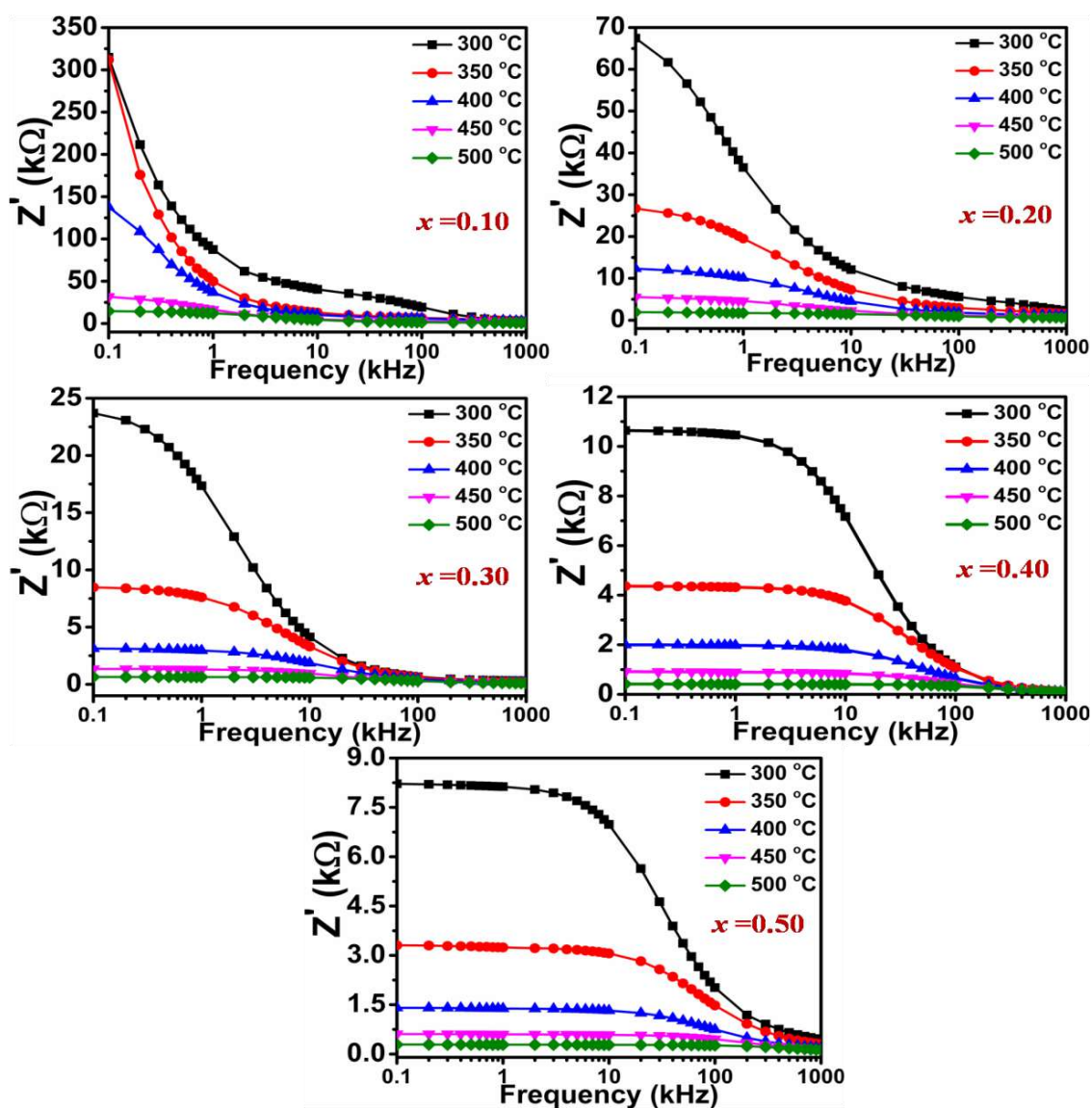


Figure 3.21 Variation of real part of impedance (Z') with frequency for (x) $CoMn_{0.2}Fe_{1.8}O_{4-(1-x)}(K_{0.5}Na_{0.5})NbO_3$ ($x = 0.10, 0.20, 0.30, 0.40$ and 0.50) composites at different temperatures

It is evident from Figure 3.21 that the magnitude of Z' decreases with increase in temperature, frequency and CMFO content. This indicates the possibility of increase in conductivity and signals the negative temperature coefficient of resistance (NTCR) type behaviour of the composites. The curves of Z' at different temperatures are found to merge above frequency of 100 kHz, indicating Z' to be almost independent of frequency and measured temperatures. This may be attributed to release of space charges as a result of barrier properties of materials at high temperature in high frequency regime [173-174].

Figure 3.22 depicts the variation of imaginary part of impedance (Z'') in the frequency range of 100 Hz-1MHz at different temperatures for CMFO/KNN composites.

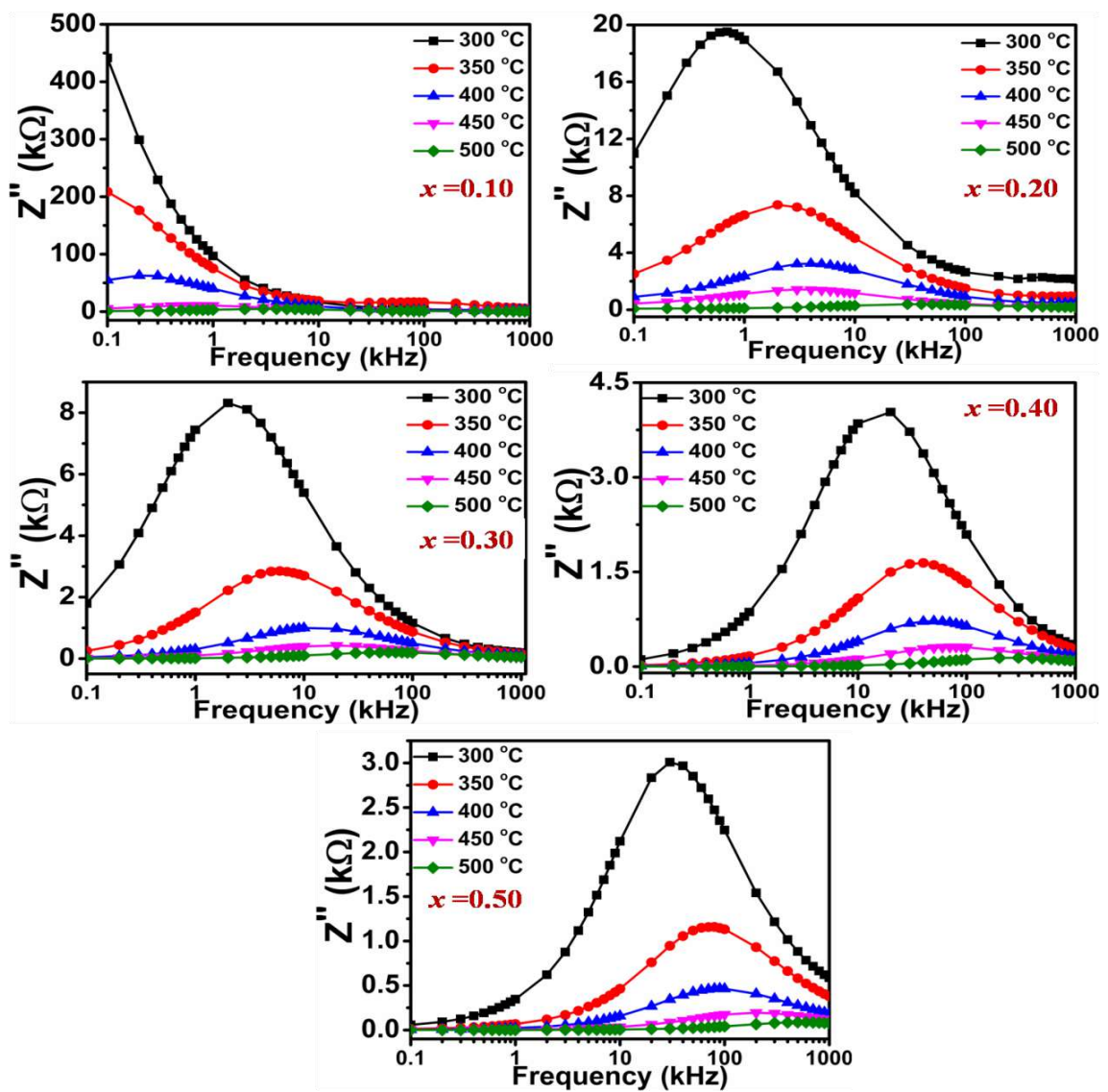


Figure 3.22 Variation of imaginary part of impedance (Z'') with frequency for (x) $CoMn_{0.2}Fe_{1.8}O_4-(1-x)(K_{0.5}Na_{0.5})NbO_3$ ($x = 0.10, 0.20, 0.30, 0.40$ and 0.50) composites at different temperatures

In Figure 3.22 we can see the appearance of Z''_{max} peak which is found to decrease and shift towards high frequency regime with increase in temperature. This may be attributed to temperature dependent electrical relaxation present in the material. For all the composites we obtain broadening of Z''_{max} peaks with increase in temperature, indicating the spread of relaxation times. In low temperature regime, relaxation may be due to electrons or immobile charges and in high temperature regime it may be due to oxygen vacancies or defects. Hopping of electrons or oxygen ion vacancies among the localized states is the reason for electrical conduction in the materials [175].

The temperature dependence of complex impedance spectrum Z' vs. Z'' (Nyquist plots) are shown in Figure 3.23 for CMFO/KNN composites.

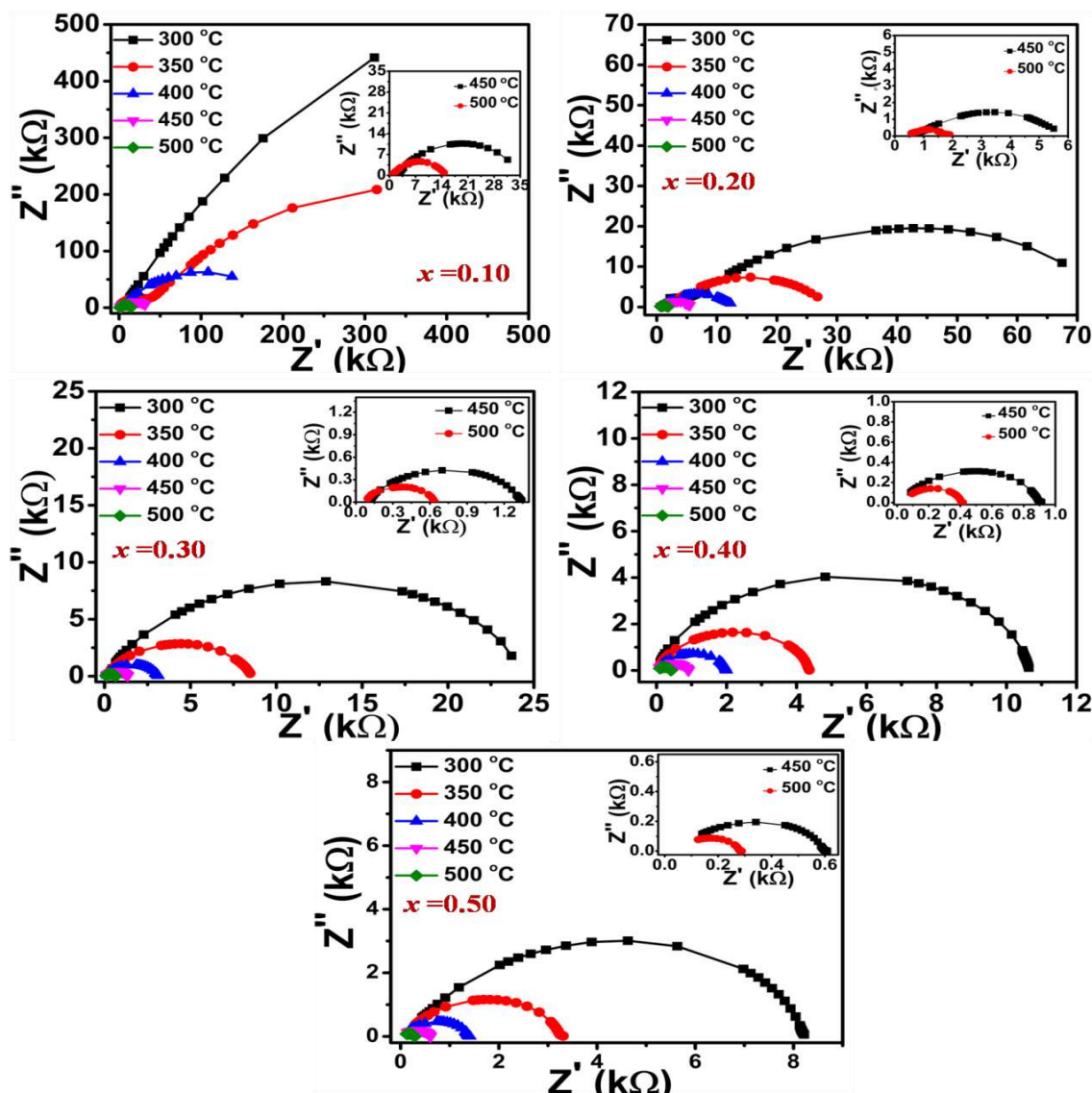


Figure 3.23 Nyquist plots for (x) $CoMn_{0.2}Fe_{1.8}O_4-(1-x)$ $(K_{0.5}Na_{0.5})NbO_3$ ($x = 0.10, 0.20, 0.30, 0.40$ and 0.50) in the temperature range $300 - 500$ °C

Nyquist plots are generally characterized by formation of semicircular arcs which relax in distinct frequency regions. Each semicircle may be ascribed as parallel combination of bulk resistance (R_b), bulk capacitance (C_b) and grain boundary resistance (R_{gb}), grain boundary capacitance (C_{gb}) respectively, which corresponds to contribution from bulk material (intergranular properties) and grain boundaries respectively, thereby relaxing in distinct frequency regimes [139]. It is evident from Figure 3.23 that we observe two semicircular arcs for composites with $x \leq 0.20$ indicating the presence of bulk (grain) (R_b) and grain boundary resistance (R_{gb}) effect. The bulk resistance (R_b) and grain resistance (R_{gb}) are obtained from the intercept on the Z' -axis and are tabulated in Table 3.7. This electrical behaviour may be described in terms of an equivalent circuit comprising of series combination of parallel RC circuits. The capacitances akin to the bulk (C_b) and grain boundary (C_{gb}) are calculated by knowing the peak maxima frequency of semicircular arcs and then using the equations 3.5 and 3.6. It is evident from Table 3.7 that values of R_b and R_{gb} decrease with increase in temperature indicating the negative temperature coefficient of resistance (NTCR) behaviour of composites. It is also observed that complex impedance plots are not full semicircles and their centres lie below the abscissa (Z' axis), indicating the non-Debye type dielectric relaxation in the CMFO/KNN composites. This may be due to the presence of distributed elements in the material-electrode system [176].

In order to establish the coupling between ferroelectric and ferrite phases in (x) $CoMn_{0.2}Fe_{1.8}O_4-(1-x)$ ($K_{0.5}Na_{0.5}$) NbO_3 ($x = 0.10, 0.20, 0.30, 0.40$ and 0.50) composites, ME voltage coefficient (α_{ME}) has been determined using dynamic method [144]. ME effect is the product of interaction among distinct orderings of constituent phases. It is an interface coupled electrical and magnetic ordering via elastic interaction among piezomagnetic and piezoelectric phases [30].

The ME voltage coefficient, α_{ME} , was determined using the equation (3.10). While measuring α_{ME} , same procedure was followed as described in section 3.3.1. Figure 3.24 (a-e) shows the variation of α_{ME} with applied DC magnetic field for (x) $CoMn_{0.2}Fe_{1.8}O_4-(1-x)$ ($K_{0.5}Na_{0.5}$) NbO_3 ($x = 0.10, 0.20, 0.30, 0.40$ and 0.50) composites. α_{ME} is found to increase with magnetic field till 3 kOe and then starts decreasing. This reason for such behaviour is that the magnetostriction coefficient ' λ ' increases with applied field and reaches to its saturation value at certain value of applied magnetic field and hence the magnetization and associated strain produce an unvarying electric field in the

piezoelectric phase beyond the saturation limit. This in turn accounts for decrease in α_{ME} at higher values of magnetic field.

Table 3.7 The variation of AC impedance parameters for CMFO/KNN composites at different temperatures

Composition (x)		300 °C	350 °C	400 °C	450 °C	500 °C
x = 0.10	R _b (kΩ)	2017.54	349.99	80	6	3.76
	C _b (nF)	0.79	0.045	0.038	0.033	0.084
	R _{gb} (kΩ)	858.29	243.61	44.5	17.88
	C _{gb} (nF)	1.85	3.27	5.11	2.22
x = 0.20	R _b (kΩ)	27.77	10.81	5	2.31	1.89
	C _b (nF)	0.011	0.018	0.039	0.011	2.81
	R _{gb} (kΩ)	117.76	35.77	15	6.53	2.28
	C _{gb} (nF)	1.93	2.22	2.65	8.12	1.39
x = 0.30	R _b (kΩ)	25.90	9.77	3.45	1.55	0.72
	C _b (nF)	1.53	2.71	4.61	5.13	3.14
	R _{gb} (kΩ)
	C _{gb} (nF)
x = 0.40	R _b (kΩ)	14.36	5.40	2.38	0.82	0.53
	C _b (nF)	0.55	0.74	1.33	2.41	1.05
	R _{gb} (kΩ)
	C _{gb} (nF)
x = 0.50	R _b (kΩ)	10.22	3.99	1.74	0.79	0.33
	C _b (nF)	0.78	0.49	1.02	1.005	0.96
	R _{gb} (kΩ)
	C _{gb} (nF)

Figure 3.24 (f) shows variation of α_{ME} with CMFO content in the composites. α_{ME} is found to decrease with addition of ferrite. This is due to decrease in resistivity with increase in ferrite content as shown in inset of Figure 3.24 (f). Due to decrease in resistivity charges leak out from the piezoelectric phase through the surrounding conducting ferrite grains. The maximum value of $\alpha_{ME} = 5.941$ mV/cm-Oe is observed for 10% CMFO – 90% KNN composition.

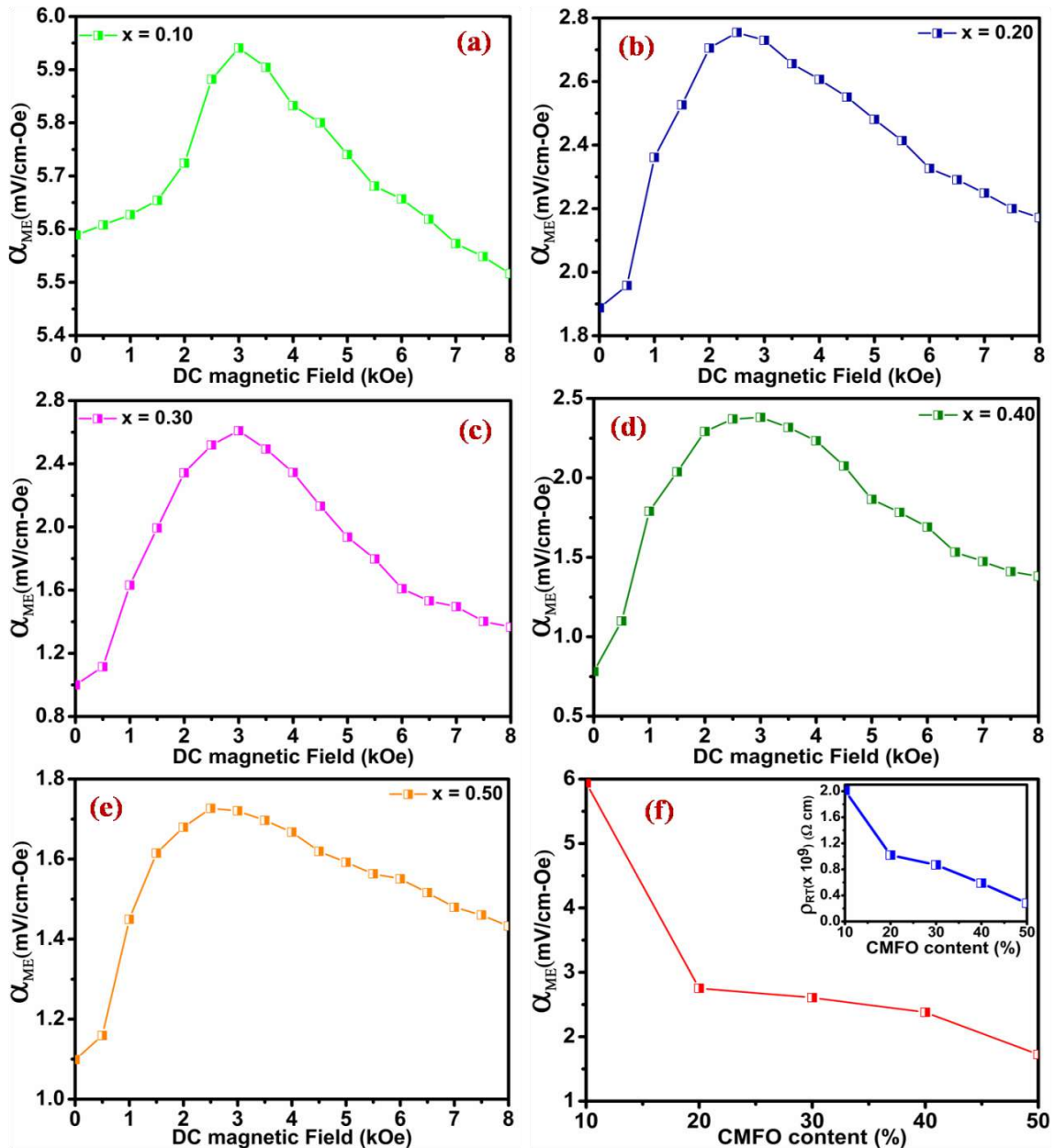


Figure 3.24 Variation of α_{ME} with DC magnetic field for (x) $CoMn_{0.2}Fe_{1.8}O_4-(1-x)$ $(K_{0.5}Na_{0.5})NbO_3$ (a) $x = 0.10$, (b) $x = 0.20$, (c) $x = 0.30$, (d) $x = 0.40$, (e) $x = 0.50$ composites and (f) variation of α_{ME} with CMFO content, inset shows variation of resistivity with CMFO content

The impedance loss spectrum has been used to evaluate the relaxation time (τ) of the charge carriers of the composites by using the relation, $\omega_{\max}\tau = 2\pi f_{\max}\tau = 1$. The relaxation time basically gives an estimation of the dynamics of the electrical relaxation process occurring in the material. Figure 3.25 shows the variation of $\ln \tau$ as a function of inverse of absolute temperature ($10^3/T$) for different compositions of CMFO/KNN composites. The nature of variation of τ with temperature follows the Arrhenius relation given by equation 3.7. The activation energies are calculated from $\ln \tau$ vs. $10^3/T$ plots and found to be 0.86, 0.61, 0.56, 0.49 and 0.47 eV for $x = 0.10, 0.20, 0.30, 0.40$ and 0.50 compositions respectively.

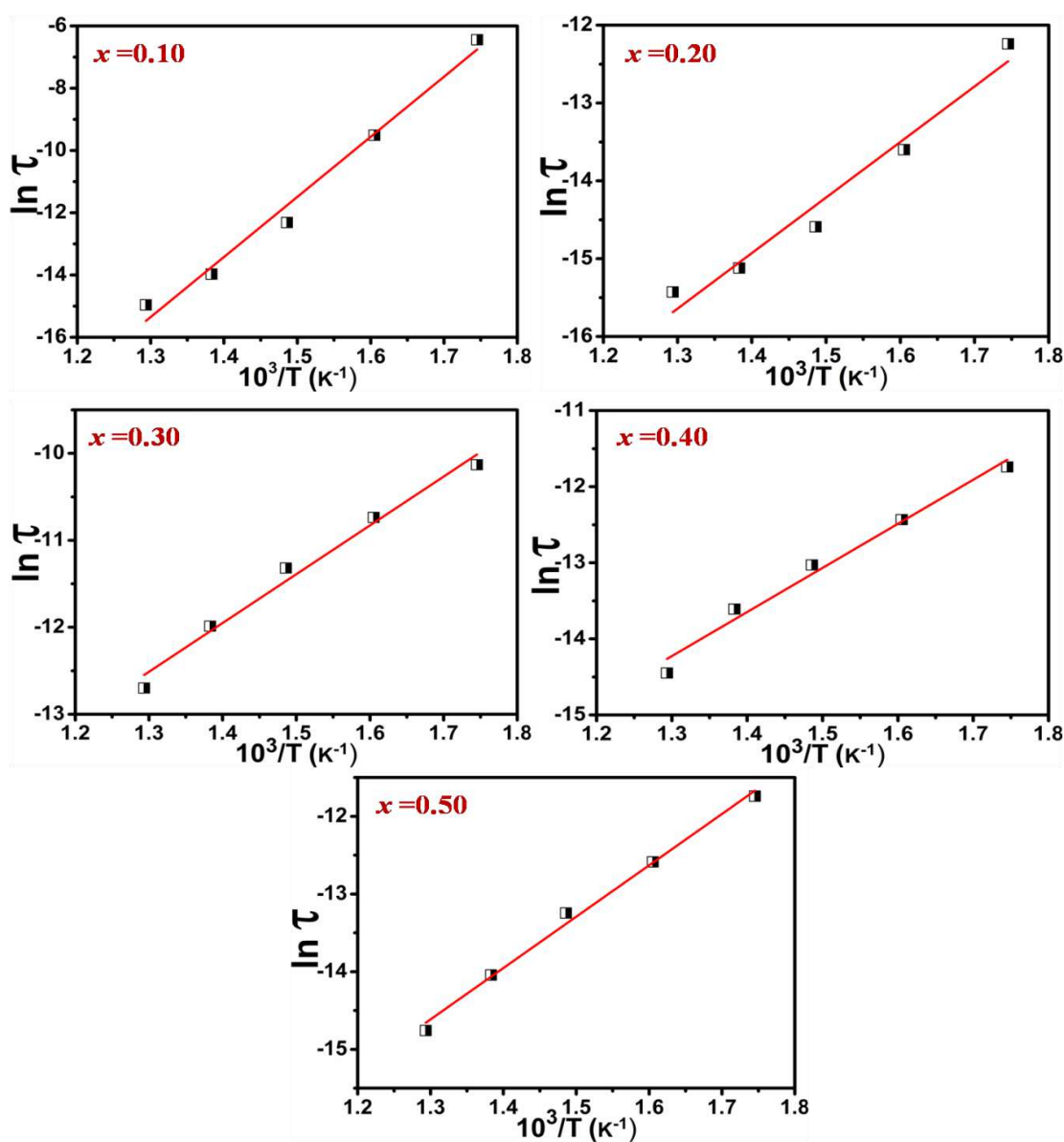


Figure 3.25 Variation of relaxation time ($\ln \tau$) with $10^3/T$ for (x) $CoMn_{0.2}Fe_{1.8}O_{4-(1-x)}$ ($K_{0.5}Na_{0.5}$) NbO_3 ($x = 0.10, 0.20, 0.30, 0.40$ and 0.50) composites

3.4 Summary

The ME composites (x) $Ni_{0.2}Co_{0.8}Fe_2O_4-(1-x)$ $(K_{0.5}Na_{0.5})NbO_3$ (NCFO/KNN) ($x = 0.10, 0.20, 0.30, 0.40$ and 0.50) comprising of NCFO as a ferrite phase and KNN as ferroelectric phase were synthesised by solid state reaction method. X-ray diffraction asserts the existence of both the constituent phases in the composites without any intermediate phase. FE-SEM micrographs indicate that both the constituent phases in the composites are firmly packed and average grain size varies in the range $574\text{ nm} - 914\text{ nm}$. Dielectric response of the composites was studied as a function of temperature and found to enhance with addition of NCFO. The obtained P-E and M-H hysteresis loops confirm the existence of ferroelectric and magnetic ordering simultaneously in the composites at room temperature. FC-ZFC magnetization curves provide a better insight of magnetic ordering in the composites. ZFC curves for pure NCFO and composites indicate that they undergo charge ordering, metal insulator transition commonly known as Verwey transition around $140-145\text{ K}$. The complex impedance analysis reveals grain contribution in the resistance up to $x = 0.20$ and both grain and grain boundary contribution in the resistance is observed for $x > 0.20$. Bulk resistance decreases with increase in temperature suggesting negative temperature coefficient of resistance (NTCR) for the composites analogous to a semiconductor. ME coupling is observed in the composites which was confirmed by measuring α_{ME} corresponding to different compositions. The highest α_{ME} is found to be 5.389 mV/cm-Oe for the composite with 20% NCFO and 80% KNN. The results imply that the obtained composites may have potential applications as multiferroic materials for fabrication of multifunctional devices.

ME composites having general formula (x) $CoMn_{0.2}Fe_{1.8}O_4-(1-x)$ $(K_{0.5}Na_{0.5})NbO_3$ ($x = 0.10, 0.20, 0.30, 0.40$ and 0.50) were successfully synthesized using solid state reaction method. XRD analysis confirms the existence of both the constituent phases in the composites. Dielectric properties including dielectric constant (ϵ') and dielectric loss ($\tan \delta$) were studied as a function of temperature and found to enhance with addition of CMFO. The obtained P-E hysteresis loops confirm the existence of ferroelectric ordering in the composites at room temperature. Remnant polarization (P_r) and coercive field (E_C) were found to decrease with addition of CMFO. Magnetic hysteresis measurements at 300 K and 5 K suggest the ferromagnetic nature of the composites. Complex impedance analysis shows that electrical conductivity increases with temperature suggesting (NTCR) behaviour of the composites. ME voltage coefficient (α_{ME}) was measured indicating the

presence of ME coupling in the composites. The maximum value of α_{ME} (5.941 mV/cm-Oe) was observed for 10% CMFO – 90% KNN composition. This value of α_{ME} obtained for CMFO/KNN composites is higher than as compared to other lead-free ME composites. The results imply that the obtained composites may have potential applications as multiferroic materials for fabrication of multifunctional devices.

Chapter 4

Synthesis and Characterization of $\text{Bi}_{0.5}\text{Na}_{0.5}\text{TiO}_3$ based Magnetoelectric Composites

This chapter has been published in the form of following papers

- (1) Dielectric, magnetic and magnetoelectric properties of ferrite-ferroelectric based particulate composites, Yogesh Kumar, K.L. Yadav, Jyoti Shah and R.K. Kotnala, **Materials Research Express 5 (2018) 085701-1 – 11.**
- (2) Investigation of magnetoelectric effect in $\text{Bi}_{0.5}\text{Na}_{0.5}\text{TiO}_3\text{-CoMn}_{0.2}\text{Fe}_{1.8}\text{O}_4$ composites, Yogesh Kumar, K.L. Yadav, Jyoti Shah and R.K. Kotnala, **IEEE Transactions on Dielectrics and Electrical Insulation 26 (2) (2019) 561-567**
- (3) Structural, dielectric, magnetic and magnetoelectric properties of $(x) \text{Bi}_{0.5}\text{Na}_{0.5}\text{TiO}_3\text{-}(1-x) \text{Ni}_{0.2}\text{Co}_{0.8}\text{Fe}_2\text{O}_4$ composites, Yogesh Kumar, K.L. Yadav, Manjusha, Jyoti Shah and R.K. Kotnala, **Materials Research Express 3 (2016) 065701-1 – 8.**

4.1 Introduction

The composites based on ferroelectrics and ferrites have seized profuse attention over the last decade or so due to their multi-functionalities with tunable electric and magnetic properties. One of the major fields of interest in these composites is exploration of magnetoelectricity. The magnetoelectric (ME) composites exhibit higher magnetoelectricity than their single phase multiferroic counterparts, compelling the research fraternity to amply explore the expansive area of ME composites. ME composites provide us with the cushion of altering the magnetization by application of electric field and electric polarization through magnetic field [177]. These ME composites find their fair share of applications in magnetic probes, sensors, actuators, phase shifters, transducers, memory applications, electric field controlled magnetic data storage, antenna miniaturization etc.[4, 7, 133, 178, 179-181]. ME effect arises because of induced strain in the piezomagnetic phase due to application of magnetic field. This strain is mechanically coupled to induce stress in the piezoelectric phase that results into the production of induced voltage. For getting a better ME effect in the composite, the constituent phases of the composites should be in equilibrium with each other, the magnetic phase should have high magnetostriction coefficient and high resistivity for avoiding charge leakage. Similarly, ferroelectric phase should have high piezoelectric coefficient [29].

Bi_{0.5}Na_{0.5}TiO₃ (BNT) was discovered by Smolenskii et al. [182] has been considered as an excellent candidate for lead-free piezoelectric ceramics because of large remnant polarization ($P_r = 38 \mu\text{C}/\text{cm}^2$) and high Curie temperature ($T_C = 320 \text{ }^\circ\text{C}$) and excellent dielectric and piezoelectric properties [183-185]. In the previous years, distinct ME composites based on Bi_{0.5}Na_{0.5}TiO₃ (BNT) have been synthesized and studied including Na_{0.5}Bi_{0.5}TiO₃-CoFe₂O₄ [92], NiFe₂O₄-Na_{0.5}Bi_{0.5}TiO₃ [95], Na_{0.5}Bi_{0.5}TiO₃-Ni_{0.93}Co_{0.02}Mn_{0.05}Fe_{1.95}O₄ [186], Na_{0.5}Bi_{0.5}TiO₃-MgFe₂O₄ [101], (1-x) (Bi_{0.5}Na_{0.5}TiO₃)/xCoFe₂O₄ [187], Na_{0.5}Bi_{0.5}TiO₃-Tb_{0.3}Dy_{0.7}Fe_{1.95} [188]. In order to obtain significant ME effect, an appropriate combination of ferrite and ferroelectric phase is a necessary requirement. To achieve this we have synthesized and studied the BNT based ME composites including (x) Co_{0.8}Zn_{0.2}Fe₂O₄-(1-x) Bi_{0.5}Na_{0.5}TiO₃ (CZF/BNT), (1-x) Bi_{0.5}Na_{0.5}TiO₃-(x) CoMn_{0.2}Fe_{1.8}O₄ (BNT/CMFO) and (x) Bi_{0.5}Na_{0.5}TiO₃-(1-x) Ni_{0.2}Co_{0.8}Fe₂O₄ (BNT/NCFO).

Zinc doped cobalt ferrite exhibits high resistivity, magnetostriction and piezomagnetic coefficient [189, 190]. On the other hand, BNT is an excellent candidate for lead-free piezoelectric ceramics due to its outstanding ferroelectric and piezoelectric properties. Keeping in mind these aforesaid facts, in the first section of this chapter we present the synthesis and organized study of the structural, dielectric, magnetic and magnetolectric properties of (x) Co_{0.8}Zn_{0.2}Fe₂O₄-(1-x) Bi_{0.5}Na_{0.5}TiO₃ ME composites comprising of CZF and BNT as their ferrite and ferroelectric phase respectively.

Pure CoFe₂O₄ exhibits higher magnetostriction as compared to other ferrites [141]. It also exhibits high T_C and magnetocrystalline anisotropy. In order to reduce magnetocrystalline anisotropy and T_C , manganese substitution can be very effective [142-143]. Keeping in mind the above facts, in the second section of this chapter we have focused on another lead-free ME composite comprising of BNT and CMFO as their ferroelectric and ferrite phase. In this section we present a systematic study on synthesis and the structural, dielectric, magnetic and magnetolectric properties of (1-x) Bi_{0.5}Na_{0.5}TiO₃-(x) CoMn_{0.2}Fe_{1.8}O₄ ME composites.

Co²⁺ doped nickel ferrite is a soft ferromagnetic material having high electrical resistivity, saturation magnetization, magnetostriction coefficient and high Curie temperature. Cobalt doped nickel ferrite (NCFO) has mixed spinel structure (AB₂O₄) in which Fe³⁺ ions occupy both tetrahedral A sites and octahedral B sites whereas Ni²⁺ and Co²⁺ ions prefer to occupy octahedral B sites. Ni_{0.2}Co_{0.8}Fe₂O₄ has high electrical

resistivity [136] and magnetostriction coefficient [137]. Keeping in mind the afore said facts, the third section of this chapter deals with synthesis and systematic studies of structural, dielectric and magnetolectric properties of (x) Bi_{0.5}Na_{0.5}TiO₃-(1-x) Ni_{0.2}Co_{0.8}Fe₂O₄ ME composites having BNT and NCFO as their constituent ferroelectric and ferrite phase respectively.

4.2 Experimental Details

4.2.1 Synthesis of (x) Co_{0.8}Zn_{0.2}Fe₂O₄-(1-x) Bi_{0.5}Na_{0.5}TiO₃ ME composite system with x = 10, 20, 30, 40, 50 wt. %

The lead-free ME composite (x) Co_{0.8}Zn_{0.2}Fe₂O₄-(1-x) Bi_{0.5}Na_{0.5}TiO₃ (CZF/BNT) comprising of two distinct phases were synthesized using conventional solid state reaction (SSR) method. Ferrite phase CZF was synthesized by employing SSR method using high purity AR grade powders of Co₃O₄ (98.5 %, Himedia, India), ZnO (98.5 %, Qualigens, India) and Fe₂O₃ (98 %, Himedia, India). These powders were weighed in appropriate stoichiometric ratio, then mixed and grounded thoroughly in acetone medium for 3 h. The well mixed and grounded powder was dried and pre-sintered at 1000 °C for 3 h in air atmosphere. This pre-sintered powder was again grounded to get homogeneous CZF powder. The ferroelectric phase BNT was also synthesized using SSR method by taking high purity AR grade powders of Bi₂O₃ (99.5 %, Himedia, India), Na₂CO₃ (99.5 %, Qualigens, India) and TiO₂ (99 %, Himedia, India). The weighed powders in appropriate stoichiometry were mixed and grounded thoroughly in acetone medium for 4 h. An extra amount of 4.5 wt.% of Bi₂O₃ and Na₂CO₃ were added into the starting powder mixture to compensate for Bismuth and Sodium losses, because they evaporate at high temperatures. The well mixed powder was calcined at 1050 °C for 2 h in air atmosphere. The calcined powder was again grounded to obtain homogeneous BNT powder. The lead-free (x) CZF-(1-x) BNT (x = 10, 20, 30, 40 and 50 wt.%) ME composites were synthesized by mixing obtained powders of CZF and BNT in appropriate molar proportions. The obtained powders of the composites were pressed in die to obtain pellets (of 10 mm diameter and 1-2 mm in thickness) using PVA as binder with hydraulic press. The obtained pellets of the composites were finally sintered at 1150 °C for 4 h in air atmosphere.

4.2.2 Synthesis of (1-x) Bi_{0.5}Na_{0.5}TiO₃-(x) CoMn_{0.2}Fe_{1.8}O₄ ME composite system with x = 0.10, 0.20, 0.30, 0.40 and 0.50

The lead-free ME composite (1-x) Bi_{0.5}Na_{0.5}TiO₃-(x) CoMn_{0.2}Fe_{1.8}O₄ (BNT/CMFO)

comprising of BNT and CMFO as ferroelectric and ferrite phases respectively were synthesized using conventional SSR method. In the first stage, the ferrite phase CMFO was synthesized by employing SSR method using high purity AR grade powders of Co_3O_4 (98.5 %, Himedia, India), Mn_2O_3 (98.5 %, Qualigens, India) and Fe_2O_3 (98 %, Himedia, India). These powders were weighed in appropriate stoichiometric ratio, then mixed and grounded thoroughly in acetone medium for 3 h. The well mixed and grounded powder was dried and calcined at 970 °C for 3 h in air atmosphere. This calcined powder was again grounded to obtain homogeneous CMFO phase. In the second stage, BNT was synthesized using same methodology as discussed in section 4.2.1. In the third and final stage we mixed the homogeneously obtained powders of BNT and CMFO in appropriate molar proportions to obtain desired $(1-x)$ BNT- (x) CMFO ($x = 0.10, 0.20, 0.30, 0.40$ and 0.50) ME composites. The homogenous powders of the composites were pressed in die to obtain pellets (of 10 mm diameter and 1-2 mm in thickness) using PVA as binder with hydraulic press. The obtained pellets of the composites were finally sintered at 1100 °C for 4 h in air atmosphere.

4.2.3 Synthesis of (x) $\text{Bi}_{0.5}\text{Na}_{0.5}\text{TiO}_3$ - $(1-x)$ $\text{Ni}_{0.2}\text{Co}_{0.8}\text{Fe}_2\text{O}_4$ ME composite system with $x = 0.30, 0.40, 0.50, 0.60, 0.70$ and 0.80

The lead-free ME composite (x) $\text{Bi}_{0.5}\text{Na}_{0.5}\text{TiO}_3$ - $(1-x)$ $\text{Ni}_{0.2}\text{Co}_{0.8}\text{Fe}_2\text{O}_4$ (BNT/NCFO) were also synthesized using conventional SSR method comprising of BNT as ferroelectric and NCFO as ferrite phase. The ferrite phase NCFO was synthesized with SSR method using high purity AR grade powders of NiO (98.5 %, Himedia, India), Co_3O_4 (98.5 %, Qualigens, India) and Fe_2O_3 (98 %, Himedia, India). These powders were weighed in appropriate stoichiometry, then mixed and grounded thoroughly in acetone medium for 5 h. The obtained powder was then calcined at 1000 °C for 2 h in air atmosphere. This calcined powder was again grounded to obtain homogeneous NCFO phase. BNT was synthesized using same methodology as discussed in section 4.2.1. The obtained BNT and NCFO powders were mixed in six different molar ratios viz. 30/70, 40/60, 50/50, 60/40, 70/30 and 80/20 respectively, to obtain (x) BNT- $(1-x)$ NCFO ($x = 0.30 - 0.80$) ME composites. The homogenous powders of the obtained composites were pressed in die to obtain pellets (of 10 mm diameter and 1-2 mm in thickness) using PVA as binder with hydraulic press. The obtained pellets of the composites were finally sintered at 1150 °C for 4 h in air atmosphere.

4.2.4 Characterizations

The structural analysis of the synthesized samples was carried out using X-ray diffractometer (Bruker D8 Advance) over wide Bragg angle range ($20^\circ \leq 2\theta \leq 60^\circ$) with a scanning speed of $1^\circ/\text{min}$ at room temperature using Cu (K_α) ($\lambda=1.5432 \text{ \AA}$) radiation. The surface morphology and microstructures of composites were obtained using field emission scanning electron microscopy (FE-SEM; Carl Zeiss) operating at an accelerating voltage of 15 kV. It was also used for analyzing the grain size distribution of the samples. Electrical measurements were obtained after polishing both the flat sides of pellets with high purity silver paste and drying them at 150°C for 1 h in the muffle furnace. The dielectric measurements including dielectric constant (ϵ') and dielectric loss ($\tan \delta$) were studied, using HIOKI-3532-50 Hi Tester LCR meter in the temperature range of $30\text{--}500^\circ \text{C}$ at a ramp rate of $2^\circ \text{C}/\text{min}$ and at a measuring electric field of 1 Volt. Ferroelectric properties of the composites were measured at room temperature using modified Sawyer-Tower circuit (automated Marine India P-E loop tracer). Complex impedance analysis was done at room temperature by using HIOKI LCR meter in a wide frequency range of 100 Hz – 1 MHz. The magnetic properties of the composites including M-H hysteresis loops were measured using vibrating sample magnetometer (VSM, Quantum Design, PAR 155) in the magnetic field range of $-10 \text{ kOe} \leq H \leq +10 \text{ kOe}$. The chemical state of all the ferrites was investigated using X-ray photoelectron spectroscopy (XPS) using PHI 5000 VersaProbe III (Physical Electronics). ME voltage coefficient (α_{ME}) was determined by dynamic field method using an in house built measurement setup [144].

4.3 Results and Discussions

4.3.1 (x) Co_{0.8}Zn_{0.2}Fe₂O₄-(1-x) Bi_{0.5}Na_{0.5}TiO₃ ME composite system with x = 10, 20, 30, 40, 50 wt. %

The XRD patterns of (x) CZF-(1-x) BNT (x = 10, 20, 30, 40 and 50 wt.%) composites are shown in Figure 4.1 (a). The patterns unveil that all peaks were recognized akin to both the constituent phases BNT and CZF of the composites, indicating the efficacious synthesis of the composite samples. It is evident from XRD patterns that intensity of peaks akin to ferrite phase increases gradually with addition of ferrite. From Figure 4.1 (b) it is evident that most intense peaks of BNT and CZF phases are found to shift slightly towards lower angle side. This may be accredited to substitution model, where Bi³⁺ (ionic radii,

1.17 Å) or Na^+ (1.18 Å) ions substitute Co^{2+} (0.65 Å) or Zn^{2+} (0.60 Å) ions at A site and Ti^{4+} (0.68 Å) ions substitute Fe^{3+} (0.64 Å) at B site. Hence this A/B co-substitution will slightly expand the cell size, thereby creating slight left shift in the position of peaks [191].

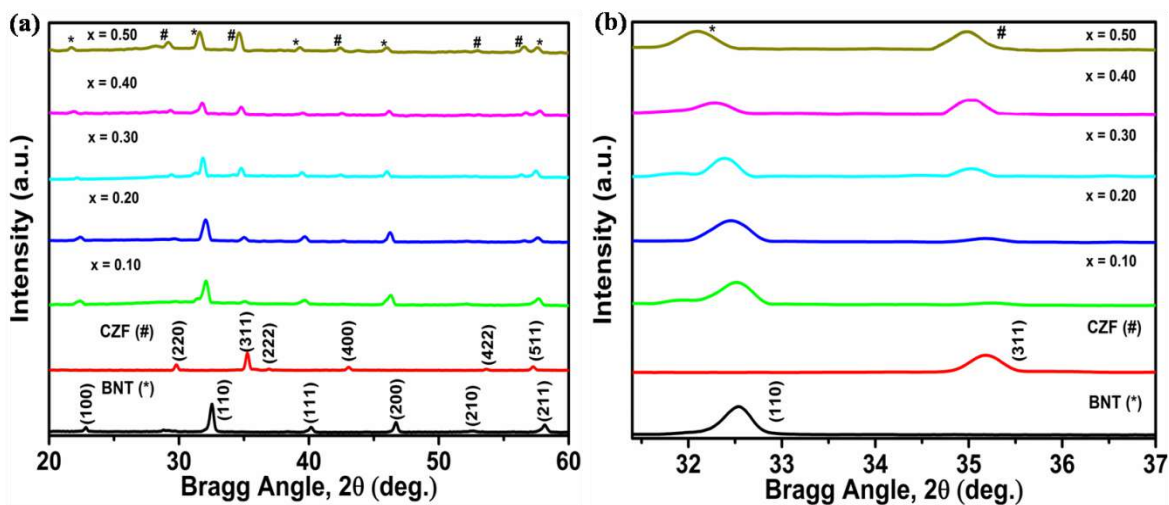


Figure 4.1 XRD patterns of $(x) \text{Co}_{0.8}\text{Zn}_{0.2}\text{Fe}_2\text{O}_4-(1-x) \text{Bi}_{0.5}\text{Na}_{0.5}\text{TiO}_3$ (a) $x = 10, 20, 30, 40$ and 50 wt.% composites along with pure BNT and CZF phases and (b) XRD patterns of the composites in the angle range $31.4^\circ-37^\circ$

The FE-SEM micrographs of $(x) \text{CZF}-(1-x) \text{BNT}$ ($x = 10, 20, 30, 40$ and 50 wt.%) composites along with pure BNT and CZF phases are shown in Figure 4.2 (a)-(g).

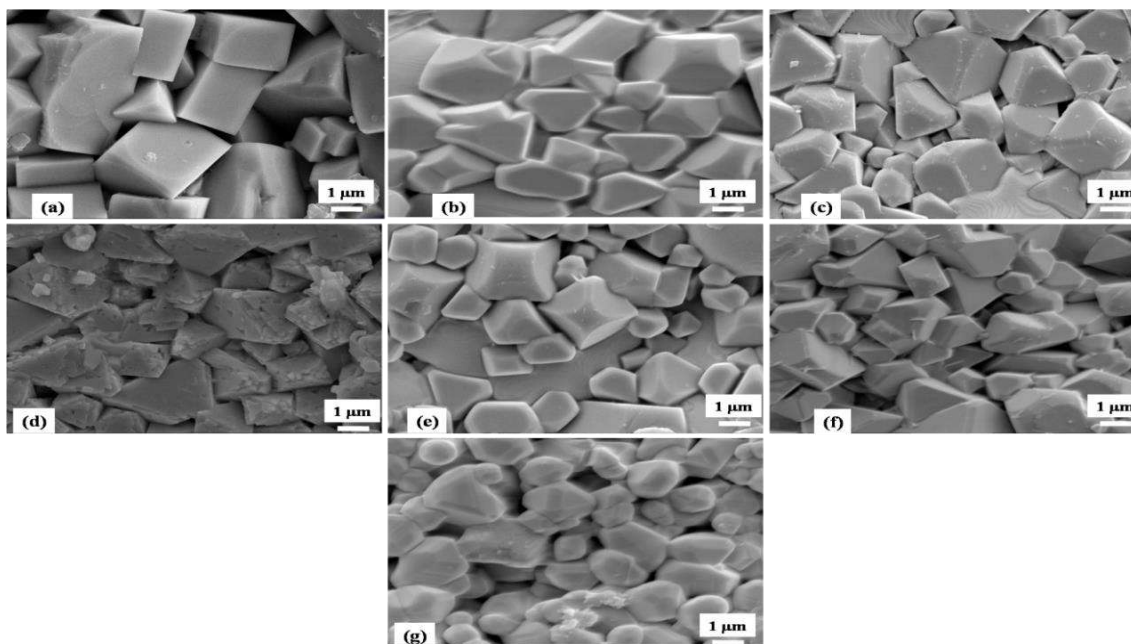


Figure 4.2 FE-SEM micrographs of $(x) \text{Co}_{0.8}\text{Zn}_{0.2}\text{Fe}_2\text{O}_4-(1-x) \text{Bi}_{0.5}\text{Na}_{0.5}\text{TiO}_3$ (a) BNT, (b) $x = 10$, (c) $x = 20$, (d) $x = 30$, (e) $x = 40$, (f) $x = 50$ wt.% composites and (g) CZF respectively

These micrographs reveal that the composites comprise of randomly oriented, non-uniform grains having some intergranular porosity in which small sized CZF grains are dispersed in large grained matrix of BNT. The larger grains correspond to BNT phase and smaller grains correspond to CZF phase. Thus FE-SEM micrographs assert the development of diphasic composites with fairly condensed CZF grains in BNT matrix. The average grain size of the composites was calculated using Image J software and the obtained data has been plotted and fitted using log-normal distribution. Figure 4.3 (a)-(g) shows the plot of grain size distribution and obtained grain sizes are shown in their insets. The average grain size is found to decrease with addition of ferrite in the composites.

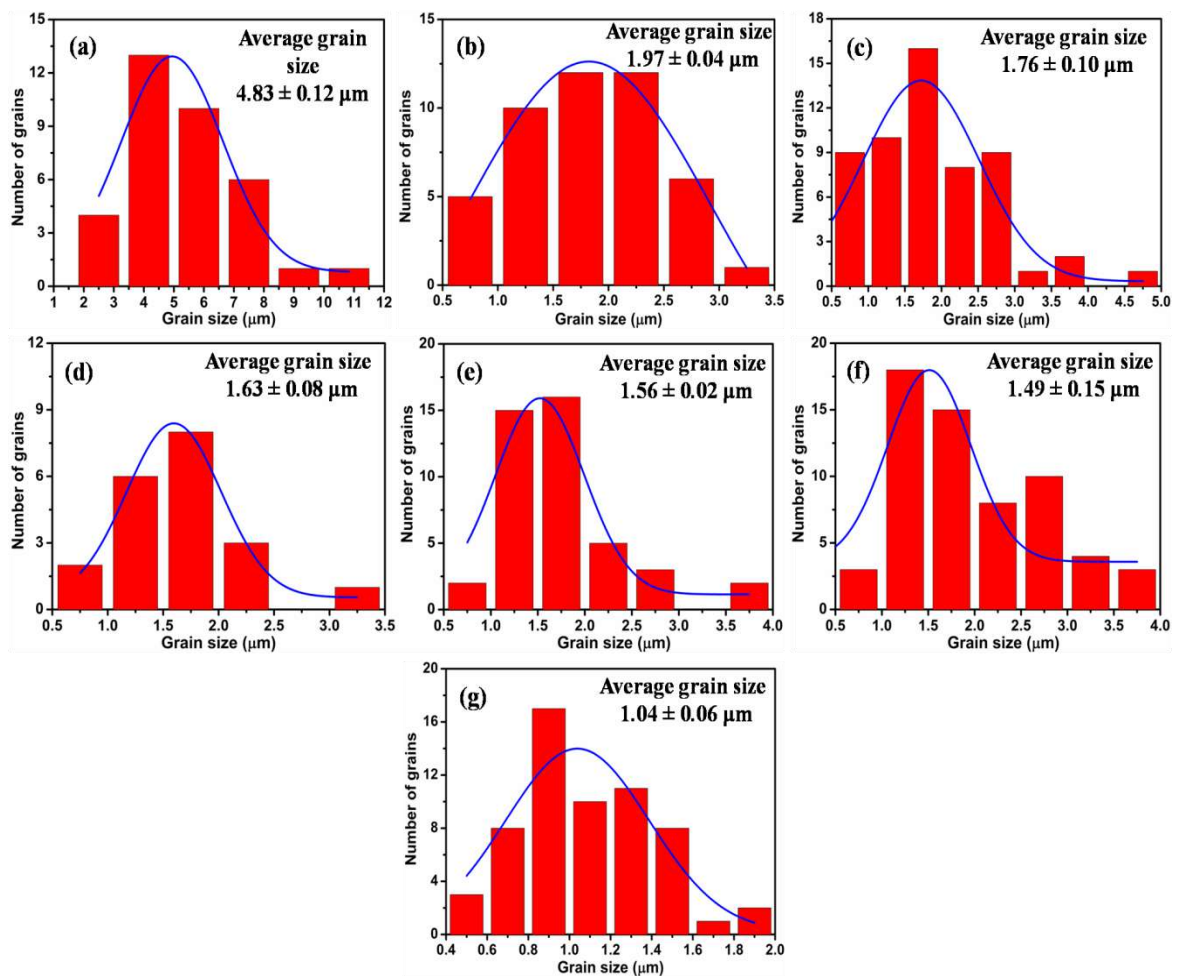


Figure 4.3 Log normal distribution of grain size of (x) $\text{Co}_{0.8}\text{Zn}_{0.2}\text{Fe}_2\text{O}_4-(1-x)$ $\text{Bi}_{0.5}\text{Na}_{0.5}\text{TiO}_3$ (a) BNT, (b) $x = 10$, (c) 20, (d) 30, (e) 40, (f) 50 wt.% and (g) CZF respectively. Inset shows the average grain size

The purity and efficacious synthesis of composites which has been confirmed by Energy dispersive X-ray analysis (EDAX). EDAX analysis providing the quantitative elemental analysis for composites with $x = 30$ and 40 wt.% is shown in Figure 4.4 (a)-(b). The

The corresponding energy spectrum reveals the presence of expected elements including Bi, Na, Ti, Co, Zn, Fe and O.

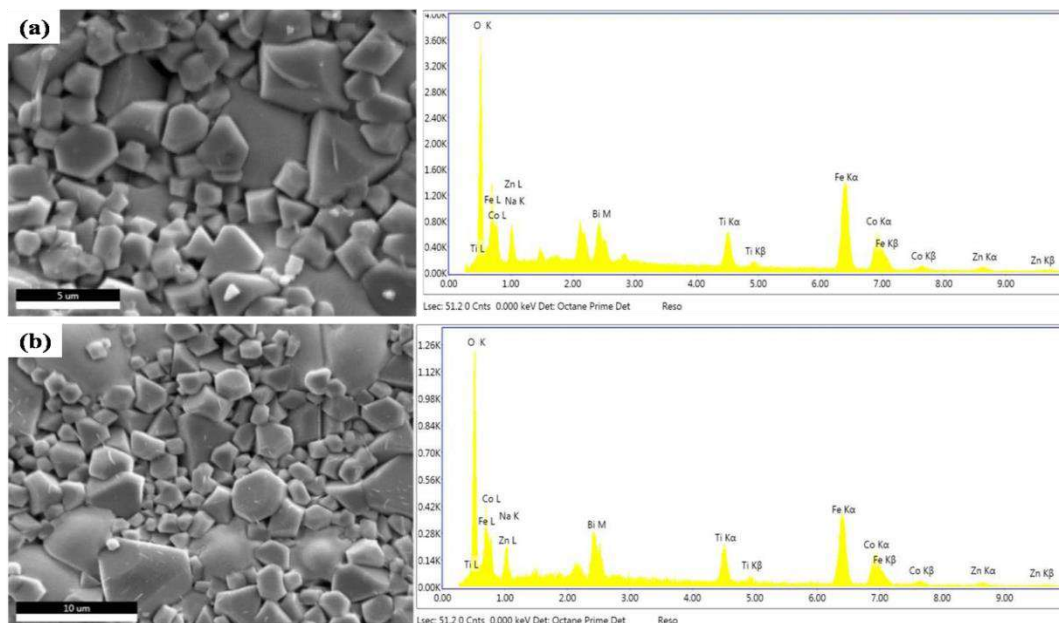


Figure 4.4 EDAX spectrum of (x) $\text{Co}_{0.8}\text{Zn}_{0.2}\text{Fe}_2\text{O}_4$ -(1-x) $\text{Bi}_{0.5}\text{Na}_{0.5}\text{TiO}_3$ (a) $x = 30$ wt.% and (b) $x = 40$ wt.% composites

The variation of dielectric constant (ϵ') and loss ($\tan \delta$) for (x) CZF-(1-x) BNT ($x = 10, 20, 30, 40$ and 50 wt %) composites as a function of frequency at room temperature are shown in Figure 4.5 (a)-(b).

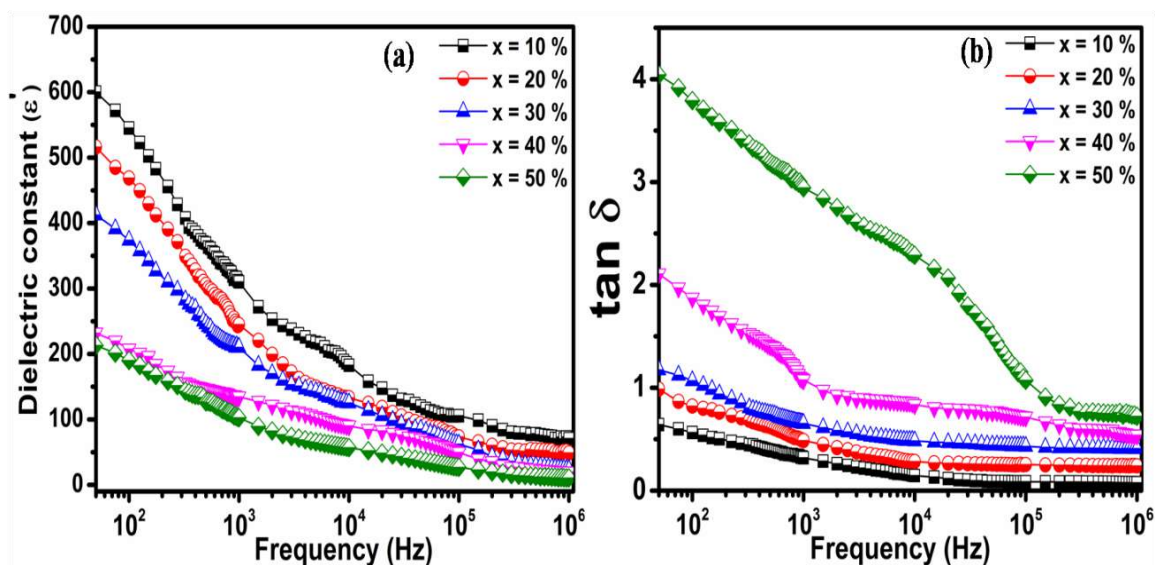


Figure 4.5 Frequency dependence of (a) dielectric constant (ϵ') and (b) dielectric loss ($\tan \delta$) for (x) $\text{Co}_{0.8}\text{Zn}_{0.2}\text{Fe}_2\text{O}_4$ -(1-x) $\text{Bi}_{0.5}\text{Na}_{0.5}\text{TiO}_3$ ($x = 10, 20, 30, 40$ and 50 wt %) composites at room temperature

Both dielectric parameters ϵ' and $\tan \delta$ are found to decrease rapidly in low frequency regime while remain nearly invariant in high frequency regime, signalling dielectric dispersion. This type of response may be attributed to Maxwell-Wagner type interfacial polarization [192, 193] which occurs when two phases of different conductivities are connected to each other, giving rise to uncompensated charges at the interface separating two phases. These uncompensated charges are responsible for interfacial or space charge polarization. Grain boundaries are more resistive in comparison to grains [85, 194], consequently favouring electrons to gather at grain boundaries on application of AC electric field. This gives rise to space charge polarization which accounts for higher values of dielectric constant in low frequency regime. With increase in frequency of applied AC field, it becomes difficult for electrons to keep pace with applied electric field, thereby decreasing the dielectric constant in high frequency regime.

The temperature dependence of dielectric constant (ϵ') and dielectric loss ($\tan \delta$) for (x) CZF-(1-x) BNT ($x = 10, 20, 30, 40$ and 50 wt.%) composites at applied field frequency of 1 kHz is illustrated in Figure 4.6 (a-b).

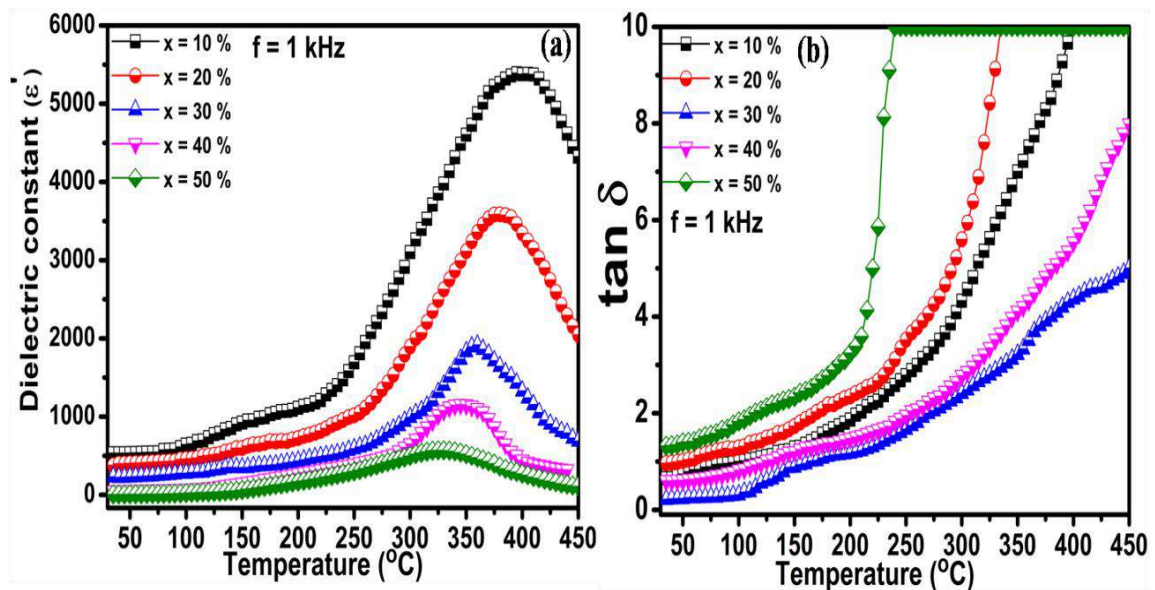


Figure 4.6 Temperature dependence of (a) dielectric constant (ϵ') and (b) dielectric loss ($\tan \delta$) for (x) $\text{Co}_{0.8}\text{Zn}_{0.2}\text{Fe}_2\text{O}_4$ -(1-x) $\text{Bi}_{0.5}\text{Na}_{0.5}\text{TiO}_3$ ($x = 10, 20, 30, 40$ and 50 wt %) composites at a frequency of 1 kHz

It has been observed that for all compositions, dielectric constant increases with temperature up to a particular temperature (T_C) and then decreases beyond T_C . This is because with an increase in temperature the movement of space charge carriers also

increase, giving rise to enhancement in space charge polarization, which further contributes to increase in dielectric constant up to T_C . Beyond T_C , the vibrational motion of carriers/ions becomes more random, consequently making it strenuous for them in aligning with applied field direction thereby resulting for a decrease in dielectric constant. The broadening of phase transition peak for composites may be due to disorder in arrangement of cations at different crystallographic sites, giving rise to microscopic heterogeneity in the composites and thus leading to distribution of distinct localized Curie points [195]. These can be associated to nanoscale ordered microregions prevailing in samples which act as locations of spontaneous polarization [196-198]. It is also evident from Figure 4.6 (a) that, with addition of ferrite phase the observed ϵ' is found to decrease. We can correlate the decrease in ϵ' with grain size of the composites. Grain size of the composites is found to decrease with addition of ferrite [Figure 4.3 (a-g)]. A ferroelectric material has multiple ferroelectric domains separated by interfaces known as domain walls. The ϵ' depends on the mobility and number of domain walls [199]. According to space charge theory from Okazaki and Nagata [200], there are specific amounts of space charge sites inside grain boundaries and domain walls. These space charge sites give rise to electric field which significantly affects the movement of domain walls. With a decrease in grain size, the surface area of space charge layer increase thereby increasing the space charge field. Hence the movement of domain walls becomes relatively strenuous and irregular consequently decreasing the ϵ' . Also T_C shows a shift from 380 °C for $x = 10$ wt.% to 340 °C for 50 wt.%. The shift in T_C of the composites towards lower temperature side may be attributed to the diffusion of non-magnetic ions in the spinel lattice. These non-magnetic ions weaken the interaction between A and B sites in the spinel lattice. This weaker A-B interaction is majorly affected by thermal motion, accounting for a shift in T_C of the composites. The energy loss is usually expressed by dielectric loss factor ($\tan \delta$). The variation of $\tan \delta$ for (x) CZF-(1-x) BNT ($x = 10, 20, 30, 40$ and 50 wt.%) composites with temperature at applied field frequency of 1 kHz is illustrated in Figure 4.6 (b). It is found to increase with increase in temperature and ferrite content. This type of loss behaviour arises due to enhancement in space charge polarization, which attains thermal energy with increase in temperature and leads to conduction losses [94]. We observe a rapid increase in $\tan \delta$ at higher temperatures, indicating the increased space charge conduction which is further related to movement of oxygen vacancies towards dielectric-electrode interface [201]

For understanding the mechanism of conduction, the AC conductivity of the composite samples was calculated using dielectric parameters making use of the equation

$$\sigma_{ac} = 2\pi f \epsilon' \epsilon_0 \tan \delta \quad (4.1)$$

Here σ_{ac} represents ac conductivity, f represents the frequency of applied AC field, ϵ_0 is the permittivity of free space and $\tan \delta$ is the dielectric loss. The measurement was made in the frequency range of 50 Hz–1 MHz at room temperature. Figure 4.7 illustrates the frequency dependence of ac conductivity.

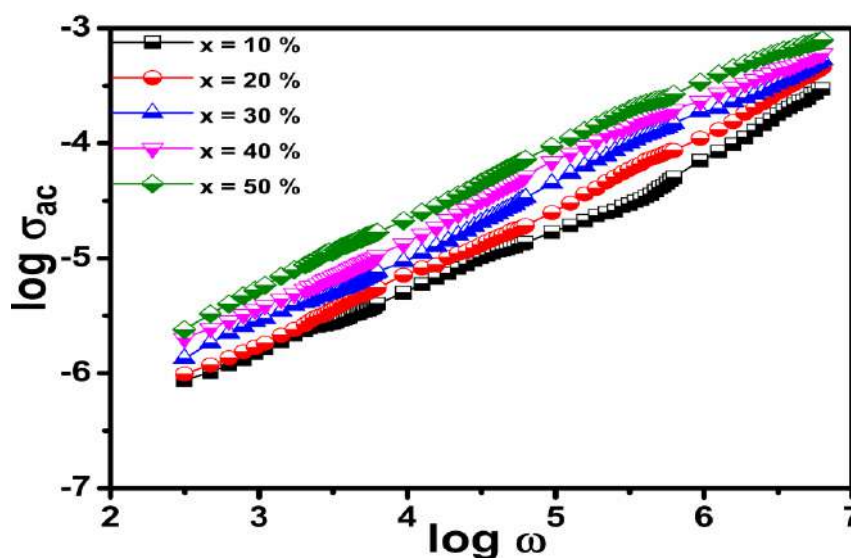


Figure 4.7 Frequency dependence of AC conductivity for (x) $\text{Co}_{0.8}\text{Zn}_{0.2}\text{Fe}_2\text{O}_4-(1-x)$ $\text{Bi}_{0.5}\text{Na}_{0.5}\text{TiO}_3$ ($x = 10, 20, 30, 40$ and 50 wt %) composites at room temperature

It is evident that conductivity increases with increase in frequency for all composite samples. Similar results were reported by other workers [202-204]. This type of behaviour may be attributed to polaron hopping between the localized states, which favours in ionic lattices having similar cation in two distinct oxidation states. The linearity of conductivity plots for composites signals that the conduction is attributed to small polarons [205]. The frequency dependent conduction is accredited to small polarons [206].

Ferroelectric ordering in the composites is confirmed by measuring P-E hysteresis loops. All the measurements were made at room temperature and at a frequency of 50 Hz. The P-E hysteresis loops of (x) CZF-(1-x) BNT ($x = 10, 20, 30, 40$ and 50 wt.%) composites are shown in Figure 4.8 (a)-(f). Ferroelectric properties are generally affected

by composition, homogeneity, defects, applied field and domain orientation. Uniform orientation of domain usually enhances the ferroelectric properties [207].

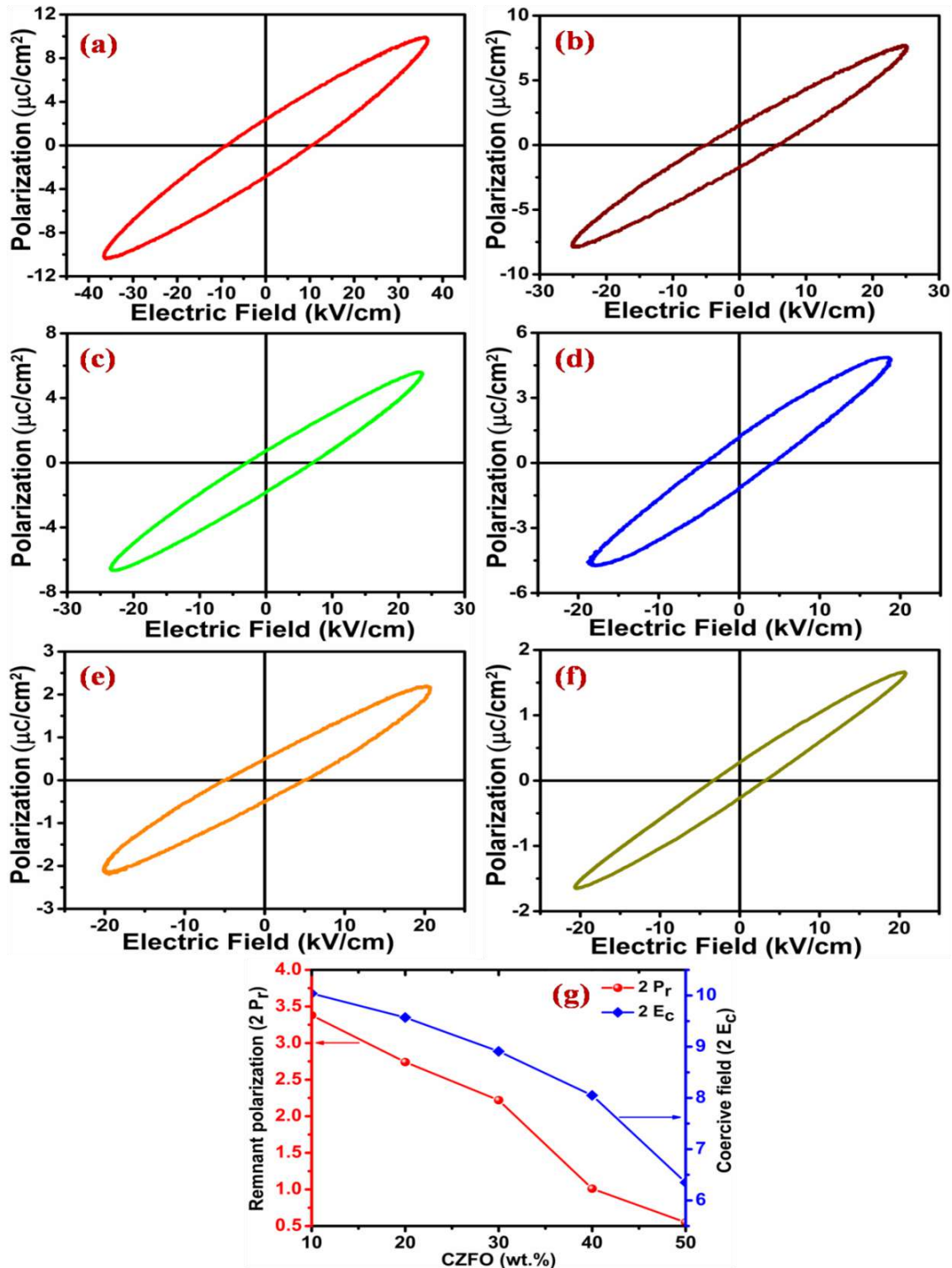


Figure 4.8 P-E hysteresis loops for $(x) \text{Co}_{0.8}\text{Zn}_{0.2}\text{Fe}_2\text{O}_4$ - $(1-x) \text{Bi}_{0.5}\text{Na}_{0.5}\text{TiO}_3$ (a) BNT, (b) $x = 10$, (c) $x = 20$, (d) $x = 30$, (e) $x = 40$, (f) $x = 50$ wt.% composites measured at room temperature and (g) variation of remnant polarization ($2P_r$) and coercive field ($2E_c$) with CZF content

It is evident from Figure 4.8 (a)-(f) that the loops are lossy and unsaturated and show low quality hysteresis. This type of hysteresis behaviour may be attributed to existence of conduction mechanisms which are innate of ferrites, which coincide with the ferroelectric activity of the ferroelectric phase [208]. The increase in conductivity of multiferroic composites is generally ascribed to creation of oxygen vacancies due to presence of Fe³⁺ and Fe²⁺ attributed to polaron mechanism [209]. This process enhances the current instead of inducing electric polarization with the application of external electric field, consequently giving rise to lossy and unsaturated P-E hysteresis loops. Also obtained P-E hysteresis loops are found to be slightly asymmetrical about the origin. This may be due to inner electric field generated by small distance, off center and innate motion of bound electrons in the composites [195]. Figure 4.8 (g) shows the variation of remnant polarization (2P_r) and coercive field (2E_c) with ferrite content. They both are found to decrease monotonously with addition of ferrite. Decrease in remnant polarization with ferrite addition may be associated to electromechanical coupling, less inner polarizability and strain [210]. The variation of coercive field with addition of ferrite may be attributed to switching of ferroelectric domains with change in charge carrier concentration, resulting in domain pinning [154].

The electrical behaviours of the composites were studied over wide range of frequency using complex impedance spectroscopy (CIS) [176]. It is generally based on treating the sample with sinusoidal perturbation and analyzing its ac response and eventually calculating the variation of impedance with frequency of applied perturbation. The complex impedance (Z^*) is ideally described by Debye equation whose response is simulated by parallel circuit comprising a resistor (R) and ideal capacitor (C) given by equation 3.2. The real and imaginary parts of complex impedance are obtained using equations 3.3 and 3.4 respectively. Figure 4.9 displays the complex impedance spectra (Nyquist plots) i.e., plot of imaginary part Z'' vs. real part Z' of complex impedance (Z^*) for (x) CZF-(1-x) BNT (x = 10, 20, 30, 40 and 50 wt. %) composites at room temperature in the frequency range of 100 Hz–1MHz. Nyquist plots of composites exhibit two semicircular arcs relaxing in different frequency regions. Each semicircular arc may be ascribed to parallel combination of bulk resistance (R_b), bulk capacitance (C_b) and grain boundary resistance (R_{gb}), grain boundary capacitance (C_{gb}) akin to contribution from bulk material and grain boundaries respectively, thereby relaxing in different frequency region.

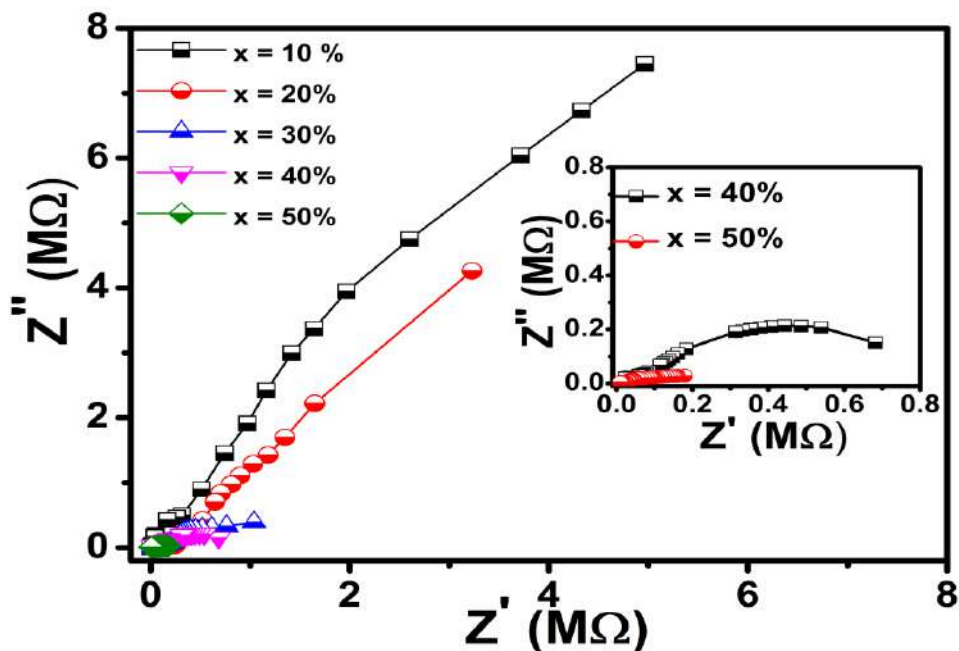


Figure 4.9 Complex impedance spectra of $(x) \text{Co}_{0.8}\text{Zn}_{0.2}\text{Fe}_2\text{O}_4-(1-x) \text{Bi}_{0.5}\text{Na}_{0.5}\text{TiO}_3$ ($x = 10, 20, 30, 40$ and 50 wt.%) composites measured at room temperature. Inset shows complex impedance spectra for $x = 40$ and 50 wt.% composite

The appearance of two semi-circular arcs in impedance spectrum of the composites signals about existence of bulk and grain boundary contribution to its overall electric property. The intercepts of these two semicircular arcs on the real (Z') axis gives us an estimate of bulk or grain resistance (R_b) in high frequency regime and grain boundary resistance (R_{gb}) in low frequency regime. The magnitude of Z' and Z'' are found to decrease with addition of ferrite. This indicates the possibility of increase in AC conductivity. The Nyquist plots also reveal that both semicircular arcs exhibit some degree of depression indicating that their centre lies below Z' axis signalling the presence of non- Debye type of relaxation in the composites.

For confirming the presence of magnetic ordering in the composites, the M–H hysteresis loops of the composites were measured using VSM with an applied magnetic field of $-10 \text{ kOe} \leq H \leq +10 \text{ kOe}$ at 300 K. Figure 4.10 (a) exhibits the M–H hysteresis loops of $(x) \text{CZF}-(1-x) \text{BNT}$ ($x = 10, 20, 30, 40$ and 50 wt.%) composites along with that of pure CZF. Inset shows the magnified image of M-H hysteresis loops of the composites. The magnetization observed in our composites is solely due to ferrite phase CZF.

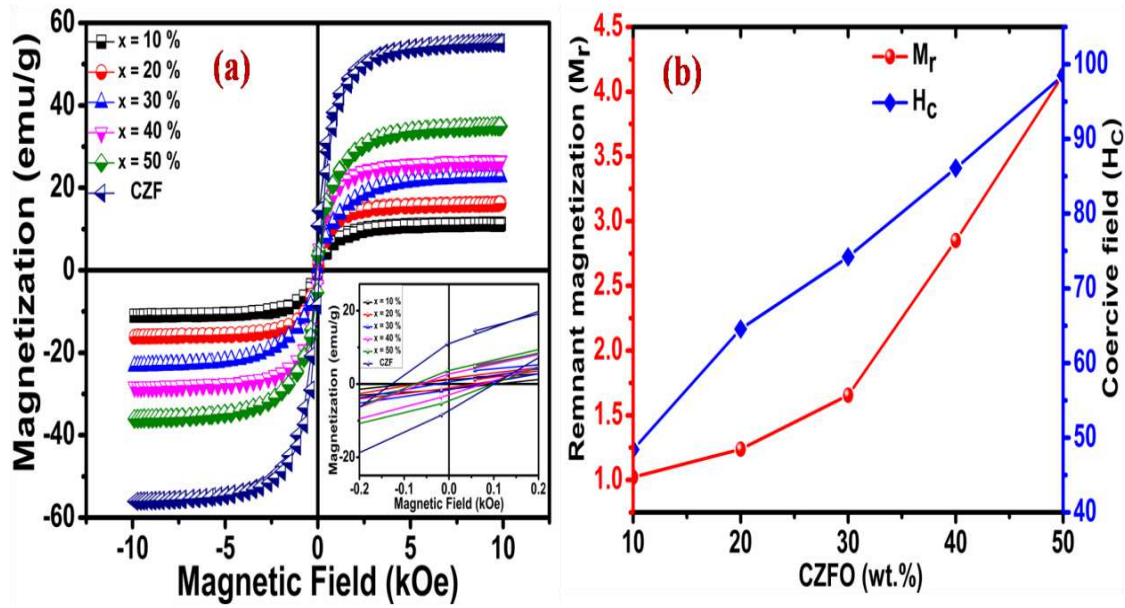


Figure 4.10 (a) M-H hysteresis loops of $(x) \text{Co}_{0.8}\text{Zn}_{0.2}\text{Fe}_2\text{O}_4-(1-x) \text{Bi}_{0.5}\text{Na}_{0.5}\text{TiO}_3$ ($x = 10, 20, 30, 40$ and 50 wt.%) composites at room temperature and (b) variation of remnant magnetization (M_r) and coercivity (H_c) with CZF content

It is evident from Figure 4.10 (a) that all composites show usual ferromagnetic hysteresis loops, signalling the presence of magnetically ordered structure [211]. Saturation magnetization (M_s) and remnant magnetization (M_r) are found to increase with addition of ferrite. M_r increases from 1.29 emu/g for $x = 10$ wt. % to 9.22 emu/g for $x = 100$ wt.% (CZF) while M_s increases from 11.23 emu/g for $x = 10$ wt.% to 55.22 emu/g for $x = 100$ wt.% (CZF). The magnetic parameters of the composites are listed in Table 4.1.

Table 4.1 Magnetic parameters of $(x) \text{Co}_{0.8}\text{Zn}_{0.2}\text{Fe}_2\text{O}_4-(1-x) \text{Bi}_{0.5}\text{Na}_{0.5}\text{TiO}_3$ ($x = 10, 20, 30, 40,$ and 50 wt.%) composites measured at room temperature

Composition (x)	M_r (emu/g)	M_s (emu/g)	Coercivity (Oe)
0.10	1.02	10.78	48.44
0.20	1.24	15.98	64.55
0.30	1.66	21.77	74.20
0.40	2.85	26.36	86.11
0.50	4.13	35.05	98.50
1.0	10.52	55.48	129.60

Figure 4.10 (b) shows the variation of M_r and coercive field (H_C) with ferrite content. Both are found to increase with addition of ferrite. The increase in magnetization may be attributed to the fact that single ferrite grain in the composite act as centre of magnetization and magnetization is basically sum of these individual contributions. Magnetic contacts profoundly enhance with addition of ferrite thereby increasing overall magnetization [212]. The variation of H_C with ferrite can be related to variation of grain size of the composites. The average grain size of the composites is found to decrease with addition of ferrite. Decrease in grain size leads to an increase in grain boundaries. These grain boundaries are commonly associated to domain wall pinning. Due to this the pinning of domain wall motion increases with decrease in grain size. Since coercivity evinces amount and effectiveness of pinning, therefore we expect H_C to increase as grain size decrease with addition of ferrite [201].

Figure 4.11 shows the XPS spectra of Co 2p, Fe 2p, Zn 2p and O1s regions of ferrite phase CZF. It provides information about the oxidation states of the different elements.

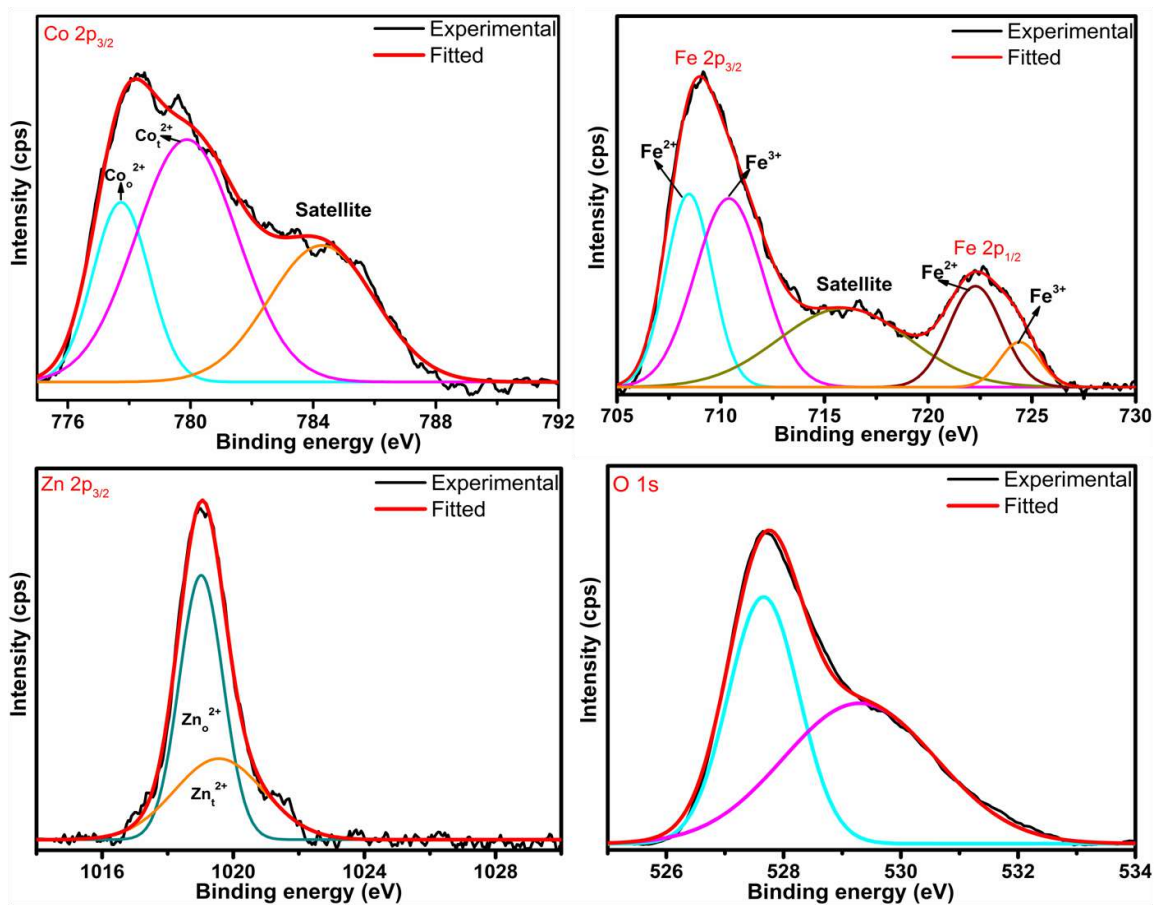


Figure 4.11 XPS spectra of Co 2p_{3/2}, Fe 2p_{3/2,1/2}, Zn 2p_{3/2} and O 1s for $Co_{0.8}Zn_{0.2}Fe_2O_4$

The XPS spectra of Co $2p_{3/2}$ region comprises of two deconvoluted photopeaks around 777.78 and 779.62 eV corresponding to Co^{2+} at octahedral and tetrahedral sites respectively with a satellite peak around 784.55 eV. The Fe 2p region shows two peaks of Fe $2p_{3/2}$ and Fe $2p_{1/2}$ around 710 and 724 eV. These two peaks are further deconvoluted into two peaks signifying the presence of Fe^{2+} and Fe^{3+} oxidation states. The XPS spectra of Zn $2p_{3/2}$ region comprises of two deconvoluted photopeaks around 1019.20 and 1019.82 eV corresponding to Zn^{2+} at octahedral and tetrahedral sites respectively [213].

It is a well established fact that magnetolectric (ME) effect in composite materials arise due to interaction between magnetostriction and piezoelectric effects of ferrite and ferroelectric phases respectively. ME effect in the present composites was confirmed by measuring ME voltage coefficient (α_{ME}) using dynamic method [144]. Figure 4.12 illustrates the variation of ME voltage coefficient (α_{ME}) of (x) CZF-($1-x$) BNT ($x = 10, 20, 30, 40$ and 50 wt.%) composites as a function of DC magnetic field.

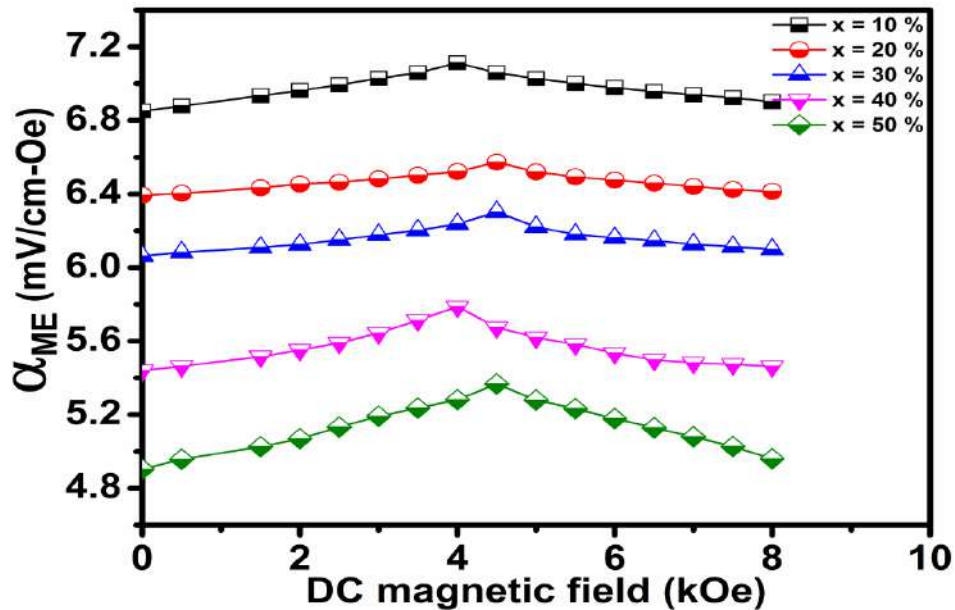


Figure 4.12 Variation of α_{ME} with DC magnetic field for (x) $\text{Co}_{0.8}\text{Zn}_{0.2}\text{Fe}_2\text{O}_4$ -($1-x$) $\text{Bi}_{0.5}\text{Na}_{0.5}\text{TiO}_3$ ($x = 10, 20, 30, 40$ and 50 wt.%) composites

Before measuring α_{ME} , the composite samples were poled at an applied electric field of 0.5–1 kV/cm for 40 min at 100 °C by keeping the samples in silicone oil which is highly insulating. This ensures alignment of domains in the field direction. In the dynamic method for measurement of α_{ME} , we apply an AC magnetic field of 5 Oe having frequency 999 Hz

in tandem with a sweeping DC magnetic field from 0–8 kOe and α_{ME} is computed using equation 3.8.

It is evident from Figure 4.12 that α_{ME} increases with increase in DC bias magnetic field up to 4 kOe, reaches maximum and then starts decreasing gradually with a decrease in DC bias magnetic field. This may be attributed to increase in magnetostriction coefficient ‘ λ ’ with an increase in magnetic field. At ~ 4 kOe we obtain saturation in the CZF phase, therefore ‘ λ ’ also reaches its saturation value. Once ‘ λ ’ attains saturation value, the piezomagnetic coupling coefficient, $q = \delta\lambda/\delta H_{bias}$ starts decreasing rapidly with further increase in magnetic field and tends towards zero, thereby gradually decreasing α_{ME} . Alternatively, the increase in DC bias magnetic field favours the domain growth, resulting an increase in magnetostress coupling. As magnetic field increases up to ~ 4 kOe, the magnetostress coupling becomes highly strong, leading to a maximum value of ‘ q ’ and in turn α_{ME} . A further increase in magnetic field beyond this point inhibits magnetic domains in the CZF phase thereby suppressing piezomagnetic coupling and in turn the ME output gradually becomes weak [164]. We obtained maximum α_{ME} of 7.11 mV/cm-Oe for 10 wt.% CZF – 90 wt.% BNT ME composite. This observed value of α_{ME} for 10 wt.% CZF is found to be higher than other ME composites reported in literature [81, 101, 102] as shown in Table 4.2.

Table 4.2 Comparison of α_{ME} for (x) Co_{0.8}Zn_{0.2}Fe₂O₄-(1-x) Bi_{0.5}Na_{0.5}TiO₃ composites with other lead-free composites

Composites	Maximum α_{ME} (mV/cm-Oe)	References
(0.80) Bi_{0.5}Na_{0.5}TiO₃–(0.20) MgFe₂O₄	4.79	[101]
(0.10)Ni_{0.8}Zn_{0.2}Fe₂O₄–(0.90) Ba_{0.9}Sr_{0.1}Zr_{0.04}Ti_{0.96}O₃	1.62	[81]
(0.10) Co_{0.8}Zn_{0.2}Fe₂O₄–(0.90) Bi_{0.5}Na_{0.5}TiO₃	7.11	Present work

4.3.2 (1-x) Bi_{0.5}Na_{0.5}TiO₃-(x) CoMn_{0.2}Fe_{1.8}O₄ ME composite system with x = 0.10, 0.20, 0.30, 0.40, 0.50

Figure 4.13 exhibits the X-ray diffraction patterns for (1 -x) BNT/(x) CMFO (x = 0.10, 0.20, 0.30, 0.40 and 0.50) composites in addition to that of pure BNT and CMFO phases. It is evident from Figure 4.13 that the XRD patterns of the composites exhibit the existence

of both the parent phase i.e. ferrite phase of CMFO (#) [166] and ferroelectric phase of BNT (*) (JCPDS Card No. 36-0340) without any impurity.

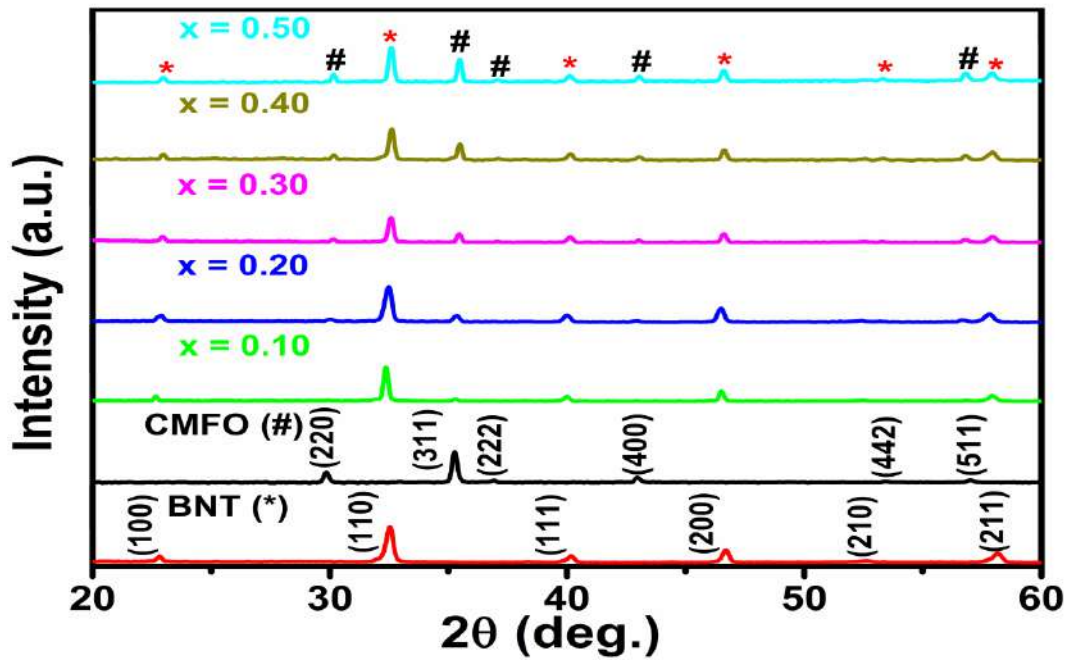


Figure 4.13 X-ray diffraction patterns of $(1-x)\text{Bi}_{0.5}\text{Na}_{0.5}\text{TiO}_3-(x)\text{CoMn}_{0.2}\text{Fe}_{1.8}\text{O}_4$ ($x = 0.10, 0.20, 0.30, 0.40$ and 0.50) composites along with BNT and CMFO phases, where (asterisk,*) represents BNT and (hash, #) represents CMFO phase

Pure BNT and CMFO phases exhibit rhombohedral perovskite structure having lattice parameter $a = 3.896 \text{ \AA}$ and cubic spinel structure having lattice parameter $a = 8.412 \text{ \AA}$ respectively. The intensities of the peaks in the composites are found to vary according to the wt.% of the individual phases. The lattice parameters of constituent phases in the composites are provided in Table 4.3. It is evident that lattice parameters of BNT and CMFO in the composites are approximately identical to pure BNT and CMFO phases respectively. This signifies the absence of any structural change arising in the constituent phases amid synthesis of composites. The theoretical density of the composites is calculated using equation 3.1 and experimental density is computed using Archimedes method. The relative density is calculated using equation 3.2 and is provided in Table 4.3.

Table 4.3 Lattice parameters, grain sizes and relative densities of $(1-x) \text{Bi}_{0.5}\text{Na}_{0.5}\text{TiO}_3$ - $(x) \text{CoMn}_{0.2}\text{Fe}_{1.8}\text{O}_4$ ($x = 0.10, 0.20, 0.30, 0.40$ and 0.50) composites

Compositions (x)	Lattice Parameters (Å)		Average grain size (nm)	Crystallite size (nm)	ρ_{rel} (%)
	CMFO	BNT			
	<i>a</i>	<i>a</i>			
0.0	-	3.896	3.012	-	90.12
0.10	8.441	3.904	2.774	40.16	88.23
0.20	8.449	3.919	2.561	38.54	89.56
0.30	8.444	3.914	2.425	39.24	87.54
0.40	8.441	3.912	2.323	38.39	86.52
0.50	8.443	3.913	2.121	38.07	87.43
1.0	8.412	-	0.896	35.23	85.21

Figure 4.14 (a-g) displays the FE-SEM micrographs of $(1-x) \text{BNT}/(x) \text{CMFO}$ ($x = 0, 0.10, 0.20, 0.30, 0.40, 0.50$ and 1.0) composites.

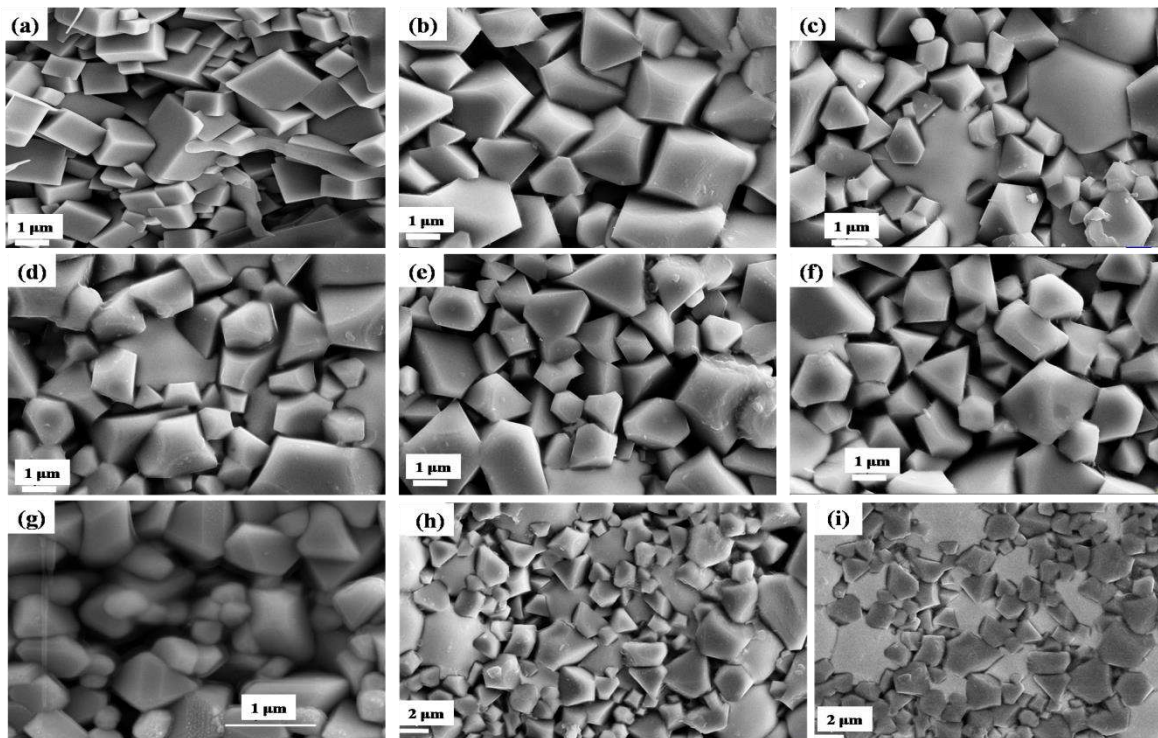


Figure 4.14 FE-SEM micrographs of $(1-x) \text{Bi}_{0.5}\text{Na}_{0.5}\text{TiO}_3$ - $(x) \text{CoMn}_{0.2}\text{Fe}_{1.8}\text{O}_4$ (a) $x = 0$, (b) $x = 0.10$, (c) $x = 0.20$, (d) $x = 0.30$, (e) $x = 0.40$, (f) $x = 0.50$, (g) $x = 1.0$ composites and (h-i) secondary and backscattered electron mode ($x = 0.30$)

Figure 4.14 (h-i) shows the FE-SEM micrographs for $x=0.30$ composition in backscattered (BSE) mode with corresponding secondary electron mode. We observed two distinct types of grains, one is white (large) grain and other is black (small) in the BSE mode. The larger grain corresponds to BNT phase and smaller grains correspond to CMFO phase. These micrographs reveal that microstructure of the composites comprises of fairly entwined, randomly oriented, non-uniform (in shape and size) grains having some inter granular porosity. The average grain size of the composites is computed using Image J and is given in Table 4.3. It is found to decrease with addition of ferrite phase CMFO. All composites exhibit distribution of small sized CMFO grains in large grained BNT matrix.

The variation of dielectric constant (ϵ') and dielectric loss ($\tan \delta$) with frequency for $(1-x)$ BNT/ (x) CMFO ($x = 0.10, 0.20, 0.30, 0.40$ and 0.50) composites in the frequency range 50 Hz-1 MHz measured at room temperature is shown in Figure 4.15 (a-b).

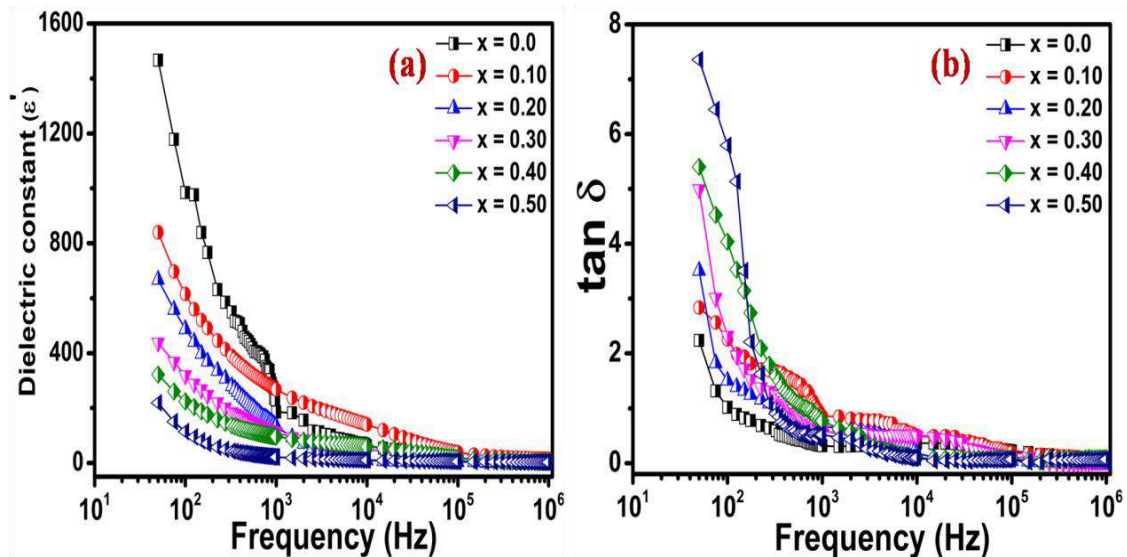


Figure 4.15 Frequency dependence of (a) Dielectric constant (ϵ') and (b) dielectric loss ($\tan \delta$) for $(1-x)$ $\text{Bi}_{0.5}\text{Na}_{0.5}\text{TiO}_3$ - (x) $\text{CoMn}_{0.2}\text{Fe}_{1.8}\text{O}_4$ ($x = 0, 0.10, 0.20, 0.30, 0.40$ and 0.50) composites.

It is evident from Figure 4.15 (a-b) that ϵ' and $\tan \delta$ show decreasing trend with increase in frequency. The ϵ' and $\tan \delta$ decrease sharply as frequency increases from 50 Hz- 10 kHz, then decrease gradually and then become unvarying up to 1 MHz for all composites. These charges are responsible for interfacial or space charge polarization. The grains are less resistive as compared to grain boundaries in pure phases and composites [214]. On application of AC electric field electrons gather at highly resistive grain boundaries giving rise to space charge polarization which is accountable for higher values of dielectric

constant at lower frequencies. As the frequency of applied AC field increases, the electrons fail to move in tandem with applied field and fail to gather at grain boundaries, consequently resulting in downfall of dielectric constant.

The variation of dielectric constant (ϵ) for the $(1-x)$ BNT- (x) CMFO ($x = 0, 0.10, 0.20, 0.30, 0.40$ and 0.50) composites with temperature, measured at three distinct frequencies (1 kHz, 5 kHz and 10 kHz) is shown in Figure 4.16 (a-f).

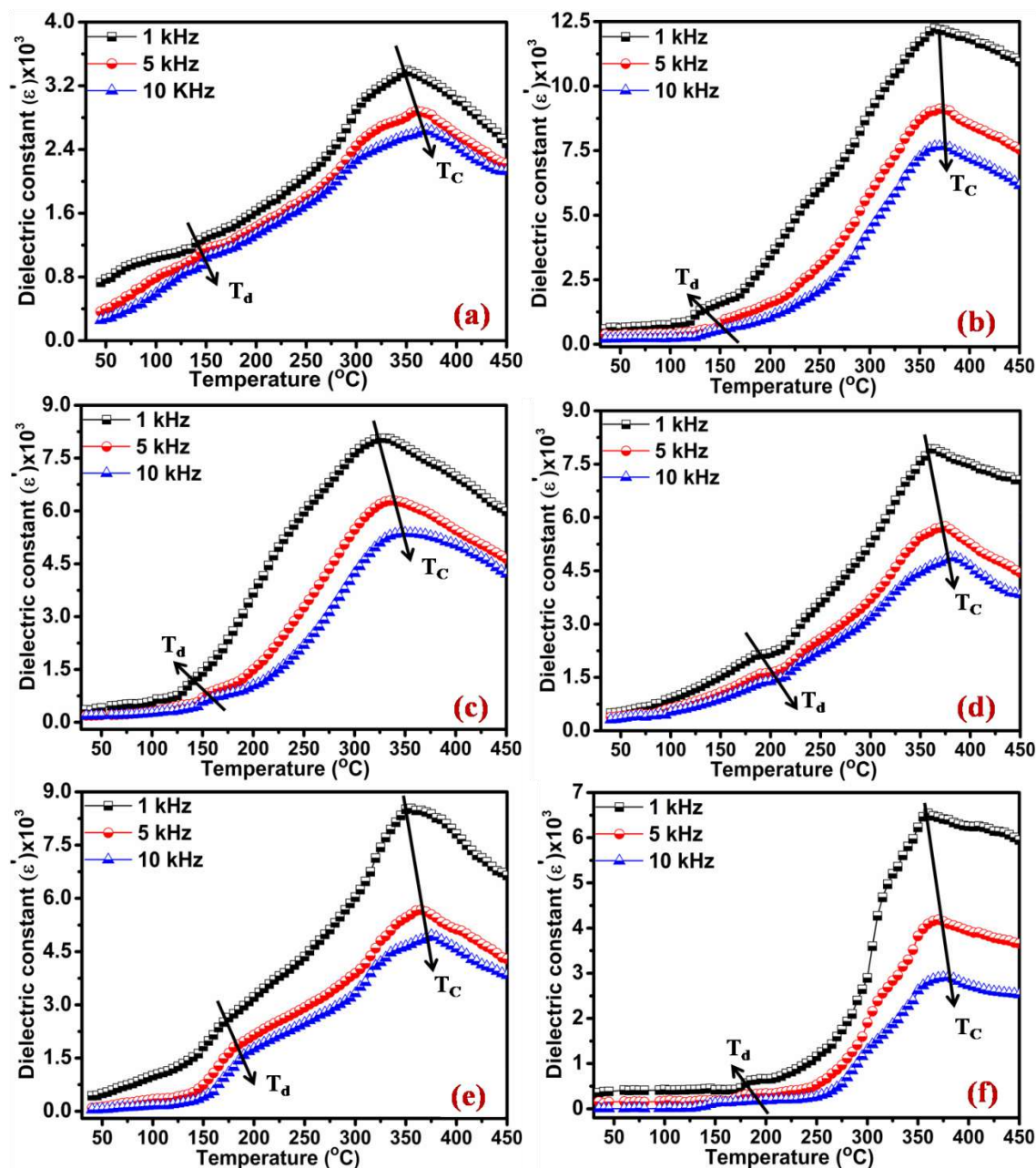


Figure 4.16 Temperature dependence of dielectric constant for $(1-x)$ $\text{Bi}_{0.5}\text{Na}_{0.5}\text{TiO}_3$ - (x) $\text{CoMn}_{0.2}\text{Fe}_{1.8}\text{O}_4$ (a) $x = 0$, (b) $x = 0.10$, (c) $x = 0.20$, (d) $x = 0.30$, (e) $x = 0.40$, (f) $x = 0.50$ composites

Two dielectric anomalies have been observed for pure BNT – a feeble hump and broad dielectric peak. This type of dielectric response of BNT is similar to those of formerly synthesized BNT and BNT based composites [215, 216]. The two dielectric anomalies correspond to transition from ferroelectric to antiferroelectric phase (T_d) with subsequent transition to paraelectric phase (T_C) respectively. Temperature akin to transition from ferroelectric–antiferroelectric phase is named as depolarization temperature (T_d), because the specimen loses its piezoelectric property above T_d [216].

From Figure 4.16, it is evident that for pure BNT, $T_d = 160\text{ }^\circ\text{C}$ and $T_C = 350\text{ }^\circ\text{C}$ at 1 kHz. The $(1-x)$ BNT/ (x) CMFO composites also exhibit these two dielectric anomalies. The transition peak (T_C) of pure BNT and the composites is broad and is frequency dependent. It is also evident from Figure 4.16 that T_C increases slightly with increase in measuring frequency indicating the presence of diffused phase transition. There is no orderly variation in value of T_d and T_C for the composites studied. This may be attributed to the fact that the composition of the ferroelectric or ferrite phase is not changed in the studied composites. The Curie temperature of any ferroelectric or ferrite phase depends on its composition and the metal ions present in it [217]. Dielectric constant (ϵ') is found to decrease with increase in CMFO content. Since, this composite has ferrite phase distributed among ferroelectric phase matrix, therefore decrease in value of ϵ' is a consequence of incorporation of CMFO in BNT phase with decrease in grain size. Decrease in grain size broadens the grain boundaries, thereby opposing the flexible alignment of dipoles, which contribute towards the dielectric phenomenon. It is also noted that dielectric constant increases as temperature increases up to T_C and beyond T_C it starts decreasing. For ME composites containing ferrites as one of its constituent phases, this behaviour may arise due to hopping of electrons among Fe^{2+} and Fe^{3+} ions existing at octahedral sites. Since hopping is thermally operated process, it tends to increase with temperature, consequently increasing electrical conductivity. The hopping initiates dielectric polarization, arising from local displacement in direction of applied electric field due to which dielectric constant increase up to T_C . As temperature surpasses T_C , the random vibrational motions of electrons and ions escalates, thereby making it difficult for them to orient in the direction of applied field, consequently decreasing the dielectric constant [151].

Figure 4.17 (a-f) exhibits the variation of dielectric loss ($\tan \delta$) for the $(1-x)$ BNT- (x) CMFO ($x = 0, 0.10, 0.20, 0.30, 0.40$ and 0.50) composites with temperature, measured at three distinct frequencies (1 kHz, 5 kHz and 10 kHz).

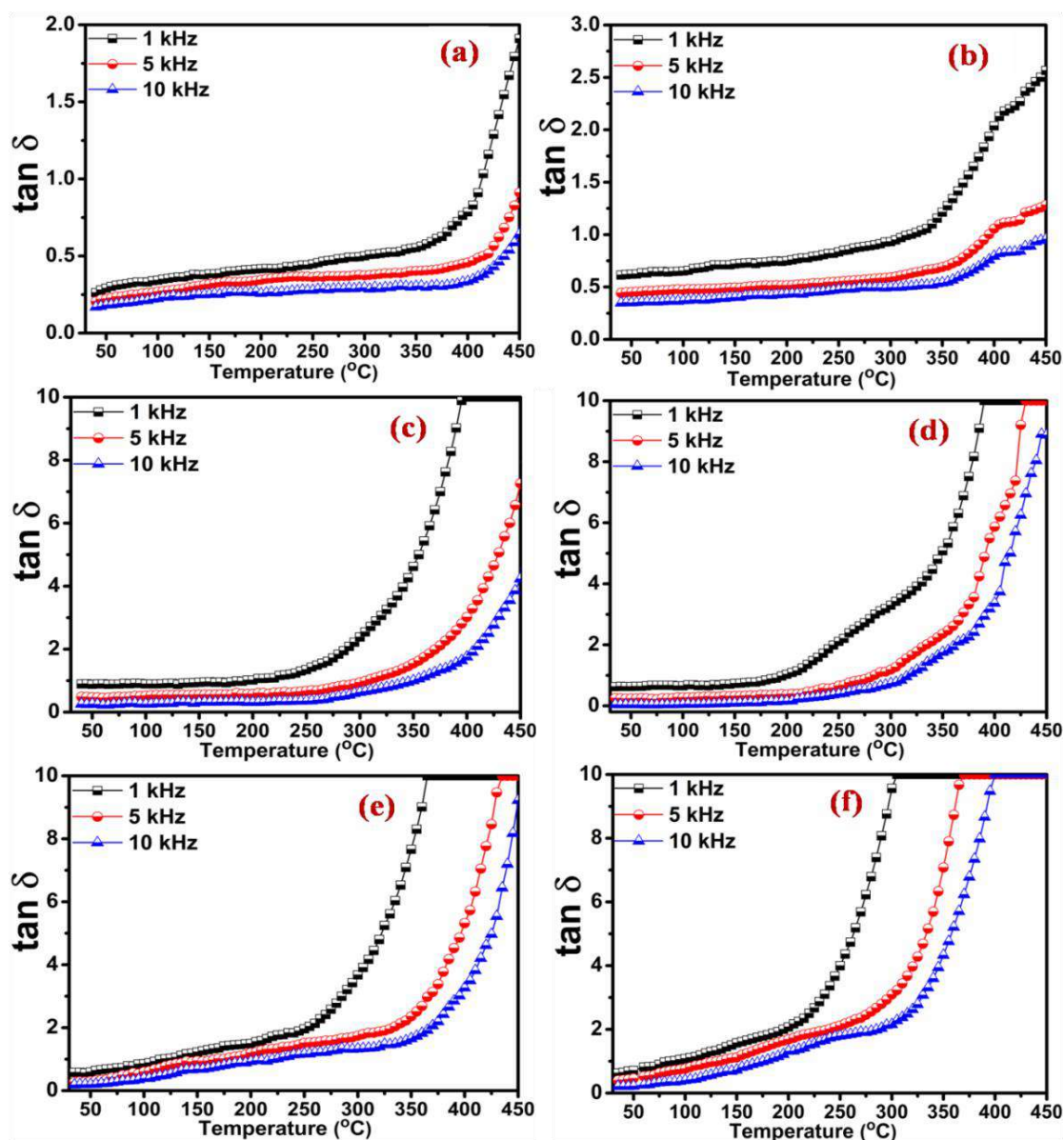


Figure 4.17 Temperature dependence of dielectric loss for $(1-x)$ $\text{Bi}_{0.5}\text{Na}_{0.5}\text{TiO}_3$ - (x) $\text{CoMn}_{0.2}\text{Fe}_{1.8}\text{O}_4$ (a) $x = 0$, (b) $x = 0.10$, (c) $x = 0.20$, (d) $x = 0.30$, (e) $x = 0.40$, (f) $x = 0.50$ composites

The dielectric loss is found to increase with temperature. This can be accredited to enhancement in space charge polarization as the temperature increases. These charges acquire thermal energy with increment in temperature leading to conduction losses [94]. It is also evident from Figure 4.17 that dielectric loss is higher at 1 kHz than 10 kHz, indicating that it is higher at lower frequencies and decrease with increasing frequency.

At low frequencies, higher loss may be due to the resemblance amidst the hopping frequency of ferrous and ferric ions at adjacent octahedral sites and external electric field. As we increase the frequency of applied electric field, the hopping frequency of electron exchange does not match with external electric field's frequency which consequently minimizes the dielectric loss [218].

To calculate the diffuseness of phase transition the diffusivity parameter (γ) is calculated using the modified Curie-Weiss law [219] expressed by equation

$$\left(\frac{1}{\epsilon'} - \frac{1}{\epsilon_{\max}'} \right) = A(T - T_m)^\gamma \quad (4.3)$$

Here γ is the diffusivity parameter lying in the range $1 < \gamma \leq 2$. For $\gamma = 1$ we obtain normal Curie-Weiss law and having value in between 1 and 2 is indicative of diffuse phase transition [220, 221], ϵ_{\max}' is the maximum value of dielectric constant and T_m is the temperature corresponding to the maximum dielectric constant. The value of γ is calculated from the slope of straight line fitted to plots of $\ln(1/\epsilon' - 1/\epsilon_{\max}')$ vs. $\ln(T - T_m)$ for pure BNT and composites at 1 kHz frequency as shown in Figure 4.18 (a).

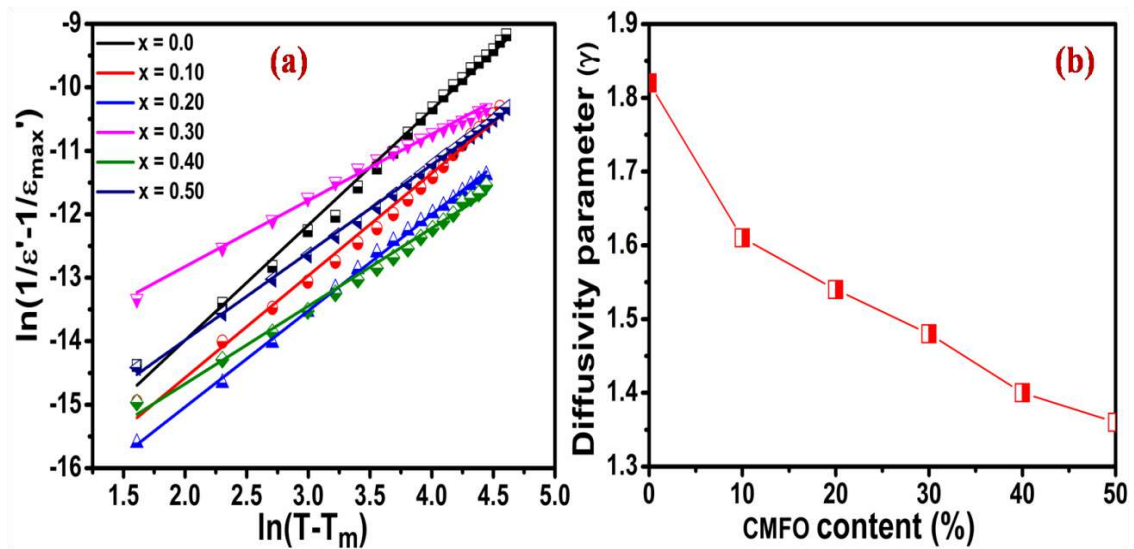


Figure 4.18 (a) Plot of $\ln(1/\epsilon' - 1/\epsilon_{\max}')$ vs $\ln(T - T_m)$ at a frequency of 1 kHz for $(1-x)\text{Bi}_{0.5}\text{Na}_{0.5}\text{TiO}_3 - (x)\text{CoMn}_{0.2}\text{Fe}_{1.8}\text{O}_4$ ($x = 0, 0.10, 0.20, 0.30, 0.40$ and 0.50) composites and (b) Variation of diffusivity parameter (γ) with CMFO content

We obtained $\gamma > 1$ for pure BNT and all compositions implying diffuse phase transition. Figure 4.17 (b) shows the variation of γ with CMFO content. It is evident from Figure 4.18

(b) that there is a decrease in γ with addition of CMFO in the composites.

The ferroelectric properties of $(1-x)$ BNT/ (x) CMFO ($x = 0.10, 0.20, 0.30, 0.40$ and 0.50) composites are determined by measuring the P-E hysteresis loops at room temperature and frequency of 50 Hz. The obtained P-E hysteresis loops of the composites are shown in Figure 4.19 (a-e).

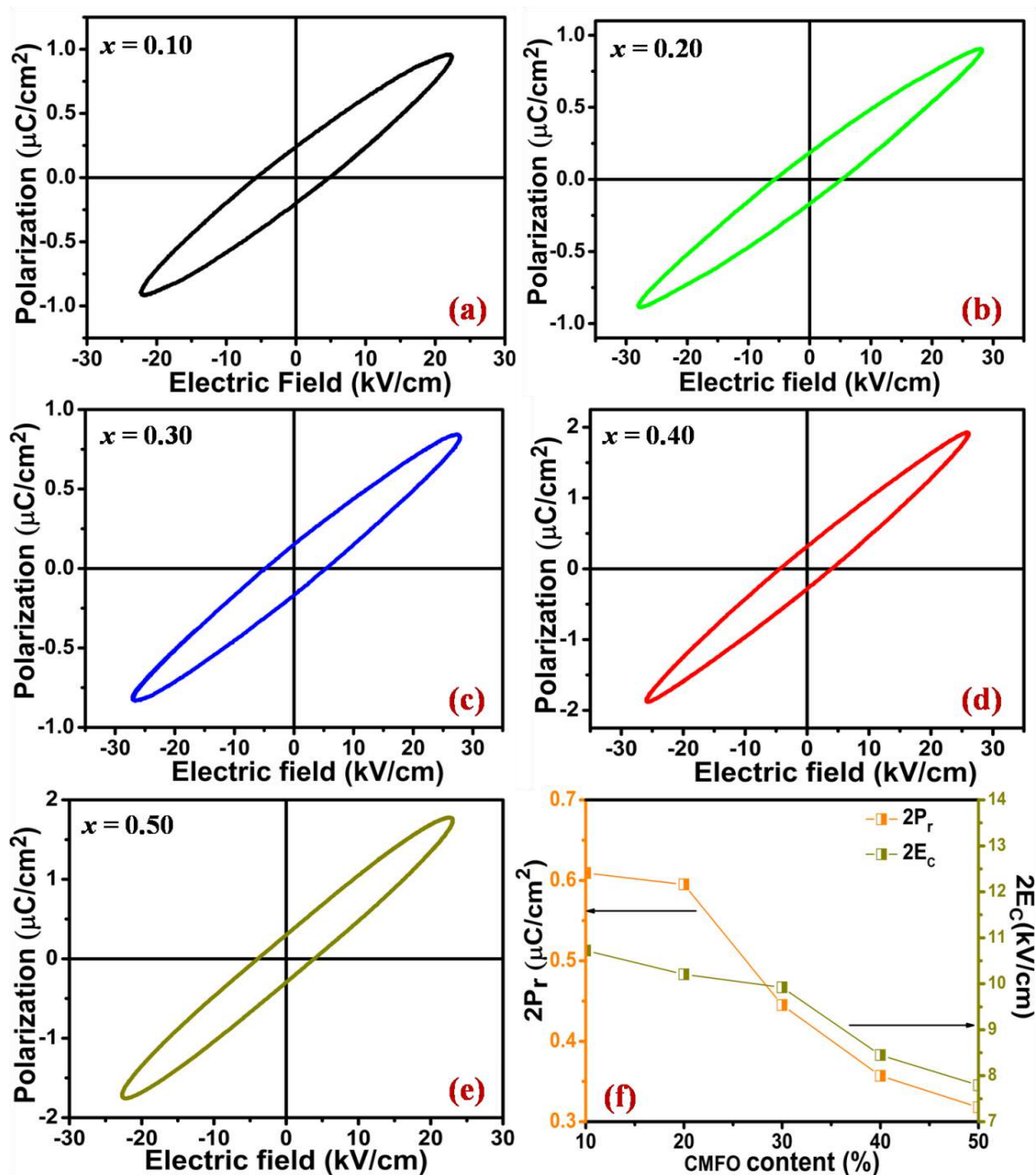


Figure 4.19 P-E hysteresis loops of $(1-x)$ $\text{Bi}_{0.5}\text{Na}_{0.5}\text{TiO}_3$ - (x) $\text{CoMn}_{0.2}\text{Fe}_{1.8}\text{O}_4$ (a) $x = 0.10$, (b) $x = 0.20$, (c) $x = 0.30$, (d) $x = 0.40$, (e) $x = 0.50$ composites at room temperature and (f) variation of remnant polarization ($2P_r$) and coercive field ($2E_c$) with CMFO content

It is evident from Figure 4.19 that the loops are not fully saturated. This may be attributed to the lower resistance of the ferrite phase. The polarization of ferrites having low resistance becomes strenuous because they can withstand only low voltages [222]. Figure 4.19 (f) exhibits the variation of remnant polarization ($2P_r$) and coercive field ($2E_C$) for $(1-x)$ BNT/ (x) CMFO composites with CMFO content and the measured values of these parameters are given in Table 4.4.

Table 4.4 Ferroelectric parameters of $(1-x)$ Bi_{0.5}Na_{0.5}TiO₃- (x) CoMn_{0.2}Fe_{1.8}O₄ ($x = 0.10, 0.20, 0.30, 0.40$ and 0.50) composites measured at room temperature

Composition (x)	Remnant Polarization ($2P_r$) ($\mu\text{C}/\text{cm}^2$)	Coercivity ($2E_C$) (kV/cm)
0.10	0.609	10.523
0.20	0.595	10.205
0.30	0.445	9.923
0.40	0.357	8.450
0.50	0.318	7.792

Both parameters viz. remnant polarization and coercive field are found to decrease with addition of CMFO. Decrease in remnant polarization of the composites indicates dilution in ferroelectric properties of composites with addition of CMFO. This may be attributed to the lower resistance of CMFO phase, consequently giving rise to heterogeneous conduction amidst BNT/CMFO interfaces [223]. The variation of coercive field with ferrite content may be attributed to domain pinning arising from switching of ferroelectric domains with change in charge carrier concentration [154].

The magnetic characteristics of the $(1-x)$ BNT/ (x) CMFO ($x = 0.10, 0.20, 0.30, 0.40$ and 0.50) composites are determined by measuring the M-H hysteresis loops at room temperature by applying magnetic field in the range $-10 \text{ kOe} \leq H \leq +10 \text{ kOe}$ and are shown in Figure 4.20 (a). Inset of Figure 4.20 (a) shows the M-H hysteresis loops of pure CMFO. The magnetic moment of the composites is computed in terms of Bohr Magnetron using equation 3.1 [224]. The variation of remnant magnetization (M_r), saturation magnetization (M_s) and magnetic moment of the composites with CMFO content is shown in Figure 4.20 (b) and their magnitudes are listed in Table 4.5.

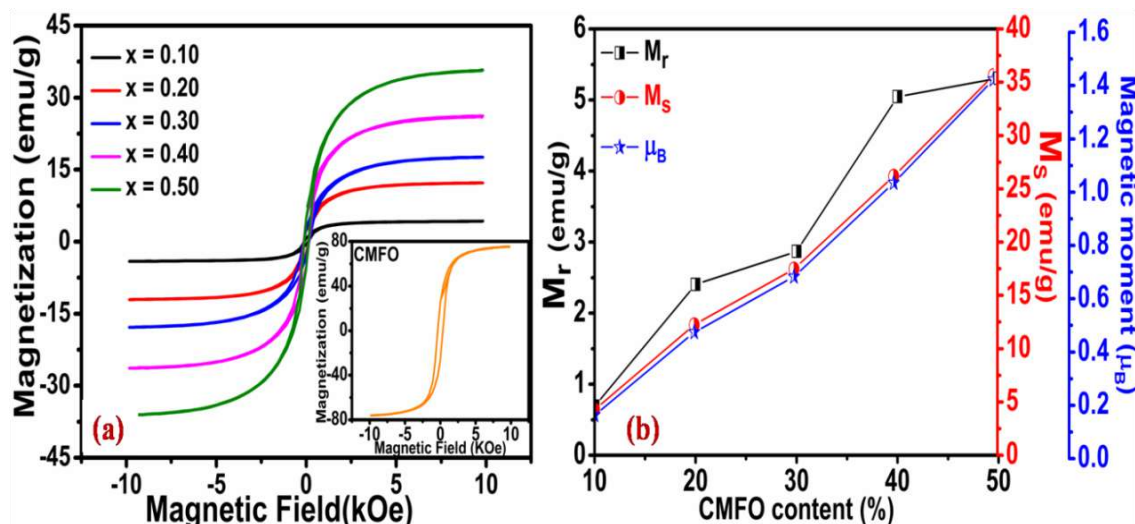


Figure 4.20 (a) M-H hysteresis loops of $(1-x) \text{Bi}_{0.5}\text{Na}_{0.5}\text{TiO}_3-(x) \text{CoMn}_{0.2}\text{Fe}_{1.8}\text{O}_4$ ($x = 0.10, 0.20, 0.30, 0.40, 0.50$ and 1.0) composites at room temperature and (b) variation of remnant magnetization (M_r), saturation magnetization (M_s) and magnetic moment with CMFO content

The M-H hysteresis loops of the composites are found to be well saturated, indicating the presence of ordered magnetic structure [197]. The magnetization and magnetic moment are found to enhance with volume fraction of CMFO in the composites. This may be attributed to the fact that each ferrite grain in the composites act as magnetization centre and the saturation magnetization is the vector sum of these single contributions. In the ME composites each ferrite grain is linked with adjoining ferroelectric grains and these contacts are found to enhance with addition of ferrite, thereby increasing the magnetization [212].

Table 4.5 Magnetic parameters of $(1-x) \text{Bi}_{0.5}\text{Na}_{0.5}\text{TiO}_3-(x) \text{CoMn}_{0.2}\text{Fe}_{1.8}\text{O}_4$ ($x = 0.10, 0.20, 0.30, 0.40$ and 0.50) composites measured at room temperature

Composition (x)	M_r (emu/g)	M_s (emu/g)	Magnetic moment (μ_B)
0.10	0.692	4.264	0.163
0.20	2.404	12.236	0.474
0.30	2.868	17.469	0.683
0.40	5.048	26.191	1.035
0.50	5.304	35.646	1.423

Complex impedance spectroscopy (CIS) [176] has been used to study the electrical behaviour of the composites over wide frequency and temperature range. CIS helps to segregate the real and imaginary parts of electrical properties, enabling us to obtain the underlying material properties. CIS examines the ac response of sample exposed to a sinusoidal perturbation and subsequently calculates the variation of impedance with frequency of perturbation. The analysis of complex impedance can give useful information about frequency dependent properties of composites.

Figure 4.21 (a-f) depicts the variation of real part of impedance (Z') for $(1-x)$ BNT/ (x) CMFO ($x = 0, 0.10, 0.20, 0.30, 0.40$ and 0.50) composites with frequency at different temperatures.

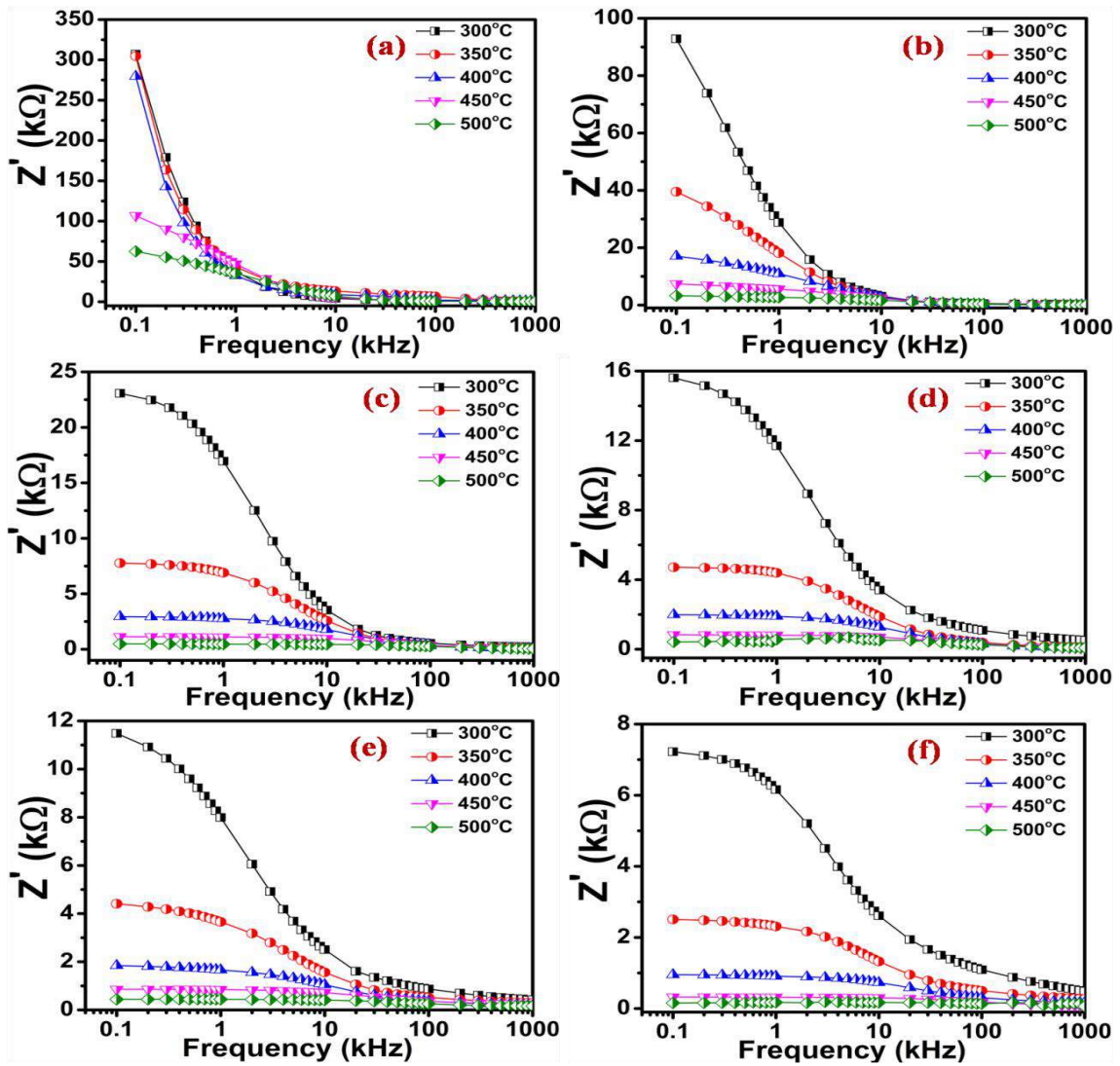


Figure 4.21 Variation of real part of impedance (Z') with frequency for $(1-x)$ $\text{Bi}_{0.5}\text{Na}_{0.5}\text{TiO}_3$ - (x) $\text{CoMn}_{0.2}\text{Fe}_{1.8}\text{O}_4$ (a) $x = 0$, (b) $x = 0.10$, (c) $x = 0.20$, (d) $x = 0.30$, (e) $x = 0.40$ and (f) $x = 0.50$ composites at different temperatures

It is evident that Z' decreases monotonically as frequency increases and achieves a static value at higher frequencies regardless of temperature. The static value of Z' is shifted to high frequency regime as temperature increases. Magnitude of Z' decreases with temperature. It may be attributed to an increment in ac conductivity with temperature and frequency [173]. The values of Z' are found to merge in high frequency regime for all temperatures, suggesting a probable emancipation of space charge and subsequent lowering of barrier properties in samples [225, 174].

The frequency response of imaginary part of impedance (Z'') for $(1-x)$ BNT/ (x) CMFO ($x = 0, 0.10, 0.20, 0.30, 0.40$ and 0.50) composites is illustrated in Figure 4.22 (a-f).

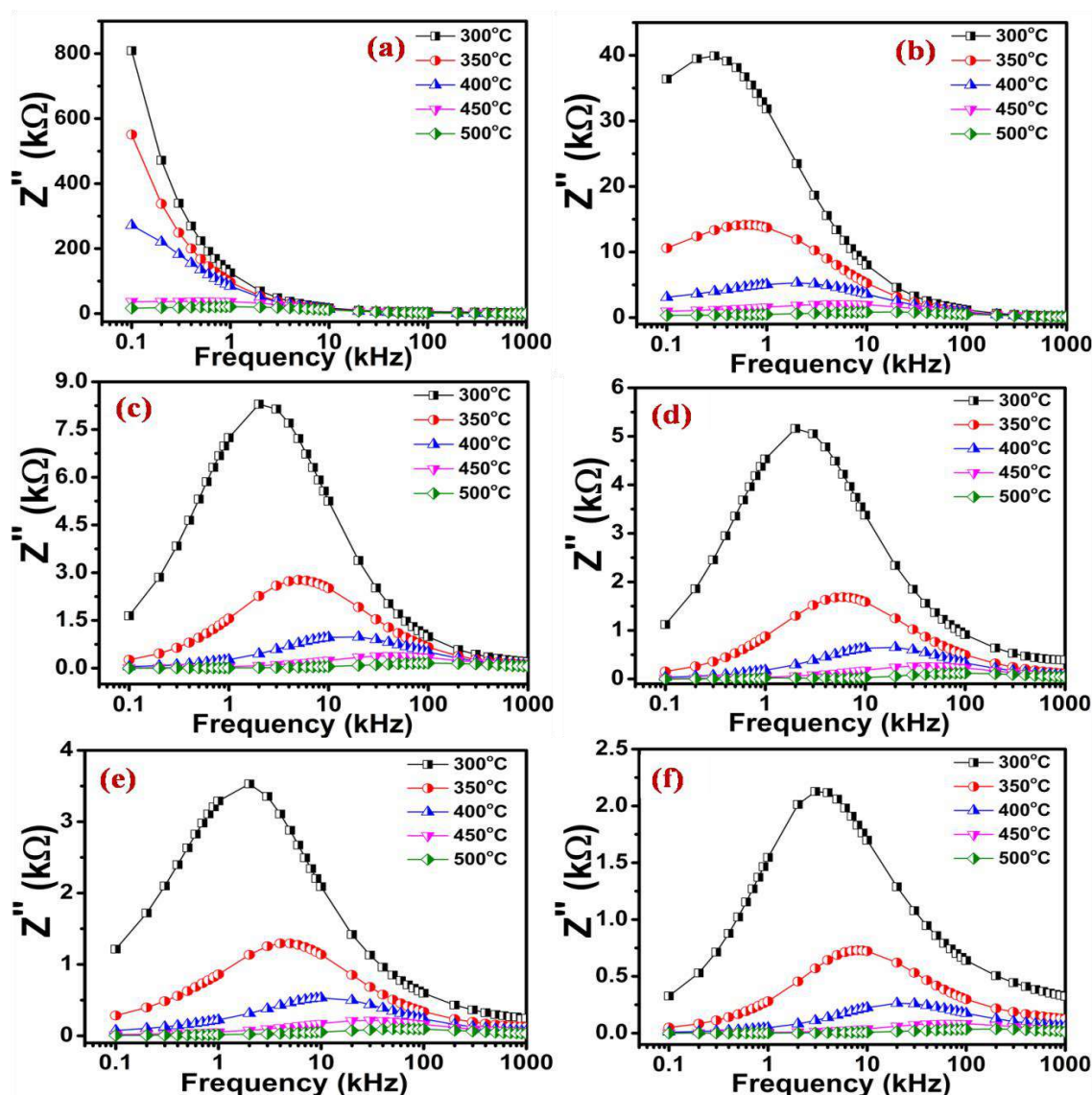


Figure 4.22 Variation of imaginary part of impedance (Z'') with frequency for $(1-x)$ $(\text{Bi}_{0.5}\text{Na}_{0.5})\text{TiO}_3$ - $(x)\text{CoMn}_{0.2}\text{Fe}_{1.8}\text{O}_4$ (a) $x = 0$, (b) $x = 0.10$, (c) $x = 0.20$, (d) $x = 0.30$, (e) $x = 0.40$ and (f) $x = 0.50$ composites at different temperatures

Variation of Z'' as a function of frequency exhibit interesting properties which include: (1) peak appearance at distinct frequency (relaxation frequency) at which Z'' attains maximum value, (2) decrement in value of Z'' with a shift in peak frequency towards high frequency regime (3) asymmetric peak broadening with temperature and (4) merging of spectra in high frequency regime independent of temperature. These features may be attributed to temperature dependence of electrical relaxation phenomena in the materials [226] which is governed by electrons or immobile charges at low temperature and oxygen vacancies or defects at higher temperatures. The peak heights also decrease with frequency and temperature indicating the presence of space charge at low frequencies and perishing at high frequencies [225, 227].

The temperature dependent plot of Z'' vs. Z' known as Nyquist plot is shown in Figure 4.23 (a-f) for $(1-x)$ BNT/ (x) CMFO ($x = 0, 0.10, 0.20, 0.30, 0.40$ and 0.50) composites.

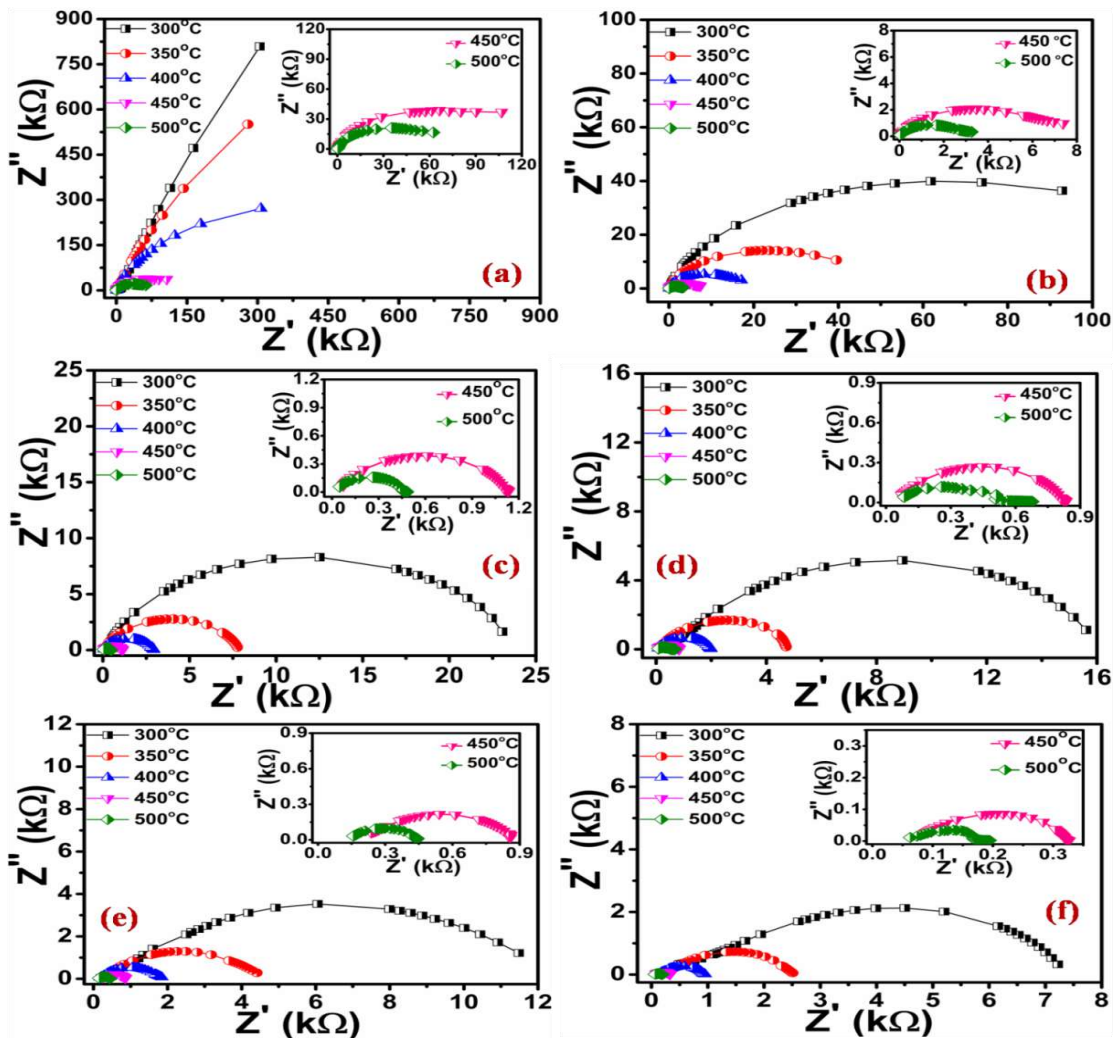


Figure 4.23 Nyquist plots for $(1-x)$ $(\text{Bi}_{0.5}\text{Na}_{0.5})\text{TiO}_3$ - (x) $\text{CoMn}_{0.2}\text{Fe}_{1.8}\text{O}_4$ (a) $x = 0$, (b) $x = 0.10$, (c) $x = 0.20$, (d) $x = 0.30$, (e) $x = 0.40$ and (f) $x = 0.50$ composites

Nyquist plots for the composites exhibit small and large radii semicircular arcs in high and low frequency regime corresponding to contribution from bulk (grain) and grain boundaries to overall electric property. The intercepts of these two semicircles on real (Z') axis gives us magnitude of bulk and grain boundary resistance (R_b and R_{gb}). Corresponding capacitances are calculated using equations 3.5 and 3.6. The obtained AC impedance parameters are listed in Table 4.6.

Table 4.6 The variation of AC impedance parameters for BNT/CMFO composites measured at different temperatures

Composition (x)		300 °C	350 °C	400 °C	450 °C	500 °C
x = 0.10	R_b (k Ω)	152.2	53.57	23.90	9.97	4.04
	C_b (nF)	21.90	26.66	20.92	20.06	12.37
	R_{gb} (k Ω)
	C_{gb} (nF)
x = 0.20	R_b (k Ω)	23.91	7.96	2.78	1.12	0.46
	C_b (nF)	20.91	25.12	17.98	22.32	21.74
	R_{gb} (k Ω)	3.07	1.30	0.55
	C_{gb} (nF)	325.73	769.23	909.09
x = 0.30	R_b (k Ω)	16.74	4.84	2.03	0.82	0.60
	C_b (nF)	19.91	34.43	24.63	40.65	18.52
	R_{gb} (k Ω)	0.94	0.86
	C_{gb} (nF)	1063.83	232.56
x = 0.40	R_b (k Ω)	12.28	4.54	0.95	0.53	0.46
	C_b (nF)	27.14	55.06	3.51	9.43	31.05
	R_{gb} (k Ω)	1.95	0.88	0.53
	C_{gb} (nF)	51.28	37.87	1886.79
x = 0.50	R_b (k Ω)	3.0	1.11	0.94	0.31	0.18
	C_b (nF)	1.66	4.50	53.19	46.08	277.78
	R_{gb} (k Ω)	7.5	2.54	1.06	0.35	0.21
	C_{gb} (nF)	44.44	43.74	943.34	2857.14	680.27

The semicircular arcs begin to emerge at 400 °C for BNT and at 300 °C for composites. BNT is more insulating than ferrite (CMFO) phase and their composites. The conductivity of the composites increases with addition of ferrite. This is the possible reason for obtaining semicircular arcs at given temperatures for BNT and composites. Below this temperature range semicircles are not obtained due to large impedance values, which is beyond the measuring range of system used. The higher frequency semicircles are more prominent indicating the major contribution of bulk effect to the electric property. It is evident that R_b decreases with temperature indicating the negative temperature coefficient of resistance (NTCR) behaviour of the composites analogous to conventional semiconductors.

Figure 4.24 shows the XPS spectra of Co 2p, Fe 2p, Zn 2p and O1s regions of ferrite phase CMFO.

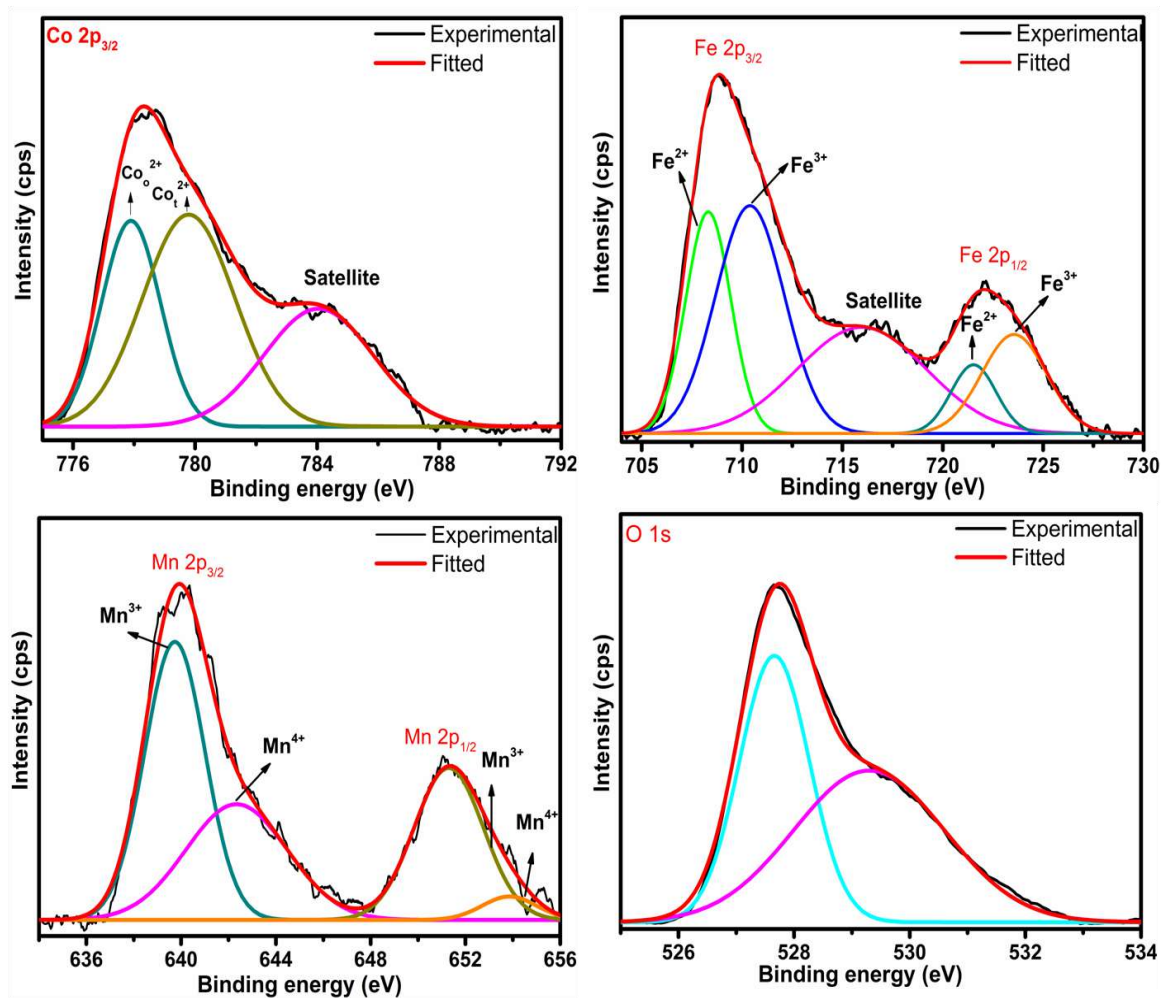


Figure 4.24 XPS spectra of Co 2p_{3/2}, Fe 2p_{3/2,1/2}, Mn 2p_{3/2,1/2} and O 1s for $\text{CoMn}_{0.2}\text{Fe}_{1.8}\text{O}_4$

The XPS spectra of Co 2p_{3/2} region comprises of two deconvoluted photopeaks around 777.91 and 779.82 eV corresponding to Co²⁺ at octahedral and tetrahedral sites respectively with a satellite peak around 784.30 eV. The Fe 2p region shows two peaks centred around 711 and 723.5 eV corresponding to Fe 2p_{3/2} and Fe 2p_{1/2} states. These two peaks are further deconvoluted to two peaks indicating the presence of Fe²⁺ and Fe³⁺ oxidation states [213]. The XPS spectra of Mn 2p shows two peaks centred at 640.13 and 651.45 eV corresponding to Mn 2p_{3/2} and Mn 2p_{1/2} states. These two peaks are further deconvoluted into two peaks corresponding to Mn³⁺ and Mn⁴⁺ oxidation states [228]. The O 1s spectra shows two peaks centred at 527.66 and 529.37 eV. The former is the major contribution which arises due to oxygen in the spinel structure and the latter may be attributed to structural defects [229].

Co-existence of ferrite (CMFO) and ferroelectric (BNT) phase in the composites gives rise to ME coupling in the composites, which has been confirmed by measuring the ME voltage coefficient (α_{ME}) using dynamic method [144] and shown in Figure 4.25. While measuring α_{ME} , same procedure has been followed as discussed in section 4.3.1 and then ME voltage coefficient has been calculated using equation 3.8. Composite with $x = 0.10$ shows highest value of $\alpha_{\text{ME}} = 6.765$ mV/cm-Oe. Figure 4.25 (f) depicts the variation of α_{ME} with CMFO content. Inset of Figure 4.25 (f) depicts the variation of resistivity with CMFO content. It has been observed that α_{ME} is found to decrease with addition of CMFO in the composites. This may be attributed to decrease in resistivity of the composites with increase in CMFO content [230]. Decrement in resistivity of the composites results in leakage of charges that are created in ferroelectric phase through neighbouring ferrite phase, consequently decreasing the induced output voltage which further accounts for decrease in α_{ME} . The value of α_{ME} observed for $x = 0.10$ composite is found to be higher than the ME composites reported as shown in Table 4.7.

Table 4.7 Comparison of α_{ME} for $(1-x) \text{Bi}_{0.5}\text{Na}_{0.5}\text{TiO}_3-(x) \text{CoMn}_{0.2}\text{Fe}_{1.8}\text{O}_4$ composites with other lead-free composites

Composites	Maximum α_{ME} (mV/cm-Oe)	References
(0.25)CoMn_{0.2}Fe_{1.8}O₄-(0.75)BaZr_{0.08}Ti_{0.92}O₃	2.340	[100]
(0.80)Bi_{0.5}Na_{0.5}TiO₃-(0.20)MgFe₂O₄	4.793	[101]
(0.90)Bi_{0.5}Na_{0.5}TiO₃-(0.10)CoMn_{0.2}Fe_{1.8}O₄	6.765	Present work

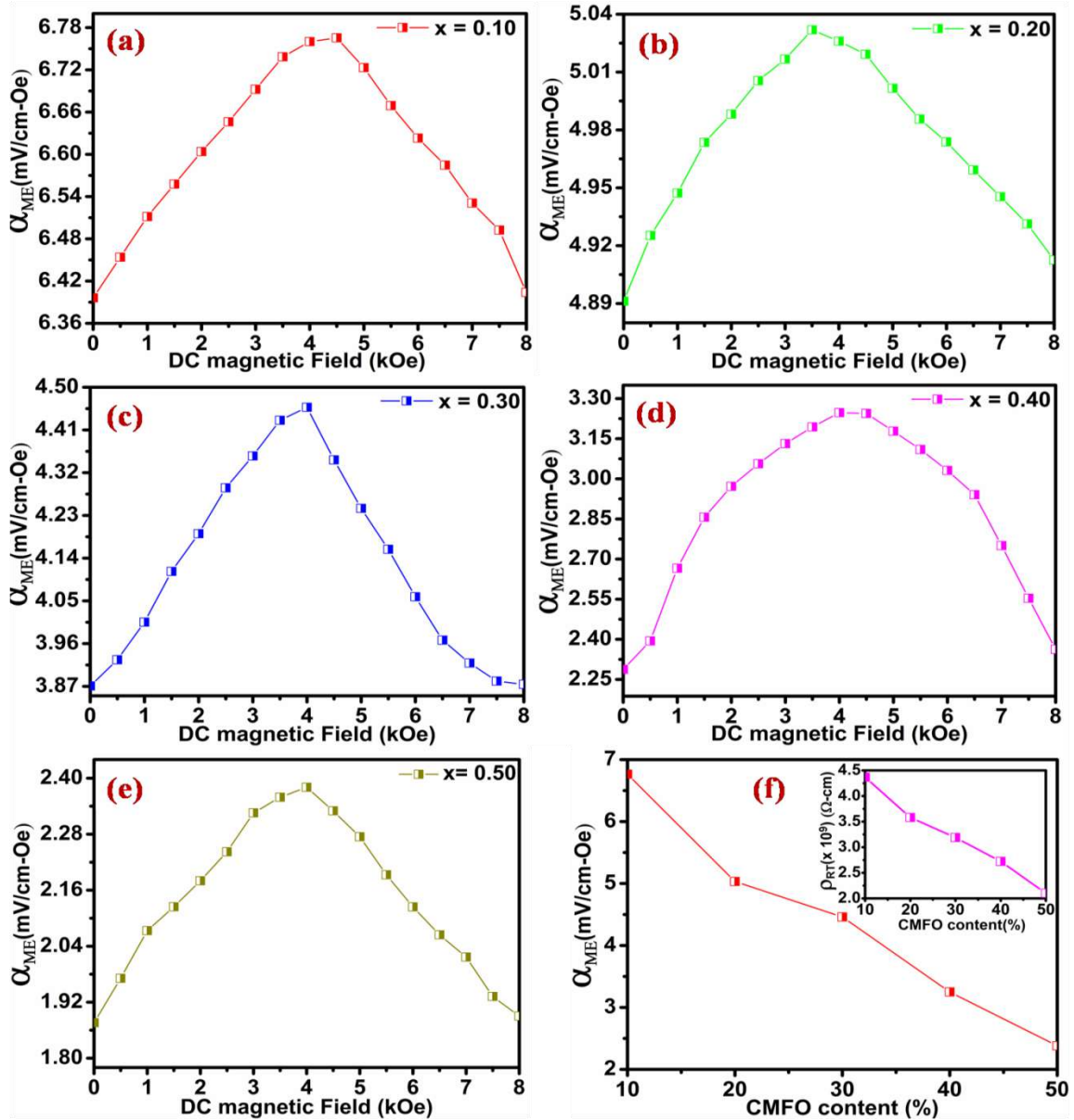


Figure 4.25 Variation of α_{ME} with DC magnetic field for $(1-x) \text{Bi}_{0.5}\text{Na}_{0.5}\text{TiO}_3-(x) \text{CoMn}_{0.2}\text{Fe}_{1.8}\text{O}_4$ (a) $x = 0.10$, (b) $x = 0.20$, (c) $x = 0.30$, (d) $x = 0.40$, (e) $x = 0.50$ and (f) variation of α_{ME} with CMFO content, inset shows the variation of resistivity with CMFO content

4.3.3 $(x) \text{Bi}_{0.5}\text{Na}_{0.5}\text{TiO}_3 - (1-x) \text{Ni}_{0.2}\text{Co}_{0.8}\text{Fe}_2\text{O}_4$ ME composite system with $x = 0.30, 0.40, 0.50, 0.60, 0.70$ and 0.80

The X-ray diffraction pattern for $(x) \text{Bi}_{0.5}\text{Na}_{0.5}\text{TiO}_3-(1-x) \text{Ni}_{0.2}\text{Co}_{0.8}\text{Fe}_2\text{O}_4$ [(x)BNT/($1-x$)NCFO], where $x = 0.30 - 0.80$ along with the constituent phases of BNT and NCFO are shown in Figure 4.26. The indexing of the XRD peaks of the composites is in agreement with reported values of NCFO [125] and for the BNT phase the pattern agreed with JCPDS card No. 36-0340. The ferrite phase NCFO shows cubic spinel-ferrite structure, whereas

BNT shows perovskite rhombohedral structure. No impurity traces are found in the XRD patterns of the composites, confirming that both the constituent phases have retained their structure. The XRD pattern of the composites shows mixed crystalline spinel-perovskite structure. The lattice parameters calculated for BNT and NCFO phases for the composites are listed in Table 4.8.

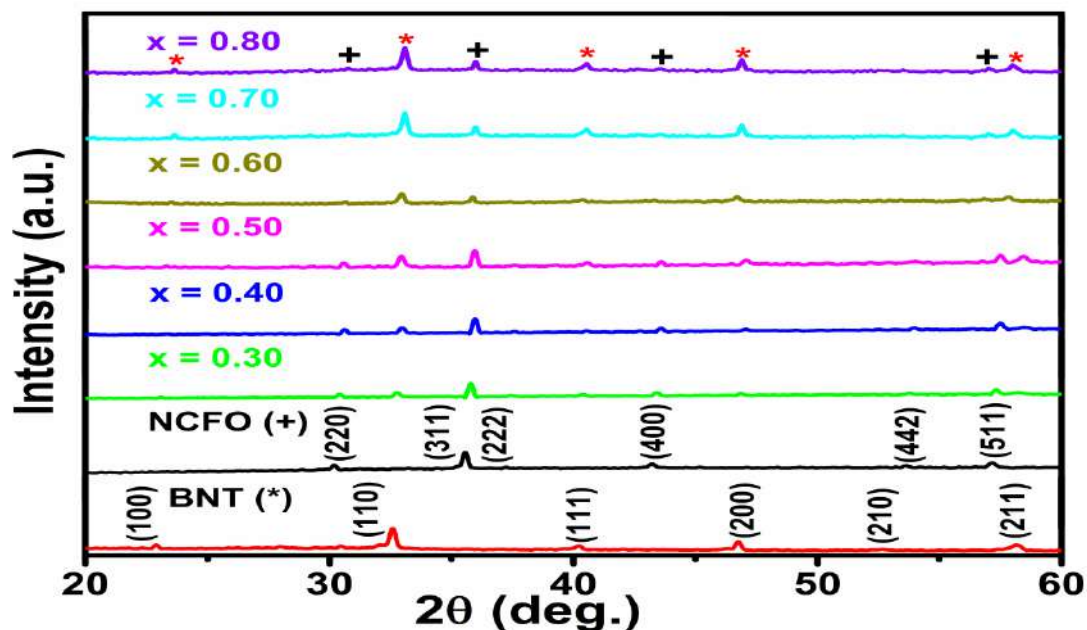


Figure 4.26 X-ray diffraction patterns of $(x) \text{Bi}_{0.5}\text{Na}_{0.5}\text{TiO}_3-(1-x) \text{Ni}_{0.2}\text{Co}_{0.8}\text{Fe}_2\text{O}_4$ ($x = 0.30 - 0.80$) composites along with pure BNT (*) and NCFO (+) phases

Table 4.8 Lattice parameters, grain sizes and relative densities of $(x) \text{Bi}_{0.5}\text{Na}_{0.5}\text{TiO}_3-(1-x)\text{Ni}_{0.2}\text{Co}_{0.8}\text{Fe}_2\text{O}_4$ ($x = 0.30-0.80$) composites

Compositions (x)	Lattice Parameters (Å)		Average grain size (µm)	ρ_{rel} (%)
	NCFO (a)	BNT (a)		
0	8.383	-	3.813	85.43
0.30	8.324	3.871	4.307	87.42
0.40	8.294	3.848	4.270	88.21
0.50	8.280	3.855	4.125	86.32
0.60	8.453	3.925	3.190	88.93
0.70	8.421	3.911	3.709	86.52
0.80	8.435	3.918	4.058	85.63
1.0	-	3.885	3.302	90.52

The FE-SEM micrographs of $(x) \text{Bi}_{0.5}\text{Na}_{0.5}\text{TiO}_3-(1-x) \text{Ni}_{0.2}\text{Co}_{0.8}\text{Fe}_2\text{O}_4$ ($x = 0.30-0.70$) composites along with pure NCFO and BNT phases are shown in Figure 4.27 (a-g) exhibiting their surface morphology. Figure 4.27 (f-g) shows the FE-SEM micrograph for $x = 0.80$ composition in backscattered (BSE) mode with corresponding secondary electron mode. We observed two distinct types of grains, one is white (large) grain and other is black (small) in the BSE mode. The larger grain corresponds to BNT phase and smaller grains correspond to NCFO phase.

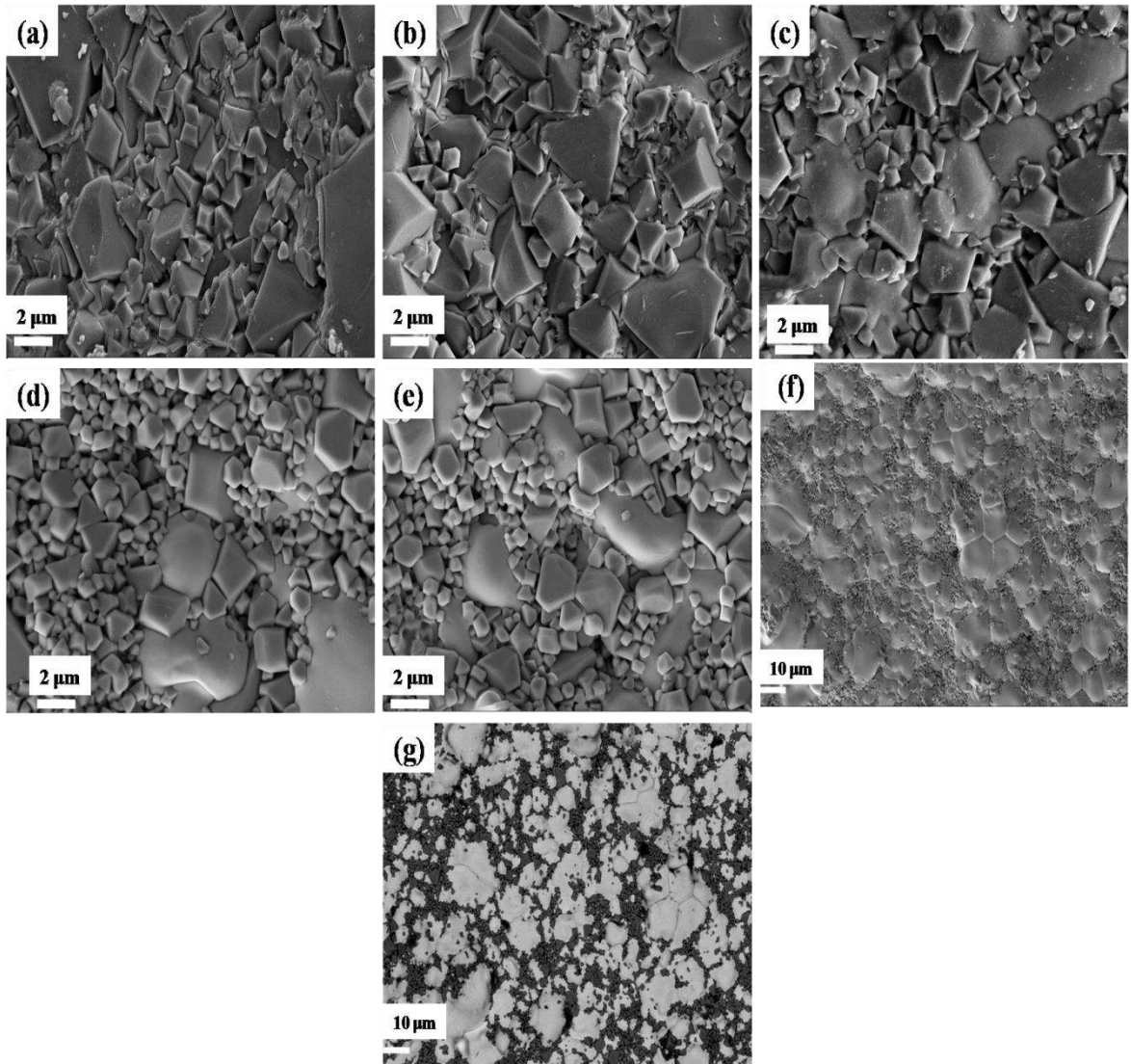


Figure 4.27 FE-SEM micrographs of $(x) \text{Bi}_{0.5}\text{Na}_{0.5}\text{TiO}_3-(1-x) \text{Ni}_{0.2}\text{Co}_{0.8}\text{Fe}_2\text{O}_4$ (a) $x = 0.30$, (b) $x = 0.40$, (c) $x = 0.50$, (d) $x = 0.60$, (e) $x = 0.70$, (f-g) secondary and backscattered electron mode for $x = 0.80$ composition

It is evident from Figure 4.27 and 4.28 that all composites exhibit mixed, non uniform and dense microstructure having firmly constituted grains of both the phases. The grain sizes of the composites are calculated using MS office VISIO software and are listed in Table 4.8. The addition of BNT resulted in densification of the microstructure of the composites. In co-fired composites the internal stress cannot be averted because of disparity in densification rate and thermal expansion coefficients of individual phases. This could be the possible reason for non-uniform microstructure with the different grain size as exhibited in our different compositions [231].

Figure 4.28 (a-b) shows the frequency dependence of dielectric constant (ϵ') and dielectric loss ($\tan \delta$) of $(x) \text{Bi}_{0.5}\text{Na}_{0.5}\text{TiO}_3-(1-x) \text{Ni}_{0.2}\text{Co}_{0.8}\text{Fe}_2\text{O}_4$ ($x = 0.30-0.80$) composites from 100 Hz- 1 MHz at room temperature

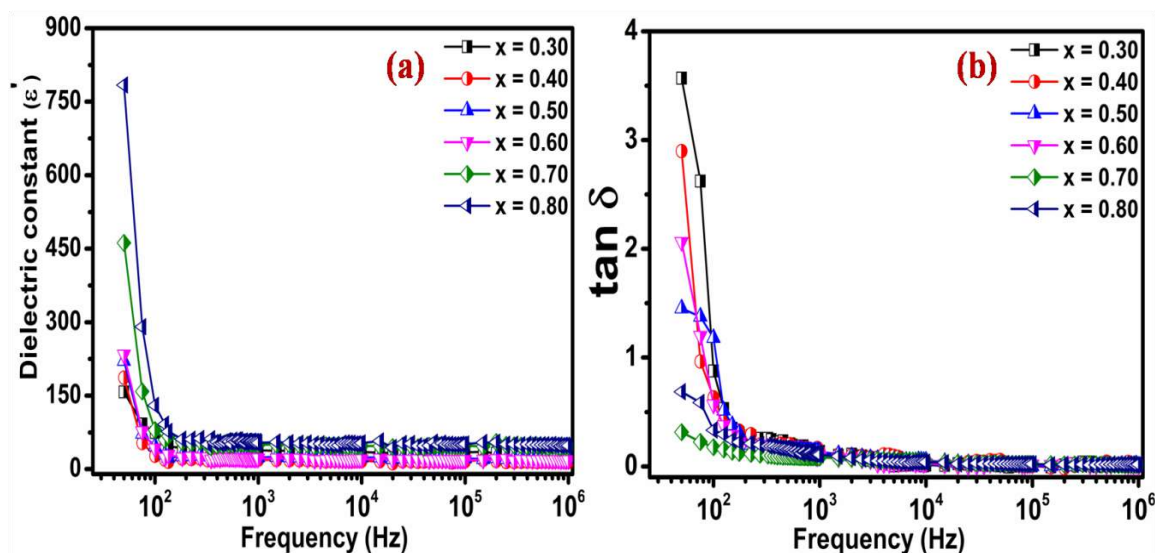


Figure 4.28 Frequency dependence of (a) Dielectric constant (ϵ') and (b) dielectric loss ($\tan \delta$) for $(x) \text{Bi}_{0.5}\text{Na}_{0.5}\text{TiO}_3-(1-x) \text{Ni}_{0.2}\text{Co}_{0.8}\text{Fe}_2\text{O}_4$ ($x = 0.30-0.80$) composites

It is evident from Figure 4.28 that dielectric constant increases with addition of BNT in the composites as expected, clearly indicating the dependence of dielectric properties on BNT phase in the composites. Both ϵ' and $\tan \delta$ are found to decrease sharply in lower frequency regime and remain nearly invariant in high frequency regime. All composites reveal typical dielectric dispersion at low frequencies, which can be ascribed to Maxwell-Wagner interfacial polarization [192, 193 & 232] in accordance with Koop's phenomenological theory [149]. Maxwell-Wagner type interfacial polarization results from the heterogeneity of composites consisting of ferroelectric regions enclosed by ferrite regions.

These two regions have different conductivities. When they are in contact with each other, it results to formation of uncompensated charges at the interface known as the space charges. These charges are responsible for generation of polarization in the material known as space charge or interfacial polarization. While sintering, composites lose few oxygen traces. On cooling them, reoxidation is limited at the surface and near grain/grain boundary interface [233]. When AC electric field operates electrons pile up at insulating grain boundaries resulting into space charge or interfacial polarization. This polarization is responsible for high value of dielectric constant at lower frequencies. With increase in frequency of external AC field, electrons are not able to follow the AC field's variation and are not able to collect at the grain boundaries, thereby decreasing the dielectric constant. This dielectric behaviour can also be interpreted on the basis of polarization mechanism analogous to conduction process in ferrites. The presence of Fe³⁺ and Fe²⁺ ions have made ferrites dipolar. The electron hopping between Fe²⁺ and Fe³⁺ sites is the main conduction mechanism in ferrites. When the frequency of applied AC electric field is lesser than the hopping frequency of electrons amid Fe³⁺ and Fe²⁺ ions, electrons pile up at grain boundaries giving rise to polarization in the composites. As the frequency of AC electric field becomes greater than the hopping frequency of electrons, electron hopping becomes out of phase with the applied field and polarization value decreases [94]. The dielectric loss also displays same trend as observed for dielectric constant. Two processes contribute to dielectric loss: relaxation and resistive loss. In relaxation loss, dipole relaxation is the source of energy dissipation. In resistive loss energy is consumed by mobile charges present in ceramics. In lower frequency regime, higher loss may be attributed to resemblance amidst hopping frequency of electrons among Fe²⁺ and Fe³⁺ ions and frequency of external AC field. In higher frequency regime, the hopping frequency of electron exchange cannot match the applied field above particular frequency and loss becomes minimum [218].

The variation of dielectric constant (ϵ') with temperature for (x) BNT/(1-x) NCFO (x = 0.30–0.70) composites, measured at frequencies of 1, 5 and 10 kHz is shown in Figure 4.29. We observe two dielectric anomalies for pure BNT denoted by T_d and T_C respectively, as discussed in section 4.3.2. We observe T_d at around 170 °C and T_C at 360 °C for BNT at 1 kHz. It is evident from Figure 4.29 that the transition peak (T_C) for BNT

and the composites is broad and frequency dependent.

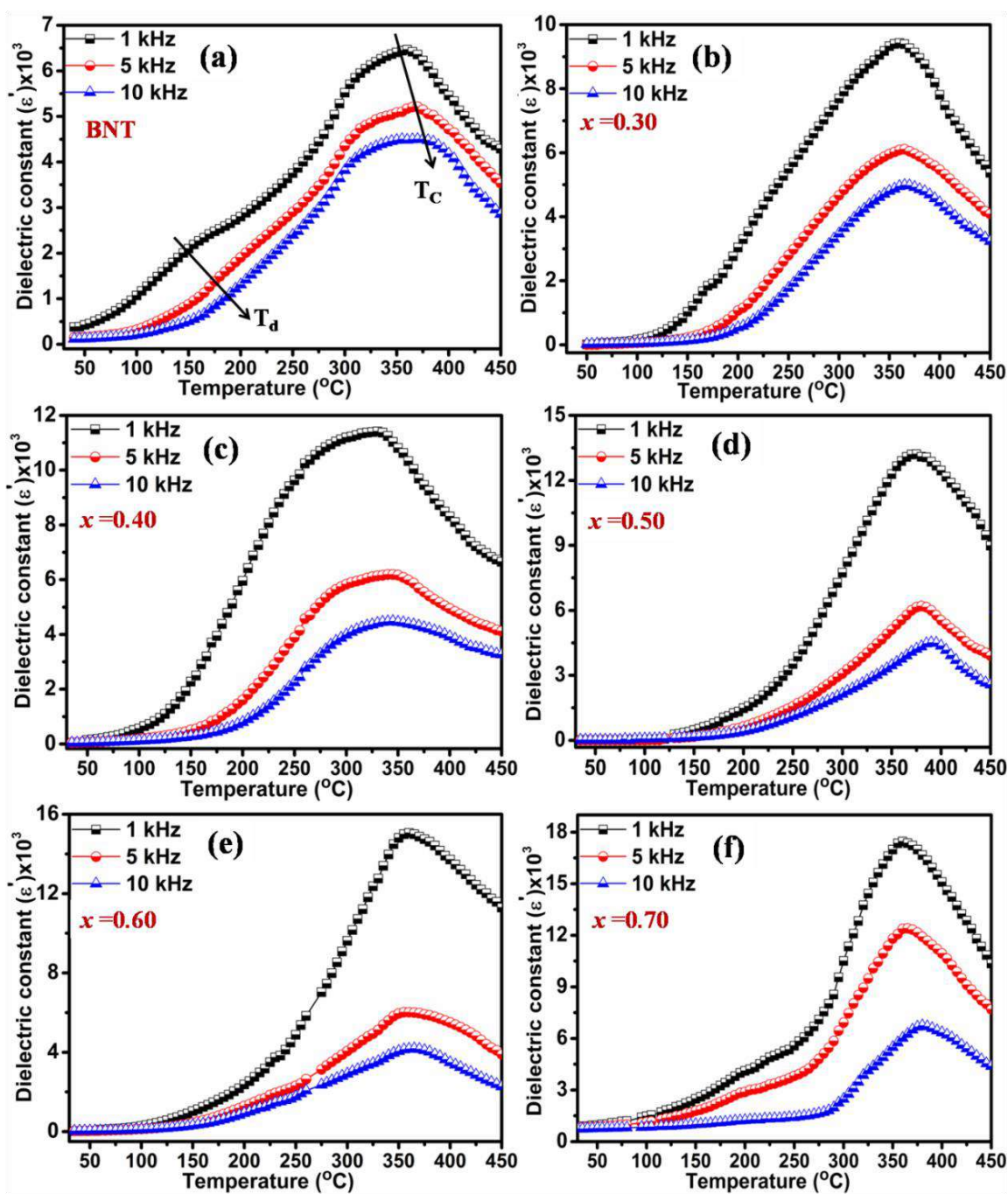


Figure 4.29 Temperature dependence of dielectric constant for $(x) \text{Bi}_{0.5}\text{Na}_{0.5}\text{TiO}_3-(1-x) \text{Ni}_{0.2}\text{Co}_{0.8}\text{Fe}_2\text{O}_4$ (a) BNT, (b) $x = 0.30$, (c) $x = 0.40$, (d) $x = 0.50$, (e) $x = 0.60$ and (f) $x = 0.70$ composites

We also observe very small frequency dispersion at low temperatures in Figure 4.29, which may be attributed to lack of dynamics [234]. With increase in x from 0.40 – 0.70 the anomaly T_d is not observed. This may be attributed to lower crystallinity, existing at sintering temperature of the composite samples [235]. Dielectric constant is found to increase with addition of BNT in the composites, indicating the dependence of dielectric properties on BNT content. Increase in dielectric constant with addition of BNT may be attributed to increase in the number of dipoles contributing to dielectric polarization, since the composite comprised of ferroelectric phase dispersed in the matrix of ferrite phase [236]. The variation of dielectric loss ($\tan \delta$) with temperature for (x) BNT/($1-x$) NCFO ($x = 0.30-0.70$) composites, measured at frequencies of 1, 5 & 10 kHz is shown in Figure 4.30 (a-f).

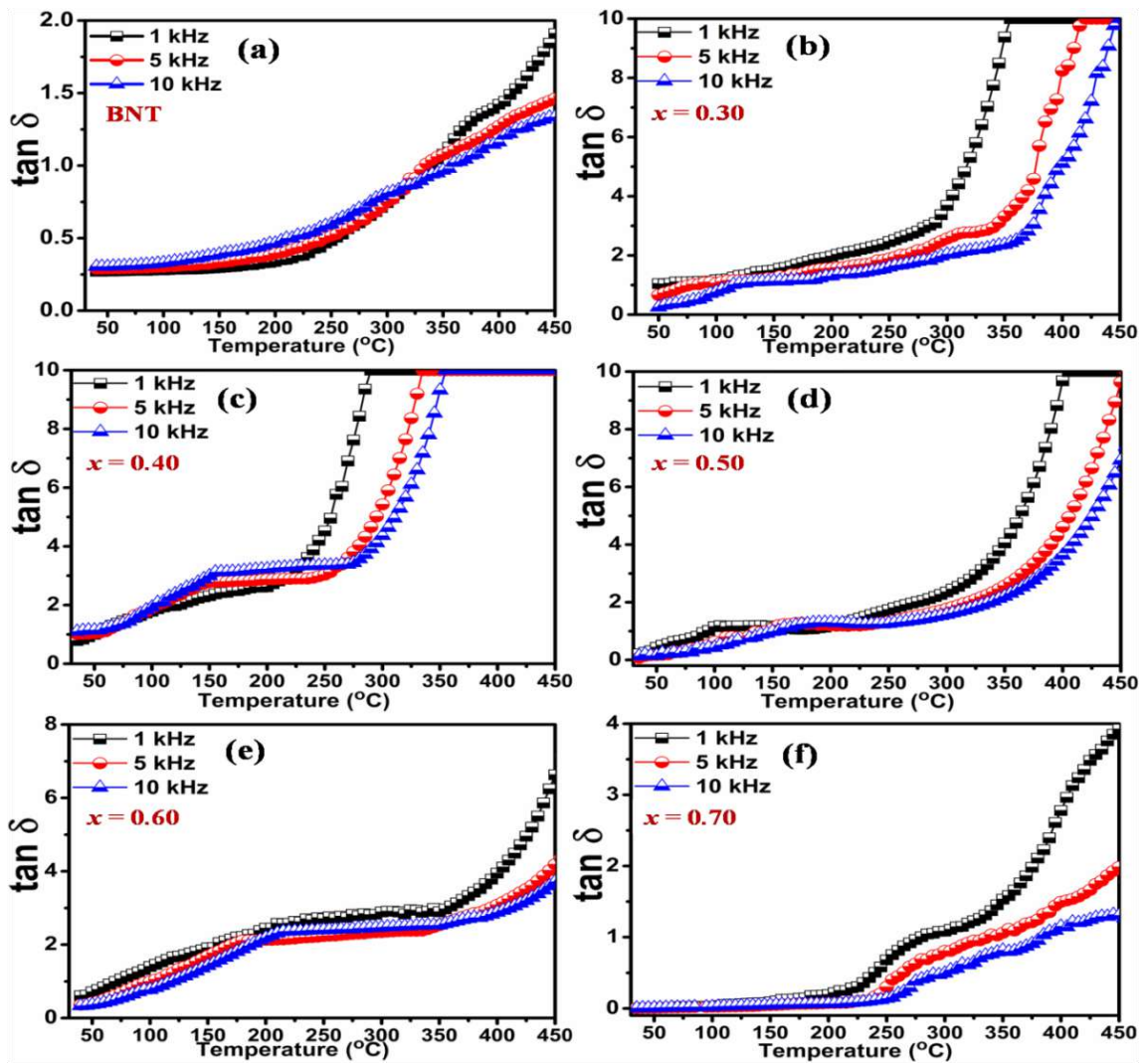


Figure 4.30 Temperature dependence of dielectric loss for (x) $\text{Bi}_{0.5}\text{Na}_{0.5}\text{TiO}_3$ -($1-x$) $\text{Ni}_{0.2}\text{Co}_{0.8}\text{Fe}_2\text{O}_4$ (a) BNT, (b) $x = 0.30$, (c) $x = 0.40$, (d) $x = 0.50$, (e) $x = 0.60$ and (f) $x = 0.70$ composites

Dielectric loss is found to decrease with increase in frequency of the applied field. This variation is related in accordance with Koop's phenomenological model [237]. Higher dielectric loss at lower frequencies arises possibly due to resemblance amidst hopping frequency of electrons among Fe^{2+} and Fe^{3+} ions and that of applied AC field. At higher frequencies the hopping frequencies of electron exchange are not synchronized with the frequency of the applied electric field, consequently minimizing the loss [218]. Moreover, $\tan \delta$ is found to increase with temperature, which is accredited to increase in conduction through residual and absorption current [101]. We observe a decrease in $\tan \delta$ with addition of BNT in the composites. This is attributed to Maxwell-Wagner polarization occurring at the interface [238, 239].

The magnetic characteristics of $(x) \text{Bi}_{0.5}\text{Na}_{0.5}\text{TiO}_3-(1-x) \text{Ni}_{0.2}\text{Co}_{0.8}\text{Fe}_2\text{O}_4$ ($x = 0.30-0.80$) composites are studied at room temperature using VSM with applied magnetic field in the range $-10 \text{ kOe} \leq H \leq 10 \text{ kOe}$ and are shown in Figure 4.31 (a-c).

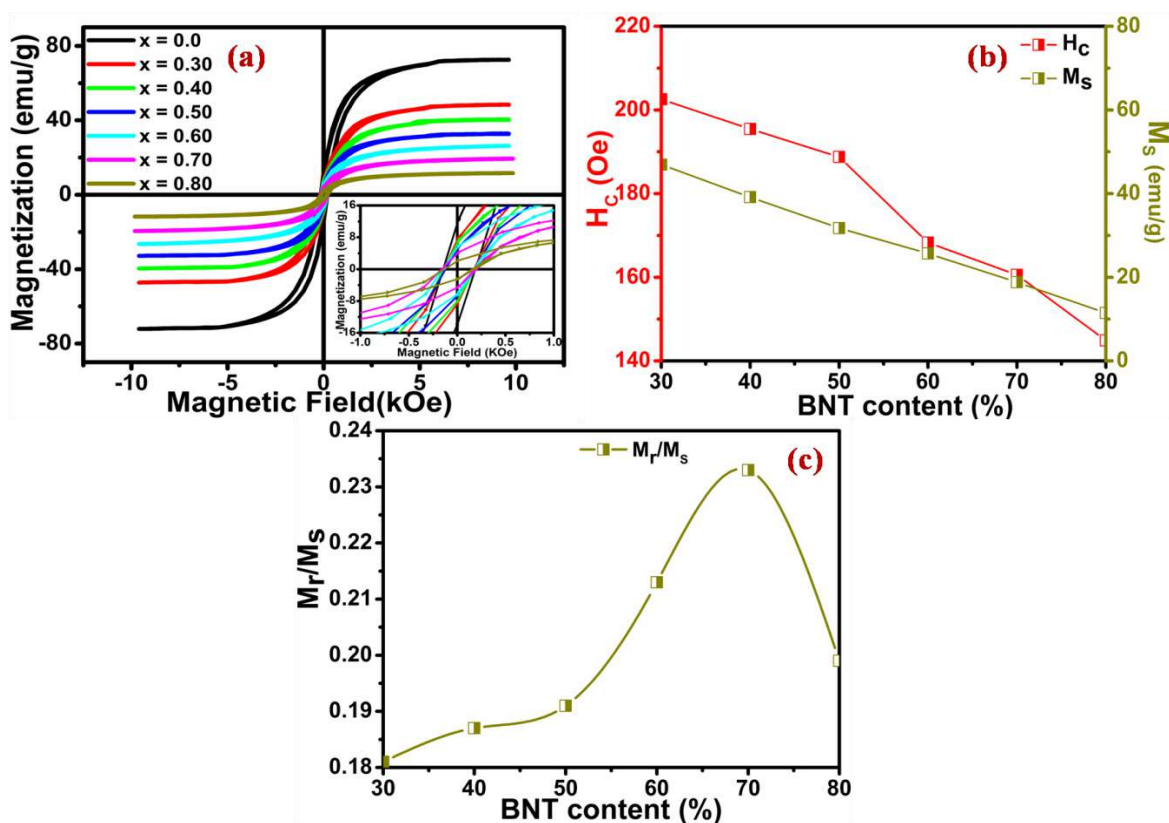


Figure 4.31 (a) M-H hysteresis loops of $(x) \text{Bi}_{0.5}\text{Na}_{0.5}\text{TiO}_3-(1-x) \text{Ni}_{0.2}\text{Co}_{0.8}\text{Fe}_2\text{O}_4$ ($x = 0.30-0.80$) composites at room temperature. Inset shows magnified image of M-H loops around the origin, (b) variation of coercivity (H_c) and saturation magnetization (M_s) and (c) variation of squareness (M_r/M_s) of composites with BNT content

It is evident from Figure 4.31 (a) that all composites show small hysteresis loops, indicating their soft ferromagnetic nature, analogous to that of NCFO. The values of saturation magnetization (M_s), remnant magnetization (M_r) and coercivity (H_c) are listed in Table 4.9. M_s and M_r are found to decrease with addition of BNT. This is because of the fact that individual ferrite grains act as magnetization centres and the incorporation of ferroelectric material in the ferrite phase act as non- magnetic phase thereby breaking the magnetic circuit, leading to a downturn in the values of magnetic parameters [151]. H_c is found to decrease with increasing BNT concentration in the composites. This may be due to the fact that the interaction between the NCFO grains in the composites becomes weak as the NCFO grains are supposed to be surrounded by BNT grains, as we increase the BNT concentration in the composites. This effectively increases the distance between the magnetic grains of NCFO thereby reducing the interaction strength [240]. Figure 4.31 (c) depicts the variation of squareness (M_r/M_s) of the composites with variation of BNT content. The squareness increases with an increase in BNT concentration and becomes maximum at $x = 0.70$, after which it decreases. This may result from additional nanocrystallite growth. There may be incorporation of magnetization pinning defects arising, because of lattice mismatch between the intergrowing nanocrystallites after the onset of significant crystallite growth at $x = 0.70$. These defects would reduce after increasing the BNT concentration further and results a decrease in squareness.

Table 4.9 Magnetic parameters of (x) $\text{Bi}_{0.5}\text{Na}_{0.5}\text{TiO}_3$ -($1-x$) $\text{Ni}_{0.2}\text{Co}_{0.8}\text{Fe}_2\text{O}_4$ ($x = 0.30$ – 0.80) composites measured at room temperature

Composition (x)	M_r (emu/g)	M_s (emu/g)	H_c (Oe)	M_r/M_s
0.0	13.651	70.685	234.113	0.193
0.30	8.494	46.921	202.55	0.181
0.40	7.303	39.134	195.526	0.187
0.50	6.067	31.753	187.754	0.191
0.60	5.466	25.685	169.294	0.213
0.70	4.382	18.809	160.573	0.233
0.80	2.275	11.427	145.209	0.199

To establish the coupling between electric and magnetic dipoles in the composites, we measured their ME voltage coefficients (α_{ME}). The ME coupling originally emerges from

magnetic-mechanical-electrical interconnection through stress driven transfer at the interface [241]. α_{ME} has been computed for the composites using equation 3.8 following the same procedure as adopted in section 4.3.1. The variation of α_{ME} for the (x) BNT/ $(1-x)$ NCFO ($x = 0.30-0.80$) composites are shown in Figure 4.32. It is evident that α_{ME} increases with DC magnetic field initially up to 4–4.5 kOe and then starts decreasing as we increase the field again to 7 kOe as discussed earlier in section 4.3.1

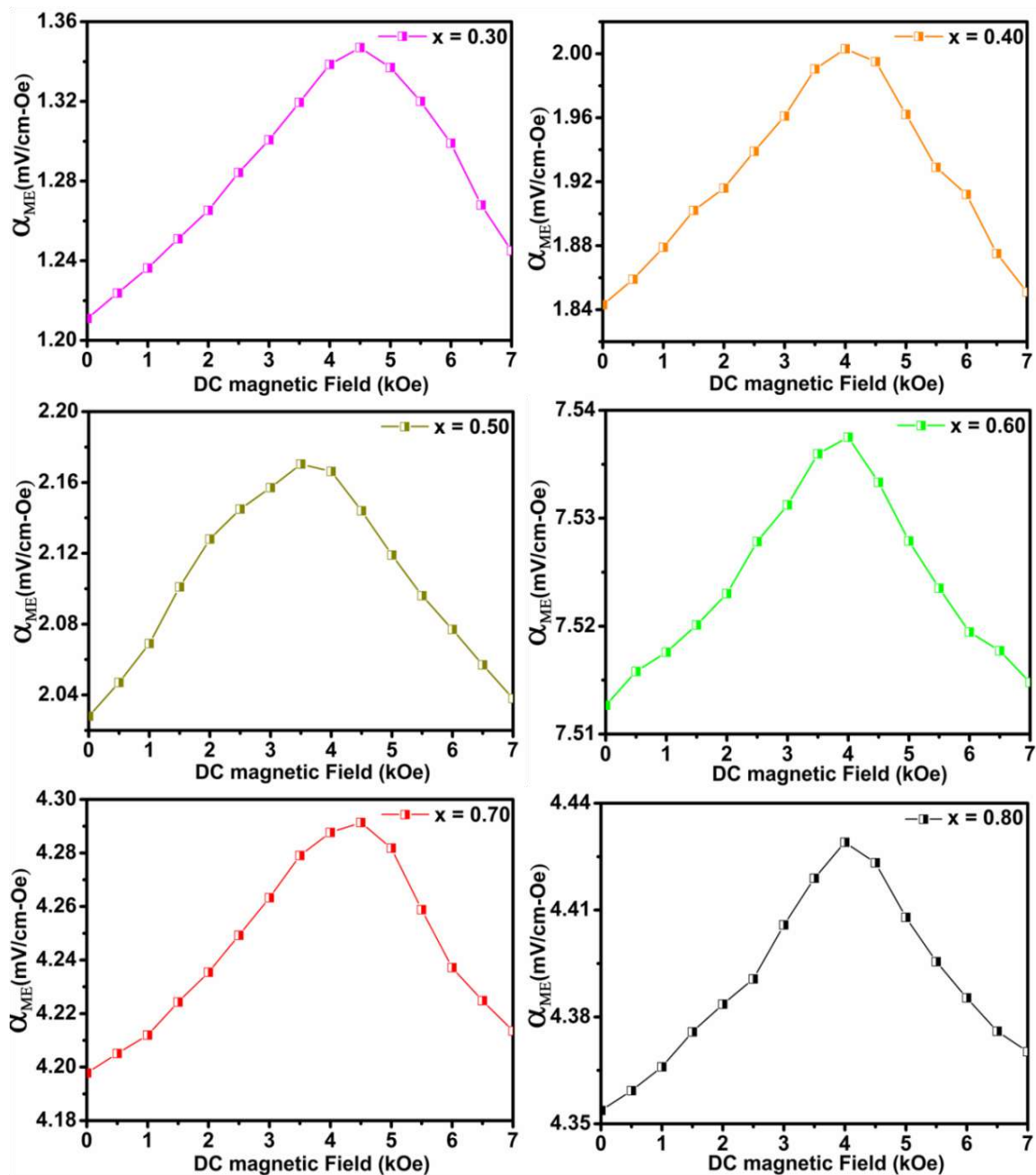


Figure 4.32 Variation of α_{ME} with DC magnetic field for (x) $\text{Bi}_{0.5}\text{Na}_{0.5}\text{TiO}_3$ - $(1-x)$ $\text{Ni}_{0.2}\text{Co}_{0.8}\text{Fe}_2\text{O}_4$ ($x = 0.30-0.80$) composites

The combined plot, representing the variation of α_{ME} is shown in Figure 4.33 (a). We also plotted the variation of maximum α_{ME} with BNT content which is shown in Figure 4.33 (b). It is evident that maximum α_{ME} increases with addition of BNT and reaches a maximum value of 7.538 mV/cm-Oe at $x=0.60$ and then decreases. This variation of α_{ME} may be attributed to the fact that the ME coupling arising in ME composites comprising of piezoelectric and piezomagnetic phases depends on various factors including piezoelectric coefficient, piezomagnetic coefficient and mechanical coupling [144]. The effective α_{ME} of the composites can be significantly affected by connectivity and weight fraction of the constituent phases. A low concentration of ferrite or ferroelectric phase effects in the declination of piezoelectricity or magnetostriction respectively, consequently decreasing α_{ME} as predicted theoretically [110]. Similar behaviour of α_{ME} has been reported earlier [242, 243].

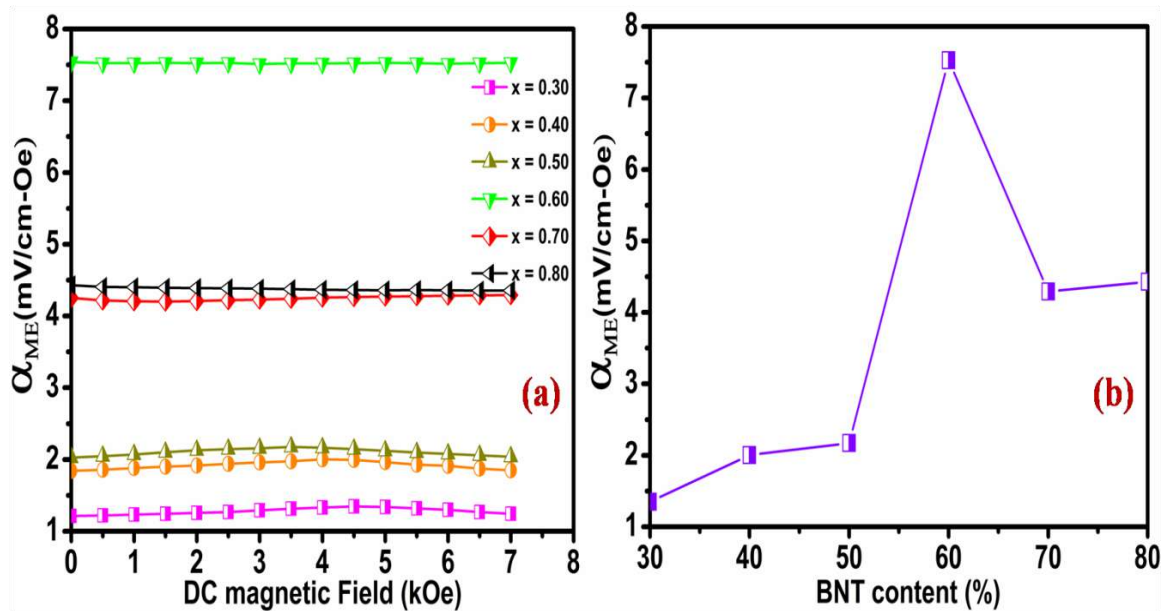


Figure 4.33 (a) Combined plot of ME voltage coefficient, α_{ME} with DC magnetic field for (x) $\text{Bi}_{0.5}\text{Na}_{0.5}\text{TiO}_3$ - $(1-x)$ $\text{Ni}_{0.2}\text{Co}_{0.8}\text{Fe}_2\text{O}_4$ ($x = 0.30$ – 0.80) composites and (b) variation of α_{ME} with BNT content

Figure 4.34 shows the XPS spectra of Ni 2p, Co 2p, Fe 2p and O 1s regions of ferrite phase NCFO. The XPS spectra of Co 2p_{3/2} region comprises of two deconvoluted photopeaks around 778.21 and 779.35 eV corresponding to Co^{2+} at octahedral and tetrahedral sites respectively with a satellite peak around 785.23 eV. The Fe 2p region shows two peaks centred around 710.91 and 724.05 eV corresponding to Fe 2p_{3/2} and Fe 2p_{1/2} states. These two peaks are further deconvoluted to two peaks indicating the presence

of Fe^{2+} and Fe^{3+} oxidation states. The XPS spectra of Ni $2p_{3/2}$ regions consists of two deconvoluted photopeaks centred at 854.23 and 856.48 eV corresponding to Ni^{2+} at octahedral and tetrahedral sites respectively [229].

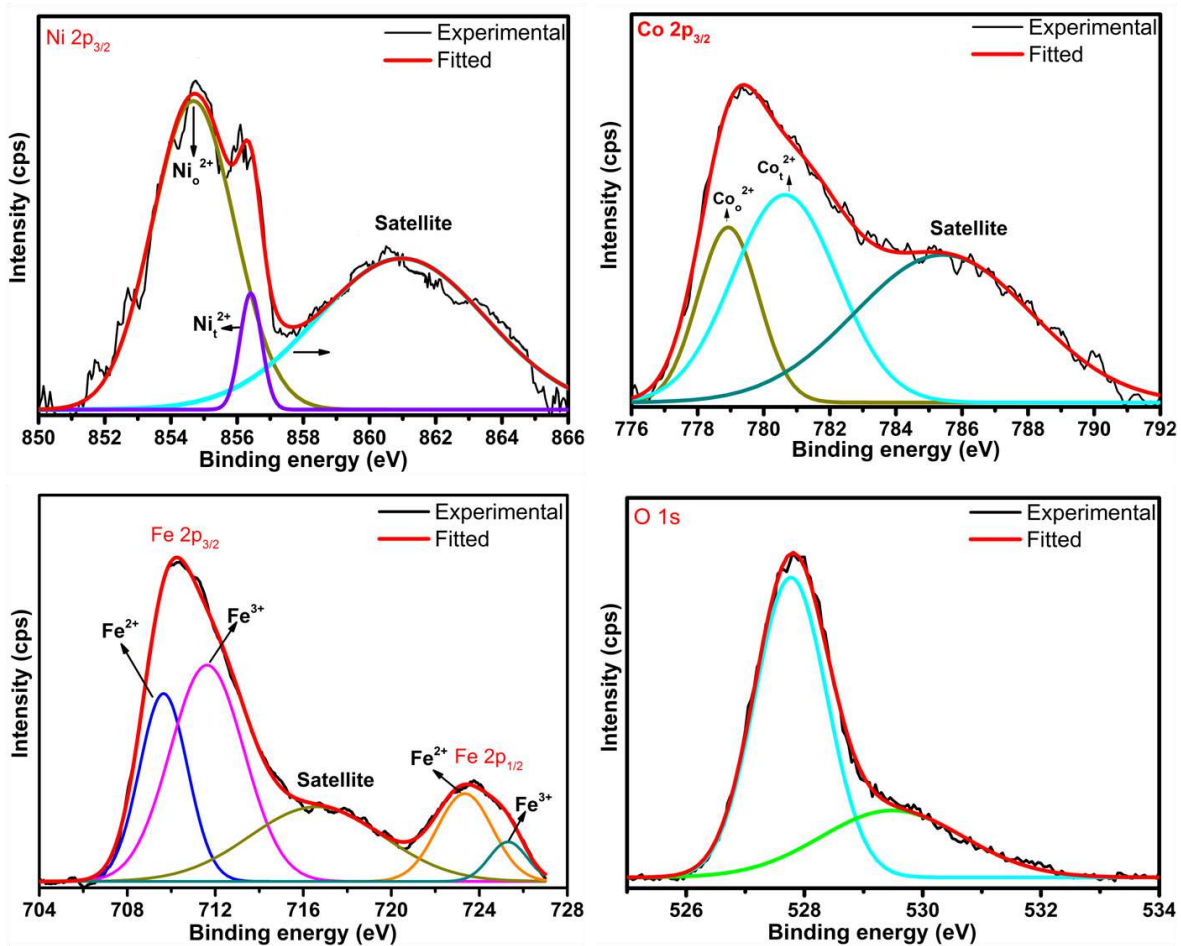


Figure 4.34 XPS spectra of Ni $2p_{3/2}$, Co $2p_{3/2}$, Fe $2p_{3/2,1/2}$ and O $1s$ for $\text{Ni}_{0.2}\text{Co}_{0.8}\text{Fe}_2\text{O}_4$

4.4 Summary

The ME composites (x) $\text{Co}_{0.8}\text{Zn}_{0.2}\text{Fe}_2\text{O}_4-(1-x)$ $\text{Bi}_{0.5}\text{Na}_{0.5}\text{TiO}_3$ ($x = 10, 20, 30, 40, 50$ wt.%) equivalently denoted as CZF/BNT comprising of CZF as ferrite phase and BNT as ferroelectric phase were synthesized using solid state reaction method. XRD analysis confirms the presence of both the constituent phases in the composites. Average grain size of the composites determined from FE-SEM micrographs was found to decrease with addition of CZF phase in the composites. Variation of dielectric constant with temperature signifies a broad phase transition peak which shifts towards low temperature side with addition of CZF. P-E and M-H hysteresis loops obtained at room temperature indicate the presence of ferroelectric and magnetic ordering in the composites. Impedance analysis suggests the NTCR behaviour of the composites and indicates bulk and grain boundary

contribution to the overall electric properties. The composites also exhibited ME coupling which was confirmed by measuring ME voltage coefficient (α_{ME}) with maximum α_{ME} of 7.11 mV/cm-Oe ($x = 10$ wt.%) . The obtained results imply that these composites may be useful for device based applications.

The ME composites $(1-x)$ Bi_{0.5}Na_{0.5}TiO₃- (x) CoMn_{0.2}Fe_{1.8}O₄ ($x = 0, 0.10, 0.20, 0.30, 0.40$ and 0.50) equivalently denoted as BNT/CMFO comprising of BNT as ferroelectric and CMFO as ferrite phase were synthesized successfully using conventional SSR method. Average grain size was computed using FE-SEM micrographs and was found to decrease with addition of CMFO. Temperature dependent dielectric study exhibits two dielectric anomalies corresponding to phase transition temperatures of BNT one of which is broad and frequency dependent which indicates the relaxor behaviour. The dielectric constant was found to decrease with addition of CMFO. P-E and M-H hysteresis loops obtained at room temperature indicate the presence of ferroelectric and magnetic ordering in the composites. Addition of CMFO significantly improves the magnetization but lowers the polarization and coercive field (E_C). The composites also exhibit room temperature ME coupling which was found to decrease with addition of CMFO.

The ME composites (x) Bi_{0.5}Na_{0.5}TiO₃- $(1-x)$ Ni_{0.2}Co_{0.8}Fe₂O₄ ($x = 0.30-0.80$) equivalently denoted as BNT/NCFO were synthesized successfully using conventional SSR method. XRD analysis confirms the mixed spinel-perovskite phase of the composites. FE-SEM micrographs indicate the fairly dense micrographs comprising of both the constituent phases in the composites. Frequency and temperature dependent dielectric study indicates that the magnitude of dielectric constant (ϵ') increased and dielectric loss ($\tan \delta$) decreased with addition of BNT. The magnetic properties of the composites were diluted with addition of BNT as expected. ME coupling in the composites was found to enhance with addition of BNT up to $x = 0.60$ and highest α_{ME} of 7.538 mV/cm-Oe was obtained. The enhanced dielectric and magnetolectric properties of the obtained composites may be useful in device based applications.

Chapter 5

Synthesis and Characterization of BaFe₁₂O₁₉ based Magnetolectric Composites

This chapter has been published in the form of following paper:

- (1) Investigation of magnetolectric effect in lead free K_{0.5}Na_{0.5}NbO₃ – BaFe₁₂O₁₉ novel composite system, Yogesh Kumar, K.L. Yadav, Jyoti Shah, R.K. Kotnala, **Journal of Advanced Ceramics (2019) 8 (3): 333-344.**

5.1 Introduction

In this contemporary era of device miniaturization and device multi-functionality, magnetolectric (ME) composites have enticed the science fraternity towards themselves owing their large ME coupling with respect to their single phase counterparts. Presence of large ME effect in composite materials has compelled the researchers to exploit their use in diverse applications including: spintronic devices [8, 244], high sensitivity magnetic field sensors [245], sensors and transducers [246, 247], electric field controlled ferromagnetic resonance devices [248]. Large scale applications of ME composites given their high ME coupling than single phase materials make them a beguiling research concern. ME coupling in the composites is basically a product property arising due to combination of magnetostrictive (magnetic/mechanical) phenomena in ferrite and piezoelectric (mechanical/electrical) phenomena of ferroelectric phases respectively [249]. Low value of ME coupling in single phase materials as compared to their ME composite counterpart, opens wider prospects for evolution of the latter. In late years focus has been laid on synthesis and development of lead-free ME composites, due to environmental and health related concerns posed by lead based ME composites.

Barium ferrite is basically an M-type ferrite with general formula BaFe₁₂O₁₉ (BHF). It is largely used as hard magnetic material since it was firstly proposed by Smit [250]. The M-type hexaferrites are widely studied materials due to their unique physical properties. The crystal structure of BHF is described by *P6₃/mmc* (No. 194) space group. These ferrites are generally termed as hard ferrites because of their high electrical resistivity, saturation magnetization, coercivity and mechanical hardness [251]. At higher frequencies,

hexaferrites have low-eddy current losses and high resistivity as compared to other magnetic materials [252]. Moreover they have high Curie temperature, decent chemical stability and corrosion resistivity [253, 254]. Also they are ferrimagnetic systems having larger magnetostrictive nature [255]. In the previous years, distinct lead-free composites comprising of BaFe₁₂O₁₉ as a constituent phase including 0.9BaTiO₃-0.1Ba_(1-x)Sr_xFe₁₂O₁₉ [256], 0.5BaFe₁₂O₁₉-0.5Na_{0.5}Bi_{0.5}TiO₃ [257], BaTiO₃-BaFe₁₂O₁₉ [258], Na_{0.5}Bi_{0.5}TiO₃-BaFe₁₂O₁₉ [259], (BaFe_{11.9}Al_{0.1}O₁₉)_{1-x}-(BaTiO₃)_x [260] etc. are studied. In order to obtain significant ME effect, an appropriate combination of ferrite and ferroelectric phase is a necessary requirement. To achieve this we have synthesized and studied the BaFe₁₂O₁₉ based ME composites including (1-x) (K_{0.5}Na_{0.5})NbO₃-(x) BaFe₁₂O₁₉ [(1-x)KNN/(x)BHF].

(K_{0.5}Na_{0.5})NbO₃ (KNN) is considered as outstanding lead free piezoelectric ceramic owing to its improved ferroelectric, dielectric and piezoelectric properties. KNN has large piezoelectric longitudinal response and a high planar coupling coefficient ($k_p \sim 45\%$) [138-139]. Moreover it also shows large remnant polarization and coercive field [119]. On the other hand, BHF is an excellent candidate for ferrite phase due to its outstanding properties discussed above. Also very few reports are available on the ME composites having BHF as ferrite phase and KNN as ferroelectric phase. Keeping the above facts in mind, in this chapter we present the synthesis and organized study of the structural, dielectric, magnetic and magnetolectric properties of (1-x) (K_{0.5}Na_{0.5})NbO₃-(x) BaFe₁₂O₁₉ (x = 30, 40 and 50 wt.%) novel ME composite system.

5.2 Experimental Details

5.2.1 Synthesis of (1-x) (K_{0.5}Na_{0.5})NbO₃-(x) BaFe₁₂O₁₉ novel ME composite system with x = 30, 40 and 50 wt. %

Novel lead-free ME composites viz. (1-x) (K_{0.5}Na_{0.5})NbO₃-(x) BaFe₁₂O₁₉ (x = 30, 40 and 50 wt.%) were synthesized using conventional solid state reaction method. Ferroelectric phase (K_{0.5}Na_{0.5})NbO₃ was synthesized using solid state reaction method as discussed in section 3.2.1. Ferrite phase BaFe₁₂O₁₉ was synthesized with sol-gel method, employing Barium nitrate Ba(NO₃)₂ (99 %, Himedia, India) Ferric nitrate Fe (NO₃)₃.9H₂O (98 % Himedia, India), citric acid and ethylene glycol as starting materials. Initially Barium nitrate and Ferric nitrate were mixed in appropriate molar proportions in aqueous

solution of citric acid prepared in distilled water. The mixture was continuously stirred at 80 °C to get a homogeneous solution. Then ethylene glycol was added to the solution with a proportion of citric acid/ethylene glycol in the ratio of 70:30. This solution was then transformed into xerogel, which started to swell thereby producing a foamy precursor. The obtained xerogel was then dried in hot air oven at 120 °C for 12 h. The obtained powder from xerogel was then pre sintered at 900 °C for 3 h in air atmosphere to obtain the desired phase. The desired (1- x) (K_{0.5}Na_{0.5})NbO₃-(x) BaFe₁₂O₁₉, ME composites were then synthesized by mixing the obtained KNN and BHF powders in different wt.% ratios: 70:30, 60:40 and 50:50. The obtained composite powders were then shaped in the form of cylindrical pellets (10 mm diameter and thickness between 1-2 mm) using hydraulic press and then sintered in air atmosphere at optimized temperature of 1050 °C for 3 h.

5.2.2 Characterizations

Phase formation and structural characterizations of the composites was examined with X-ray diffractometer (Bruker D8 X-ray Advance) with Cu K α radiation ($\lambda = 1.5432 \text{ \AA}$), in a wide Bragg angle range ($20^\circ \leq 2\theta \leq 60^\circ$). Field emission scanning electron microscopy (FE-SEM), Carl Zeiss operating at an accelerating voltage of 15 kV was used to study the surface morphology and microstructures of the composites. For measurement of electrical properties, electrical contacts on the samples were made by coating both the flat surfaces of the pellets with high purity silver paste and then drying them at 150 °C for 1 h. The dielectric measurements including dielectric constant (ϵ') and dielectric loss ($\tan \delta$) were studied, using HIOKI-3532-50 Hi Tester LCR meter in the temperature range of 30–500°C at a ramp rate of 2 °C/min and at a measuring electric field of 1 Volt. Ferroelectric properties of the composites were measured at room temperature using modified Sawyer-Tower circuit (automated Marine India P-E loop tracer). Complex impedance analysis was done at room temperature by using HIOKI LCR meter in a wide frequency range of 100 Hz–1 MHz. The room temperature magnetic properties of the composites were measured using vibrating sample magnetometer (VSM) Quantum Design, PAR 15) in the magnetic field range of $-10 \text{ kOe} \leq H \leq +10 \text{ kOe}$. The temperature dependent magnetization in field cooled (FC) and zero field cooled (ZFC) modes was measured using superconducting quantum interference device (SQUID) from 5 K to 300 K at 1 kOe. ME coupling in the composite samples was confirmed by measuring ME voltage coefficient (α_{ME}) employing dynamic method using an in house built measurement setup.

5.3 Results and Discussions

The XRD patterns of $(1-x)$ (K_{0.5}Na_{0.5})NbO₃- (x) BaFe₁₂O₁₉ ($x = 30, 40$ and 50 wt.%) ME composite system, along with that of pure KNN and BHF phases are shown in Figure 5.1.

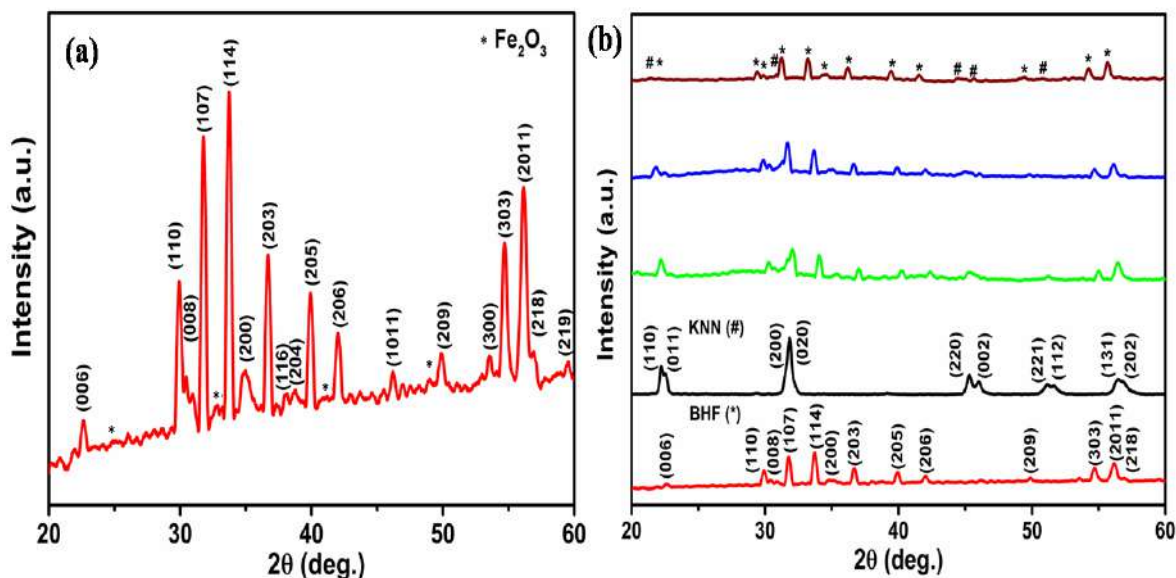


Figure 5.1 XRD patterns of $(1-x)$ (K_{0.5}Na_{0.5})NbO₃- (x) BaFe₁₂O₁₉ (a) Pure BaFe₁₂O₁₉ and (b) ($x = 30, 40$ and 50 wt.%) composites along with individual KNN and BHF phases where (hash, #) represents KNN and (asterisk,*) represents the BHF phase

XRD peak indexing for composite samples agrees with reported KNN [145] having perovskite orthorhombic structure with space group *Amm2* and BHF (JCPDS card 84 - 0757) having hexagonal structure with space group *P6₃/mmc*. XRD patterns of the composite samples assert that all the peaks corresponding to both the constituent phases are present and absence of impurity traces confirm that both the constituent phases have retained their identity in the composites, thereby confirming their efficacious synthesis.

The calculated values of lattice parameters of the composite samples and their constituent phases are listed in Table 5.1. The ferrite phase (BHF) has hexagonal structure and ferroelectric phase (KNN) shows perovskite orthorhombic structure. Any particular trend has not been observed for the unit cell parameters with the concentration of individual phases. Since, the composite systems are synthesized from separately prepared individual phases mixed in the required stoichiometry. Also the composite system is not a

single phase, rather it is a mixture of two individual phases. So when we are increasing the wt.% of a particular phase in the composite, it is not affecting the structure as a whole. Consequently, no particular trend is observed in the variation of lattice parameters for the composites. The relative density of the composites is obtained using the experimental and theoretical densities related by equation 3.2 and is listed in Table 5.1

Table 5.1 Lattice parameters, grain sizes and relative densities of (1-x) (K_{0.5}Na_{0.5})NbO₃- (x) BaFe₁₂O₁₉ (x = 30, 40 and 50 wt.%) ME composites

Compositions (x)	Lattice Parameters (Å)					Average grain size (nm)	ρ_{rel} (%)
	BHF		KNN				
	a	c	a	b	c		
KNN	-	-	5.675	5.626	3.948	538.53	91.25
0.30	5.086	23.328	5.656	5.599	3.963	345.53	89.63
0.40	5.037	23.299	5.622	5.575	3.957	317.36	89.21
0.50	5.105	23.434	5.781	5.712	3.981	301.89	88.45
BHF	5.159	23.596	-	-	-	231.93	86.42

Surface morphology of the composite samples has been investigated using field emission scanning electron microscopy (FE-SEM). FE-SEM micrographs of the composites samples along with their constituent phase viz. KNN and BHF are shown in Figure 5.2 (a-e). It is evident from Figure 5.2 that all the composites exhibit homogeneous microstructure. These micrographs confirm the formation of desired composites comprising of both the grains of the constituent phases. It is evident from the micrographs that composites comprise of two distinct phases viz. small hexagonal shaped grains akin to BHF phase and large polygonal shaped grains akin to KNN phase. The purity and assertion of composite formation is revealed from the presence of expected elements (K, Na, Nb, Ba, Fe and O) in the EDAX spectra of x = 40 wt.% composite shown in Figure 5.2 (f).

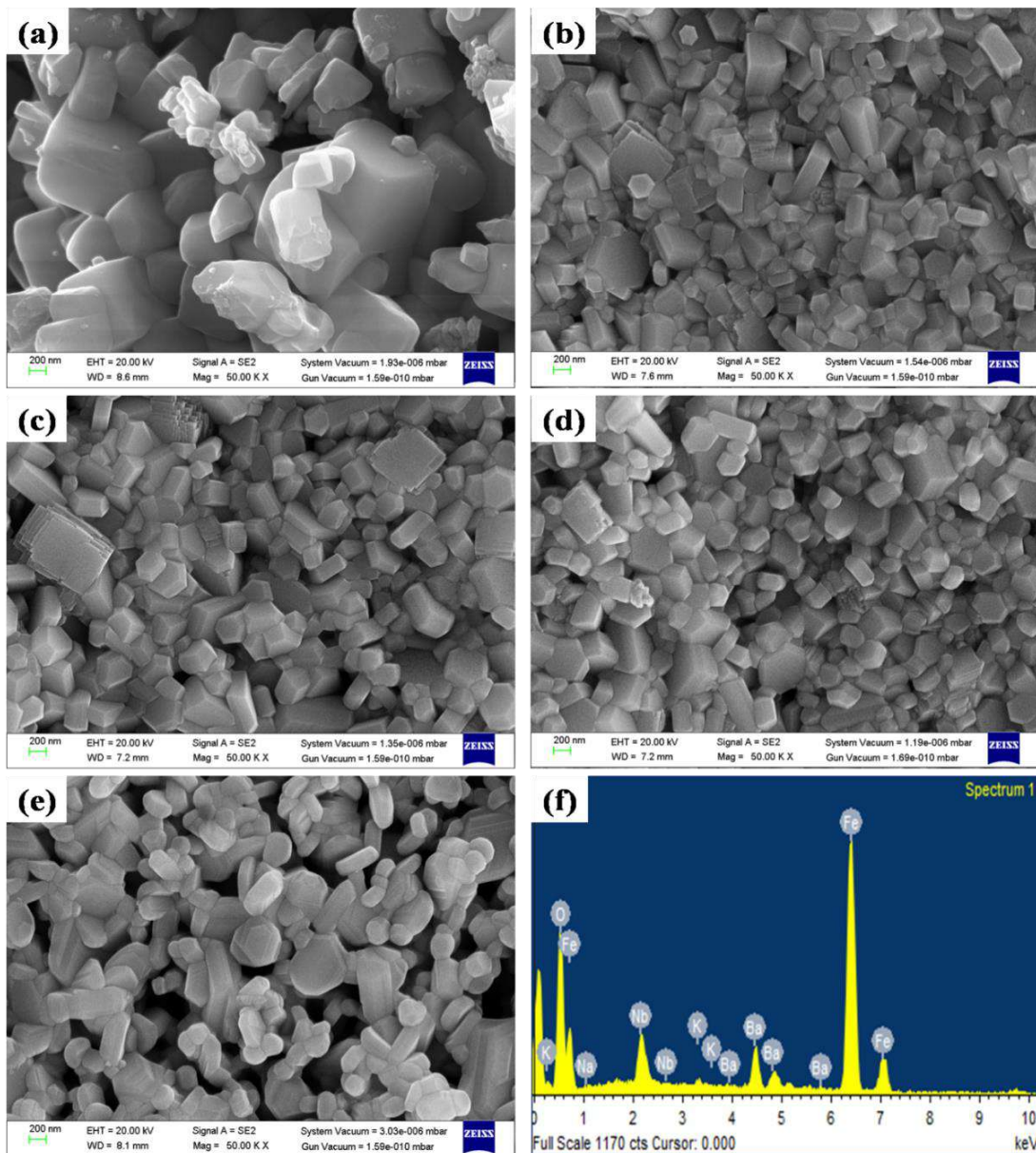


Figure 5.2 FE-SEM micrographs of $(1-x)(K_{0.5}Na_{0.5})NbO_3-x BaFe_{12}O_{19}$ (a) KNN (b) $x = 30$ wt.%, (c) $x = 40$ wt.%, (d) $x = 50$ wt.% composites, (e) BHF and (f) EDAX spectrum of composite with $x = 40$ wt.%

Average grain size of the composite samples has been computed using Image J software and fitted using log-normal distribution as shown in Figure 5.3 (a-e). The average grain size of the composites is found to decrease with addition of BHF in the composites.

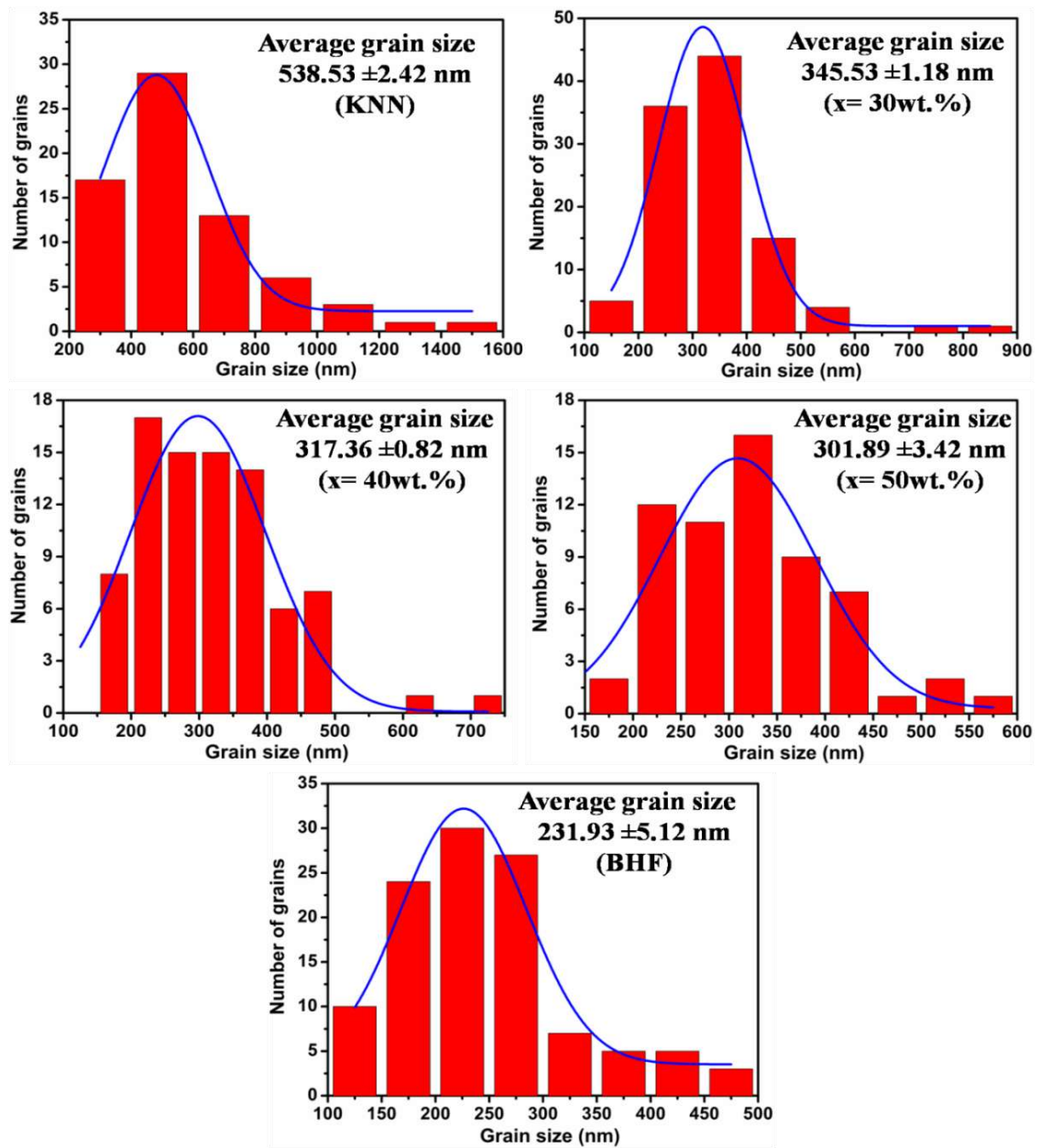


Figure 5.3 Log normal distribution of grain sizes of $(1-x) (K_{0.5}Na_{0.5})NbO_3-(x) BaFe_{12}O_{19}$ ($x = 30, 40$ and 50 wt.%) ME composites along with pure BHF and KNN phase

The elemental mapping in $(1-x) (K_{0.5}Na_{0.5})NbO_3-(x) BaFe_{12}O_{19}$ for $x = 40$ wt.% composite is shown in Figure 5.4. It displays uniform distribution of K, Na, Nb, Ba, Fe, and O in the synthesized composite system without any trace of impurity indicating the purity of the synthesized composites.

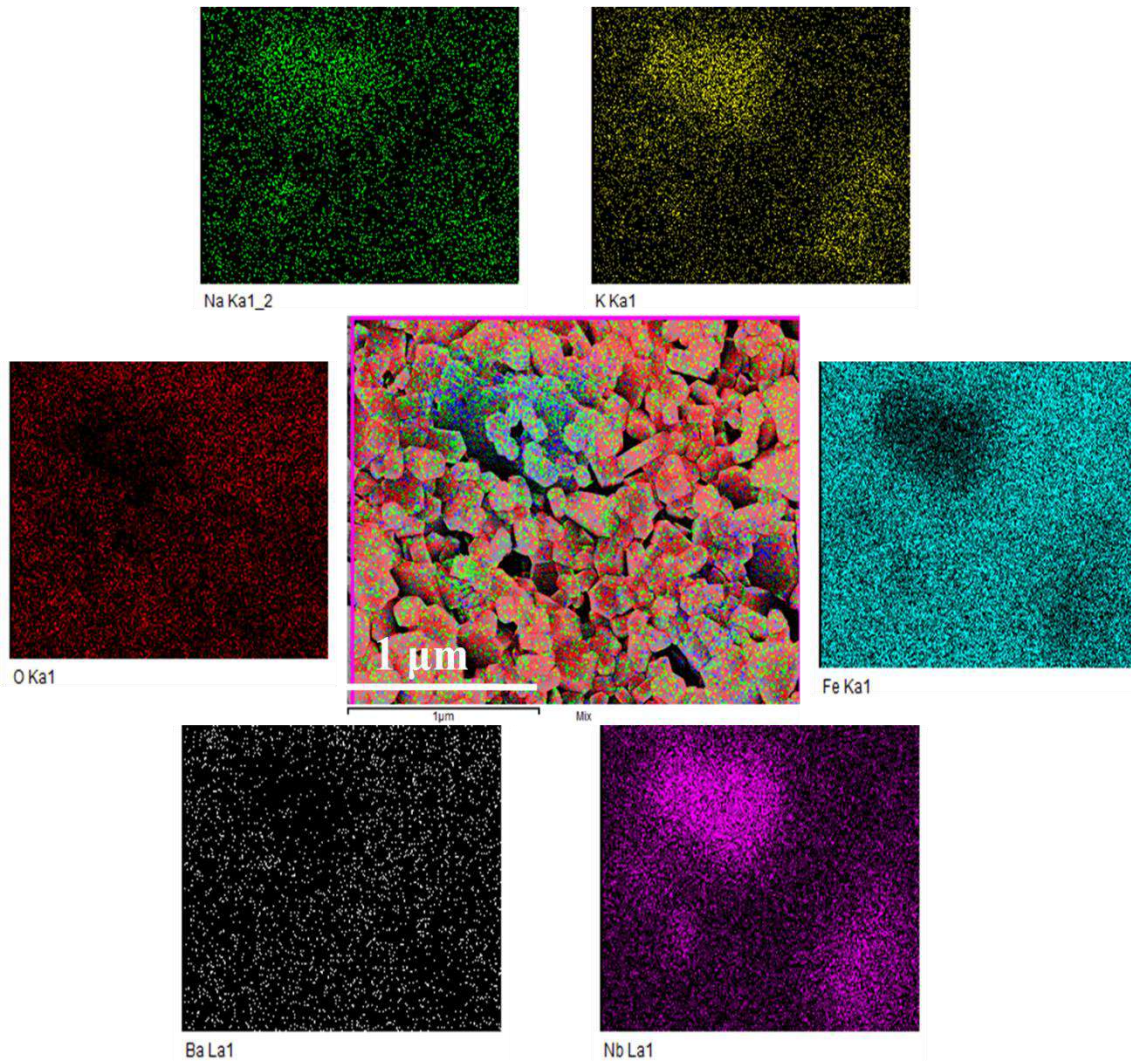


Figure 5.4 Elemental mapping showing distribution of different elements in $(1-x)(K_{0.5}Na_{0.5})NbO_3-(x) BaFe_{12}O_{19}$ composite with $x = 40$ wt.%

The variation of dielectric constant (ϵ') of the $(1-x)(K_{0.5}Na_{0.5})NbO_3-(x) BaFe_{12}O_{19}$ ($x = 30, 40$ and 50 wt.%) composite samples is studied with temperature at three distinct frequencies (1, 5 and 10 kHz) in the temperature range $30-500$ °C. Figure 5.5 (a-e) exhibits the temperature dependence of dielectric constant of the composite samples along with their constituent phases including KNN and BHF. The ferroelectric (KNN) phase exhibits two transition peaks with first peak appearing in temperature range $170 - 200$ °C akin to orthorhombic-tetragonal phase transition (T_{O-T}) and second peak in the high temperature range of $420-440$ °C akin to tetragonal-cubic phase transition (T_C). The temperature dependence of dielectric constant for ferrite (BHF) phase comprises of first transition peak in the range $150-190$ °C and the second transition peak which appears at ~ 455 °C corresponds to ferroelectric – paraelectric like phase transition.

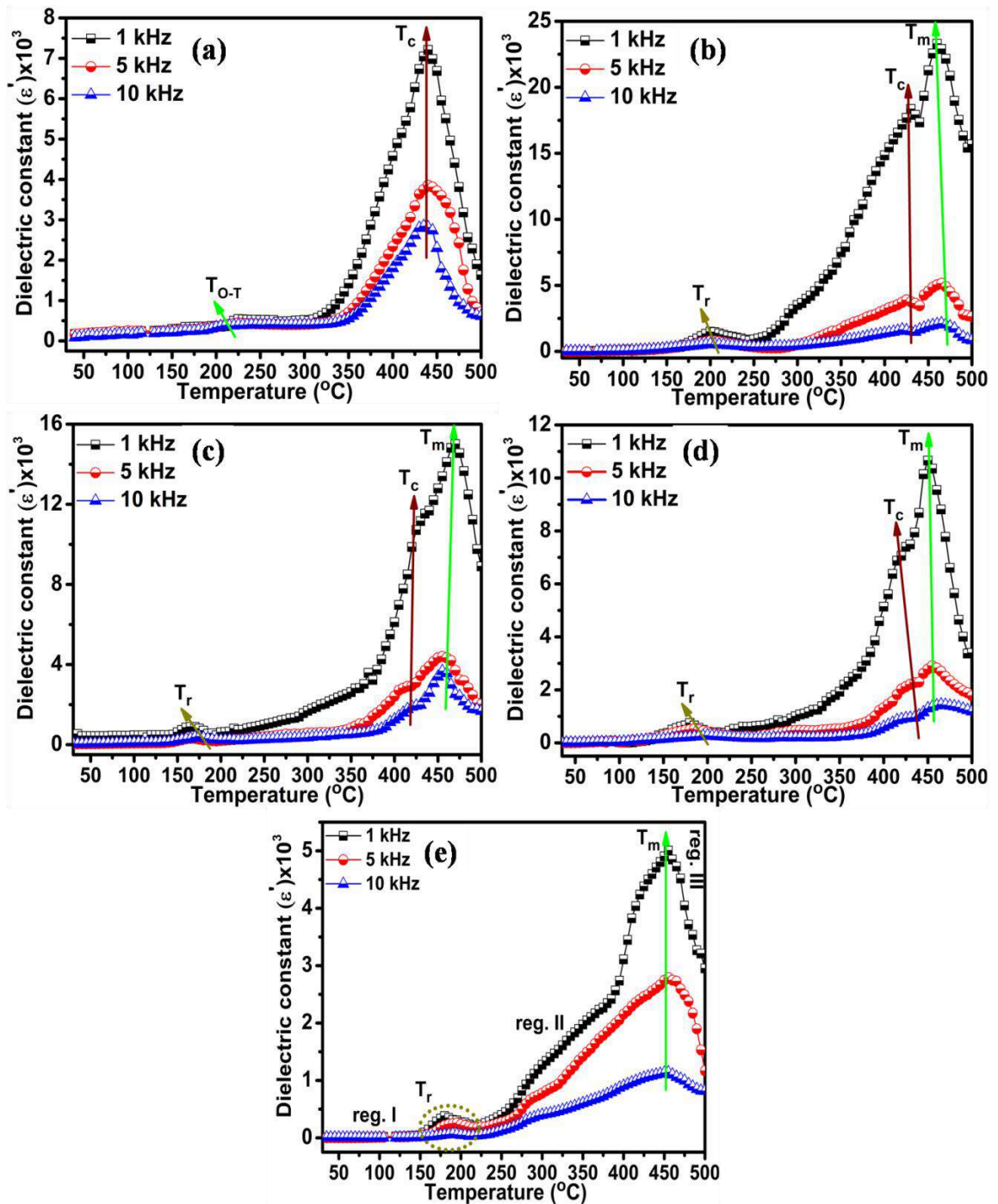


Figure 5.5 Temperature dependence of dielectric constant (ϵ') at various frequencies for $(1-x)(\text{K}_{0.5}\text{Na}_{0.5})\text{NbO}_3-(x)\text{BaFe}_{12}\text{O}_{19}$ (a) KNN, (b) $x = 30$ wt.%, (c) $x = 40$ wt.%, (d) $x = 50$ wt.% composites and (e) BHF

When electric field is applied to BHF, a huge number of dipoles are formed owing to inter ionic hopping via oxygen, giving it a ferroelectric character [261]. The plot of ϵ' vs. T of BHF has been divided into three regions as shown in Figure 5.5 (e). The compositional disorder in the crystal structure gives rise to formation of polar regions [262] thereby

affecting the dielectric behaviour. In region I the polar regions remain frozen at lower temperatures and ϵ' increases with temperature. The increase in temperature initiates the conversion of big polar region to nano size polar regions in order to minimize the thermal energy. During this process ϵ' starts to decrease as evident from region II of Figure 5 (e) giving rise to first peak (T_r). This in particular indicates the relaxor type characteristic of the sample and is not a phase transition. After this ϵ' again increase with temperature owing to existence of large number of nano polar regions. In the nano polar regions, electric dipoles require lower energy to be polarized, thereby giving rise to high ϵ' between regions II and III. On increasing the temperature further, the ordered electric dipoles become disordered owing to surplus of thermal energy consequently causing a sudden decrease in ϵ' with temperature. This peak temperature corresponds to ferroelectric–paraelectric phase transition (T_m) [263]. The obtained results are nearly consistent with the previous reports [264]. Both T_r and T_c are found to increase slightly with frequency. It is interesting to note that BHF exhibits multiferroic character [265, 266]. Therefore we cannot neglect the magnetic phase transition (ferro-paramagnetic) of BHF, which occurs at ~ 445 °C and other appears around 130 °C. These transitions in BHF require further study by measuring temperature dependent magnetization above room temperature.

Figure 5.5 (b-d) shows that the composite samples exhibit transition peaks corresponding to both the constituent phases which are marked by their corresponding symbol in the respective plots. It is evident from Figure 5.5 that dielectric constant decrease with addition of BHF wt.% in the composites. This may be accounted for a decrease in grain size with addition of BHF in the composite samples. It is assumed that the ferroelectric phase has large number of ferroelectric domains separated from each other by domain walls. Number of domain walls and their mobility affects ϵ' [199]. From the point of view of Okazaki and Nagata [200], the grain boundaries and domain walls comprise of space charge sites in a certain amount. These sites are responsible for producing electric field which significantly affects domain walls mobility. When grain size decreases it leads to an increase in surface area of space charge layer, consequently enhancing the space charge field. As a result of this the domain wall motion becomes comparatively arduous and non uniform which is responsible for decrease in dielectric constant.

Figure 5.6 (a-d) exhibits the variation of dielectric constant (ϵ') with frequency for the composite samples at room temperature in the frequency range of 50 Hz-1 MHz. Dielectric constant is found to decrease over whole frequency range having very subtle changes in the

high frequency regime. This type of behaviour in composites may be attributed to Maxwell-Wagner interfacial polarization [192, 193] which gives rise to uncompensated charges at the interface separating two constituent phases of the composites. Grains are less resistive as compared to grain boundaries, thereby favouring the gathering of electrons at grain boundaries on application of external AC field giving rise to space charge polarization. This accounts for higher values of ϵ' at lower frequencies. With increase in frequency further the electrons are not able to align with the frequency of applied field, consequently decreasing the dielectric constant at higher frequencies. Magnitude of ϵ' is found to decrease with increase BHF content from $x = 30$ – 50 wt.%. Similar trend has been reported earlier for other BHF based compounds [267-269].

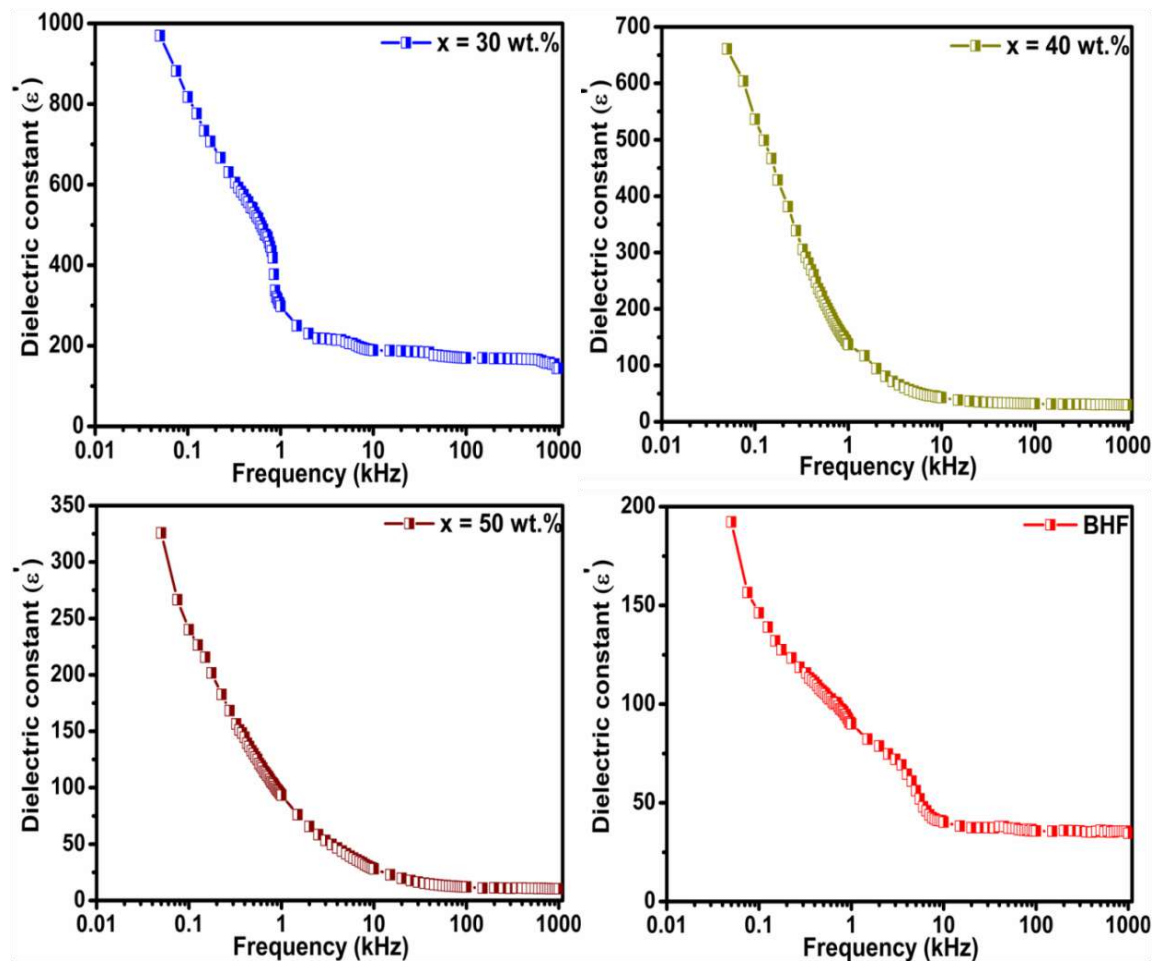


Figure 5.6 Frequency dependence of dielectric constant at room temperature for $(1-x)(\text{K}_{0.5}\text{Na}_{0.5})\text{NbO}_3-(x)\text{BaFe}_{12}\text{O}_{19}$ ($x = 30, 40$ and 50 wt.%) composites

The ferroelectric ordering in the composite samples has been established by measuring P-E hysteresis loops. Figure 5.7 (a-e) exhibits the P-E hysteresis loops of pure KNN and BHF phases along with that of $(1-x)\text{KNN}-(x)\text{BHF}$ ($x = 30, 40$ and 50 wt.%)

composites obtained at 50 Hz frequency and at room temperature.

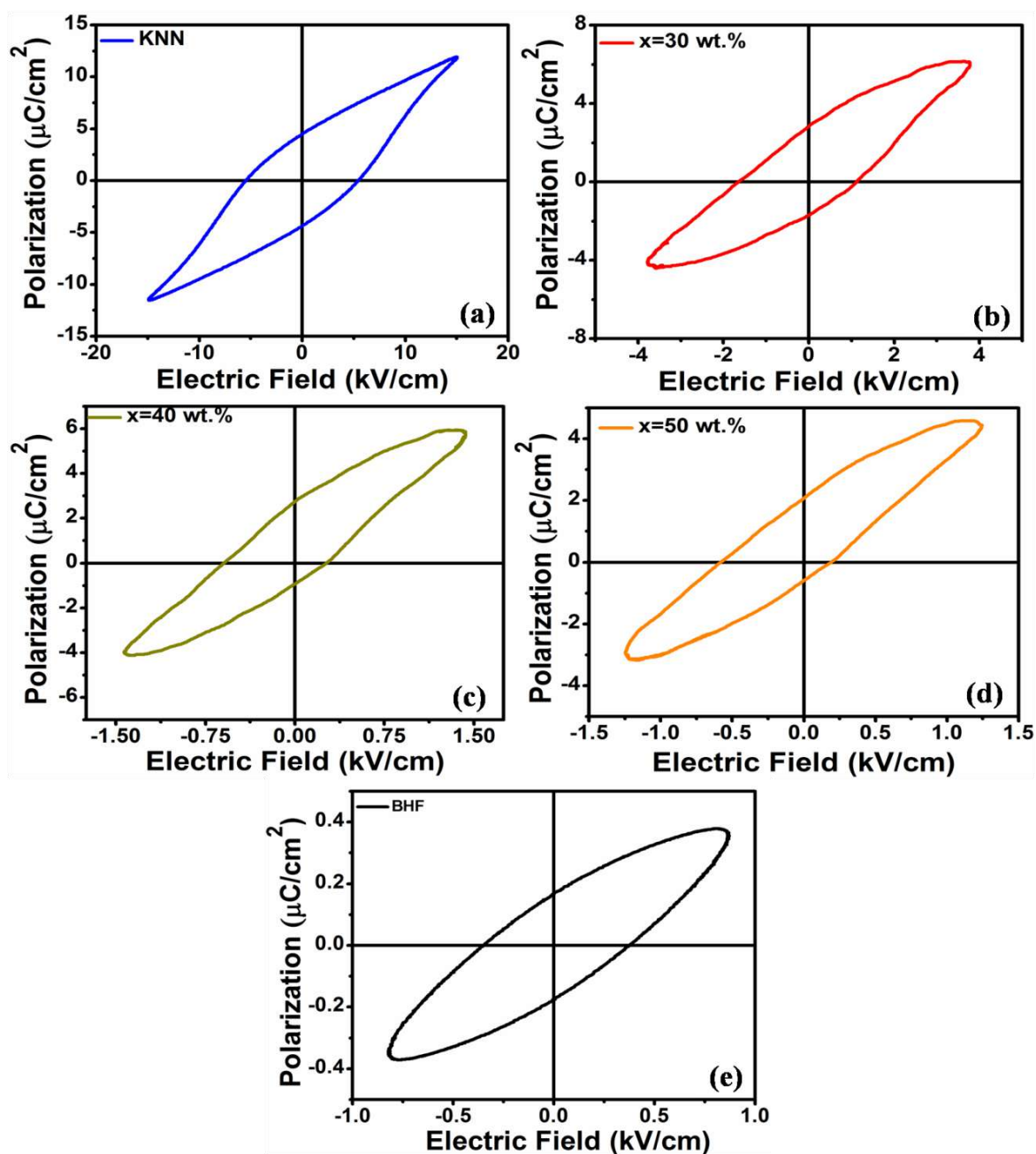


Figure 5.7 P-E hysteresis loops for $(1-x)(K_{0.5}Na_{0.5})NbO_3-(x) BaFe_{12}O_{19}$ (a) KNN, (b) $x = 30$ wt.%, (c) $x = 40$ wt. %, (d) $x = 50$ wt.% composites and (e) BHF obtained at room temperature

The polarization in BHF may be attributed to the change in the central position of Fe in the FeO_6 octahedron of the subunit cell of BHF. Generally Fe is found at the centre of octahedron. When an external field is applied, it gives rise to off center shift for Fe thereby inducing electric polarization [270]. Remnant polarization (P_r) of the composites is found to decrease with BHF wt.%. This may be attributed to enhancement in conductivity,

consequently increasing the leakage current. This behaviour may also be correlated with the Nyquist plots obtained for the composites [Figure 5.12 (a-d)] which provide information about resistance by calculating the intercept made by semicircular arcs on the abscissa axis of Nyquist plots. The resistance is found to decrease with increase in BHF wt.% thereby reducing the electromechanical coupling which consequently lowers P_r [210].

The magnetic characteristics of the (1-x) KNN-(x) BHF (x = 30, 40 and 50 wt.%) composites are studied using M-H hysteresis loops at room temperature at an applied magnetic field of -10 kOe $\leq H \leq$ 10 kOe. Figure 5.8 (a-b) exhibits the M-H hysteresis loops of the composites along with pure BHF phase. As evident from the Figure 5.8 that composite samples and pristine BHF exhibit rapid increase in magnetization at lower fields which further slows down at higher fields and they also not show saturation in magnetization in the applied field range. The saturation magnetization (M_s) of the composites is approximated using law of saturation [271-273] employing following relation between magnetization (M) and magnetic field (H) given by equation 5.1

$$M(H) = M_s \left(1 + \frac{A}{H} + \frac{B}{H^2} \right) + \chi_p H \quad (5.1)$$

Here M_s is the saturation magnetization, χ_p is the high field susceptibility, A/H term is related with inhomogeneities and usually neglected at higher magnetic field and B/H^2 is related to magnetocrystalline anisotropy [273]. The saturation magnetization is computed using equation 5.1 (Table 5.2) and found to increase with addition of BHF in the composite samples. The coercive field (H_c) of the composite samples is also estimated from the M-H hysteresis loops (Table 5.2) and found to decrease with increase in BHF wt.%. The variation of M_s and H_c with BHF content is shown in Figure 5.9 (a). Individual grains of ferrite in the composite samples act as magnetization centres. The net magnetization arises from sum of these individual contributions. The ferrite addition in the composites, strongly enhance the magnetic contacts, consequently increasing the net magnetization. The decreasing trend of H_c may be attributed to change of easy axis of magnetization from c-axis to basal plane which may lower the anisotropic field (H_a) [259, 274]. For Hexagonal ferrites the anisotropic parameter is given using equation 5.2 [275]

$$B = -\frac{1}{15} * H_a^2 \quad (5.2)$$

Here H_a is the anisotropy field, expressed using equation 5.3 [276]

$$H_a = \frac{2K_1}{M_s} \quad (5.3)$$

Here K₁ is the first order anisotropy constant and M_s is the saturation magnetization.

Combining equations (5.1) and (5.3) we get the following equation

$$M(H) = M_s \left(1 - \frac{4K_1^2}{15M_s^2 H^2} \right) + \chi_p H \quad (5.4)$$

The anisotropy field H_a is estimated using equation (5.3) and (5.4) and tabulated in Table 5.2. Since H_a is proportional to H_C, so analogous to H_C, H_a also follows the same trend as expected and is found to reduce with addition of BHF (Figure 5.9 (b)). This may be attributed to growth of interface magnetization at KNN-BHF interfaces which act as reverse pinning effect [277].

Table 5.2 Magnetic parameters of (1-x) (K_{0.5}Na_{0.5})NbO₃-(x) BaFe₁₂O₁₉ (x = 30, 40 and 50 wt.%) ME composites

Composition (x)	H _C (kOe)	H _a (kOe)	M _s (emu/g)
BHF	5.30	31.55	71.52
30 wt.%	2.96	28.84	49.54
40 wt.%	2.28	26.75	55.87
50 wt.%	1.63	25.49	60.8

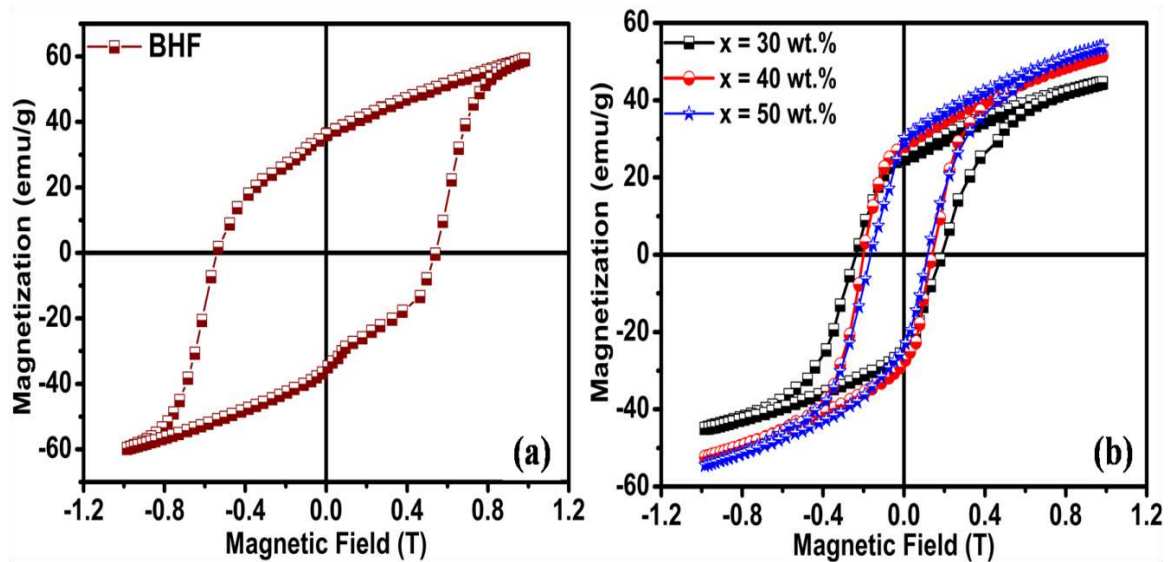


Figure 5.8 M-H hysteresis loops for (a) BHF, (b) $(1-x)(\text{K}_{0.5}\text{Na}_{0.5})\text{NbO}_3-(x)\text{BaFe}_{12}\text{O}_{19}$ ($x = 30, 40$ and 50 wt.%) composites

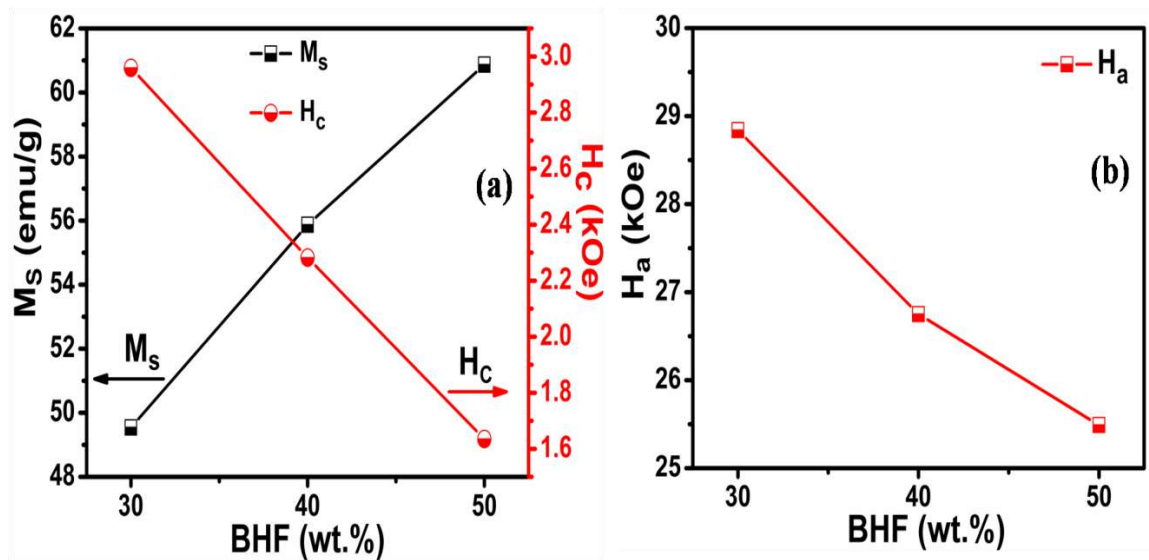


Figure 5.9 (a) Variation of saturation magnetization (M_s) and coercive field (H_c) and (b) anisotropy field (H_a) of $(1-x)(\text{K}_{0.5}\text{Na}_{0.5})\text{NbO}_3-(x)\text{BaFe}_{12}\text{O}_{19}$ ($x = 30, 40$ and 50 wt.%) composites with BHF wt.%

In order to understand the nature of magnetic ordering in the composites we obtained temperature dependent zero field cooled (ZFC) and field cooled (FC) magnetizations at a magnetic field of 1 kOe in the temperature range of 5–300 K and are shown in Figure 5.10 (a-d). The measurements were taken ZFC and FC modes. In ZFC mode we cooled the samples in the absence of magnetic field up to 5 K and then applied a magnetic field of 1 kOe. Then we measured the magnetization while heating the sample from 5–300 K. In FC

mode we cooled the samples in the presence of magnetic field of 1 kOe up to 5 K and then measured the magnetization while heating the samples from 5–300 K. The main features of the M-T curves as evident from Figure 5.10 are: (i) They exhibit large irreversibility among ZFC and FC magnetizations and (ii) presence of wide maxima (cusp) in ZFC magnetization. The irreversibility between ZFC and FC magnetizations indicate the absence of long range ferromagnetic ordering. This indicates the presence of ferromagnetic and antiferromagnetic ordering in the composites below room temperature, but mainly dominated by ferromagnetic ordering. Also the irreversibility temperature of the composites is well above room temperature because we don't see any overlapping in ZFC and FC magnetization up to 300 K as observed earlier [278]. The ZFC magnetization exhibits a broad maxima around 50 K, whereas FC magnetization exhibits almost temperature independent behaviour below this temperature. The cusp like or broad maxima behaviour of ZFC may be due to existence of spin glass behaviour [279]. This type of behaviour may be attributed to randomness of neighbouring coupling or magnetic moments and mixed interactions which results in frustration [280].

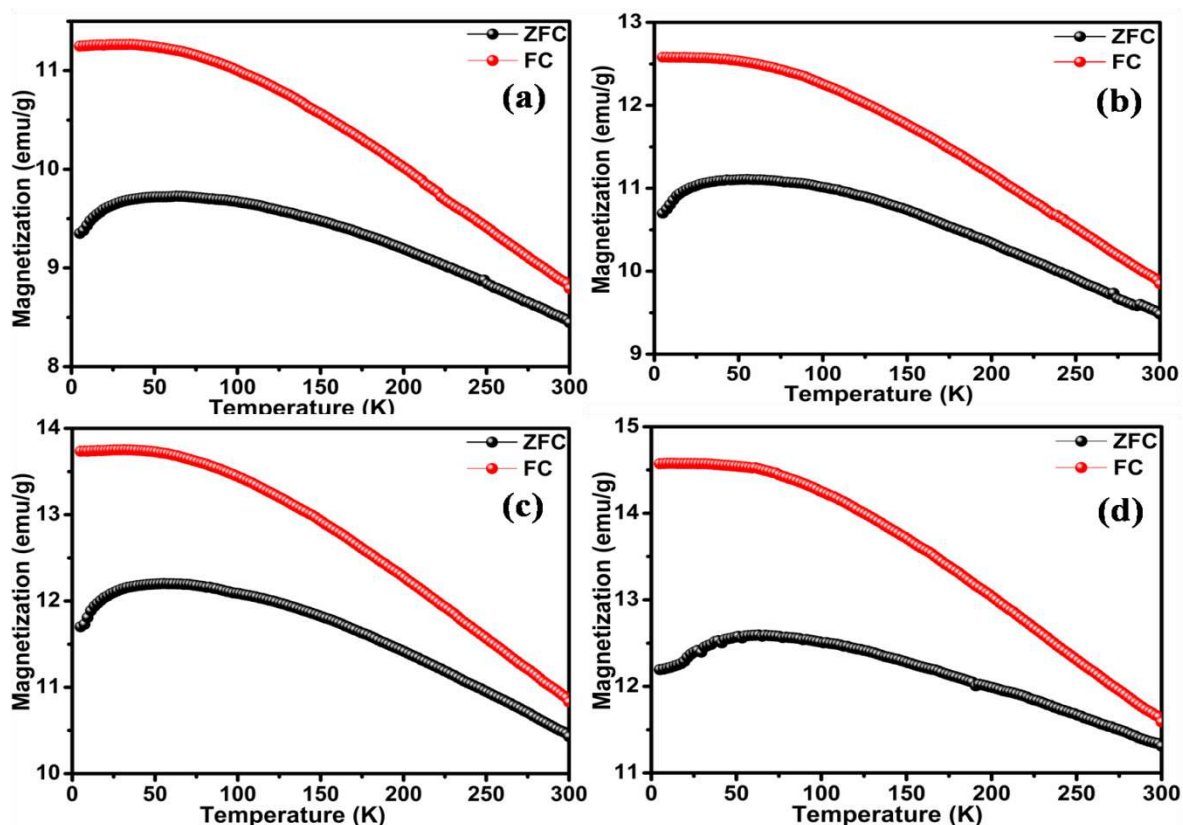


Figure 5.10 ZFC and FC magnetization curves for $(1-x)(\text{K}_{0.5}\text{Na}_{0.5})\text{NbO}_3-x \text{BaFe}_{12}\text{O}_{19}$ (a) $x = 30$ wt.%, (b) $x = 40$ wt.%, (c) $x = 50$ wt.% composites and (d) BHF

It is a well known fact that a polycrystalline compound comprises of heterogeneous microstructures viz. grains, grain boundaries and other interfaces, each of which corresponds to specific conduction mechanism [281]. The plot of Z'' vs. Z' known as Nyquist plot helps us to differentiate distinct relaxation process described by semicircular arcs. Each semicircular arc corresponds to specific relaxation [282, 283]. The different relaxation processes can be modelled using an equivalent circuit comprising of resistance and capacitance in parallel as shown in Figure 5.11 [284].

Complex impedance Z^* can be represented as

$$Z^* = (R_b^{-1} + i\omega C_b)^{-1} + (R_{gb}^{-1} + i\omega C_{gb})^{-1} \quad (5.5)$$

Evaluating equation 5.5 we will get real and imaginary parts of impedance as follows:

$$Z' = R_b/[1+(\omega R_b C_b)^2] + R_{gb}/[1+(\omega R_{gb} C_{gb})^2] \quad (5.6)$$

and
$$Z'' = \omega R_b^2 C_b/[1+(\omega R_b C_b)^2] + \omega R_{gb}^2 C_{gb}/[1+(\omega R_{gb} C_{gb})^2] \quad (5.7)$$

where R_b , R_{gb} and C_b , C_{gb} represents grain (bulk) resistance, grain boundary resistance and capacitances respectively.

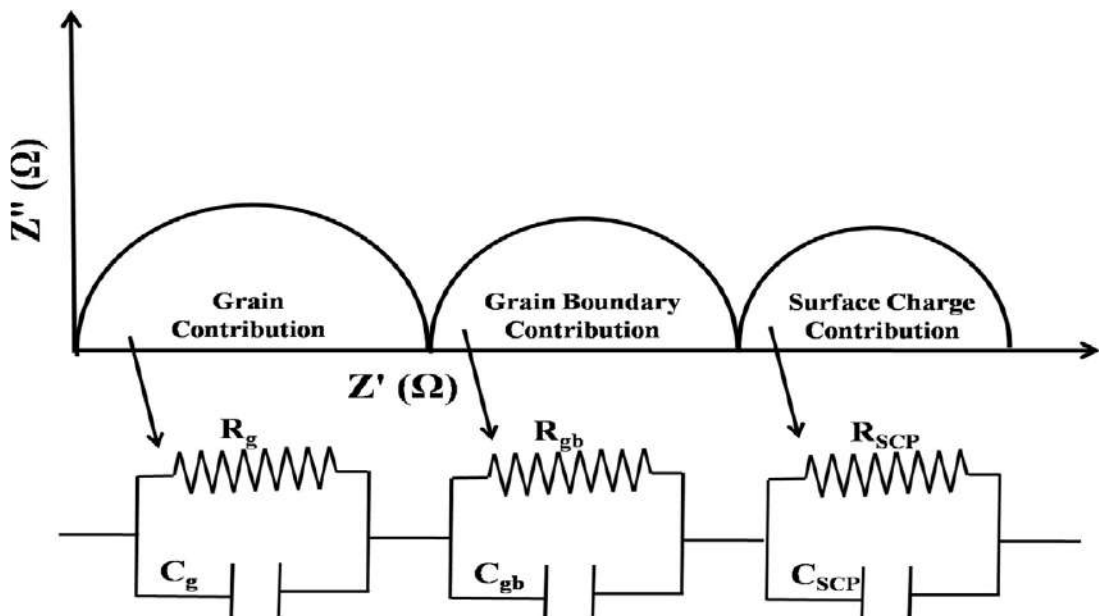


Figure 5.11 Equivalent circuits showing distinct effects including contributions from grain, grain boundaries and surface charge polarization [284]

The temperature dependent complex impedance spectra, Z'' vs. Z' known as Nyquist plots are shown in Figure 5.12 (a-c) for the $(1-x)(\text{K}_{0.5}\text{Na}_{0.5})\text{NbO}_3$ - (x) BaFe₁₂O₁₉ ($x = 30, 40$ and 50 wt.%) composites. It is evident from Figure 5.12 that we obtained two semicircular arcs at distinct temperatures (30, 50 and 100 °C). The high and low frequency semicircular arcs signify the presence of bulk (grain) and grain boundary contributions respectively. Bulk contribution mainly arise by parallel integration of bulk resistance and capacitance (R_b and C_b), while grain boundary contribution comes into play with parallel combination of grain boundary resistance and capacitance (R_{gb} and C_{gb}) respectively as shown in Figure 5.11. Both R_g and R_{gb} can be directly obtained from the intercepts of the semicircular arcs on the abscissa axis of Nyquist plots. It is evident from Figure 5.12 (a-c) that both R_b and R_{gb} are found to decrease with increase in temperature confirming the negative temperature coefficient of resistance (NTCR) behaviour of the composites analogous to semiconductors [161]. It is also observed that all the semicircles exhibit some degree of depression signalling that the centre of these semicircles lie below the abscissa axis, indicating presence of non-Debye type of relaxation phenomena in the composite samples. Figure 5.12 (d) exhibits the combined Nyquist plots of $(1-x)(\text{K}_{0.5}\text{Na}_{0.5})\text{NbO}_3$ - (x) BaFe₁₂O₁₉ ($x = 30, 40$ and 50 wt.%) ME composites at room temperature signalling the decrease in impedance with addition of BHF wt.% in the composites.

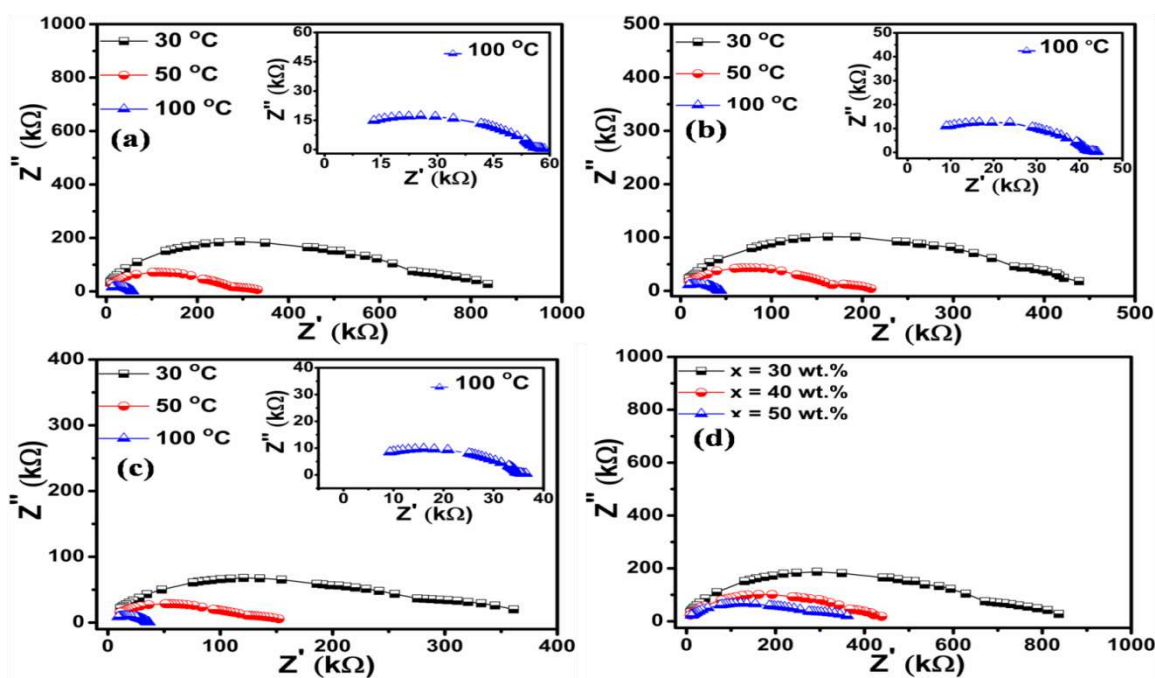


Figure 5.12 Nyquist plots of $(1-x)(\text{K}_{0.5}\text{Na}_{0.5})\text{NbO}_3$ - (x) BaFe₁₂O₁₉ (a) $x = 30$ wt.%, (b) $x = 40$ wt. %, (c) $x = 50$ wt.% composites at 30, 50 and 100 °C and (d) Nyquist plots of composites at room temperature

Electrical modulus studies are used to analyze the electrical transport process in the polycrystalline samples. It enables us to detect various phenomena including electrode polarization and bulk conductivity properties. Moreover it also helps us to analyse the effects of changing temperatures and frequency, on the relaxation processes [285, 286]. The complex electrical modulus M^* is generally treated as reciprocal of permittivity given by equation 5.8

$$M^* = 1/\varepsilon^* = M' + iM'' \quad (5.8)$$

Where, M' and M'' are obtained using relations,

$$M' = \omega C_0 Z'' \text{ and } M'' = \omega C_0 Z'$$

Here $C_0 = \varepsilon_0 A/d$ in which A is the area of the sample, d is its thickness and ω is the angular frequency [287, 288].

In order to see the presence of surface charge effects we have obtained imaginary part of complex electric modulus (M'') and plotted its variation with frequency at three different temperatures (30, 50 and 100 °C) in the frequency range of 100 Hz – 1MHz. Figure 5.13 (a-c) exhibits the dependence of M'' on frequency for $(1-x)$ (K_{0.5}Na_{0.5})NbO₃-(x) BaFe₁₂O₁₉ ($x = 30, 40$ and 50 wt.%) composites at different temperatures. It is evident from Figure 5.13 that we do not observe any relaxation peak in the lower frequency window of the M'' spectrum, which confirms about the surface charge effect in the composite samples [284, 289]. Furthermore the M'' vs. f plots, are characterized by: **(a)** appearance of peaks at a particular frequency at different temperatures and **(b)** peaks shift towards higher frequency side with increase in temperature. The lower frequency regime on left side of peak indicates the frequency range for which the charge carriers are capable of moving over a long distance, which means they can perform hopping from one site to neighbouring site easily [290]. The higher frequency range on right side of peak indicates the range of frequency for which the charge carriers remain spatially restricted to own potential wells and execute localized motion within them [226]. Appearance of peak in the modulus spectrum indicates the transition from long range to short range mobility with enhancement in frequency. Moreover, it also indicates the conductivity relaxation in the composites. Shifting of peaks towards higher frequency regime with increase in temperature indicates thermally activated relaxation process in which charge carrier hopping with small polarons is dominated intrinsically for all compounds [275].

In order to differentiate whether the relaxation phenomena occurring in the composites occurs due to long range or short range movement of charge carriers we plotted the combined frequency dependence of M'' and Z'' . If the relaxation process is dominated by short range movement of charge carriers then peaks akin to M'' and Z'' will occur at different frequencies and for long range movement of charge carriers we obtain peaks akin to M'' and Z'' at same frequency [291]. Figure 5.14 shows the combined plots of M'' and Z'' for $(1-x)$ $(\text{K}_{0.5}\text{Na}_{0.5})\text{NbO}_3$ - x $\text{BaFe}_{12}\text{O}_{19}$ ($x = 30, 40$ and 50 wt.%) composites with frequency at room temperature. It is evident from Figure 5.14 that peaks akin to M'' and Z'' are occurring at different frequencies confirming the short range movement of charge carriers contributes to dielectric relaxation. Moreover we can interpret three distinct features from Figure 5.14 viz. (i) indication of localized charge carrier movement, (ii) presence of non Debye type relaxation as confirmed from impedance analysis and (iii) distribution of relaxation times.

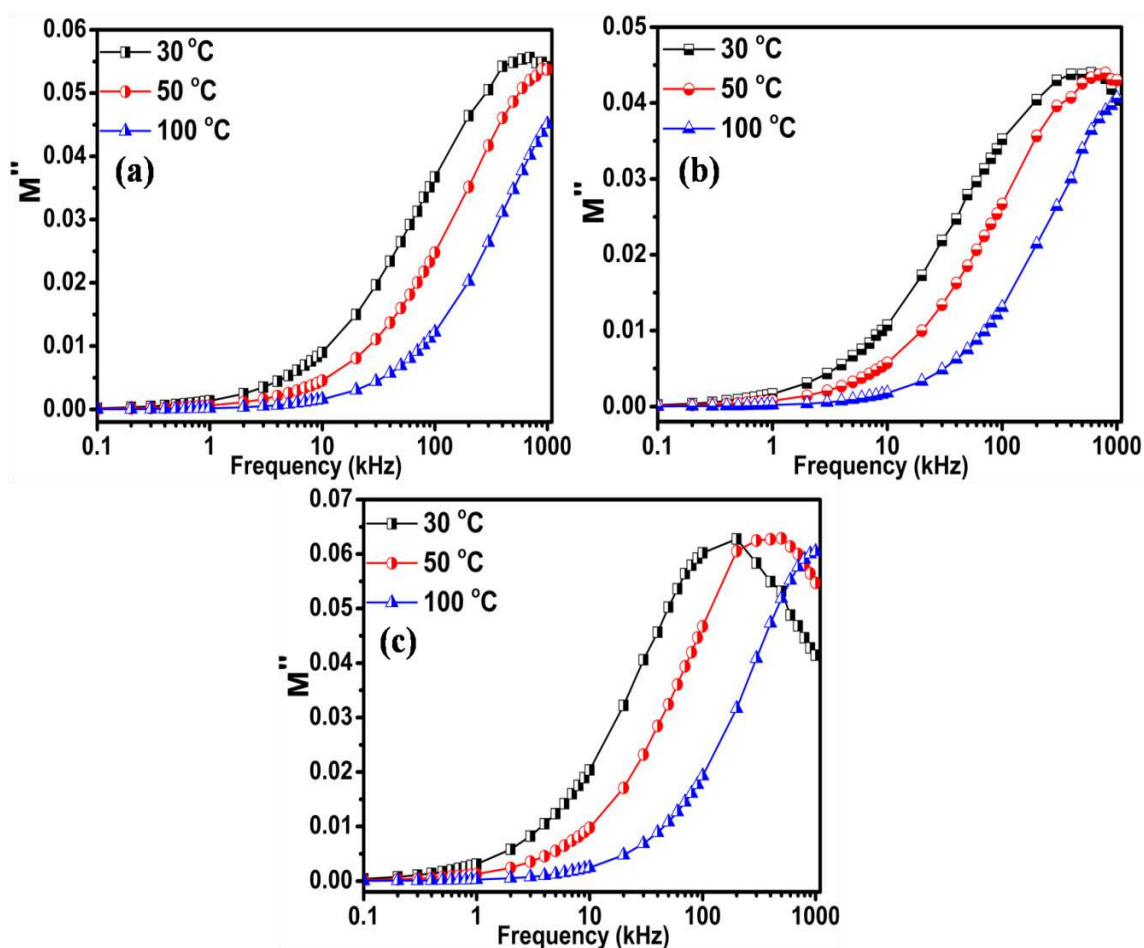


Figure 5.13 Variation of imaginary part (M'') of modulus with frequency for $(1-x)$ $(\text{K}_{0.5}\text{Na}_{0.5})\text{NbO}_3$ - x $\text{BaFe}_{12}\text{O}_{19}$ (a) $x = 30$ wt.%, (b) $x = 40$ wt. %, (c) $x = 50$ wt.% composites

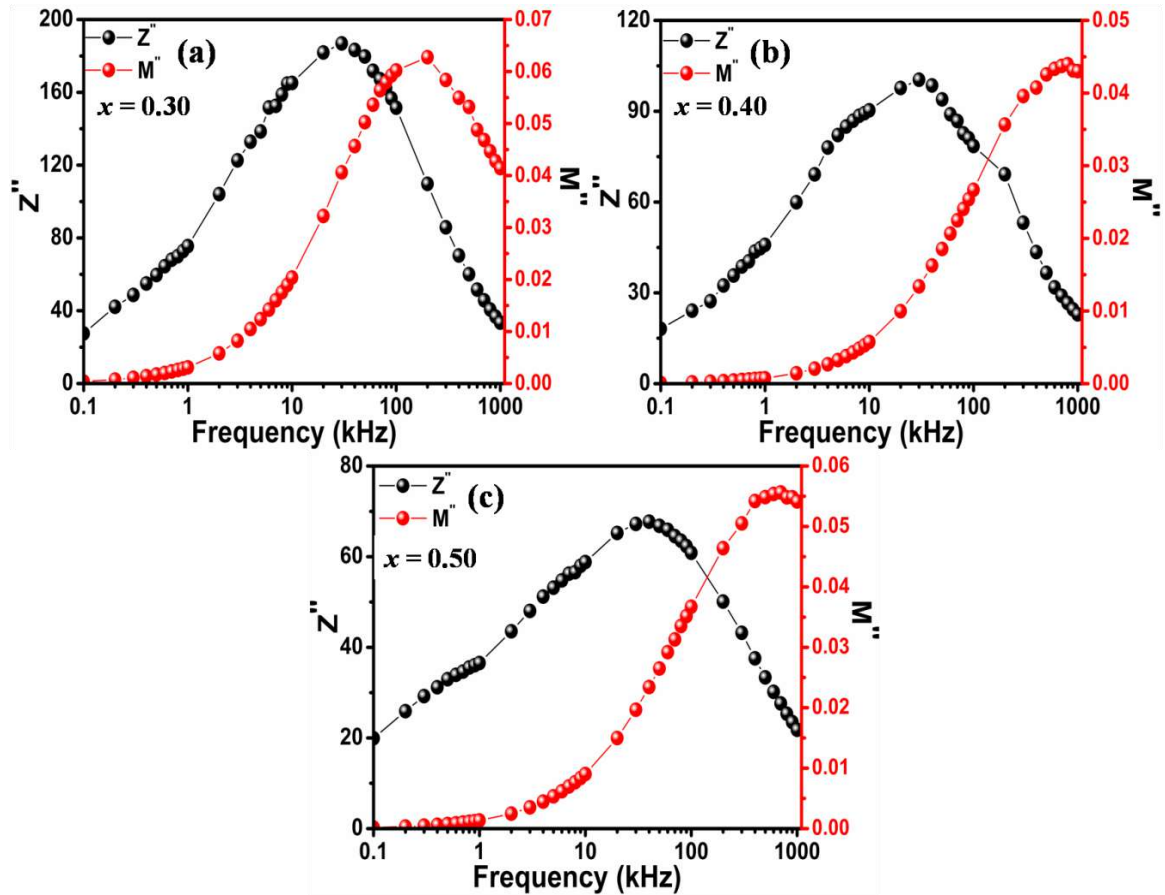


Figure 5.14 Combined plots of imaginary parts of modulus and impedance vs. frequency for $(1-x)(\text{K}_{0.5}\text{Na}_{0.5})\text{NbO}_3-(x)\text{BaFe}_{12}\text{O}_{19}$ (a) $x = 30$ wt.%, (b) $x = 40$ wt. %, (c) $x = 50$ wt.% composites at room temperature

In order to confirm the presence of ME coupling in the $(1-x)(\text{K}_{0.5}\text{Na}_{0.5})\text{NbO}_3-(x)\text{BaFe}_{12}\text{O}_{19}$ ($x = 30, 40$ and 50 wt.%) composites, we measured ME voltage coefficient (α_{ME}). Before measurement, the composite samples were electrically poled for 1 h at 100°C . α_{ME} was then computed using equation 3.8, by applying a 5 Oe AC magnetic field having a frequency of 999 Hz simultaneously, while varying the DC magnetic field from 0–8000 Oe. Figure 5.15 (a-c) exhibits the behaviour of α_{ME} with DC magnetic field for the $(1-x)(\text{K}_{0.5}\text{Na}_{0.5})\text{NbO}_3-(x)\text{BaFe}_{12}\text{O}_{19}$ ($x = 30, 40$ and 50 wt.%) composites. The highest value of $\alpha_{\text{ME}} = 4.08$ mV/cm-Oe is achieved for composite having $x = 30$ wt.% of BHF. α_{ME} is found to increase with application of DC magnetic field and highest value is obtained at 8 kOe. Identical behaviour of α_{ME} is also reported earlier [87, 110]. It is also evident from Figure 5.15 that α_{ME} is found to decrease with addition of BHF. This is generally due to low resistivity of ferrite (BHF) phase as compared to ferroelectric (KNN) phase. Also with increase in BHF wt.%, the effective poling of the composite samples becomes tedious due to leakage of charges through low resistive ferrite grains leading to enhancement in

conduction at the BHF-KNN interfaces thereby hampering the polarization, consequently decreasing α_{ME} with addition of BHF [292]. Our present investigation shows larger values of ME voltage coefficient in comparison to other magnetolectric composites having BaFe₁₂O₁₉ as one of its constituent phases as shown in Table 5.3.

Table 5.3 Comparison of α_{ME} for (1-x) (K_{0.5}Na_{0.5})NbO₃-(x) BaFe₁₂O₁₉ composites with other BaFe₁₂O₁₉ based ME composites

Composites	Maximum α_{ME} (mV/cm-Oe)	References
(0.75) BaTiO ₃ -(0.25) BaFe ₁₂ O ₁₉	2.05	[258]
(0.10) BaFe ₁₂ O ₁₉ -(0.90) Bi _{0.5} Na _{0.5} TiO ₃	0.65	[293]
(0.70) K _{0.5} Na _{0.5} NbO ₃ -(0.30) BaFe ₁₂ O ₁₉	4.08	Present results

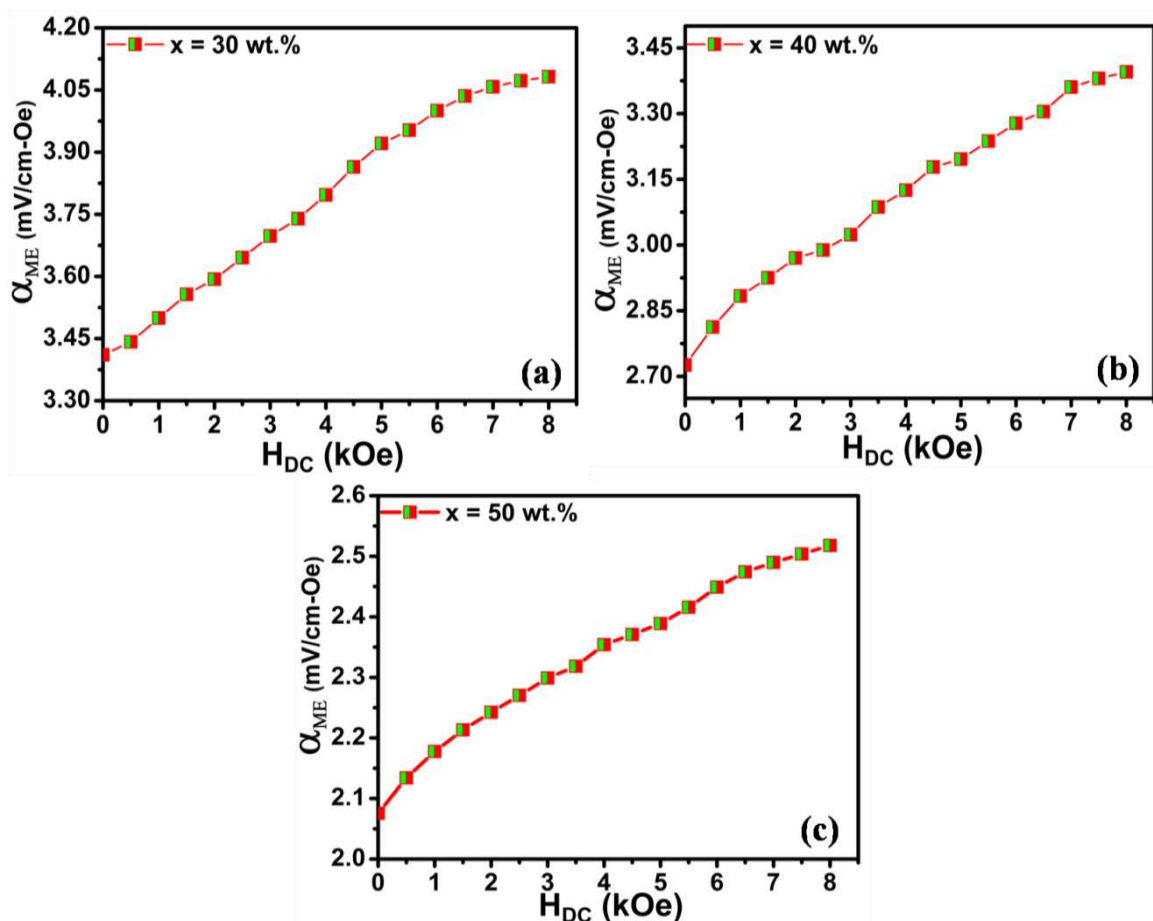


Figure 5.15 Variation of α_{ME} with DC magnetic field for (1-x) (K_{0.5}Na_{0.5})NbO₃-(x) BaFe₁₂O₁₉ (a) $x = 30$ wt.%, (b) $x = 40$ wt. %, (c) $x = 50$ wt.% composites at room temperature

5.4 Summary

Novel lead-free ME composites (1-x) (K_{0.5}Na_{0.5})NbO₃-(x) BaFe₁₂O₁₉ (x = 30, 40 and 50 wt.%) equivalently denoted as (1-x)KNN/(x)BHF were successfully synthesized using solid state reaction method, in which BHF was synthesized using sol-gel and KNN by SSR method. FE-SEM micrographs assert the existence of both the individual phases and the average grain size varies between 232–540 nm. Dielectric properties of the composites were studied as a function of temperature and the dielectric constant of the composites was found to decrease with BHF wt.%. Remnant polarization (P_r) of the composites was found to reduce with BHF wt.%. Magnetization of the composites was found to enhance with addition of BHF unlike coercive and anisotropy field which decrease with BHF wt.%. Temperature dependent ZFC and FC magnetization measurements hints towards the existence of spin glass behaviour. The highest value of $\alpha_{ME} = 4.08$ mV/cm-Oe is achieved for composite having x = 30 wt.% of BHF and is found to be higher than other BHF based ME composites. The substantial ME response of the composites may be exploited for potential applications in multifunctional devices.

Chapter 6

Conclusions and Future Suggestions

In this thesis, we have studied and discussed the structural, dielectric, magnetic and magnetoelectric properties of lead-free multiferroic/magnetoelectric composites comprising of distinct ferroelectric and ferrite phases. In this chapter, we present a short summary of the work done as reported in chapter 3 to chapter 5. The major objective of the work was to do the synthesis and characterization of new multiferroic/magnetoelectric composites with a perspective to amplify the room temperature magnetoelectric properties. In order to achieve the objective, we synthesized some magnetoelectric composites comprising of distinct ferroelectric and ferrite phases viz. $(x) \text{Ni}_{0.2}\text{Co}_{0.8}\text{Fe}_2\text{O}_4-(1-x) (\text{K}_{0.5}\text{Na}_{0.5})\text{NbO}_3$, $(x) \text{CoMn}_{0.2}\text{Fe}_{1.8}\text{O}_4-(1-x) (\text{K}_{0.5}\text{Na}_{0.5})\text{NbO}_3$, $(x) \text{Co}_{0.8}\text{Zn}_{0.2}\text{Fe}_2\text{O}_4-(1-x) (\text{Bi}_{0.5}\text{Na}_{0.5})\text{TiO}_3$, $(1-x) (\text{Bi}_{0.5}\text{Na}_{0.5})\text{TiO}_3-(x) \text{CoMn}_{0.2}\text{Fe}_{1.8}\text{O}_4$, $(x) (\text{Bi}_{0.5}\text{Na}_{0.5})\text{TiO}_3-(1-x) \text{Ni}_{0.2}\text{Co}_{0.8}\text{Fe}_2\text{O}_4$ and $(1-x) (\text{K}_{0.5}\text{Na}_{0.5})\text{NbO}_3-(x) \text{BaFe}_{12}\text{O}_{19}$ and studied their structural, dielectric, ferroelectric, magnetic, impedance and magnetoelectric properties.

The motivation of the work has been set up in the chapter 1 of thesis, which is followed by a concise overview of the experimental techniques that are used in characterization of the prepared samples, as discussed in chapter 2. A comprehensive analysis related to the major findings of the work done has been discussed in chapter 3 to chapter 5. The major conclusions obtained from the systematic study of the synthesized composites discussed in chapter 3 to chapter 5 are as follows:

In **chapter 3**, magnetoelectric composites comprising of $(\text{K}_{0.5}\text{Na}_{0.5})\text{NbO}_3$ (KNN) as ferroelectric phase with $\text{Ni}_{0.2}\text{Co}_{0.8}\text{Fe}_2\text{O}_4$ and $\text{CoMn}_{0.2}\text{Fe}_{1.8}\text{O}_4$ respectively as ferrite phases were synthesized and their multiferroic properties were studied. The dielectric properties are found to be strongly influenced by Maxwell-Wagner interface phenomena arising because of electrical inhomogeneity. In the temperature dependent dielectric study, two dielectric anomalies viz. T_{O-T} and T_c are observed for pristine KNN around ~ 190 and 430 °C respectively. These anomalies are also observed for different compositions of both the composites. Ferroelectric character of the composites was confirmed at room temperature through P-E hysteresis loops measurement and was found to decrease monotonously with an increase in ferrite content. Complex impedance spectroscopy indicates the negative temperature coefficient of resistance (NTCR) behaviour for both the composites analogous

to semiconductors. Magnetic hysteresis (M-H) loops indicate the presence of ferromagnetic ordering in the composites at room temperature. Magnetoelectric (ME) coupling in the composites was confirmed by measuring their ME voltage coefficient (α_{ME}) and we observed maximum $\alpha_{ME} = 5.389$ mV/cm-oe and 5.941 mV/cm-oe for $x = 0.20$ in (x) $Ni_{0.2}Co_{0.8}Fe_2O_4-(1-x)$ $(K_{0.5}Na_{0.5})NbO_3$ and for $x = 0.10$ in (x) $CoMn_{0.2}Fe_{1.8}O_4-(1-x)$ $(K_{0.5}Na_{0.5})NbO_3$ composites respectively. These values of α_{ME} are found to be larger than those of earlier reported composites.

The magnetoelectric composites comprising of $(Bi_{0.5}Na_{0.5})TiO_3$ (BNT) as ferroelectric phase with $Co_{0.8}Zn_{0.2}Fe_2O_4$ (CZFO), $CoMn_{0.2}Fe_{1.8}O_4$ (CMFO) and $Ni_{0.2}Co_{0.8}Fe_2O_4$ (NCFO) respectively as ferrite phase were synthesized and their multiferroic properties were studied which are reported in **chapter 4**. Variation of dielectric properties with frequency at room temperature exhibits dispersion in lower frequency regime for the composites. The transition temperature (T_C) is found to shift slightly towards higher temperature side with increase in frequency indicating the relaxor behaviour of the composites. Ferroelectric properties are found to decrease monotonously with addition of ferrite unlike magnetic properties which enhance with ferrite addition in the composites. The highest value of α_{ME} was found to be 7.11 mV/cm-Oe for $x = 0.10$ in (x) $Co_{0.8}Zn_{0.2}Fe_2O_4-(1-x)$ $(Bi_{0.5}Na_{0.5})TiO_3$, 6.765 mV/cm-Oe for $x = 0.10$ in $(1-x)$ $(Bi_{0.5}Na_{0.5})TiO_3-(x)$ $CoMn_{0.2}Fe_{1.8}O_4$ and 7.538 mV/cm-Oe for $x = 0.60$ in (x) $(Bi_{0.5}Na_{0.5})TiO_3-(1-x)$ $Ni_{0.2}Co_{0.8}Fe_2O_4$ composites. These values of α_{ME} are found to be larger than those of earlier reported $(Bi_{0.5}Na_{0.5})TiO_3$ based composites and may be exploited for use in potential device applications.

Furthermore, novel lead-free magnetoelectric composites comprising of $(K_{0.5}Na_{0.5})NbO_3$ (KNN) as ferroelectric phase with $BaFe_{12}O_{19}$ (BHF) as ferrite phase viz. $(1-x)$ $(K_{0.5}Na_{0.5})NbO_3-(x)$ $BaFe_{12}O_{19}$ were synthesized and reported in **chapter 5**. Dielectric properties are influenced by Maxwell-Wagner interface phenomena arising because of electrical inhomogeneity and found to dilute with increase in BHF wt.%. Magnetic hysteresis loops for the composites are found to be unsaturated and saturation magnetization (M_S) was computed from law of saturation. The magnetization increased monotonously with BHF wt.% unlike coercivity (H_c) and anisotropic field (H_a) which show a decreasing trend. Temperature dependent ZFC and FC magnetization measurements hints towards spin glass behaviour in the composites. Magnetoelectric coupling in the composites was confirmed by measuring their ME voltage coefficient (α_{ME}) and we observed maximum $\alpha_{ME} = 4.08$ mV/cm-oe for $x = 30$ wt.%. The obtained values of

α_{ME} are found to be higher than those of earlier reported BaFe₁₂O₁₉ based ME composites.

The main motive of the thesis was to synthesize and characterize the different lead-free multiferroic composites and study their magnetoelectric response which may be exploited for use in device based technological applications. Thus, based on the findings of the present work, it is concluded that the highest magnetoelectric voltage coefficient of 7.538 mV/cm-Oe is obtained for (x) (Bi_{0.5}Na_{0.5})TiO₃-(1- x) Ni_{0.2}Co_{0.8}Fe₂O₄ with $x = 0.60$ composition amongst all the studied composites. This may be due to enhanced dielectric properties of BNT-NCFO composites with reduced dielectric loss as compared to other studied composites. Moreover, ferrite phase NCFO has high magnetostriction coefficient (λ) and high resistivity in comparison to CMFO and CZFO phases. This shows that the observed multiferroic properties and magnetoelectric response of the synthesized composites is found to be significantly affected by the concentration of the constituent ferroelectric and ferrite phases and their respective properties. We obtained higher magnetoelectric response for (Bi_{0.5}Na_{0.5})TiO₃ based multiferroic composites with distinct ferrite phases in comparison to (K_{0.5}Na_{0.5})NbO₃ which may be attributed to its higher dielectric and piezoelectric response. Based on the findings of the present research work, we can achieve enhanced magnetoelectric response in the multiferroic composites by choosing a ferroelectric phase which shows high dielectric and piezoelectric properties and ferrite phase having high resistivity and magnetostriction. The improved magnetoelectric response of the composites may be exploited for use in potential multiferroic device based applications.

Future suggestions

Significant efforts can be made to enhance the magnetoelectric response of the studied composites further by making composite thick films with Polyvinylidene fluoride (PVDF) polymer. From the technological point of view, due to complications arising regarding the use of bulk magnetoelectric composites in devices, it is required to study these bulk magnetoelectric composites in the thin film form in order to make them more effective and suitable for multiferroic device based applications. Furthermore, we can make a comparative study of the studied magnetoelectric composites by adopting different synthesizing methods and changing the process parameters.

Bibliography

- [1] Donald R. Askeland, P.P. Fulay and W.J. Wright, “The Science and Engineering of Materials”, Cengage Learning, Stanford, USA 6th Ed. (2011).
- [2] M.W. Borosum, “Fundamental of Ceramics”, Taylor and Francis (2003).
- [3] K.F. Wang, J.M. Liu and Z.F. Ren, “Multiferroicity: the coupling between magnetic and polarization orders”, *Adv. in Phys.* **58** (2009) 321.
- [4] N.A. Hill, “Why are there so few multiferroics?”, *J. Phys. Chem. B* **104** (2000) 694.
- [5] H. Schmid, “Some symmetry aspects of ferroics and single phase multiferroics”, *J. Phys.: Cond. Matter* **20** (2008) 434201.
- [6] M. Bibes and A. Barthélémy, “Multiferroics: Towards a magnetoelectric memory”, *Nature Mater.* **7** (2008) 425.
- [7] J.F. Scott, “Data storage: Multiferroic memories”, *Nature Mater.* **6** (2007) 256.
- [8] Y. Wang, J. Li and D. Viehland, “Magnetoelectrics for magnetic sensor applications: Status, challenges and perspectives”, *Mater. Today* **17** (2014) 269.
- [9] J.F. Scott, “Applications of magnetoelectrics”, *J. Mater. Chem.* **22** (2012) 4567.
- [10] A.K. Zvezdin, A.S. Logginov, G.A. Meshkov and A.P. Pyatakov, “Multiferroics: Promising materials for microelectronics, spintronics and sensor technique”, *Bull. Russian. Acad. Sci. Phys.* **71** (2007) 1561.
- [11] M.M. Vopson, “Fundamentals of Multiferroic Materials and Their Possible Applications”, *Critical Rev. in Solid State and Mater. Sci.* **40** (2015) 223.
- [12] D.I. Khomskii, “Classifying multiferroics: Mechanisms and effects”, *Physics* **2** (2009) 20.
- [13] J.F. Scott, “Ferroelectric Memories”, Springer-Verlag Berlin, Heidelberg (2000).
- [14] B.D. Cullity, and C.D. Graham, “Introduction to magnetic materials”, 2nd ed. Wiley (2009).
- [15] S.C. Abrahams, “Ferroelasticity”, *Mater. Res. Bull.* **6** (1971) 881.
- [16] H. Schmid, “Multi-ferroic magnetoelectrics”, *Ferroelectrics* **162** (1994) 317.
- [17] D.I. Khomskii, “Multiferroics: Different ways to combine magnetism and ferroelectricity”, *J. Magn. Magn. Mater.* **306** (2006) 1.
- [18] I.E. Dzyaloshinskii, “On the magneto-electrical effect in antiferromagntes”, *Sov. Phys. JETP* **10** (1960) 628.
- [19] D.N. Astrov, “Magnetoelectric effect in chromium oxide”, *Sov. Phys. JETP* **11** (1960) 708.

- [20] G.T. Rado and V.J. Folen, "Observation of the magnetically induced magnetoelectric effect and evidence for antiferromagnetic domains", *Phys. Rev. Lett.* **7** (1961) 310.
- [21] T. Kimura, T. Goto, H. Shintani, K. Ishizaka, T. Arima and T. Yokura, "Magnetic control of ferroelectric polarization", *Nature* **426** (2003) 55.
- [22] B.B.V. Aken, T.T.M. Palstra, A. Filippetti and N.A. Spaldin, "The origin of ferroelectricity in magnetoelectric YMnO₃", *Nature Mater.* **3** (2004) 164.
- [23] N.A. Spaldin, S.-W. Cheong and R. Ramesh, "Multiferroics: Past, present and future", *Phys. Today* **63** (2010) 38.
- [24] N.A. Spaldin and M. Fiebig, "The Renaissance of Magnetoelectric Multiferroics", *Science* **309** (2005) 391.
- [25] W. Eerenstein, N.D. Mathur and J.F. Scott, "Multiferroic and Magnetoelectric materials", *Nature* **442** (2006) 759.
- [26] M. Fiebig, "Revival of the magnetoelectric effect", *J. Phys. D: Appl. Phys.* **38** (2005) R123.
- [27] J. Ryu, S. Priya, K. Uchino and H. Kim, "Magnetoelectric Effect in Composites of Magnetostrictive and Piezoelectric Materials", *J. Electroceram.* **8** (2002) 107.
- [28] J.V. Suchtelen, "Product properties: a new application of composite materials", *Philips Res. Rep.* **27** (1972) 28.
- [29] J.V. Boomgard and R.A.J. Born, "A sintered magnetoelectric composite BaTiO₃-Ni(Co,Mn)Fe₃O₄", *J. Mater. Sci.* **9** (1978) 1538.
- [30] J. Ma, J. Hu, Z. Li and C.W. Nan, "Recent Progress in Multiferroic Magnetoelectric Composites: from Bulk to Thin Films", *Adv. Mater.* **23** (2011) 1062.
- [31] Y. Wang, J. Hu, Y. Lin and C.W. Nan, "Multiferroic magnetoelectric composite nanostructures", *NPG Asia Mater.* **2** (2010) 61.
- [32] B. Jaffe, W.R. Cook and H.L. Jaffe, "Piezoelectric Ceramics" Academic Press (1971).
- [33] M.E. Lines and A.M. Glass, "Principles and Applications of Ferroelectrics and Related Materials", Clarendon, Oxford (1977).
- [34] G. Lawes, A.P. Ramirez, C.M. Varma and M.A. Subramaniam, "Magnetodielectric effects from spin fluctuations in isostructural ferromagnetic and antiferromagnetic systems", *Phys. Rev. Lett.* **91** (2003) 257208.

- [35] G. Haertling, “Ferroelectric ceramics: history and technology”, *J. Amer. Ceram. Soc.* **82** (1999) 718.
- [36] Y. Xu, “Ferroelectric materials and their applications”, North Holland (1991).
- [37] K.C. Kao, “Dielectric phenomenon in solids”, Elsevier Academic Press (2004).
- [38] <http://nptel.ac.in/courses/115103039/module1/lec1/5.html>
- [39] https://chem.libretexts.org/Textbook_Maps/Inorganic_Chemistry
- [40] X. Wang, G. Gou, D. Wang, H. Xiao, Y. Liu, M. Zhang, B. Dkhil, X. Ren and X. Lou, “Structural, electronic and magnetic properties of metal-organic-framework perovskites [AmH][Mn(HCOO)₃]: a first-principles study”, *RSC Adv.* **6** (2016) 48779.
- [41] G.A. Smolenskii and I.E. Chupis, “Ferroelectromagnets”, *Sov. Phys. Usp.* **25** (1982) 475.
- [42] A.S. Bhalla, R. Guo and R. Roy, “The perovskite structure-a review of its role in ceramic science and technology”, *Mat. Res. Innovat.* **4** (2000) 3.
- [43] V.M. Goldschmidt, “Geochemische Verterlungsgesetze der Elemente Norske Videnskap”, Oslo (1927).
- [44] C. Li, K.C.K. Soh, P. Wu “Formability of ABO₃ perovskites”, *J. Alloy Compd.* **372** (2004) 40.
- [45] K.E. Sickafus, J.M. Wills and N.W. Grimes, “Structure of Spinel”, *J. Amer. Ceram. Soc.* **82** (1999) 3279.
- [46] S.O. Pillai, “Solid State Physics”, New Age International Limited Publishers (1999).
- [47] http://nptel.ac.in/Courses/113104005/lecture3/3_9.html
- [48] R. Mazumder, P.S. Devi, D. Bhattacharya, P. Choudhury, A. Sen, “Ferromagnetism in nanoscale BiFeO₃”, *Appl. Phys. Lett.* **91** (2007) 062510.
- [49] S. Goswami, D. Bhattacharya, P. Choudhary, B. Ouladdiaf, T. Chatterji, “Multiferroic coupling in nanoscale BiFeO₃”, *Appl. Phys. Lett.* **99** (2011) 073106.
- [50] U. Choudhury, S. Goswami, D. Bhattacharya, J. Ghosh, S. Basu and S. Neogi, “Room temperature multiferroicity in orthorhombic LuFeO₃”, *Appl. Phys. Lett.* **105** (2014) 052911.
- [51] B. Kumari, P.R. Mandal, T.K. Nath, “Magnetic, magnetocapacitance and dielectric properties of BiFeO₃”, *Adv. Mat. Lett.* **5** (2) (2014) 84.

- [52] S. Mukherjee, R. Gupta, A. Garg, “Dielectric response and magnetoelectric coupling in single crystal gallium ferrite”, *AIP Advances* **3** (2013) 052115.
- [53] A. Roy, S. Mukherjee, R. Gupta, R. Prasad, A. Garg, “Structure and Properties of Magnetoelectric Gallium Ferrite: A Brief Review”, *Ferroelectrics* **473** (2014) 154.
- [54] F. Gheorghiu, L. Curecheriu, I. Lisiecki, P. Beaunier, S. Feraru, M.N. Palamaru, V. Musteata, N. Lupu, L. Mitoseriu, “Functional properties of $\text{Sm}_2\text{NiMnO}_6$ multiferroic ceramics prepared by spark plasma sintering”, *J. Alloy Compd.* **649** (2015) 151.
- [55] A.R. James, G.S. Kumar, M. Kumar, S.V. Suryanarayana, T. Bhimasankaram, “Magnetic and Magnetoelectric Studies in Polycrystalline $\text{LaBi}_4\text{FeTi}_3\text{O}_{15}$ ”, *Modern Phys. Lett. B* **11** (1997) 633.
- [56] S.R. Das, R.N.P. Choudhary, P. Bhattacharya, R.S. Katiyar, P. Dutta, A. Manivannan, M.S. Seehra, “Structural and multiferroic properties of La modified BiFeO_3 ceramics”, *J. Appl. Phys.* **101** (2007) 034104.
- [57] J.V. Suchetelene, “Product Properties: a new application of composite materials”, *Philips. Res. Rep.* **27** (1972) 28.
- [58] D. Viehland, J.F. Li, Y. Yang, T. Costanzo, A. Yourdkhani, G. Caruntu, P. Zhou, T. Zhang, T. Li, A. Gupta, M. Popov and G. Srinivasan, “Tutorial: Product properties in multiferroic nanocomposites”, *J. Appl. Phys.* **124** (2018) 061101.
- [59] J.V.D Boomgaard, D.R. Terrell, R.A.J. Born and H.F.J.I. Giller, “An *in situ* grown eutectic magnetoelectric composite material”, *J. Mater. Sci.* **9** (1974) 1705.
- [60] M.I. Bichurin, I.A. Kornev, V.M. Petrov and I. Lisnevskaya, “Investigation of magnetoelectric interaction in composites”, *Ferroelectrics* **204** (1997) 289.
- [61] S. Lopatin, I. Lopatin and I. Lisnevskaya, “Magnetoelectric PZT/ferrite composite materials”, *Ferroelectrics* **162** (1994) 63.
- [62] G. Harshey, J.P. Dougherty and R.E. Newnham, “Theoretical modelling of multilayer magnetoelectric composites” *Int. J. Appl. Electromag. Mater.* **4** (1993) 145.
- [63] J. Ryu, A.V. Carazo, K. Uchino and H.E. Kim, “Magnetoelectric properties in piezoelectric and magnetostrictive laminate composites”, *Jpn. J. Appl. Phys.* **40** (2001) 4948.

- [64] J. Ryu, S. Priya, A.V. Carazo, K. Uchino and H.E. Kim, "Effect of the magnetostrictive layer on magnetoelectric properties in lead zirconate titanate/terfenol-D laminate composites", *J. Amer. Ceram. Soc.* **84** (2001) 2905.
- [65] K. Mori and M. Wuttig, "Magnetoelectric coupling in terfenol-D/polyvinylidene fluoride composites", *Appl. Phys. Lett.* **81** (2002).
- [66] R. Katoch, R. Gupta, A. Garg, "Structural investigation of multiferroic BiFeO₃-PbTiO₃ solid solution", *AIP Conf. Proc.* **1591** (2014) 1755.
- [67] S. Sharma, V. Singh, R.K. Dwivedi, R. Ranjan, A. Anshul, S.S. Amritphale, N. Chandra, "Phase transformation, improved ferroelectric and magnetic properties of (1-x) BiFeO₃-xPb(Zr_{0.52}Ti_{0.48})O₃ solid solutions", *J. Appl. Phys.* **115** (2014) 224106.
- [68] S. Sharma, V. Singh, R.K. Kotnala, R. Ranjan, R.K. Dwivedi, "Co-existence of tetragonal and monoclinic phases and multiferroic properties for x < 0.30 in the (1-x) Pb(Zr_{0.52}Ti_{0.48})O₃-xBiFeO₃ system", *J. Alloy Compd.* **614** (2014) 165.
- [69] D.K. Pradhan, R.N.P. Chowdhury, T.K. Nath, "Magnetoelectric properties of PbZr_{0.53}Ti_{0.47}O₃-Ni_{0.65}Zn_{0.35}Fe₂O₄ multiferroic nanocomposites", *Appl. Nanosci.* **2** (2012) 261.
- [70] A. Singh, A. Gupta, R. Chatterjee, "Enhanced magnetoelectric coefficient (α) in the modified BiFeO₃-PbTiO₃ system with large La substitution", *Appl. Phys. Lett.* **93** (2008) 022902.
- [71] A. Singh, R. Chatterjee, "Multiferroic Properties of La-Rich BiFeO₃-PbTiO₃ Solid Solutions", *Ferroelectrics* **433** (2012) 180.
- [72] P. Galizia, C.E. Ciomaga, L. Mitoseriu, C. Galassi, "PZT-Cobalt ferrite particulate composites: Densification and lead-loss controlled by quite-fast sintering", *J. Eur. Ceram. Soc.* **37** (2017) 161.
- [73] P. Dey, T.K. Nath, M.L.N. Goswami, T. K. Kundu, "Room temperature ferroelectric and ferromagnetic properties of multiferroics xLa_{0.7}Sr_{0.3}MnO₃-(1-x)ErMnO₃ (weight percent x= 0.1, 0.2) composites", *Appl. Phys. Lett.* **90** (2007) 162510.
- [74] R. Debnath, P. Dey, S. Singh, J.N. Roy, S.K. Mandal, T.K. Nath, "Magnetically tunable alternating current electrical properties of xLa_{0.7}Sr_{0.3}MnO₃-(1-x)ErMnO₃ (x = 0.1, 0.3 and 0.5) multiferroic nanocomposite", *J. Appl. Phys.* **118** (2015) 044104.

- [75] A. Gupta, A. Huang, S. Shannigrahi, R. Chatterjee, “Improved magnetoelectric coupling in Mn and Zn doped $\text{CoFe}_2\text{O}_4\text{-PbZr}_{0.52}\text{Ti}_{0.48}\text{O}_3$ particulate compsite”, *Appl. Phys. Lett.* **98** (2011) 112901.
- [76] L. Curecheriu, P. Postolache, M.T. Buscaglia, V. Buscaglia, A. Lanculescu, L. Mitoseriu, “Novel magnetoelectric ceramic composites by control of the interface reactions in $\text{Fe}_2\text{O}_3\text{@BaTiO}_3$ core-shell structures”, *J. Appl. Phys.* **116** (2014) 084102.
- [77] K.P. Pramoda, A. Huang, S.R. Shannigrahi, “On some properties of PZT-NZF composite films manufactured by hybrid synthesis routes”, *Ceram. Int.* **37** (2011) 431.
- [78] H. Zheng, J. Wang, S.E. Lofland et al., “Multiferroic $\text{BaTiO}_3\text{-CoFe}_2\text{O}_4$ Nanostructures”, *Science* **303** (2004) 66.
- [79] S.Y. Tan, S.R. Shannigrahi, S.H. Tan and F.E.H. Tay, “Synthesis and characterization of composite $\text{MgFe}_2\text{O}_4\text{-BaTiO}_3$ multiferroic system”, *J. Appl. Phys.* **103** (2008) 094105.
- [80] J.P. Zhou, L. Lv, Q. Liu, Y.X. Zhang and P. Liu, “Hydrothermal synthesis and properties of $\text{NiFe}_2\text{O}_4\text{-BaTiO}_3$ composites with well matched interface”, *Sci. Tech. Adv. Mater.* **13** (2012) 045001.
- [81] R. Rani, J. K. Juneja, S. Singh, C. Prakash and K. K. Raina, “Structural, electrical, magnetic and magnetoelectric properties of composites”, *J. Magn. Magn. Mater.* **345** (2013) 55.
- [82] B. K. Bammannavar and L. R. Naik, “Magnetic properties and Magnetoelectric effect in ferroelectric rich $\text{Ni}_{0.5}\text{Zn}_{0.5}\text{Fe}_2\text{O}_4\text{+BPZT}$ ME composites”, *J. Magn. Magn. Mater.* **321** (2009) 382.
- [83] B. K. Bammannavar, L. R. Naik and B. K. Chougale, “Studies on dielectric and magnetic properties of $(x)\text{Ni}_{0.2}\text{Co}_{0.8}\text{Fe}_2\text{O}_4\text{+(1-x)barium lead zirconate titanate magnetoelectric composites}$ ”, *J. Appl. Phys.* **104** (2008) 064123.
- [84] R. Sharma, P. Pahuja and R.P. Tandon, “Structural, dielectric, ferromagnetic, ferroelectric and ac conductivity studies of the $\text{BaTiO}_3\text{-CoFe}_{1.8}\text{Zn}_{0.2}\text{O}_4$ multiferroic particulate composites”, *Ceram. Int.* **40** (2014) 9027.
- [85] C.M. Kanamadi, J.S. Kim, H.K. Yang, B.K. Moon, B.C. Choi and J.H. Jeong, “Synthesis and characterization of $\text{CoFe}_2\text{O}_4\text{-Ba}_{0.9}\text{Sr}_{0.1}\text{TiO}_3$ magnetoelectric composites with dielectric and magnetic properties”, *Appl. Phys. A* **97** (2009) 575.

- [86] O.M. Hemed, A. Tawfik, M.A. Amer, B.M. Kamal and D.E.E. Refaay, “Structural, spectral and dielectric properties of piezoelectric-piezomagnetic composites”, *J. Magn. Magn. Mater.* **324** (2012), 3229.
- [87] A. Sharma, R.K. Kotnala and N.S. Negi, “Observation of multiferroic properties and magnetoelectric effect in (x) CoFe_2O_4 - $(1-x)\text{Pb}_{0.7}\text{Ca}_{0.3}\text{TiO}_3$ composites”, *J. Alloy Compd.* **582** (2014) 628.
- [88] P.R. Mandal and T.K. Nath, “Magnetoelectric response and Dielectric property of Multiferroic $\text{Co}_{0.65}\text{Zn}_{0.35}\text{Fe}_2\text{O}_4$ - $\text{PbZr}_{0.52}\text{Ti}_{0.48}\text{O}_3$ ”, *Appl. Phys. A* **112** (2013) 789.
- [89] P.R. Mandal and T.K. Nath, “Enhanced Magnetocapacitance and Dielectric property of Multiferroic $\text{Co}_{0.65}\text{Zn}_{0.35}\text{Fe}_2\text{O}_4$ - $\text{PbZr}_{0.52}\text{Ti}_{0.48}\text{O}_3$ Magnetodielectric composites”, *J. Alloy Compd.* **599** (2014) 71.
- [90] A. Gupta and R. Chatterjee, “Dielectric and magnetoelectric properties of BaTiO_3 - $\text{Co}_{0.6}\text{Zn}_{0.4}\text{Fe}_{1.7}\text{Mn}_{0.3}\text{O}_4$ ”, *J. Eur. Ceram. Soc.* **33** (2013) 1017.
- [91] Y. Han, L. Li, D. Guo, X. Ren and W. Xia, “Magnetodielectric effect in NaNbO_3 - NiFe_2O_4 particulate composites”, *Mat. Lett.* **98** (2013) 19.
- [92] R.V. Krishnaiah, A. Srinivas, S.V. Kamat, T. Karthik and S. Asthana, “Effect of CoFe_2O_4 mole percentage on multiferroic and magnetoelectric properties of $\text{Na}_{0.5}\text{Bi}_{0.5}\text{TiO}_3/\text{CoFe}_2\text{O}_4$ particulate composites”, *Ceram. Int.* **40** (2014) 7799.
- [93] C.M. Kanamadi, B.K. Das, C.W. Kim, D.I. Kang, H.G. Cha, E.S. Ji, A.P. Jadhav, B.-E Jun, J.H. Jeong, B.C. Choi, B.K. Chougule and Y.S. Kang, “Dielectric and magnetic properties of (x) CoFe_2O_4 - $(1-x)$ $\text{Ba}_{0.8}\text{Sr}_{0.2}\text{TiO}_3$ magnetoelectric composites”, *Mater. Chem. Phys.* **116** (2009) 6.
- [94] P. Pahuja, C. Prakash and R.P. Tandon, “Comparative study of magnetoelectric composite system $\text{Ba}_{0.95}\text{Sr}_{0.05}\text{TiO}_3$ - $\text{Ni}_{0.8}\text{Co}_{0.2}\text{Fe}_2\text{O}_4$ with ferrite prepared by different methods”, *Ceram. Int.* **40** (2014) 5731.
- [95] S.N. Babu, J.-H. Hsu, Y.S. Chen and J.G. Lin, “Magnetoelectric response in lead-free multiferroic NiFe_2O_4 - $\text{Na}_{0.5}\text{Bi}_{0.5}\text{TiO}_3$ composites”, *J. Appl. Phys.* **109** (2011) 07D904.
- [96] S.L. Kadam, K.K. Patankar, V.L. Mathe, M.B. Kothale, R.B. Kale and B.K. Chougule, “Electrical properties and magnetoelectric effect in $\text{Ni}_{0.75}\text{Co}_{0.25}\text{Fe}_2\text{O}_4$ + $\text{Ba}_{0.8}\text{Pb}_{0.2}\text{TiO}_3$ composites”, *Mater. Chem. Phys.* **78** (2003) 684.

- [97] M. Kumar and K.L. Yadav, “Magnetolectric characterization of (x) $\text{Ni}_{0.75}\text{Co}_{0.25}\text{Fe}_2\text{O}_4$ - $(1-x)$ BiFeO_3 composites”, *J. Phys. Chem. Solids* **68** (2007) 1791.
- [98] M.J. Miah, M.N.I. Khan and A.K.M. Akhter Hossain, “Weak ferromagnetism and magnetolectric effect in multiferroic $(x)\text{Ba}_{0.95}\text{Sr}_{0.05}\text{TiO}_3$ - $(1-x)\text{BiFe}_{0.9}\text{Gd}_{0.1}\text{O}_3$ realxors”, *J. Magn. Magn. Mater.* **401** (2016) 600.
- [99] S.C. Mazumdar, M.N.I. Khan, Md. Fakhrul Islam and A.K.M. Akhter Hossain, “Tuning of magnetolectric coupling in $(1-y)\text{Bi}_{0.8}\text{Dy}_{0.2}\text{FeO}_3$ - $(y)\text{Ni}_{0.5}\text{Zn}_{0.5}\text{Fe}_2\text{O}_4$ multiferroic composites”, *J. Magn. Magn. Mater.* **401** (2016) 443.
- [100] R.C. Kamble, P.A. Shaikh, Y.D. Kolekar, C.H. Bhosale and K.Y. Rajpure, “Studies on dielectric and magnetolectric behaviour of 25% CMFO ferrite and 75% BZT ferroelectric multiferroic magnetolectric composites”, *Mat. Lett.* **64** (2010) 520.
- [101] Manjusha, K.L. Yadav, N. Adhlakha, J. Shah and R.K. Kotnala, “Strain mediated magnetolectric coupling induced in $(x)\text{Bi}_{0.5}\text{Na}_{0.5}\text{TiO}_3$ - $(1-x)\text{MgFe}_2\text{O}_4$ composites”, *Physica B* **514** (2017) 541.
- [102] S.G. Chavan, S.D. Chavan, S.S. Mane, S.B. Kulkarni and D.J. Salunkhe, “Investigations on magnetodielectric and magnetolectric properties of CNFO-BST composites”, *Mater. Chem. Phys.* **208** (2018) 163.
- [103] R. Rakhikrishna, J. Isaac and J. Philip, “Magnetolectric characterization of x $(\text{Na}_{0.5}\text{K}_{0.5})_{0.94}\text{Li}_{0.06}\text{NbO}_3$ - $(1-x)$ NiFe_2O_4 ”, *J. Electroceram.* **35** (2015) 120.
- [104] R. Rani, J. K. Juneja, S. Singh, K. K. Raina and C. Prakash, “Dielectric, ferroelectric, magnetic and magnetolectric properties of $0.1\text{Ni}_{0.8}\text{Zn}_{0.2}\text{Fe}_2\text{O}_4$ - $0.9\text{Pb}_{1-3x/2}\text{Sm}_x\text{Zr}_{0.65}\text{Ti}_{0.35}\text{O}_3$ magnetolectric composites”, *Ceram. Int.* **39** (2013) 7845.
- [105] H.F. Zhang, S.W. Or and H.L.W. Chan, “Fine-grained multiferroic $\text{BaTiO}_3/(\text{Ni}_{0.5}\text{Zn}_{0.5})\text{Fe}_2\text{O}_4$ composite ceramics synthesized by novel powder-in-sol precursor hybrid processing route”, *Mater. Res. Bull.* **44** (2009) 1339.
- [106] Z. Yu and C. Ang, “Maxwell-Wagner polarization in ceramic composites BaTiO_3 - $\text{Ni}_{0.3}\text{Zn}_{0.7}\text{Fe}_{2.1}\text{O}_4$ ”, *J. Appl. Phys.* **91** (2002) 794.
- [107] J. Huang, P. Du, L. Hong, Y. Dong and M. Hong, “A Percolative Ferromagnetic-Ferroelectric Composite with Significant Dielectric and Magnetic Properties”, *Adv. Mater.* **19** (2007) 437.

- [108] M.V. Ramana, S.H. Song and B.S. Murty, “Enhanced magnetoelectric properties in lead-free $\text{Ni}_{0.83}\text{Co}_{0.15}\text{Cu}_{0.02}\text{Fe}_{1.9}\text{O}_4-(1-x)\text{Na}_{0.5}\text{Bi}_{0.5}\text{TiO}_3$ composites by spark plasma sintering”, *Scripta Mater.* **82** (2014) 9.
- [109] A. Testino, L. Mitoseriu, V. Buscaglia, M.T. Buscaglia, I. Pallecchi, A.S. Albuquerque, V. Calzona, D. Marre, A.S. Siri and P. Nanni, “Preparation of multiferroic composites of $\text{BaTiO}_3\text{-Ni}_{0.5}\text{Zn}_{0.5}\text{Fe}_2\text{O}_4$ ceramics”, *J. Eur. Ceram. Soc.* **26** (2006), 3031.
- [110] R. Gupta, J. Shah, S. Chaudhary, S. Singh and R.K. Kotnala, “Magnetoelectric coupling induced anisotropy in multiferroic nanocomposite $(1-x)\text{BiFeO}_3\text{-xBaTiO}_3$ ”, *J. Nanopart Res.* **15** (2013) 2004.
- [111] E.V. Ramana, A. Mahajan, M.P.F. Graca, A. Srinivas and M.A. Valente, “Ferroelectric and magnetic properties of magnetoelectric $(\text{Na}_{0.5}\text{Bi}_{0.5})\text{TiO}_3\text{-BiFeO}_3$ synthesized by acetic acid assisted sol-gel method”, *J. Eur. Cer. Soc.* **34** (2014) 4201.
- [112] A. Sathiya Priya, I.B. Shameem Banu and Shahid Anwar, “Investigation of multiferroic properties of doepd $\text{BiFeO}_3\text{-BaTiO}_3$ composite ceramics”, *Mat. Lett.* **142** (2015) 42.
- [113] J. Chen, Y. Qi, G. Shi, X. Yan, S. Yu and J. Cheng, “Diffused phase transition and multiferroic properties of $0.57(\text{Bi}_{1-x}\text{La}_x)\text{FeO}_3\text{-}0.43\text{PbTiO}_3$ crystalline solutions”, *J. Appl. Phys.* **104** (2008) 064124.
- [114] X.-M. Liu, S.-Y. Fu and C.-J. Huang, “Synthesis and magnetic characterization of novel $\text{CoFe}_2\text{O}_4\text{-BiFeO}_3$ nanocomposites”, *Mater. Sci. Engg. B* **121** (2005) 255.
- [115] C.P. Poole and F.J. Owens, “Introduction to Nanotechnology”, Wiley Student Edition (2008).
- [116] T. Pradeep, “Nano: The Essentials”, Macgraw-Hill Education (2007).
- [117] C.H. Bamford and C.F.H. Tipper, “Comprehensive Chemical Kinetics”, Elsevier (1980).
- [118] C.J. Brinker and G.W. Scherer, “Sol Gel Science The Physics and Chemistry of Sol Gel Processing”, Academic Press Inc. (1990).
- [119] B.D. Cullity and S.R. Stock, “Elements of X-ray Diffraction”, Prentice Hall (2001).
- [120] R.K. Puri and V.K. Babbar, “Solid State Physics”, S. Chand & Company Ltd. (2009).

- [121] P.J. Grundy and G.A. Jones, “Electron Microscopy in the Study of Materials”, Edward Arnold (1976).
- [122] S. Foner, “Versatile and Sensitive Vibrating Sample Magnetometer”, *Rev. Sci. Instrum.* **30** (1959) 548.
- [123] A. Niazi, P. Poddar and A.K. Rastogi, “A Precision Low-cost Vibrating Sample Magnetometer”, *Curr. Sci.* **79** (2000) 99.
- [124] <http://family-held.org/website/Rudy/publications/unpublished/papers/vsm/VMS%>
- [125] F. London, “Superfluids: Macroscopic Theory of Superconductivity”, Wiley New York (1950).
- [126] R. Kleiner, D. Koelle, F. Ludwig F and F. Clarke, “Superconducting Quantum Interference Devices: State of the Art and Applications”, *Proceedings of the IEEE* **92** (2004) 1534.
- [127] B.D. Josephson, “Possible new effects in superconductive tunnelling”, *Phys. Lett.* **1** (1962) 251.
- [128] J. Clarke and A.I. Braginski, “The SQUID Handbook”, Wiley-VCH Verlag GmbH & Co. KGaA, Weinheim (2004).
- [129] Giap V. Duong, R. Grossinger, M. Schoenhardt, D. Bueno-Basque, “The Lock-in technique for studying magnetoelectric effect”, *J. Magn. Magn. Mater.* **316** (2007) 390.
- [130] G.S. Bhattacharya, S. Mazumder and S. Baisnab, “Design and fabrication of few devices for dynamic measurement of magnetoelectric effect”, *Ind. J. Engg. Mater. Sci.* **11** (2004) 185.
- [131] C.W. Nan, “Magnetoelectric Effect in Composites of Piezoelectric and Piezomagnetic Phases”, *Phys. Rev. B* **50** (1994) 6082.
- [132] J.Y. Kim, Z. Li and Baltazar, “Pyroelectric and Pyromagnetic Coefficients of Functionally Graded Multilayered Multiferroic Composites”, *Acta Mech.* **223** (2012) 849.
- [133] C.W. Nan and D.R. Clarke, “Effective properties of ferroelectric and/or ferromagnetic composites: a unified approach and its application”, *J. Amer. Ceram. Soc.* **80** (1997) 1333.
- [134] J. Van Boomgard, A.M.J.G. Van Run and J.V. Suchetelene, “Magnetoelectricity in Piezoelectric-Magnetostrictive Composites”, *Ferroelectrics* **14** (1976) 727.

- [135] R. Rakhikrishna, J. Isaac and J. Philip, “Magneto-electric Coupling in Multiferroic Nanocomposites of the type x $(\text{Na}_{0.5}\text{K}_{0.5})_{0.94}\text{Li}_{0.06}\text{NbO}_3$ - $(1-x)$ CoFe_2O_4 :Role of Ferrite Phase”, *Ceram. Int.* **43** (2017) 664.
- [136] U.B. Sontu, V. Yelasani and V.R.R. Musugu, “Structural, Electrical and Magnetic Characteristics of Nickel Substituted Cobalt Ferrite Nanoparticles, Synthesized by Self Combustion Method”, *J. Magn. Magn. Mater.* **374** (2015) 376.
- [137] V.L. Mathe and A.D. Sheikh, “Magnetostrictive Properties of Nanocrystalline Co-Ni Ferrites”, *Physica B* **405** (2010) 3594.
- [138] D. Gao, K.W. Kwok, D. Lin and H.L.W. Chan, “Microstructure and Electrical Properties of La Modified $\text{K}_{0.5}\text{Na}_{0.5}\text{NbO}_3$ Lead Free Piezoelectric Ceramics”, *J. Phys. D: Appl. Phys.* **42** (2009) 035411.
- [139] Y.P. Guo, K. Kakimoto and H. Ohsato, “Phase Transitional Behavior and Piezoelectric Properties of $(\text{Na}_{0.5}\text{K}_{0.5})\text{NbO}_3$ - LiNbO_3 Ceramics”, *Appl. Phys. Lett.* **85** (2004) 4121.
- [140] J. Rani, K.L. Yadav and S. Prakash, “Modified Structure and Electrical Properties of BSZT doped KNN Hybrid Ceramic”, *Appl. Phys. A* **108** (2012) 761.
- [141] R.W. McCallum, K.W. Dennis, D.C. Jiles, J.E. Snyder and Y.H. Chen, “Composite Magnetostrictive Materials for Advanced Automotive Magnetomechanical Sensors”, *Low Temp. Phys.* **27** (2001) 266.
- [142] Y. Melikhov, J.E. Snyder, D.C. Jiles, A.P. Ring, J.A. Paulsen, C.C.H. Lo and K.W. Dennis, “Temperature Dependence of Magnetic Anisotropy in Mn-Substituted Cobalt Ferrite”, *J. Appl. Phys.* **99** (2006) 08R102.
- [143] J.A. Paulsen, A.P. Ring, C.C.H. Lo, J.E. Snyder and D.C. Jiles, “Manganese-Substituted Cobalt Ferrite Magnetostrictive Materials for Magnetic Stress Sensor Applications”, *J. Appl. Phys.* **97** (2005) 044502.
- [144] M. Mahesh Kumar, A. Srinivas, S.V. Suryanarayana, G.S. Kumar and T. Bhimasankaran, “An experimental setup for dynamic measurement of magnetoelectric effect”, *Bull. Mater. Sci.* **21** (1998) 251.
- [145] J. Rani, P.K. Patel, N. Adhlakha, H. Singh and K.L. Yadav, “ Mo^{6+} modified $(\text{K}_{0.5}\text{Na}_{0.5})\text{NbO}_3$ lead free ceramics: structural, electrical and optical properties”, *J. Mater. Sci. Tech.* **30** (2014) 459.

- [146] R.C. Kamble, P.A. Shaikh, S.S. Kamble and Y.D. Kolekar, “Effect of Cobalt Substitution on Structural, Magnetic and Electric Properties of Nickel Ferrite”, *J. Alloy Compd.* **478** (2009) 599.
- [147] N. Adhlakha and K.L. Yadav, “Structural, Dielectric, Magnetic, and Optical Properties of $\text{Ni}_{0.75}\text{Zn}_{0.25}\text{Fe}_2\text{O}_4\text{-BiFeO}_3$ Composites”, *J. Mater. Sci.* **49** (2014) 4423.
- [148] S. Dong, J. Cheng, J.F. Li and D. Viehland, “Enhanced Magnetoelectric effect in Laminate Composites of Terfenol-D/ $\text{Pb}(\text{Zr,Ti})\text{O}_3$ under Resonant Drive”, *Appl. Phys. Lett.* **83** (2003) 4812.
- [149] C.G. Koops, “On the dispersion of resistivity and dielectric constant of some semiconductors at audio frequencies”, *Phys. Rev.* **83** (1951) 121.
- [150] Y. Liu, Y. Wu, D. Li, Y. Zhang, J. Zhang and J. Yang, “A study of structural, ferroelectric, ferromagnetic, dielectric properties of $\text{NiFe}_2\text{O}_4\text{-BaTiO}_3$ multiferroic composites, *J. Mater. Sci: Mater. Elec.* **24** (2012) 1900.
- [151] K.K. Patankar, S.S. Joshi and B.K. Chougule, “Dielectric behaviour in magnetoelectric composites”, *Phys. Lett. A* **346** (2005) 337.
- [152] R.A. Islam and S. Priya, “Effect of Piezoelectric grain size on magnetoelectric coefficient of $\text{Pb}(\text{Zr}_{0.52}\text{Ti}_{0.48})\text{O}_3\text{-Ni}_{0.8}\text{Zn}_{0.2}\text{Fe}_2\text{O}_4$ ”, *J. Mater. Sci.* **43** (2008) 3560.
- [153] W.R. Buessem, L.E. Cross and A.K. Goswami, “Phenomenological theory of high permittivity in fine grained barium titanate”, *J. Amer. Ceram. Soc.* **49** (1966) 33.
- [154] S.M. Moussa, B.J. Kennedy, B.A. Hunter, C.J. Howard and T. Vogt, “Low temperature structural studies on PrAlO_3 ”, *J. Phys. Cond. Matter* **13** (2001) 203.
- [155] J. Smit and H.P.J. Wijn, “Ferrites: Physical properties of ferrimagnetic oxides in relation to their technical applications”, 1st Edition, Philips Technical Library, Eindhoven, (1959).
- [156] S. Singhal, T. Namgyal, S. Bansal and K. Chandra, “Effect of Zn Substitution on the Magnetic Properties of Cobalt Ferrite Nano Particles Prepared Via Sol-Gel Route”, *J. Electro. Analysis & App.* **2** (2010) 376.
- [157] R.D. Zysler, D. Fiorani and A.M. Testa, “Investigation of magnetic properties of interacting Fe_2O_3 nanoparticles”, *J. Magn. Magn. Mater.* **224** (2001) 5.
- [158] F. Delille, B. Dieny, J.-B. Moussy, M.-J. Guitett, S. Gota, M. Gautier-Soyer and C. Marin, “Study of the electronic paraproces and antiphase boundaries as sources of the demagnetisation phenomenon in magnetite”, *J. Magn. Magn. Mater.* **294** (2005) 27.

- [159] S. Maensiri, P. Thongbai and T. Yamwong, “Giant dielectric permittivity observed in $\text{CaCu}_3\text{Ti}_4\text{O}_{12}/(\text{Li}/\text{Ti})$ -doped NiO composites”, *Appl. Phys. Lett.* **90** (2007) 202908.
- [160] K. Prasad, L.K. Kumari, K.P. Chandra, K.L. Yadav and S. Sen, “Electrical properties of a lead free perovskite ceramic: $(\text{Na}_{0.5}\text{Sb}_{0.5})\text{TiO}_3$ ”, *Appl. Phys. A* **88** (2007) 377.
- [161] E. Atamanik and V. Thangadurai, “Study of the dielectric properties in NaNbO_3 - KNbO_3 - In_2O_3 system using impedance spectroscopy”, *Mater. Res. Bull.* **44** (2009) 931.
- [162] Lily K. Kumari, K. Prasad and K.L. Yadav, “Dielectric and impedance study of lead-free ceramic: $(\text{Na}_{0.5}\text{Bi}_{0.5})\text{ZrO}_3$ ”, *J. Mater. Sci.* **42** (2007) 6252.
- [163] R. Grossinger, G.V. Duong and R.S. Turtelli, “The Physics of magnetoelectric composites”, *J. Magn. Magn. Mater.* **320** (2008) 1972.
- [164] M. Zeng, J.G. Wan, Y. Wang, H. Yu, J.M. Liu, X.P. Jiang and C.W. Nan, “Resonance magnetoelectric effect in bulk composites of lead zirconate titanate and nickel ferrite”, *J. Appl. Phys.* **95** (2004) 8069.
- [165] A.S. Fawzi, A.D. Sheikh and V.L. Mathe, “Multiferroic properties of Ni Ferrite-PLZT composites”, *Physica B* **405** (2010) 340.
- [166] C.V. Ramana, Y.D. Kolekar, K. Kamala Bharathi, B. Sinha and K. Ghosh, “Correlation between structural, magnetic, and dielectric properties of manganese substituted cobalt ferrite”, *J. Appl. Phys.* **114** (2013) 183907.
- [167] N. Adhlakha and K.L. Yadav, “Study of structural, dielectric, and magnetic behaviour of $\text{Ni}_{0.75}\text{Zn}_{0.25}\text{Fe}_2\text{O}_4$ - $\text{Ba}(\text{Ti}_{0.85}\text{Zr}_{0.15})\text{O}_3$ composites”, *Smart Mater. Struct.* **21** (2012) 115021.
- [168] R. Zhang, J.F. Li and D. Viehland, “Effect of Aliovalent Substituents on the Ferroelectric Properties of Modified Barium Titanate Ceramics: Relaxor Ferroelectric Behaviour”, *J. Amer. Ceram. Soc.* **87** [5] (2004) 864.
- [169] D. Pandey, N. Singh and S.K. Mishra, “Effect of particle-size on ferroelectric transitions”, *J. Pure Appl. Phys.* **32** (7) (1994) 616.
- [170] M. Rawat and K.L. Yadav, “Study of structural, electrical, magnetic and optical properties of 0.65BaTiO_3 - $0.35\text{Bi}_{0.5}\text{Na}_{0.5}\text{TiO}_3$ - BiFeO_3 multiferroic composite”, *J. Alloy Compd.* **597** (2014) 188.

- [171] A. Gupta and R. Chatterjee, “Magnetic, dielectric, magnetoelectric, and microstructural studies demonstrating improved magnetoelectric sensitivity in three- phase BaTiO₃-CoFe₂O₄-poly(vinylidene fluoride) composite”, *J. Appl. Phys.* **106** (2009) 024110.
- [172] H. Singh and K.L. Yadav, “Dielectric, magnetic and magnetoelectric properties of La and Nb co-doped Bismuth ferrite”, *J. Phys.:Cond. Matter.* **23** (2011) 385901.
- [173] H. Singh, A. Kumar and K.L. Yadav, “Structural, dielectric, magnetic, magnetodielectric and impedance spectroscopic studies of multiferroic BiFeO₃-BaTiO₃ ceramics”, *Mat. Sci. Engg. B.* **176** (2011) 540.
- [174] B. Tiwari and R.N.P. Choudhary, “Frequency-temperature response of Pb(Zr_{0.65}-_xCe_xTi_{0.35})O₃ ferroelectric ceramics: Impedance spectroscopic studies”, *J. Alloy Compd.* **493** (2010) 1.
- [175] A. Kumar, B.P. Singh, R.N.P. Choudhary and A.K. Thakur, “A.C. Impedance analysis of the effect of dopant concentration on electrical properties of calcium modified BaSnO₃”, *J. Alloy Compd.* **394** (2005) 292.
- [176] J.R. McDonald, “Impedance spectroscopy: emphasizing solid materials and systems”, Macdonald (Ed.), Wiley, New York (1987).
- [177] W. Chen, S.R. Shannigrahi, X.F. Chen, Z.H. Wang, W. Zhu, O.K. Tan, “Multiferroic behaviour and magnetoelectric effect in CoFe₂O₄/Pb(Zr_{0.53}Ti_{0.47})O₃ thick films”, *Solid State Comm.* **150** (2010) 271.
- [178] N.A. Hill, “Density Functional Studies of Multiferroic Magnetoelectrics”, *Ann. Rev. Mater. Res.* **32** (2002) 1.
- [179] M. Fiebig, T. Lottermoser, D. Frohlich, A.V. Goltsev, R.V. Pisarev, “Observation of coupled magnetic and electric domains”, *Nature* **419** (2002) 818.
- [180] Y. Tokura, “Multiferroics as Quantum Electromagnets”, *Science* **312** (2006) 1481.
- [181] P.M.T. Ikonen, S.I. Maslovski, C.R. Simovski, S.A. Tretyakov, “On artificial magnetodielectric loading for improving the impedance bandwidth properties of microstrip antennas”, *IEEE Trans. Antennas* **64** (2006) 1654.
- [182] G.A. Smolenskii, V.A. Isupv, A.I. Agranovskaya, N.N. Krainik, “New ferroelectrics of complex composition IV”, *Sov. Phys. Solid State* **2** (1961) 2651.
- [183] Z. Yang, B. Liu, L. Wei, Y. Hou, “Structure and electrical properties of (1-x) Bi_{0.5}Na_{0.5}TiO₃-xBi_{0.5}K_{0.5}TiO₃ ceramics near morphotropic phase boundary”, *Mater. Res. Bull.* **43** (2008) 81.

- [184] T. Takenaka, T. Okuda, K. Takegahara, “Lead-free piezoelectric ceramics based on $(\text{Bi}_{1/2}\text{Na}_{1/2})\text{TiO}_3\text{-NaNbO}_3$ ”, *Ferroelectrics* **196** (1997) 175.
- [185] H. Nagata, N. Koizumi, T. Takenaka, “Lead-Free Piezoelectric Ceramics of $(\text{Bi}_{1/2}\text{Na}_{1/2})\text{TiO}_3\text{-BiFeO}_3$ system”, *Key Engg. Mater.* **169-170** (1999) 37.
- [186] S.N. Babu, K. Srinivas, T. Bhimasankaram, “Studies on lead-free multiferroic magnetoelectric composites”, *J. Magn. Magn. Mater.* **321** (2009) 3764.
- [187] J. Rani, K.L. Yadav, Satya Prakash, “Enhanced magnetodielectric effect and optical property of lead-free multiferroic $(1-x)(\text{Bi}_{0.5}\text{Na}_{0.5})\text{TiO}_3/x\text{CoFe}_2\text{O}_4$ composites”, *Mater. Chem. Phys.* **147** (2014) 1183.
- [188] K. Prabakar, J. Mirunalini, N.S. Sowmya, J.A. Chelvane, M. Mahendiran, S.V. Kamat, A. Srinivas, “Development of lead-free magnetoelectric laminates of $\text{Na}_{0.5}\text{Bi}_{0.5}\text{TiO}_3\text{-Tb}_{0.3}\text{Dy}_{0.7}\text{Fe}_{1.95}$ for power generation”, *Physica B* **448** (2014) 336.
- [189] A.K.M. Akhter Hossain, H. Tabata, T. Kiwai, “Magnetoresistive properties of $\text{Zn}_{1-x}\text{Co}_x\text{Fe}_2\text{O}_4$ ferrites”, *J. Magn. Magn. Mater.* **320** (2008) 1157.
- [190] N. Somaiah, T.V. Jayaraman, P.A. Joy, D. Das, “Magnetic and magnetoelastic properties of Zn- doped cobalt-ferrites”, *J. Magn. Magn. Mater.* **324** (2012) 2286.
- [191] Manjusha, K.L. Yadav, “Structural, Dielectric, Ferroelectric and Magnetic Properties of $(x)\text{CoFe}_2\text{O}_4\text{-(1-x)}\text{BaTiO}_3$ composite”, *IEEE Trans. Die. Elec. Ins.* **22** (3) (2015) 1462.
- [192] J.C. Maxwell, *Electricity and Magnetism* (London Oxford University Press (1973).
- [193] K.W. Wagner, “The Distribution of Relaxation Times in Typical Dielectrics”, *Ann. Phys.* **40** (1973) 817.
- [194] K. Maaz, S. Karim, G.H. Kim, “Effect of particle size on the magnetic properties of $\text{Ni}_x\text{Co}_{1-x}\text{Fe}_2\text{O}_4$ ($x\sim 0.3$) nanoparticles”, *Chem. Phys. Lett.* **549** (2012) 67.
- [195] C.E. Ciomaga, A.M. Neagu, M.V. Pop, M. Airimioaei, S. Tascu, G. Schileo, C. Galassi, L. Mitoseriu, “Ferroelectric and dielectric properties of ferrite-ferroelectric ceramic composites”, *J. Appl. Phys.* **113** (2013) 074103.
- [196] L.E. Cross, “Relaxor ferroelectrics”, *Ferroelectrics* **76** (1987) 241.
- [197] H. Zhang, S.W. Or, H.L.W. Chan, “Multiferroic properties of $\text{Ni}_{0.5}\text{Zn}_{0.5}\text{Fe}_2\text{O}_4\text{-Pb}(\text{Zr}_{0.53}\text{Ti}_{0.47})\text{O}_3$ ceramic composites”, *J. Appl. Phys.* **104** (2004) 104109.
- [198] Q.H. Jiang, Z.J. Shen, J.P. Zhou, Z. Shi, C.W. Nan, “Magnetoelectric composites of nickel ferrite and lead zirconate titanate prepared by spark plasma sintering”, *J. Eur. Ceram. Soc.* **27** (2007) 279.

- [199] T.M. Shaw, S.M. Troiler, P.C. McIntyre, "The Properties of Ferroelectric Films at Small Dimensions", *Ann. Rev. Mater. Sci.* **30** (2000) 263.
- [200] K. Okazaki, K. Nagata, "Effects of Grain Size and Porosity on Electrical and Optical Properties of PLZT Ceramics", *J. Amer. Ceram. Soc.* **56** (1973) 82.
- [201] A.S. Fawzi, "Effect of sintering temperature on structural, electrical, magnetic hysteresis and magnetoelectric effect on $(x) \text{Ni}_{0.7}\text{Zn}_{0.3}\text{Fe}_2\text{O}_4+(1-x)$ PLZT composite by co-precipitation method", *Adv. Appl. Sci. Res.* **2** (2011) 577.
- [202] M.B. Kothale, K.K. Patankar, A.V. Rao, V.L. Mathe, B.K. Chougule, "Electrical Conduction and Magnetoelectric Effect in $\text{Cu}_{0.4}\text{Co}_{0.6}\text{Fe}_2\text{O}_4\text{-Ba}_{0.8}\text{Pb}_{0.2}\text{TiO}_3$ ME Composites", *Ferroelectrics* **325** (2005) 143.
- [203] R.C. Kamble, P.A. Shaikh, K.Y. Rajpure, P.B. Joshi, Y.D. Kolekar, "Studies on Structural and Dielectric Properties of CMFO Ferrite and BZT Ferroelectric Magnetoelectric Composites", *Int. Ferroelectrics* **121** (2010) 1.
- [204] S.A. Lokare, R.S. Devan, B.K. Chougule, "Structural analysis and electrical properties of ME composites", *J. Alloy Compd.* **454** (2008) 471.
- [205] R.C. Kamble, P.A. Shaikh, C.H. BHosale, K.Y. Rajpure, Y.D. Kolekar, "Dielectric properties and complex impedance spectroscopy studies of mixed Ni-Co ferrites", *Smart. Mater. Struct.* **18** (2009) 085014.
- [206] D. Alder, J. Feinleib, "Electrical and Optical Properties of Narrow Band Materials", *Phys. Rev. B* **2** (1970) 3112.
- [207] M. Rawat, K.L. Yadav, "Structural, Dielectric and Ferroelectric Properties of $\text{Ba}_{1-x}(\text{Bi}_{0.5}\text{Na}_{0.5})_x\text{TiO}_3$ ", *Ceram. Int.* **39** (2012) 3627.
- [208] Y.P. Wang, L. Zhou, M.F. Zhang, X.Y. Chen, J.-M liu, Z.G. Liu, "Room-temperature saturated ferroelectric polarization in BiFeO_3 ceramics synthesized by rapid liquid phase sintering", *Appl. Phys. Lett.* **84** (2004) 1731.
- [209] I.G. Austin and N.F. Mott, "Polarons in Crystalline and Non-Crystalline Materials", *Adv. Phys.* **18** (1969) 41.
- [210] A.S. Fawzi, A.D. Sheikh, V.L. Mathe, "Dielectric, electrical and magnetoelectric characterization of $(x)\text{Ni}_{0.8}\text{Zn}_{0.2}\text{Fe}_2\text{O}_4+(1-x)\text{Pb}_{0.93}\text{La}_{0.07}(\text{Zr}_{0.60}\text{Ti}_{0.40})\text{O}_3$ composites", *Mater. Res. Bull* **45** (2010) 1000.
- [211] N. Adhlakha, K.L. Yadav, Ripandeep Singh, "Effect of BaTiO_3 addition on structural, multiferroic and magneto-dielectric properties of $0.3\text{CoFe}_2\text{O}_4\text{-}0.7\text{BiFeO}_3$ ceramics", *Smart Mater. Struct.* **23** (2014) 105024.

- [212] R.S. Devan, B.K. Chougule, “Effect of composition on coupled electric, magnetic and dielectric properties of two phase particulate magnetoelectric composite”, *J. Appl. Phys.* **101** (2007) 014109.
- [213] R.S. Yadav, J. Havlica, M. Hnatko et al., “Magnetic properties of $\text{Co}_{1-x}\text{Zn}_x\text{Fe}_2\text{O}_4$ spinel ferrite nanoparticles synthesized by starch-assisted sol-gel auto-combustion method and its ball milling”, *J. Magn. Magn. Mater.* **378** (2015) 190.
- [214] C.M. Kanamadi, J.S. Kim, H.K. Yang, B.K. Moon, B.C. Choi, J.H. Jeong, “Magnetoelectric effect and complex impedance analysis of (x) $\text{CoFe}_2\text{O}_4+(1-x)$ $\text{Ba}_{0.8}\text{Sr}_{0.2}\text{TiO}_3$ multiferroics”, *J. Alloy Compd.* **481** (2009) 781.
- [215] I.P. Pronin, P.P. Syrnikov, V.A. Isupov, V.M. Egorov, N.V. Zaitseva, “Peculiarities of phase transition in sodium-bismuth titanate”, *Ferroelectrics* **25** (1980) 395.
- [216] T. Badapanda, S. Venkatesan, S. Panigrahi, P. Kumar, “Structure and dielectric properties of bismuth sodium titanate ceramic prepared by auto combustion technique”, *Process. Appl. Ceram.* **7** (2013) 135.
- [217] L.S. Ashwini, R. Sridhar, S.S. Bellad, “Dielectric and magnetoelectric properties of Li-Mg ferrite: Barium titanate composites” *Mater. Chem. Phys.* **200** (2017) 136.
- [218] H.B. Sharma, K. Nomita Devi, V. Gupta, J.H. Lee, S. Bobby Singh, “AC electrical conductivity and magnetic properties of $\text{BiFeO}_3\text{-CoFe}_2\text{O}_4$ nanocomposites”, *J. Alloy Compd.* **599** (2014) 32.
- [219] K. Uchino, S. Nomura, “Critical exponents of the dielectric constants in diffused-phase-transition crystals”, *Ferroelectrics* **44** (1982) 55.
- [220] R. Clarke, J.C. Burfoot, “The diffuse phase transition in potassium strontium niobate”, *Ferroelectrics* **8** (1974) 505.
- [221] R.L. Moreira, R.P.S.M. Lobo, “Phenomenological study of diffuse phase transitions”, *J. Phys. Soc. Japan*, **61** (1992) 1992.
- [222] P. Pahuja, R. Sharma, C. Prakash, R.P. Tandon, “Synthesis and characterization of $\text{Ni}_{0.8}\text{Co}_{0.2}\text{Fe}_2\text{O}_4\text{-Ba}_{0.95}\text{Sr}_{0.05}\text{TiO}_3$ multiferroic composites”, *Ceram. Int.* **39** (2013) 9435.
- [223] M. Rawat, K.L. Yadav, “Electrical, magnetic and magnetodielectric properties in ferrite-ferroelectric particulate composites”, *Smart Mater. Struct.* **24** (2015) 045041 (1).

- [224] R.C. Kambale, N.R. Adhate, B.C. Chougule, Y.D. Kolekar, “Magnetic and dielectric properties of mixed spinel Ni-Zn ferrites synthesized by citrate-nitrate combustion method”, *J. Alloy Compd.* **491** (2010) 372.
- [225] S. Sen, S.K. Mishra, S.S. Palit, S.K. Das, A. Tarafdar, “Impedance analysis of 0.65Pb(Mg_{1/3}Nb_{2/3})O₃-0.35(PbTiO₃) ceramic”, *J. Alloy Compd.* **453** (2008) 395.
- [226] D.K. Pradhan, R.N.P. Choudhary, C. Rinaldi, R.S. Katiyar, “Effect of Mn substitution on electrical and magnetic properties of Bi_{0.9}La_{0.1}FeO₃”, *J. Appl. Phys.* **106** (2009) 024102.
- [227] J. Fleig, J. Maier, “The polarization of mixed conducting SOFC cathode: Effect of surface reaction coefficient, ionic conductivity and geometry”, *J. Eur. Ceram. Soc.* **24** (2004) 1343.
- [228] W. Xia, H. Wu, P. Xue, X. Zhu, “Microstructural, magnetic, and optical properties of Pr-doped perovskite manganite La_{0.67}Ca_{0.33}MnO₃ nanoparticles synthesized via sol-gel process”, *Nano. Res. Lett.* **13** (2018) 135.
- [229] F. Tudorache, P.D. Popa, M. Dobromir, F. Iacomi, “Studies on the structure and gas sensing properties of nickel-cobalt ferrite thin films prepared by spin coating”, *Mater. Sci. Engg. B* **178** (2013) 1334.
- [230] N. Sharma, A. Gaur, U.K. Gaur, R.K. Kotnala, “Observation of magnetoelectric coupling in (1-x) BaTiO₃/(x)La_{0.7}Sr_{0.3}MnO₃ composites”, *J. Alloy Compd.* **592** (244) 2014.
- [231] Y. Bai, F. Xu, L. Qiao, J. Zhou, L. Li, “The static and hyper-frequency magnetic properties of a ferromagnetic-ferroelectric composite”, *J. Magn. Mater.* **321** (2009) 148.
- [232] L. Solymar, D. Walsh, *Electrical properties of materials*, seventh ed. Oxford University Press (2004) 10.
- [233] K. Verma and S. Sharma, “Impedance spectroscopy and dielectric behaviour in barium strontium titanate – nickel zinc ferrite composites”, *Phys. Status Solidi B* **249** (2012) 209.
- [234] A.A. Bokov, Z.-G. Ye, “Recent progress in relaxor ferroelectrics and related materials with perovskite structure”, *J. Mater. Sci.* **41** (2006) 31.
- [235] P. Sittiketkorn, T. Bongkarn, “Effects of sintering temperature on phase formation, microstructure and dielectric properties of BNT-BT ceramics prepared by combustion technique”, *Ferroelectrics Lett. Sec.* **40** (2013) 77.

- [236] R. Tadi, Y.-I Kim, D. Sarkar, C.G. Kim, K.-S Ryu, “Magnetic and electrical properties of bulk $\text{BaTiO}_3+\text{MgFe}_2\text{O}_4$ composite”, *J. Magn. Magn. Mater.* **323** (2011) 564.
- [237] J. Chand, S. Verma, P. Kumar and M. Singh, “Structural, electric and dielectric properties of MgFe_2O_4 ferrite processed by solid state reaction technique”, *Int. J. Th. Appl. Sci.* **3** [2] (2011) 8.
- [238] K. Singh, N.S. Negi, R.K. Kotnala, M. Singh, “Dielectric and magnetic properties of $(\text{BiFeO}_3)_{1-x}(\text{PbTiO}_3)_x$ ferromagnetoelectric system”, *J. Solid State Comm.* **148** (2008) 18.
- [239] M. Kumar, K.L. Yadav, “Study of room temperature magnetoelectric coupling in Ti substituted bismuth ferrite system”, *J. Appl. Phys.* **100** (2006) 074111.
- [240] D.K. Pradhan, R.N.P. Chowdhury, T.K. Nath, “Magnetoelectric properties of $\text{PbZr}_{0.53}\text{Ti}_{0.47}\text{O}_3\text{-Ni}_{0.65}\text{Zn}_{0.35}\text{Fe}_2\text{O}_4$ multiferroic nanocomposites”, *Appl. Nanosci.* **2** (2012) 261.
- [241] V.S. Puli, A. Kumar, N. Panwar, I.C. Panwar, R.S. Katiyar, “Transition metal modified bulk BiFeO_3 with improved magnetization and linear magneto-electric coupling,” *J. Alloy Compd.* **509** [32] (2011) 8223.
- [242] R.S. Devan, B.K. Chougule, “Magnetic properties and dielectric behaviour in ferrite/ferroelectric particulate composites”, *Physica B* **393** (2007) 161.
- [243] B.K. Bammannavar, L.R. Naik, “Electrical properties and magnetoelectric effect in $(x)\text{Ni}_{0.5}\text{Zn}_{0.5}\text{Fe}_2\text{O}_4+(1-x)\text{BPZT}$ composites”, *Smart Mater. Struct.* **18** (2009) 085013.
- [244] C. Chappert, A. Fert, F.N.V. Dau, “The emergence of spin electronics in data storage”, *Nat. Mater.* **6** (2007) 813.
- [245] A. Zhukov, M. Ipatov, A. Talaat, J.M. Blanco, M. Churyukanova, V. Zhukova, “Studies of High-Frequency Giant Magnetoimpedance Effect in Co-rich Amorphous Microwires”, *IEEE Trans. Mag.* **51** (11) (2015) 2003904.
- [246] H. Palneedi, S. Annapureddy, V. Priya, J. Ryu, “Status and Perspectives of Multiferroic Magnetoelectric Composite Materials and Applications”, *Actuators* **5** (2016) 2.
- [247] D. Bochenek, Z. Suroviak, “Multiferroic materials for sensors, transducers and memory devices”, *Arch. Acoust.* **33** (2) (2008) 243.

- [248] J. Das, Y.Y. Song, M. Wu, “Electric-field control of ferromagnetic resonance in monolithic $\text{BaFe}_{12}\text{O}_{19}$ - $\text{Ba}_{0.5}\text{Sr}_{0.5}\text{TiO}_3$ heterostructures”, *J. Appl. Phys.* **108** (2010) 043911.
- [249] C.W. Nan, M.I. Bichurin, S. Dong, D. Viehland, G. Srinivasan, “Multiferroic magnetoelectric composites: Historical perspective, status, and future directions”, *J. Appl. Phys.* **103** (2008) 031101.
- [250] J. Smit, H.P.J. Wijn, *Ferrite*, Philips Tech Lib., Eindhoven (1960).
- [251] Ashima, S. Sanghi, A. Agarwal, Reetu, “Rietveld refinement, electrical properties and magnetic characteristics of Ca-Sr substituted barium hexaferrites”, *J. Alloy Compd.* **513** (2012) 436.
- [252] M.N. Ashiq, M.J. Iqbal, I.H. Gul, “Structural, magnetic and dielectric properties of Zr-Cd substituted strontium hexaferrite ($\text{SrFe}_{12}\text{O}_{19}$) nanoparticles”, *J. Alloy Compd.* **487** (2009) 341.
- [253] P. Campbell, “Permanent Magnet Materials and Their Application”, Cambridge University Press, Cambridge, (1994).
- [254] H. Kojima, in: E.P. Wohlfarth (Ed.) *Fundamental Properties of Hexagonal Ferrites with Magnetoplumbite Structure: Ferromagnetic Materials*, 3, North Holland Publ. Comp. Amsterdam, **3** (1982).
- [255] R.C. Pullar, “Hexagonal ferrites: A review of the synthesis, properties and applications of the hexaferrite ceramics”, *Prog. Mater. Sci.* **57** (2012) 1191.
- [256] Z. Gao, Y. Pu, M. Yao, Q. Jin, Y. Wang, H. Zheng, “Superior electromagnetic properties obtained by enhanced resistivity on multiferroic barium titanate and hexaferrite di-phase composite ceramics”, *Ceram. Int.* **43** (2017) S85.
- [257] R. Pattanayak, R. Muduli, R.K. Panda, T. Dash, P. Sahu, S. Raut, S. Panigrahi, “Investigating the effect of multiple grain-grain interfaces on electric and magnetic properties of [50 wt% $\text{BaFe}_{12}\text{O}_{19}$ -50 wt% $\text{Na}_{0.5}\text{Bi}_{0.5}\text{TiO}_3$] composite system”, *Physica B* **485** (2016) 67.
- [258] A. Srinivas, R. Gopalan, V. Chandrasekharan, “Room temperature multiferroism and magnetoelectric coupling in BaTiO_3 - $\text{BaFe}_{12}\text{O}_{19}$ system”, *Solid State Comm.* **149** (2009) 367.
- [259] R. Pattanayak, S. Raut, S. Kuila, M. Chandrasekhar, S. Panigrahi, “Multiferroism of [$\text{Na}_{0.5}\text{Bi}_{0.5}\text{TiO}_3$ - $\text{BaFe}_{12}\text{O}_{19}$] lead-free novel composite systems”, *Mat. Lett.* **209** (2016) 280.

- [260] S.V. Trukhanov, A.V. Trukhanov, M.M. Salem, E.L. Trukhanova, L.V. Panina, V.G. Kostishyn, M.A. Darwish, An. V. Trukhanov, T.I. Zubar, D.I. Tishkevich, V. Sivakov, D.A. Vinnik, S.A. Gudkova, C. Singh, "Preparation and investigation of structure, magnetic and dielectric properties of $(\text{BaFe}_{11.9}\text{Al}_{0.1}\text{O}_{19})_{1-x}(\text{BaTiO}_3)_x$ bicomponent ceramics", *Ceram. Int.* **44** (2018) 21295.
- [261] Y. Tokunaga, Y. Kaneko, D. Okuyama, S. Ishiwata, T. Arima, S. Wakimoto, K. Kakurai, Y. Taguchi, Y. Tokura, "Multiferroic M-Type Hexaferrites with a Room-Temperature Conical State and Magnetically Controllable Spin Helicity", *Phys. Rev. Lett.* **105** (2010) 257201.
- [262] Y. Hiruma, H. Nagata, T. Takenaka, "Detection of morphotropic phase boundary of $(\text{Bi}_{1/2}\text{Na}_{1/2})\text{TiO}_3\text{-Ba}(\text{Al}_{1/2}\text{Sb}_{1/2})\text{O}_3$ solid solution ceramics", *Appl. Phys. Lett.* **95** (2009) 052903.
- [263] S. Kumar, S. Supriya, M. Kar, "Correlation between temperature dependent dielectric and DC resistivity of Cr substituted barium hexaferrite", *Mater. Res. Exp.* **4** (2017) 126302.
- [264] G.L. Tan, W. Li, "Ferroelectricity and Ferromagnetism of M-Type Lead Hexaferrite", *J. Amer. Ceram. Soc.* **98** (2015) 1812.
- [265] G. Tan, X. Chen, "Structure and multiferroic properties of barium hexaferrite ceramics", *J. Magn. Magn. Mater.* **327** (2013) 87.
- [266] T. Kimura, G. Lawes, A.P. Ramirez, "Electric Polarization Rotation in a Hexaferrite with Long Wavelength Magnetic Structures", *Phys. Rev. Lett.* **94** (2005) 137201.
- [267] S.V. Trukhanov, A.V. Trukhanov, V.G. Kostishyn, L.V. Panina, An. V. Trukhanov, V.A. Turchenko, D.I. Tishkevich, E.L. Trukhanova, V.V. Oleyanik, O.S. Yakovenko, L.Y. Matzui, D.A. Vinnik, "Magnetic, dielectric and microwave properties of the $\text{BaFe}_{12-x}\text{Ga}_x\text{O}_{19}$ ($x < 1.2$) solid solutions at room temperature", *J. Magn. Magn. Mater.* **442** (2017) 300.
- [268] S.V. Trukhanov, A.V. Trukhanov, V.G. Kostishyn, L.V. Panina, An. V. Trukhanov, V.A. Turchenko, D.I. Tishkevich, E.L. Trukhanova, V.V. Oleyanik, O.S. Yakovenko, L.Y. Matzui, "Investigation into the structural features and microwave absorption of doped barium hexaferrites", *Dalton Trans.* **46** (2017) 9010.

- [269] S.V. Trukhanov, A.V. Trukhanov, V.G. Kostishyn, L.V. Panina, An. V. Trukhanov, V.A. Turchenko, D.I. Tishkevich, E.L. Trukhanova, O.S. Yakovenko, L.Y. Matzui, D.A. Vinnik, D.V. Karpinsky, “Effect of gallium doping on electromagnetic properties of barium hexaferrites”, *J. Phys. Chem. Sol.* **111** (2017) 142.
- [270] P. Kumar, A. Gaur, “Signature of multiferroicity and pyroelectricity close to room temperature in BaFe₁₂O₁₉ hexaferrite”, *Ceram. Int.* **43** (2017) 16403.
- [271] R. Grossinger, “Correlation between the inhomogeneity and magnetic anisotropy in polycrystalline ferromagnetic materials”, *J. Magn. Magn. Mater.* **28** (1982) 137.
- [272] S.B. Narang, C. Singh, Y. Bai, I.S. Hudiara, “Microstructure, hysteresis and microwave absorption analysis of Ba_{1-x}Sr_xFe₁₂O₁₉ ferrite”, *Mater. Chem. Phys.* **111** (2008) 225.
- [273] Z.W. Li, C.K. Ong, Z. Yang, F.L. Wei, X.Z. Zhou, J.H. Zhao, A.H. Morrish, “Site preference and magnetic properties for a perpendicular recording material: BaFe_{12-x}Zn_{x/2}Zr_{x/2}O₁₉ nanoparticles”, *Phys. Rev. B* **62** (2000) 6530.
- [274] O. Kubo, T. Ido, H. Yokoyama, “Properties of Ba ferrite particles for perpendicular magnetic recording media”, *IEEE Trans. Mag.* **18** (1982) 1122.
- [275] M. Han, Y. Hu, W. Chen, L. Deng, “Magnetic properties of Ba-M type hexagonal ferrites prepared by the sol-gel method with and without polyethylene glycol added”, *J. Alloy Compd.* **474** (2009) 185.
- [276] A. Ghasemi, A. Morisako, “Static and high frequency magnetic properties of Mn-Co-Zr substituted Ba-ferrite”, *J. Alloy Compd.* **456** (2008) 485.
- [277] C.G. Duan, J.P. Velev, R.F. Sabirianov, W.N. Mei, S.S. Jaswal, E.Y. Tsymlal, “Tailoring magnetic anisotropy at the ferromagnetic/ferroelectric interface”, *Appl. Phys. Lett.* **92** (2008) 122905.
- [278] J.K. Murthy, C. Mitra, S. Ram, A. Venimadhav, “Temperature dependent magnetic and dielectric properties of M-type hexagonal BaFe₁₂O₁₉ nanoparticles”, *J. Alloy Compd.* **545** (2012) 225.
- [279] Y. Ying, T.W. Eom, Y.P. Lee, L.S. Ling, V.L. Mathe, “Detailed magnetic structure of Zn_{1-x}Ni_xFe₂O₄ nanoparticles”, *J. Appl. Phys.* **108** (2010) 023911.
- [280] N. Adhlakha, K.L. Yadav, R. Singh, “Implications of La and Y co-doping on structural, multiferroic, magnetoelectric and optical properties of BiFeO₃”, *Sci. Adv. Mater.* **5** (2013) 947.

- [281] E. Barsoukov, J.R. Macdonald, "Impedance Spectroscopy Theory, Experiments and Applications", 2nd ed, Wiley, Hoboken, NJ (2005) 46.
- [282] R. Gerhardt, "Impedance and dielectric revisited: distinguishing from long-range conductivity", *J. Phys. Chem. Solids* **55** (1995) 1491.
- [283] F.D. Morrison, D.C. Sinclair, A.R. West, "Characterization of lanthanum doped barium titanate ceramics using impedance spectroscopy", *J. Amer. Ceram. Soc.* **84** (2001) 531.
- [284] R. Pattanayak, S. Raut, K.L. Routray, S. Panigrahi, "Investigating the microstructural conduction mechanism of (1-x) Na_{0.5}Bi_{0.5}TiO₃-(x) BaFe₁₂O₁₉ [x in wt.% = 10, 20, 30 and 40] novel magnetoelectric ceramic composite systems", *Physica B* **520** (2017) 43.
- [285] V.B. Saradhi, K. Srinivas, G. Prasad, S.V. Suryanarayana, T. Bhimasankaram, "Impedance spectroscopic studies in ferroelectric (Na_{1/2}Bi_{1/2})TiO₃", *Mater. Sci. Engg. B* **98** (2003) 10.
- [286] A.R. James, S. Priya, K. Uchino, K. Srinivas, "Dielectric spectroscopy of Pb(Mg_{1/3}Nb_{2/3})O₃-PbTiO₃ single crystals", *J. Appl. Phys.* **90** (2001) 3504.
- [287] M.M. Costa, G.F.M. Pires, A.J. Terejo, M.P.F. Graca, A.S.B. Sombra, "Impedance and modulus studies of magnetic ceramic oxide Ba₂Co₂Fe₁₂O₂₂ (Co₂Y) doped with Bi₂O₃", *J. Appl. Phys.* **110** (2011) 034107.
- [288] N. Ortega, A. Kumar, P. Bhattacharya, S.B. Majumder, R.S. Katiyar, "Impedance spectroscopic studies of multiferroic PbZr_xTi_{1-x}O₃-CoFe₂O₄ layered thin films", *Phys. Rev. B* **77** (2008) 14111.
- [289] R. Pattanayak, S. Panigrahi, T. Dash, R. Muduli, D. Behera, "Electric transport properties study of bulk BaFe₁₂O₁₉ by complex impedance-spectroscopy", *Physica B* **474** (2015) 57.
- [290] K. Prasad, L.K. Kumari, K.P. Chandra, K.L. Yadav and S. Sen, "Electrical conduction in (Na_{0.5}Bi_{0.5})TiO₃ ceramic: impedance spectroscopy analysis", *Adv. Appl. Ceram.* **106** (2007) 241.
- [291] M. Atif, M. Nadeem, W. Khalid, Z. Ali, "Structural, magnetic and impedance spectroscopy analysis of (0.7) CoFe₂O₄-(0.3) BaTiO₃ magnetoelectric composite", *Mater. Res. Bull.* **107** (2018) 171.
- [292] C.G. Duan, "Interface/surface magnetoelectric effects: New routes to the electric field control of magnetism", *Front. Phys.* **7** (2012) 375.

- [293] R. Pattanayak, S. Kulia, S. Raut, S.P. Ghosh, S. Dhal, S. Panigrahi, “Observation of grain size effect on multiferroism and magnetoelectric coupling of $\text{Na}_{0.5}\text{Bi}_{0.5}\text{TiO}_3$ - $\text{BaFe}_{12}\text{O}_{19}$ novel composite system”, *J. Magn. Magn. Mater.* **444** (2017) 401.

List of Publications

Articles in journals

- [1] Structural, dielectric, magnetic and magnetoelectric properties of (x) $\text{Bi}_{0.5}\text{Na}_{0.5}\text{TiO}_3$ - $(1-x)$ $\text{Ni}_{0.2}\text{Co}_{0.8}\text{Fe}_2\text{O}_4$ composites, Yogesh Kumar, K.L. Yadav, Manjusha, Jyoti Shah and R.K. Kotnala, **Materials Research Express**, **3** (2016) **065701-1-9**.
- [2] Study of structural, dielectric, electric, magnetic and magnetoelectric properties of $\text{K}_{0.5}\text{Na}_{0.5}\text{NbO}_3$ - $\text{Ni}_{0.2}\text{Co}_{0.8}\text{Fe}_2\text{O}_4$ composites, Yogesh Kumar, K.L. Yadav, Manjusha, Jyoti Shah, R.K. Kotnala, **Ceramics International**, **43** (2017) **13438-13446**.
- [3] Synthesis and study of structural, dielectric, magnetic and magnetoelectric properties of $\text{K}_{0.5}\text{Na}_{0.5}\text{NbO}_3$ - $\text{CoMn}_{0.2}\text{Fe}_{1.8}\text{O}_4$ composites, Yogesh Kumar, K.L. Yadav, **Journal of Materials Science: Materials in Electronics**, **29** (2018) **8923-8936**.
- [4] Dielectric, magnetic and magnetoelectric properties of ferrite-ferroelectric based particulate composites, **Materials Research Express**, **5** (2018) **085701-1-11**.
- [5] Investigation of magnetoelectric effect in $\text{Bi}_{0.5}\text{Na}_{0.5}\text{TiO}_3$ - $\text{CoMn}_{0.2}\text{Fe}_{1.8}\text{O}_4$ composites, Yogesh Kumar, K.L. Yadav, Jyoti Shah and R.K. Kotnala, **IEEE Transactions on Dielectrics and Electrical Insulation**, **26** (2) (2019) **561-567**
- [6] Investigation of magnetoelectric effect in lead free $\text{K}_{0.5}\text{Na}_{0.5}\text{NbO}_3$ - $\text{BaFe}_{12}\text{O}_{19}$ novel composite system, Yogesh Kumar, K.L. Yadav, Jyoti Shah, R.K. Kotnala, **Journal of Advanced Ceramics**, **8** (3) (2019) **333-344**.
- [7] Dielectric, magnetic and electrical properties of $\text{Bi}_{0.5}\text{Na}_{0.5}\text{TiO}_3$ - $\text{CoMn}_{0.2}\text{Fe}_{1.8}\text{O}_4$ composites, Yogesh Kumar and K.L. Yadav, **AIP Conference Proceedings** **1731** (2016) **050090-1-3**.

Conferences/ Workshops Attended

- [1] DAE- Solid State Physics Symposium
Amity University, Noida, U.P. (India)
December 26-30, 2015

List of Publications

- [2] 19th National Seminar on Ferroelectrics and Dielectrics
Maulana Azad National Institute of Technology, Bhopal, M.P. (India)
December 19-21, 2016

- [3] INUP Familiarization Workshop on Nanofabrication Technologies
Indian Institute of Technology Roorkee, Roorkee, Uttarakhand (India)
April 27-28, 2017

- [4] International Meeting on Energy Storage Devices
Indian Institute of Technology Roorkee, Roorkee, Uttarakhand (India)
December 10-12, 2018